Mixed Convection Heat Transfer Enhancement in Lid-Driven Cavities Filled with Nanofluids

Thesis submitted for the degree of

Doctor of Philosophy

at the University of Leicester

by

Ali Khaleel Kareem Al-Khafaji

Department of Engineering

University of Leicester

United Kingdom

June 2018

Abstract

Mixed Convection Heat Transfer Enhancement in Lid-Driven Cavities Filled with Nanofluids

Ali Khaleel Kareem

Mixed convection heat transfer in enclosures has been studied in order to enhance the associated heat transfer performance through the use of either different convective fluid types, domain configurations, boundary conditions, or combinations thereof. Analysing the enhancement in heat transfer has been accomplished through the isotherm and streamline contours, temperature isosurfaces, flow vectors, mean and root mean square velocity profiles, turbulence kinetic energy profiles and Nusselt number profiles. Firstly, laminar mixed convection in a lid-driven trapezoidal cavity using different nanoparticle types and various parameters other than configuration parameters has been investigated. It was found that any nanofluid types can provide greater heat transfer than water, especially, at high nanoparticle volume fraction and low diameter. Heat convection can be affected by changing either rotational and inclination angles, aspect ratio, or flow direction. Secondly, turbulent mixed convection due to the moving sidewalls of a lid-driven cuboid has been analysed. Remarkable enhancement in heat transfer has been achieved by either increasing the turbulent flow circulation or using nanofluids. Thirdly, turbulent mixed convection in a top wall lid-driven cuboid containing a clockwise- or anticlockwise-rotating cylinder has been studied. Significant enhancement in heat convection was noticed with the use of the rotating cylinder, especially when the direction of rotation can enhance the top wall movement. In addition, the Reynolds number and nanofluids have a positive impact on the heat transfer in the presence of the rotating cylinder. Finally, the study has been extended by artificially roughening the heated wall in order to increase the heat transfer rate. A noteworthy enhancement has been found due to the use of two rib shapes, particularly in combination with the rotating cylinder. Overall, in terms of the comparison between the URANS and LES predictions, even though both methods have performed well, the LES approach is more successful in capturing more detail of the secondary eddies.

List of publications

One journal paper has been published from the content of Chapter 4. Two journal papers and one conference paper have been taken and published from the material of Chapter 5. Two journal papers and one conference paper have been extracted and published from the results of Chapter 6. Finally, from the outcomes of Chapter 7, one journal paper and one conference paper have been excerpted and published.

Journal papers:

Journal paper 1	A.K. Kareem, H. Mohammed, A.K. Hussein, S. Gao, Numerical investigation of mixed convection heat transfer of nanofluids in a lid-driven trapezoidal cavity, International Communications in Heat and Mass Transfer, 77 (2016) 195–205.
Journal paper 2	A.K. Kareem, S. Gao, A.Q. Ahmed, Unsteady simulations of mixed convection heat transfer in a 3D closed lid-driven cavity, International Journal of Heat and Mass Transfer, 100 (2016) 121-130.
Journal paper 3	A.K. Kareem, S. Gao, Computational study of unsteady mixed convection heat transfer of nanofluids in a 3D closed lid-driven cavity, International Communications in Heat and Mass Transfer, 82 (2017) 125-138.
Journal paper 4	A.K. Kareem, S. Gao, Mixed convection heat transfer of turbulent flow in a three-dimensional lid-driven cavity with a rotating cylinder, International Journal of Heat and Mass Transfer, 112 (2017) 185-200.
Journal paper 5	A.K. Kareem, S. Gao, A comparison study of mixed convection heat transfer of turbulent nanofluid flow in a three-dimensional lid-driven enclosure with a clockwise versus an

	anticlockwise rotating cylinder, International Communications in Heat and Mass Transfer, 90 (2018) 44-55.
Journal paper 6	A.K. Kareem, S. Gao, Mixed convection heat transfer enhancement in a cubic lid-driven cavity containing a rotating cylinder through the introduction of artificial roughness on the heated wall, Physics of Fluids, 30(2) (2018) 025103.

Conference papers:

Conference paper 1	A.K. Kareem, S. Gao, CFD Investigation of Turbulent Mixed Convection Heat Transfer in a Closed Lid-Driven Cavity, International Journal of Civil, Environmental, Structural, Construction and Architectural Engineering Vol: 9, No:12, 2015.
Conference paper 2	A.K. Kareem, S. Gao, Mixed turbulent convection heat transfer in a 3D lid-driven cavity containing a rotating cylinder, ISER - 257th International Conference on Heat Transfer and Fluid Flow (ICHTFF), Toronto, Canada, 28^{th}-29^{th} January 2018.
Conference paper 3	A.K. Kareem, S. Gao, A. Q. Ahmed, Heat transfer enhancement of mixed convection in cubic lid-driven cavity containing a rotating cylinder by applying an artificial roughness on the heated wall World Academy of Science, Engineering and Technology International Journal of Mechanical and Mechatronics Engineering, Netherlands, Amsterdam, Vol:12, No:5, 2018.

Acknowledgment

First and foremost, I would like to express my special gratitude towards ‘ALLAH’, for giving me the strength and faith to complete my Ph.D, as I feel very fortunate to be blessed by his endless love.

After an intensive period of years, today is the day: writing this note of thanks is the finishing touch on my thesis. It has been a period of intense learning for me, not only in the scientific arena, but also on a personal level. Writing this thesis has had a big impact on me. I would like to reflect on the people who have supported and helped me so much throughout this period.

I would first like to thank my supervisor Dr Shian Gao for his continuous supervision and encouragement through my Ph.D. Additionally, I would like to thank my co-supervisor Dr Aldo Rona and my examiners for their effort during my Ph.D progress.

My appreciation goes to my colleagues in the engineering department (Thermal Engineering Group) for their help and their support during my research, besides warm thanks to Dr Ines Hassen for her help and support. Also, I would like to thank the Ministry of Higher Education and Scientific Research of Iraq for the financial support of the project, as well as the University of Thi-Qar for offering me the scholarship.

I would also like to thank my friends for their diligent assistance throughout the period of this thesis. Finally, words alone cannot express my thanks I owe to my lovely parents and siblings for their wise counsel and sympathetic ear. You are always there for me.

Ali Khaleel Kareem

June / 2018

Table of contents

List of figures

List of tables

Abbreviations

A	aspect ratio
Au	Gold
Al_2O_3	aluminium oxide
C	Smagorinsky coefficient
C_P	specific heat at constant pressure (J/kg K)
Cu	Copper
CuO	copper oxide
CO_2	carbon dioxide
CFL	Courant-Friedrichs-Lewy number
CFD	Computational Fluid Dynamics
E	dimensionless length of the heat source (l/L)
e	rib height (mm)
e/D_h	relative roughness height
FEM	finite element method
FDM	finite difference method
FVM	finite volume method
Gr	Grashof number ($g\beta_m \Delta T W^3/\nu_m^2$)
h	convective heat transfer coefficient (W/m^2K)
Ha	Hartmann number
k	turbulence kinetic energy (m^2/s^2)
L	width of the cavity (m)
LES	large eddy simulation method
M	molecular weight for base fluid
MEMS	microelectromechanical
MHD	magnetohydrodynamics
N	Avogadro number
Nu	Nusselt number
p	rib pitch (mm)
p/e	relative roughness pitch
Pr	Prandtl number (ν_m/α_m)
q''	heat flux (W/m^2)

Ra	Rayleigh number (Gr * Pr)
Re	Reynolds number ($U_{o*}W/v$)
Ri	Richardson number (Gr/Re^2)
RANS	Reynolds-Averaged Navier-Stokes equations
RMS	root mean square
R-c	half-circle roughness rib case
R-s	square roughness rib case
SiO_2	silicon dioxide
$\bar{S}_{ij}$	large-scale strain rate tensor for grid-filter
T	temperature of the fluid (K)
t	Time
TiO_2	titanium dioxide
TKE	turbulence kinetic energy (m^2/s^2)
u	velocity component at x-direction (m/s)
U	dimensionless velocity component at x-direction
U_0	lid velocity (m/s)
UDFs	User Defined Functions
v	velocity component at y-direction (m/s)
V	dimensionless velocity component at y-direction
W	dimensionless velocity component at z-direction
l	length of the heat source (m)
x	distance along the x-coordinate
X	distance along the non-dimensional x-coordinate (x/L)
Y	distance along the non-dimensional y-coordinate (y/H)
y^+	non-dimensional wall distance for a wall-bounded flow
Z	distance along the non-dimensional z-coordinate (z/D)
ZnO	zinc oxide
S	smooth bottom wall case

Greek symbols:

α	thermal diffusivity of the fluid (m^2/s)
α	under-relaxation factor

β	volumetric coefficient of thermal expansion (1/K)
μ	dynamic viscosity of the fluid (Pa/s)
v	kinematic viscosity of the fluid (m^2/s)
ν_{sgs}	sub-grid scale (SGS) viscosity
θ	dimensionless temperature
ρ	density of the fluid (kg/m^3)
ε	dissipation rate of turbulence kinetic energy (m^2/s^3)
δ_{ij}	Kronecker's delta
$\bar{\Delta}$	grid-filter width
τ_{ij}	subgrid-scale (SGS) stress tensor
ϕ	nanoparticle volume fraction
Ω	dimensionless rotational speed
Φ	rotational angle
γ	inclination angle
ω	rotational speed (rad/s)

Subscripts:

av	average value
b	Buoyancy
bf	base fluid
C	value of cold temperature
eff	Effective
H	value of hot temperature
m	mixture
nf	Nanofluid
np	nanoparticles
rms	root mean square
s	Source
sgs	subgrid-scale
t	Turbulent

Chapter 1 Introduction

1.1 Context

For a long time, one of the major engineering challenges has been heat transfer enhancement. The heat input into a system or the removal of heat produced in a system represents the different types of heat transfer processes, for example, removing heat from computer chips or optical devices, cooling systems for power plants, refrigeration, gas-turbine engines regenerators, indoor temperature control, etc. Directly or indirectly, the above heat transfer applications affect people's daily lives and encourage the conduct of new research in order to enhance their efficiency. From an engineering point of view, mixed convection using liquid coolants in either a laminar or turbulent flow regime is always a key heat transport solution. Sundry enhancement techniques have been discovered over the last years [1], including heat transfer surface roughness modification, rotating an obstacle object within domains, extended surfaces using fins and surface vibration. Nonetheless, these techniques have shown some drawbacks, such as dramatically higher pressure loss, and requiring an increased pumping power.

Convective thermal performance is often inefficient and creates barriers to designing heat rejecting devices by involving common heat transfer liquids such as water, ethylene glycol, ammonia, and mineral oil, which possess low thermal conductivity. Subsequently, an innovative coolant with improved heat transfer properties has been discovered by Maxwell [2], who developed the heat transfer performance of classic poor conventional fluid by mixing it with solid particles, the latter usually exhibiting greater thermal conductivity than conventional liquids. However, Maxwell's concept is outdated and has some disadvantages such as high-pressure drop as well as clogging of the channel, and sedimentation. This cannot be, therefore, used in microchannel flow. This innovation was further developed by Ahuja [3, 4] in 1975 to inspect polystyrene suspensions, who proceeded with a series of experiments of 50 – 100 μm diameter polystyrene particles spheres mixed within water. It was concluded that the effective thermal conductivity of the liquid coolants was highly improved.

However, the size of the particles was correspondingly not small enough (on the microscale) to be used perfectly, especially in small devices, because of the deficiency of technology at the time. When using microparticles or larger particle suspensions, diverse obstacles can be met due to the particles' size. However, the stability of the particles could not subsequently be reached. Erosion to flow loop components could arise through the use of microparticles. Although such large suspensions promise enhanced heat transfer ability, they have not yet been extensively used as alternative coolants.

Afterwards, a speedy growth in both manufacturing techniques and nanotechnology is considered the most important force impacting the major industrial and engineering revolution of the 21st century. The production of nanoparticles in terms of particle size (100 nm or less) has become possible. A nanofluid is a mixture of a base fluid such as water, ethylene or mineral oil that contains a low conductivity with suspended metallic nanoparticles such as Al_2O_3, CuO and TiO_2, which have a higher conductivity. The first impression of utilizing a small nanoparticle volume fraction has been observed to give greater than expected effective thermal conductivity, which provides a higher heat transfer coefficient [5, 6]. Researchers have also given considerable attention to the use of nanoparticles as additives to modify heat transfer of classic fluids and their thermal performance [7-15]. It is known that nanofluids can be treated as a homogeneous single-phase fluid or as a two-phase fluid [16]. When the base fluid and nanoparticles have the same values of velocity and temperature, it is called a 'single-phase flow', whereas if nanoparticles and the base fluid have different values of velocity and temperature, it is called a 'two-phase flow'.

On the other hand, cavity configurations and fluid types have significant effects on heat convection. Geometric shapes, fluid types and boundary conditions should be understood in order to solve the heat transfer convection problem. Lid-driven cavity is a recognized benchmark case for viscous incompressible fluid flow deals with cavity consisting of rigid walls with no-slip conditions and lid moving with a tangential unit velocity. There are many geometric shapes for enclosures or lid-driven cavities which have been analysed over the past few years, with different boundary conditions such as rectangular, circular and triangular.

Furthermore, both natural and mixed convection heat transfer types, in an enclosure or in a moving wall cavity, have been investigated in many studies by using either conventional fluids or nanofluids. A sizable amount of research has been accomplished in the last decades on both types of convection heat transfer. Many industrial and engineering applications of heat convection, such as air cooling devices and nuclear power plants [17-22], currently exist and should be therefore considered for improvement. Controlling heat convection transfer by either increasing or decreasing heat convection has numerous benefits for energy saving as well as for increasing device life and safety.

The expansion of Computational Fluid Dynamics (CFD) regarding convection heat transfer studies has rapidly developed over the years for both natural and mixed convection simulations. Hence, investigations using nanofluids in heat convection have emerged over the last few years due to their usefulness. As a result, the heat convection and nanofluids concepts should be explored and understood in more depth while acknowledging the context in which the current research is evolving.

1.2 Aims and objectives

Despite the fact that mixed convection heat transfer in enclosures has been widely studied over the last few years, it represents a broad range of different heat transfer and fluid flow cases within the different types of cavities, such as the obstructed cavity and lid-driven cavity. Heat transfer enhancement in lid-driven in the last few years has been growing interest in terms of increasing the heat transfer rate of convective cases. Since, mixed convection in moving wall cavity can represent many engineering and industrial application such as, electronic cooling, solar energy and oil extraction. Thus, several aspects have been addressed in the literature such as different enclosure shapes, boundary conditions, coolants, laminar and turbulent methods and models, etc. That could explain how much this field can be dramatically extended. Nonetheless, many areas have not been covered over the years. Therefore, the flexibility of developing and covering further aspects has helped to motivate the present research to be carried out by discovering some areas that have not been filled yet.

Accordingly, three different shapes of geometries have been designed in this project to investigate mixed convection heat transfers and flow patterns, which are the trapezoidal lid-driven enclosure, cubic double sides lid-driven enclosure and cubic lid-driven enclosure, which contain a central rotating cylinder. Laminar and turbulent flows are involved in this research as well as two different turbulent methods where RANS and LES methods are utilized. Both the conventional fluid, and the nanofluids, under different conditions, are investigated.

The first aim will be carried out with 2D laminar mixed convective flows in a trapezoidal enclosure using different types of nanofluids, volume fractions, nanoparticle diameters, Richardson numbers, enclosure rotational angles, inclined sidewall angles as well as various aspect ratios and lid-driven flow directions.

The second aim will be undertaken through a comprehensive evaluation which aims to compare the ability and the accuracy of the URANS and LES methods. This study will also analyse the flow patterns and temperature distributions of mixed convection heat transfer in a 3D two-sided cubic lid-driven enclosure with different values of Reynolds number in detail.

The third aim will address several fundamental issues on nanofluids besides pure water; it is important to have a better understanding of two-phase mixture nanofluids within a 3D geometry. It is also crucial to investigate the effects of the different types of nanoparticles and their concentration and diameter size while accurately predicting the turbulent flow and heat distribution details inside the cavity.

The fourth aim will be accomplished for a turbulent mixed convection heat transfer of a 3D rotating cylinder within the enclosure using the URANS and LES approaches. Involving nanofluids within such a geometry can lead to new predictions in mixed convection heat transfer.

The fifth aim will be an extension of previous publication of the present authors [23] (the fourth aim in existing research). The aim is to analyse the effect of the 3D rotating cylinder speeds and directions (clockwise and anticlockwise), within a top lid-driven closed cavity on the turbulent nanofluid flow using the URANS method; this study addresses the main point of emphasis of this thesis.

The sixth aim is to investigate the artificial roughness of the bottom heated wall of the top lid-driven wall cavity. Two different shapes of artificial roughness were designed and compared with the smooth bottom wall of the domain to enhance the heat transfer. The URANS method was used to deal with turbulent flow for Reynolds numbers of 5,000 and 10,000. Anticlockwise and clockwise directions of the central rotating cylinder at different rotational speeds have been considered.

This study is concerned with the numerical investigation of mixed convection flows in lid-driven enclosures. The objectives below have guided the conduct of this research and have framed the content of each chapter. The objectives of this research are as follows:

- To enhance heat transfer performance in various lid-driven cases.
- To study nanofluid mechanisms that govern the heat transfer enhancement and analyse the effects of different types of nanoparticles with different volume fractions and different diameter sizes of nanoparticles in the nanofluid.
- To analyse the effects of the rotational angles and inclination angles of the enclosure and examine the effects of the moving walls, either in the positive or negative direction, with gravity.
- To understand the influences of different values of the rotational speed and direction of the central cylinder, Reynolds and Richardson numbers on heat transfer and flow patterns.

- To understand the behavers of laminar and turbulent flow within a lid-driven enclosure using different methods such as Laminar, RANS, URANS and LES for different geometries and boundary conditions.
- To comprehend the effects of different artificial roughness types on heat transfer enhancement.

1.3 Thesis structure

This thesis contains eight chapters. Subsequent to the introduction, which introduces the context as well as the main aims and objectives of this research, the second chapter presents a review of the existing literature related to natural and mixed convection heat and mass transfer of conventional fluids and nanofluids within different geometry shapes and boundary conditions. This chapter also includes some additional objectives inside the enclosure, such as the use of a rotating cylinder.

The governing and discretized equations, and thermal-physical properties of the working fluids that are used in this study are written in chapter three. The URANS and LES methods are illustrated. The numerical schemes, numerical solvers, pressure-velocity coupling and under relaxation factor, as well as the SIMPLE and SIMPLEC algorithms, are also presented.

Chapter four includes new findings and focusses on the influences of various nanoparticle types when mixed with pure water, the concentration of nanoparticles within the conventional liquid, nanoparticle diameters, rotational angles of the domain and inclination angles of the domain sidewalls, domain aspect ratio and lid-driven direction at different Richardson numbers.

The fifth chapter reveals the second set of findings of this thesis. This chapter contains the second and third aims of the current investigation. The second concentrates on unsteady simulation of mixed convection of pure water in a 3D closed lid-driven cubic cavity, and the third one focusses on using different nanofluid kinds beside pure water at same conditions of the second aim, as mentioned under the aims and objectives subsection of Chapter one. A comparison between the URANS and the LES methods in terms of velocity vectors, instantaneous temperature field and average Nusselt number is included.

In Chapter six, mixed convection in a 3D lid-driven cavity with a rotating cylinder is completed, which correspond to both the fourth and the fifth goals of this research. Firstly, the heat transfer increment of a pure water-filled top moving wall cavity and containing an anticlockwise rotating cylinder will be investigated. The use of nanofluid with clockwise versus an anticlockwise rotating cylinder of a top lid-driven enclosure corresponds to the second investigation in this chapter. Several different result terms are completed in this chapter involving steady and Unsteady RANS and LES approaches, such as the flow and thermal fields, velocity distribution and vectors, heat transfer characteristics, wall shear stress, turbulence kinetic energy and Nusselt number.

In Chapter seven, the heat transfer enhancement of mixed convection in a cubic lid-driven cavity which contains a rotating cylinder and applying an artificial roughness on the heated bottom wall, is measured. This chapter includes a comparative study of the different rips shapes of artificial roughness and smooth plate for the bottom wall with the aim of analysing the influence on heat enhancement by studying the flow and thermal fields, mean velocity profile, wall shear stress, turbulence kinetic energy and Nusselt number.

Finally, Chapter eight will use the research and findings of the previous chapters to address the thesis questions and goals regarding heat transfer enhancement in obstructed lid-driven cavities and provide some recommendations for future study.

Chapter 2 Literature review

2.1 Cavities shapes and configurations

Considerable research into cases of convective heat transfer has been completed for diverse cavity shapes and configurations as filled by either conventional fluids or nanofluids, and considering various boundary conditions and dimensionless parameters such as Richardson, Reynolds, Rayleigh and Prandtl numbers. Heat convection occurring in enclosures or in lid-driven cavities is one of most marked investigations in thermo-fluids fields because heat transfer convection in cavities has wide industrial and engineering applications with regards to natural and mixed convection.

2.1.1 Natural convection

Natural convection takes place when fluid motion is not affected by any kind of external force as a result of thermal non-homogeneity of boundaries or density differences in the fluid caused by temperature gradients [24]. Natural convection heat transfer, in particular, has many benefits on our industrial and engineering lives. For instance, solar collectors, food preservation, heat exchangers, electronic cooling systems, nuclear and chemical reactors, double-glazed windows, thermal storage systems and drying, furnace engineering, refrigerators and room ventilating, stratified atmosphere boundary layers, flooding protection for buried pipes and solidification processes, microfluidic components, thermal insulation of pipes buried in the ground, atmospheric currents, thermal design of buildings and their location, and design of the safety alarms [20, 21, 25-39]. Figure 2-1 shows a practical enclosure that can represent a nuclear reactor or electronic components cabin in the event of a leak in a sodium pipeline.

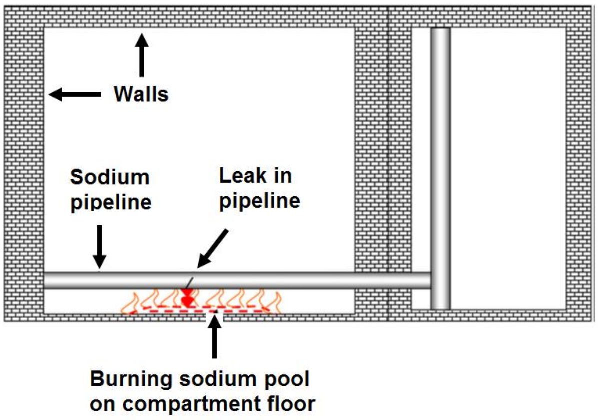

Figure 2-1: Schematic diagram of a practical enclosure [34].

Figure 2-2 shows an application of using natural heat convection in terms of solar energy cavity and in the meantime this figure also displays two different types of convective fluids that can be used as convection media.

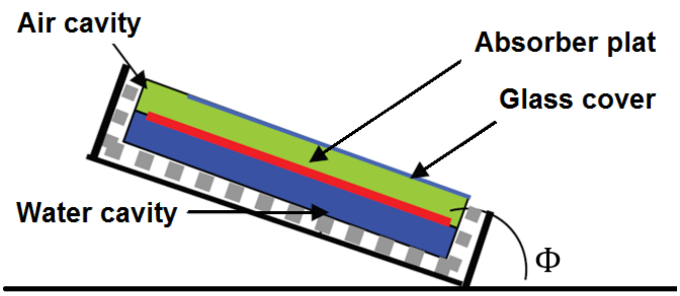

Figure 2-2: Schematic diagram of an integrated collector storage solar water heater [40].

Over the years, many studies have been carried out numerically or experimentally to quantify the natural convection in different shapes and boundary conditions of enclosures filled by conventional fluids. Changing enclosure parameters such as inclination or rotational angles, using wavy walls instead of flat ones, geometry shapes, have been calculated and analysed by numerous researchers with regards to enhancing free convection heat transfer. Concerning the geometry inclination angle concept, Cianfrini*, et al.* [41] studied the effect of the inclination angle of a square enclosure filled with air on the natural convection using a numerical analysis. In general, a remarkable heat transfer along x-direction across the cavity was noticed by changing the inclination angle of the domain, especially for a sufficiently wide range of inclination angle (135°). It is well known that solar fluid heaters are one of the common heat convection cases in cavities.

An experimental and numerical study was undertaken on Integrated Collector Storage (ICS) by Henderson*, et al.* [40]. The ICS has two enclosures (water and air cavity), which resulted in two free convection regions. The main goal was the investigation of the inclination of the ICS geometry to better understand the impact of the inclination angle on the enhancement of heat transfer. Essentially, Henderson *et al*. ultimately determined that the convection within both the air and water enclosures was increased by increasing the inclination angle of the domain.

2.1.1.1 Wall configuration

Studies that have concentrated on the configurations of the walls of the enclosures have also been presented by a number of scholars as a means to raise the heat transfer of natural convection cases. A 2D laminar natural convection in shallow, wavy closed cavity was simulated by Varol and Oztop [42]. The bottom and top walls were, respectively, a hot sinusoidal plate and a cold and flat plate, unlike the vertical walls which were thermally isolated flat surfaces; the investigation of heat convection in shallow, wavy enclosure was the main objective of this study. It was concluded that the Nusselt number (Nu) shows a wavy variation and maximum Nu was found at the top of the wave. Additionally, geometrical parameters and the Rayleigh number (Ra) can have significant effects on heat transfer rates. Furthermore, a 2D steady laminar natural convection heat transfer and the flow patterns of a wavy wall cavity with volumetric heat sources were studied numerically by Oztop*, et al.* [43]. The enclosure has a cooled right wall and heated left wall, while the horizontal wavy walls were kept adiabatic. The internal and external Rayleigh numbers (Ra) and the amplitude of the wavy walls were the effective non-dimensional parameters. It was found that changing the values of internal to external Ra and wavy wall spaces affects the heat transfer and flow patterns; also, the heat transfer direction was fully dependent on the internal and external Ra. A 2D wavy square cavity containing corner heaters was studied numerically to investigate the flow field and heat transfer of natural convection by Singh and Bhargava [28]. The cold temperature on the vertical wavy wall and the hot temperature on the left bottom corner were maintained at constant temperatures, whilst the other walls of the enclosure were kept adiabatic. The outcomes show that wavy surfaces provide higher heat transfer rates than flat surfaces, as well as a remarkable impact on heat transfer coefficient that was affected by the Rayleigh and Prandtl numbers. In addition, heater length in both the horizontal and vertical directions have a noticeable influence on average heat transfer.

2.1.1.2 Classic coolant

Through the passage of time, even though conventional fluids have low thermal conductivity, several alterations have been applied to hollow shapes that contains classic coolants in terms of their free convection. Hu*, et al.* [26] simulated and compared the 2D natural convection of complex annular-configuration enclosures filled with cold water. These were studied for both the outer and inner walls of the enclosures. It was seen that for the different enclosure shapes, Ra and density parameters have clear effects on the flow pattern and heat transfer. Additionally, it appeared that the inner wall of the enclosure had a greater expressive influence on the heat transfer than the outer wall. Cajas and Treviño [32] analysed a 2D large aspect ratio enclosure numerically. These authors reached the conclusion that for the low values of Rayleigh number, there was no effect on the heat transfer instability in a particular geometry; indeed, on the contrary, there were consequences for the heat transfer at high Rayleigh numbers. Ganzarolli and Milanez [44] studied the natural convection in a rectangular enclosure heated from below and symmetrically cooled from the sides numerically; the relatively small influence of the Prandtl number on the heat transfer and flow circulation inside the cavity was concluded. Basak*, et al.* [45] studied a steady-state laminar free convective flow within a square cavity with uniformly and non-uniformly heated bottom walls numerically. The local Nusselt number at the bottom wall was lowest at the centre for uniform heating and there were two minimum heat transfer zones at the centre and the corner points for non-uniform heating. Sojoudi*, et al.* [46] deliberated on a heat transfer field by studying and analysing a 2D steady-state free convective fluid within a trapezoidal cavity that included an inclined, cooled left wall and an inclined, heated right wall. The other walls were kept adiabatic. The authors focused on the effects of the dimensionless parameters on isotherms, streamlines and local Nusselt number. The results showed that increasing the inclination angle of trapezoid geometry side-walls leads to a decrease in Nu_{Max} on the left, while Nu_{Local} was enhanced by incrementing the Rayleigh number. Also, increasing the Prandtl number leads to a decrease in the maximum stream function.

Moreover, it is noted in the literature that cavity shape has a major impact on turbulent flow behaviour, as can be seen in following studies. Ridouane*, et al.* [47] studied the features of turbulent free convection of a 2D triangular cavity that was filled with air numerically. The bottom wall of the enclosure was heated, while the sidewalls were cooled. This kind of geometry can be found in conventional attic spaces of houses or buildings that have pitched roofs and horizontally suspended ceilings. It was concluded that this kind of geometry gains high turbulence levels compared with square enclosures at a given value of the Rayleigh number. Turbulent flow within a 2D porous cavity was investigated numerically by Carvalho and de Lemos [48]. The results of this study illustrated that the average Nusselt number reduces as porosity increases. A double-diffusive turbulent natural convection in a 2D closed square hollow, filled with air and containing CO_2, was investigated numerically by Serrano-Arellano*, et al.* [49]. It was observed that the location of the CO_2 has a considerable effect on the heat transfer in the closed cavity; in addition, the highest value of the Nusselt number was found at the highest value of the Rayleigh number within the CO_2 that was located close to the heat source. Turbulent natural convection in a 3D differentially heated cubic enclosure filled with air was studied numerically by Zhang*, et al.* [50]. The main objective of this investigation was to use the large eddy simulation (LES) method with a high Rayleigh number. It was concluded that using LES provides close results to those of previous experimental and numerical results, as well as showing that free convection has its own features in terms of the observed turbulence.

2.1.1.3 Nanofluid

In the last few years, there has been a growing interest in nanofluids acting as new working heat transfer fluids instead of conventional fluids such as oil or water. Adding nanoparticles into base fluids plays a vital role in determining the thermal properties of heat transfer fluids. Research into natural convection within cavities filled by different nanofluid types using various geometries and boundary conditions have become especially popular, among which some more notable investigations can be found in references [25, 31, 51-58]. It is clear that most of the earlier nanofluids studies were completed via analysing nanoparticle types, concentrations and diameters for uncomplicated geometries boundary conditions and fluid flow state, such as in a 2D square enclosure. A numerical study was completed by Wang*, et al.* [25] to determine a 2D natural convection of a square cavity with a cooled right vertical wall. The left vertical wall oscillated in a sinusoidal manner at the constant average temperature of the cavity with adiabatic horizontal walls. The enclosure was filled with nanofluids, with the influence of the nanoparticles volume fraction on heat transfer was the main research objective. The outcome shows that the heat transfer and the oscillatory behaviour were influenced by the nanoparticles. Ho*, et al.* [51] conducted a numerical study into the effects of uncertainties in effective dynamic viscosity and thermal conductivity of an Al_2O_3-H_2O nanofluid on laminar natural convection heat transfer in a square enclosure. It was observed that the uncertainties associated with different formulas adopted for the effective thermal conductivity and dynamic viscosity of the nanofluid have a strong bearing on the natural convection heat transfer characteristics. Cianfrini*, et al.* [52] carried out a numerical study of a 2D natural convection of Al_2O_3-H_2O within a square enclosure which was cooled on one side, whilst the opposite side was partially heated, and the remaining walls were insulated. The main finding of this study was that the position and the length of the heater had a significant effect on the heat transfer ratio. A study into the 2D natural convection of a vertical cavity filled with different nanofluid types was performed numerically by Alipanah*, et al.* [53]. Pure water has been mixed with the three different types of nanoparticles, which are TiO_2, Cu and Al_2O_3, in order to produce three types of nanofluids. Parameters such as volume fraction and aspect ratio were studied. The most important objective was the effects that were found for the three kinds of nanofluids on the vertical cavity with regards to natural convection heat transfer. Essentially, it was found that nanofluids can enhance the heat transfer with increasing volume fraction Cu nanoparticles with water provide the highest Nusselt number of the nanofluids tested. Finally, the study illustrated that aspect ratio has a significant effect on the heat transfer field.

Since nanofluids have been shown a substantial enhancement to convection heat transfer, scholars' interest in them has been growing over the time. Therefore, an increasing amount of research has been dedicated to several nanofluid types with various cases and boundary conditions. The steady state natural convection heat transfer of Au-H_2O in a cubic cavity was investigated numerically by Ternik [54]. It was concluded that nanoparticle concentration has a major effect on the heat transfer. A 2D unsteady free convection in a square cavity containing a thin heat source located in the centre of the enclosure filled by alumina-water was simulated by Sourtiji*, et al.* [31]. It was also found that increasing the concentration of the nanoparticles led to a raise in the rate of heat transfer. 2D natural convection in an open cavity filled with Al_2O_3-H_2O was analysed numerically by Mahmoudi*, et al.* [37]. The non-uniform thermal boundary condition of the cavity was presented, as well as the uniform heat generation or absorption. With a Ra between 10^3 – 10^5 and a Ha value of 30, it was found that the nanofluid has a more significant impact on heat generation than heat absorption. Increasing the Hartmann number leads to reduced heat transfer, while heat transfer was increased by augmenting the value of the Rayleigh number. A natural convective Cu-H_2O solution within an inclined L-shaped enclosure in the presence of an inclined magnetic field was examined numerically by Elshehabey*, et al.* [56]. It was concluded that the enhancement in the heat transfer rate was caused by an increase in the number of the nanoparticles and in Rayleigh number. By contrast, a reduction in Nusselt number was found when either the Hartmann number or aspect ratio increased. A numerical investigation was conducted by Bouhalleb and Abbassi [57] into the natural convection of CuO-H_2O inside a 2D rectangular enclosure using different nanoparticle concentrations, low aspect ratios and Rayleigh numbers. It was observed that increasing the number of nanoparticles in water leads to improved heat transfer; additionally, when the enclosure is set at a given Rayleigh number, the influence of the aspect ratio is more significant. A 2D half-moon configuration enclosure with a diversity of thermal boundary conditions and three types of nanofluid was calculated numerically by Rahman*, et al.* [58]. Among the three different nanofluids, it was found that increasing the concentration of the nanofluids by adding greater volume fractions led to enhanced heat transfer, particularly at high values of Ra and Cu concentration. A 2D natural convection heat transfer of Al_2O_3-H_2O within a square cavity was studied numerically and experimentally by Hu*, et al.* [36]. Basically, it was shown that a nanoparticle solution with pure water provides a higher heat transfer rate compared with just pure water.

Considering investigations in nanofluids in general into account, it can be concluded that researchers have considered the effects of different nanofluid types and thermal physical properties, domain boundary conditions and dimensionless parameters, such as Rayleigh, Reynolds and Richardson numbers. The main achievements by scholars regarding the above are that any type of nanofluid has a remarkable influence on natural heat convection and flow patterns, particularly at high nanoparticle volume fractions and small nanoparticle sizes.

2.1.2 Mixed convection

Another type of heat transfer convection in cavities is a mixed convection heat transfer in lid-driven enclosures, which have been the subject of interest in numerous research studies. The result of the combined forced convection that occurs through the effects of external sources such as a pump, fan or suction device, or by the effects of the movement of one or more walls of the cavity, with free or natural convection is called mixed convection. Shear-driven, or lid-driven, flow is one of the configurations that has many applications such as electronic devices and microelectromechanical system (MEMS) applications, lubrication technologies, multi-shield structures used for nuclear reactors, furnaces, high-performance building insulation, glass production, food processing, solar power collectors, chemical processing equipment and drying conventional liquids, acceleration and generation of magnetohydrodynamic and plasma confinement, air conditioning, coating and mixing, shear flow, core vortex eddies and transition to turbulence, float glass production and microelectronic devices [59-63]. Figure

2-3 shows an example of a mixed convection application in cooling devices. This kind of study has found a wide range of applications within modern technology.

Figure 2-3: Schematic diagram of data-centre-cooling [64].

2.1.2.1 Classic coolant

Mixed convection heat transfer in lid-driven enclosures has been accomplished for various different geometries and boundary conditions. Two-dimensional cases of mixed convection heat transfer are commonly used in the literature because they are easy to create and have much lower mesh numbers and reduced simulation times. The mixed convection heat transfer in a two-dimensional enclosure trapezoidal cavity with constant heat flux at the bottom wall was studied numerically by Mamun*, et al.* [24]. The isothermal top wall of the cavity was moved in the horizontal direction. The effects of the inclination angle of the sidewalls, Richardson number, Reynolds number, aspect ratio and the rotational angle of the cavity on mixed convection were considered. It was concluded that the optimum configuration of their trapezoidal enclosure was obtained at an inclination angle of 45º. As Ri increases, Nu_{av} increases accordingly for all aspect ratios. As the aspect ratio increases, the heat transfer rate increases. The direction of the motion of the lid also affects the heat transfer phenomena. Aiding flow conditions always provides for a better heat transfer rate than when opposing flow conditions. Combined convection heat transfer characteristics in a 2D lid-driven square cavity with various Richardson and Prandtl numbers were studied by Cheng [65], who concluded that heat transfer increases continuously when increasing both Re and Gr numbers for a Ri of 0.01, unlike when the Richardson number is in range of $0.5 \leq Ri \leq 100$. Three different study cases of mixed convection heat transfer have been separately completed by Basak et al [66-68] with regard to investigating the enhancement in heat transfer of cavities, which include mixed convective flow in a porous lid-driven square cavity, the influence of linearly heated sidewalls or a cooled right wall on a mixed convection flow of a lid-driven square cavity, and the impact of uniform and non-uniform heating of the bottom wall on mixed convection lid-driven flows in a square cavity. In addition, many other researchers have considered mixed heat convection in terms of its ability to raise the heat transfer rate. Al-Amiri*, et al.* [69] simulated a steady-state flow and heat transfer in a square, lid-driven cavity under combined convective effects. Moallemi and Jang [70] performed a numerical investigation into the flow and heat transfer of combined convection in a moving wall square cavity. It was found that the influence of buoyancy on the flow and heat transfer in the cavity is more pronounced for higher values of Pr. Reima*, et al.* [71] studied the flow of a viscous thermally-stratified fluid in a lid-driven square container numerically. Ghasemi and Aminossadati [72] completed a numerical investigation into unsteady laminar mixed convection heat transfer in a 2D square cavity. It was concluded that the average Nusselt number of the cavity with a downwards moving wall was higher than that of the cavity with an upwards moving wall. Oztop and Dagtekin [73] conducted a numerical investigation into a steady-state laminar two-dimensional mixed convection problem in a vertical two-sided, lid-driven square cavity that was differentially heated. When the vertical walls were moved upwards in the same direction, the heat transfer was found to decrease. Furthermore, a lid that opposed buoyancy forces was found to decrease the heat transfer significantly by reducing the strength of the circulation, regardless of which direction it was moved, either both upwards or both downwards. Noor*, et al.* [74] studied flow and heat transfer inside a square cavity with double-sided oscillating lids numerically. Higher heat transfer rates were found at higher Reynolds number flows due to the increment of fluid flow activities in the bulk of the interior fluids. Vishnuvardhanarao and Das [75] investigated a two-dimensional steady mixed convection flow in an enclosure filled with a uniform porous media using numerical methods. Significant suppression of the convective currents was obtained through the presence of a porous medium. Aydm [76] investigated the transport mechanisms of laminar combined convective air flow in a shear and buoyancy-driven cavity using numerical methods. The interaction of the forced convection with natural convection was studied. Two orientations of the thermal boundary conditions at the cavity walls were considered in order to simulate aiding and opposing buoyancy mechanisms. It was concluded that with increasing Richardson number, three different heat transport regimes could be defined as follows: forced convection, mixed convection and natural convection. In addition, the mixed convection range of the Richardson number for the opposing-buoyancy case was wider than that of the aiding-buoyancy case. Sivakumar*, et al.* [77] conducted numerical studies into an unsteady mixed convection heat transfer and fluid flow in lid-driven cavities with different heating portion lengths and locations. It was found that an improved heat transfer rate was obtained by reducing the heating portion length on the hot wall. Guo and Sharif [78] conducted numerical study into mixed convection heat transfer in a 2D lid-driven rectangular cavity filled with air that was subject to constant heat flux. It was concluded that as Ri number increases, the temperature variation was restricted over a gradually diminishing region located around the heat source. Chen and Cheng [79] analysed periodic flow patterns with mixed convection caused by the effects of lid oscillation and buoyancy in a triangular cavity. It was observed that the flow in the cavity may experience an oscillation at natural periodic frequencies. Three-dimensional numerical simulation of flow and heat transfer in a lid-driven cavity filled with a stably stratified fluid was investigated by Mohamad and Viskanta [80]. The effects of a sliding lid on the flow and thermal structures in the shallow cavity were studied. It was concluded that increasing the retarding force and the buoyancy force prevents the return flow from penetrating to the bottom of the cavity, and therefore that the fluid was recirculated in its upper regions. The upper recirculation induces shear on the lower fluid layer, forming another weak recirculated flow region. Admittedly, the rate of heat transfer increases as Richardson number decreases or the Reynolds number increases. The maximum local heat transfer rate occurs at the start of the sliding lid. The return flow impinging on the bottom of the cavity also increases the rate of heat transfer locally in the region of the impingement. Three-dimensional flow structures and the companion heat transfer rates in a double lid-driven cubic cavity, heated from the top and cooled from the below, were studied by Ouertatani*, et al.* [81]. Numerical solutions were generated for representative combinations of the controlling Reynolds and Richardson numbers. Typical sets of streamlines and isotherms were presented to analyse the tortuous circulatory flow patterns set up by the competition between the forced flow created by the double driven walls and the buoyancy force of the fluid. It was observed that when the Ri was small and the Re large, the flow was basically carried through, or used the lids' movement. In this case, the mechanically driven convection was, or would become, dominant. Ismael*, et al.* [63] conducted a numerical study into mixed convection heat transfer in a 2D square enclosure with a partial slip using water as the heat transfer medium. The top wall was cooled, while the bottom wall was heated. The remaining walls of the cavity were kept adiabatic. Studying the effects of pertinent parameters such as the slip parameter, Richardson number and the direction of sliding walls was the major aim. It was illustrated that the boundary condition at a partial slip of zero, the isothermal character was not affected by Ri. In addition, when the Ri was ignored, the partial slip could not influence the heat convection. Moreover, the function of Ri increases as the partial slip ($S > 0$). Pekmen and Tezer-Sezgin [61] demonstrated the effects of dimensionless parameters, such as the Darcy and Hartmann numbers, of numerically mixed convection in a moving wall enclosure on the heat transfer and flow pattern. It was concluded that roughly the same effect on heat transfer could be found by increasing the Hartmann number or Darcy number. Khanafer [82] numerically compared a 2D steady laminar mixed convection heat transfer and flow performance in a top moving wall square cavity among different types of heated bottom wall conditions, including flat, flexible, rectangular and sinusoidal wavy walls. The results showed that at $Re < 400$ and a Ri of 10^4, the flexible bottom wall can enhance heat transfer by about 61.4% compared with flat and wavy bottom walls, while increasing the Ri led to a reduction in the heat transfer percentage of the flexible bottom wall and an increased heat transfer for the rectangular wavy bottom wall. Bhattacharya*, et al.*

[83] studied numerical a 2D mixed convection heat transfer and the role of multiple solutions in a trapezoidal cavity with a moving cold top wall and hot bottom wall, while the inclination sidewalls were kept adiabatic. They found that the non-isothermal case leads to multiple steady states, and that the lid-driven wall significantly enhances heat transfer.

2.1.2.2 Nanofluid

Based on high heat transfer enhancement that can happen by involving nanofluids, various nanofluid types have been connected with the subjects of mixed convection studies that used moving wall enclosures in terms of increasing heat transfer effects. Abu-Nada and Chamkha [84] conducted numerical studies into steady laminar mixed convection flow in a lid-driven inclined square enclosure filled with an Al_2O_3-H_2O nanofluid. It was concluded that the heat transfer mechanisms and the flow characteristics inside the cavity were strongly dependent on the Richardson number. The mixed convection in a lid-driven triangular enclosure filled with Al_2O_3-H_2O nanofluid was simulated by Ghasemi and Aminossadati [85]. It was reported that the direction of the sliding wall motion affected the flow and temperature distribution within the enclosure and the heat transfer rate. A mixed convection heat transfer of a 2D moving wall square enclosure with heat derived from an inner triangular heat source was studied numerically by Kalteh*, et al.* [60], who found that Ag nanoparticles offered the highest average Nusselt number, whilst the lowest value was found when using TiO_2 nanoparticles. The Nusselt number was also increased by incrementing the nanoparticles' volume fraction, while increasing nanoparticle diameters led to a decrease in the average Nusselt number. Abu-Nada and Chamkha [86] investigated a 2D mixed convection nanofluid flow in an enclosure with a moving top wall and a wavy bottom wall numerically. It was found that at the considered Ri, the nanoparticles significantly enhanced heat transfer, as did the wavy bottom wall geometry ratios. A 2D viscous, unsteady and incompressible nanofluid flow within a heated lid-driven cavity with a pulsating flow was numerically investigated by Serna*, et al.* [87]. The influences of the amplitude of the oscillation frequency and wave number of the sinusoidal velocity waves at the lid on convection were solved. It was proved that Richardson number was increased by pulsing the flow.

In addition, when the velocity wave was phased to the size of the cavity, the heat transfer ratio reached to the highest value. A numerical investigation of mixed convection within a 2D inclined, shallow, lid-driven enclosure filled with Cu-H_2O was undertaken by Karimipour*, et al.* [88]. The top wall of the geometry was moving, whereas the other walls remained fixed. The top wall was held at a higher temperature than the bottom wall and the sidewalls were kept insulated. The effects of different nanoparticle volume fractions and enclosure inclination angle were studied at Reynolds numbers of 100 and 10. It was demonstrated that increasing the nanoparticle concentration led to an enhancement in the heat transfer rate. A 2D lid-driven inclined triangular cavity loaded with Cu-H_2O was investigated numerically by Billah*, et al.* [89]. The most important objective of their study was the investigation of unsteady heat transfer enhancement resulting from nanofluids within the enclosure. It was concluded that using nanofluids led to an improvement in the heat transfer coefficient.

However, only a few researchers have paid attention to the two-phase mixture model with nanofluids. Moreover, only limited attention has been paid to the study of turbulent flow using advanced models such as LES [50] or URANS [32, 34, 47, 49, 90]. Alinia*, et al.* [91] studied a mixed convection heat transfer of nanofluids within a two inclined-side moving wall cavity using a numerical two-phase mixture model; their main objective was the analysis of the effects of the volume fraction of nanoparticles and the inclination angle on the thermal characteristics at Richardson number from 0.01 to 100. It was observed that a considerable improvement in heat transfer could be achieved by increasing the concentration of the nanoparticles, and that inclination angle affected the heat transfer, especially when increasing the Richardson number. Goodarzi*, et al.* [90] numerically analysed both laminar and turbulent mixed convection heat transfer of nanofluids inside a 2D shallow enclosure. It was observed that increasing the nanoparticles' fraction led to an enhancement in the heat transfer rate. In addition, turbulence kinetic energy, turbulence intensity, wall shear stress and skin friction were also all affected by the nanoparticle concentration. Sharma*, et al.* [34] investigated a 2D turbulent free convection in a closed cavity that was heated from the centre of the bottom wall, and which had cooled sidewalls whilst other walls were kept adiabatic. The standard k-ε model was utilized to model turbulent natural convection. It was found that the Nusselt number increases with incremental decreases in the width of the heat source in the case of isotherm heating, while in the case of isoflux heating, the Nusselt number decreases with a decreasing width of the heat source.

Taken all natural cavities shapes and configurations sub-sections into account, many areas have not been investigated. The above survey summarises the work in the literature that has considered the various aspects of heat convection in different-shaped cavities. Consequentially, it is effortless to conclude that the case of mixed convective heat transfer in a trapezoidal enclosure utilizing nanofluids seems not to have been investigated in the past, and it is this apparent lack that has motivated the present study. Thus, most of the previous research on trapezoidal enclosures involved conventional fluids (rather than nanofluids) and there is a very little work reported in the open literature that involves nanofluids in trapezoidal enclosures. Furthermore, the majority of numerical investigations so far are restricted to two-dimensional geometries, and only very limited investigations have been undertaken into 3D lid-driven cavity problems. Moreover, too little attention has been paid to studying turbulent conventional flow using advanced turbulence methods such as LES or URANS, and into analysing heat convection and flow patterns in detail. Besides, studying different nanofluid types within 3D moving sidewall enclosures using the LES and URANS methods has not been previously realised.

2.2 Cavities with added objects

Since heat convection can be represented in many cavity configurations, it has many industrial and engineering applications; as mentioned earlier in this chapter [91-95], many researchers have investigated various free or mixed convection problems. Involving some additional passive objects within the enclosure to enhance the heat transfer ratio has become popular over the years. In particular, the convection heat transfer rate due to natural convection within an obstructed cavity has been continually improved and enhanced by a wide number of investigators via adding effective moving or fixed bodies inside the enclosures.

The main achievements of some research studies have been summarized to gain a clear vision of heat convection within cavities. Several aspects have been considered previously in terms of convective cavities containing cylinders, such as the location and the size of the cylinder, as well as rotational speed in the case of utilizing a rotating object. Studies into the cylinder location inside the hollow were carried out for different cases by Pingan*, et al.* [92], who employed numerical methods to investigate a natural 2D laminar convection in a square cavity containing a circular pipe. It was concluded that the original temperature distribution in a square cavity was influenced by the quantity of heat transfer through the pipe surface. The natural convection of a 2D square cavity containing cold and hot cylinders was investigated numerically by Park*, et al.* [38], for whom different locations of such cylinders within the cavity were their main concern. The results of their study showed that when the surfaces of the cylinders and cavity were close to each other, this led to an increase in Nusselt number. Unsteady natural convection due to two heated horizontal rotating cylinders within a 2D closed square cavity was simulated by Karimi*, et al.* [29]. The locations of the cylinders in the enclosure at various Rayleigh numbers were the objective of this study. It was observed that at a low Rayleigh number (less than 10^4), the distance between the cylinders had a clear effect on the averaged-area Nusselt number, but when the Rayleigh number was greater than 10^4 and not more than 10^7, the influence of the spacing between the cylinders could be ignored. The natural convection due to a cylinder within a 2D rhomboid enclosure filled with water was determined numerically by Choi*, et al.* [35]. The main goal was that of changing the cylinder position in the cavity, and changing the Rayleigh number. It was noticed that the thermal features of the heat transfer between the cavity and its cylinder follow the value of the Rayleigh number and cylinder location. Therefore, increasing the Rayleigh number leads to increment in Nusselt number for both enclosure and cylinder. In addition, when the cylinder is located on the bottom wall of the rhomboid cavity, the Nusselt numbers for both enclosure and its cylinder reached their maximum values. The lowest Nusselt number occurred when the cylinder was near the top of the cavity. A 2D free convection study of a laminar power-law fluid within a square cavity containing a heated cylinder was completed by Shyam*, et al.* [93], who concentrated on the effects of changing the cylinder location along the vertical central line for different dimensionless parameters. It was realised that the heat transfer ratio and streamline and isotherm contours can be affected by changing the Grashof number and Prandtl number or cylinder location.

2.2.1 Cylinder parameters

Examination of the effects of cylinder diameter or inclination angle and other parameters on the heat convection of natural convection has been the subject of various research efforts. A numerical study into 2D natural convection in a closed cooled square cavity with two horizontal inner cylinders was carried out by Yoon*, et al.* [30]. The upper cylinder was cooled, while the lower one was heated. The influences of inner cylinders' radii and buoyancy-induced convection on flow pattern and heat transfer were the main aims of this study, which were completed at different values of Rayleigh number ($10^3 \leq Ra \leq 10^5$). It was concluded that by increasing the radii of the cylinders, all values of Rayleigh number drive a raise in heat transfer rate that dominates the cold upper circular cylinder on a wider area in the cavity. An inner sinusoidally heated circular cylinder placed in a cavity was used by Roslan*, et al.* [21] to numerically study a 2D unsteady natural convection heat transfer. The main purpose was to investigate the effects of the temperature difference between the cold enclosure and the heated cylinder in terms of heat transfer and flow field development with different cylinder radii. It was concluded that the flow field had two inner vortices, and the heated cylinder provided a warm-chamber which affected heat transfer. Temporal increases in heat transfer were found by increasing the cylinder radius at the maximum value of the dimensionless parameters, unlike at the lowest value of the parameters where heat transfer was not changed by changing cylinder radius. In addition, it was observed that oscillating the heat source of the cylinder augmented the heat transfer rate. Three-dimensional free convection of laminar flow within an enclosure containing a cylinder was simulated by Souayeh*, et al.* [94] in order to understand the impact of inclination angles of the cylinder at different Rayleigh numbers on the fluid patterns and heat transfer ratio. It was noted briefly that a significant effect was discovered regarding the heat transfer ratio, especially when the Rayleigh number is 10^6 and inclination angle is 90°. A study of 2D laminar natural convection of air within a cold-walled square enclosure containing a stationary sinusoidal cylinder was undertaken by Nabavizadeh*, et al.* [95] to evaluate the influences of different angles, amplitudes and number of cylinder undulations. It was observed that changing cylinder parameters can affect the heat transfer and fluid patterns.

2.2.2 Mixed convection

Matching forced convection with natural convection and applied effective inner bodies in hollows has been completed through different study cases, boundary conditions and coolant fluids concerning the enhancement of convective heat transfer. The following paragraphs describe some mixed convection research into moving wall enclosures having either rotating or motionless cylinder, varying different cylinder parameters such as location and diameter. Inserting a circular body to enhance the heat transfer of a lid-driven cavity was investigated by Oztop*, et al.* [96]. Appending a heated triangular block at the centre of the top moving wall square enclosure has an impact on the heat transfer coefficient [97]. Studying the effects of both inserting an isothermal square object and using a nanofluid inside a lid-driven square enclosure on the heat transfer ratio was undertaken by Mehmood*, et al.* [98]. A 2D MHD mixed convection from a heated top moving wall enclosure that has inner central circular cylinder and heaters was studied numerically by Ray and Chatterjee [99]. This study showed that the inner circular cylinder leads to a remarkable increase in Nusselt number. In addition, with a large-sized heater, the thermal field mostly depends on the heat source. Also, when the magnetic field is ignored, Richardson number can increase the effects of the heat transfer rate and the bulk fluid temperature. A study of mixed and natural convection due to stationary and rotating (with different rotational speeds) central cylinders in a 2D square cavity was carried out by Liao and Lin [20]; the aim was to determine the relationship between Nu_{mean} and Ri, as well as to study the effects of the aspect ratio between the inner cylinder and outer cavity on heat transfer. It was found that this relationship was not affected by changing the aspect ratio, but it was shown that by reducing Ri can decrease the value of Nu_{mean}. Heat transfer was enhanced by using small aspect ratio, which leads to the generation of a larger value of Nu. Hydromagnetic mixed convection heat transfer in a 2D moving wall enclosure with a central rotating conducting solid cylinder was demonstrated numerically by Chatterjee*, et al.* [18]. Stationary horizontal walls were assumed as being adiabatic, whilst the right wall and left moving wall were considered to be isothermal. Rotations of the cylinder both anticlockwise and clockwise were investigated. Pertinent dimensionless parameters such as Hartmann numbers, Richardson numbers and dimensionless rotational speeds were varied, while the Reynolds number was presumed to take a constant value (Re = 100). The fundamental objective was to identify the effects of a rotating cylinder on the heat transfer; these can be summarised in that the anticlockwise rotation of the cylinder was the reason for the increase in the value of the average Nusselt number on the right wall, while clockwise rotation led to a reduction in average Nusselt number. Both anticlockwise and clockwise rotations of the cylinder with a high magnetic field strength showed an increase in heat transfer. Generally, it can be said that increasing the rotational velocity of the conductive cylinder led to an enhancement in the heat transfer rate of the cavity. Hussain and Hussein [100] simulated a laminar steady state mixed convection of air within a differentially heated cavity containing a conductive rotating cylinder, with the aim of examining the thermal and flow features of different rotating cylinder locations within a square enclosure at several values of Reynolds and Richardson numbers. It was found that when the forced convection was dominating, major vortexes formed around the cylinder. No influences were found for the flow and thermal fields by changing the cylinder location when the effects of natural and forced convection were equal. Studies into a heated hollow cylinder within the middle of a moving wall enclosure were completed by Billah*, et al.* [101] by varying such parameters as the diameter of the cylinder, the Richardson number, and the thermal conductivity of the fluid. Analysing the sequences of using a cylinder on the mixed convection heat transfer coefficient was mainly targeted. It was determined that the cylinder had a significant influence on the heat transfer ratio, as did the cylinder diameter. Khanafer and Aithal [102] evaluated a laminar combined convection heat transfer and the flow patterns of a moving wall cavity that had a central cylinder. Changing the diameter and location of the cylinder with different Richardson numbers was the principal research aim; the study concluded that heat transfer fields can be controlled by the cylinder body within the cavity. Obstacle size and location can affect the heat transfer and flow characteristics. A laminar mixed convection of a heated square blockage within a moving wall enclosure was studied numerically by Islam*, et al.* [103] to analyse the effects of central and eccentric locations of the square body using different square body sizes and a constant Reynolds number on the associated heat transfer and flow patterns. It was observed that when forced convection dominated, there were no clear differences in the heat transfer when changing either the location or the size of the installed body. Conversely, an obvious effect on the Nusselt number was noticed when natural convection was controlling the domain.

2.2.3 Nanofluid

Studying various nanofluid types and thermal physical properties within cavities that contain internal additional bodies under different conditions has been discussed because of their massive contributions to heat transfer enhancement. Focusing on both nanofluid and cylinder effects is discussed here. Magnetohydrodynamic mixed convection of nanofluids in a 2D lid-driven square cavity containing a rotating cylinder was simulated by Selimefendigil and Öztop [59]. The principal aim here was to consider the effects of dimensionless parameters such as the Hartmann number, the Richardson number, the rotational speed of the cylinder, and the concentration of the nanoparticles. It was demonstrated that increasing the Ri leads to an increase in heat transfer. However, by increasing the value of the Hartmann number, a reduction in heat transfer occurs. The rotation of the cylinder with the nanofluid has considerable effects on the heat transfer enhancement. A 2D mixed convective transport mechanism was tested numerically by Chatterjee*, et al.* [62] for a moving top wall cavity which contained a thermal adiabatic central rotating circular cylinder whose enclosure was filled by Cu-H_2O nanofluid. This enclosure had insulated sidewalls and differentially heated bottom and top walls. The aim of this study was to find the effect of the rotational speed of the cylinder on the heat transfer ratio. It was observed that at low values of Ri, forced convection dominated in fluid and heat transfer. However, at high Ri, natural convection has the dominating effect on heat transfer and fluid flow. The rotational speed of the cylinder can increase the heat transfer, as can adding nanoparticles to the base fluid. In addition, an increasing Ri enhanced the Nusselt number on the heated wall. Mixed convection heat transfer and flow patterns of a rotating cylinder within an obstructed cavity filled with a nanofluid were studied by Roslan*, et al.* [104]. Analysing the influences of nanoparticle volume fraction, diameter size and rotational speed of the cylinder were the principal goals of the investigation. It was shown that heat transfer could be increased due to an increase in nanoparticle concentration, as did the positive effect of raising the rotational speed on the heat distribution. Additionally, the impact of the radius of the cylinder on the fluid behaviour was observed. Combined convection of heat transfer and fluid structure of a 2D differentially heated square cavity that contained a central rotational cylinder was simulated by Costa and Raimundo [105] to investigate the influences of cylinder size and rotational speed. It was determined that discernible influences have been discovered due to the changes in either the cylinder size or rotational speed on the heat transfer and fluid characteristics. A 2D laminar mixed convection heat transfer of nanofluid within a moving wall square enclosure containing a rotating cylinder was considered by Mirzakhanlari*, et al.* [106] to study the impacts of the Richardson number and rotational speed. It was demonstrated that increasing either the Richardson number or the nanofluid speed causes an enhancement in heat transfer ratio, while increasing the rotational speed of the cylinder has a negative effect on the heat transfer ratio. Investigation of free and combined convective heat transfer of a differentially heated circular cylinder within an adiabatic cavity containing nanofluids was studied by Garoosi and Hoseininejad [107]. The influences of nanofluid thermophysical properties and the number of cold cylinders that the cavity contained and their locations and rotational directions are considered at different Rayleigh and Richardson numbers. It has been found that increasing or decreasing heat transfer rate strongly depends on these parameters.

By considering the literature review, and to the best of the author's knowledge, it can be concluded that only the 2D mixed convection heat transfer in a plane moving wall square cavity with rotational cylinder was studied using either classic fluids or nanofluids. However, no researcher has attempted to use LES modelling of the 3D mixed convection within a cubic enclosure with a rotating cylinder and compared this to a similar URANS method. Furthermore, it can be summarized from this literature review that the effects of three-dimensional rotating cylinder speeds and directions (clockwise and anticlockwise) within a top lid-driven closed cavity on the turbulent nanofluid flow through an unsteady RANS method are currently unprecedented.

2.3 Artificially roughened cavities

Heat transfer enhancement of convective fluid flow in a cavity is of great importance and interest in terms of raising the heat transfer rate, which can decrease thermal load and improve system effectiveness. Including additional passive objects within the enclosure to enhance the heat transfer ratio has become popular over the last few years. For instance, adding a cylinder of fins to the domain to control the heat transfer of the mixed convection case [18, 108-114]. Several engineering and industrial heating/cooling systems could be represented by heat transfer convection of differentially heated enclosures, such as solar air collectors, heat exchangers, and microelectronics to nuclear chemical reactors, air conditioning systems, electronic equipment cooling and various other cooling devices [17, 115-122]. A viscous sub-layer can be broken by introducing an artificial roughness on the walls instead of the traditional or smooth wall, which leads to a decrease in thermal resistance and raises the number of turbulent regimes; this in turn can increase the heat transfer coefficient between the heated wall/plate and the working fluid [123].

Several artificial ribs shapes and parameters have been used by researchers in order to enhance the heat transfer rate in cavities, for example in ducts and solar air channels. The appropriate literature has been summarized in this section to cover as many areas of artificial roughness ribs applications and benefits. Artificial V-rips with various parameters have been used in a noticeable amount of research [124-129]. Artificial roughness in the shape of V-down ribs within a rectangular duct was investigated experimentally by Deo*, et al.* [130] to determine and further analyse the heat transfer Reynolds numbers over the range 4000 – 12,000 and important roughness parameters such as relative roughness pitch and height. These parameters have shown a significant effect on heat transfer through Nusselt number results. The highest Nusselt number enhancement was 3.34 times than that of traditional smooth wall conditions. The study of multiple V-ribs roughness within a solar heater duct was accomplished by Hans*, et al.* [131] to enhance convection heat transfer by utilising roughness elements at Reynolds number values of the range 2000 – 20,000. Essentially, a remarkable positive influence on the Nusselt number can be produced by changing of roughness parameters' values; in a practical sense, this can be achieved when the relative roughness width value is 8. Kumar*, et al.* [124] investigated the influence of multi V-shaped ribs on the heated plate of a rectangular channel to develop the heat transfer coefficient due changes in roughness parameters, such as roughness height and pitch, experimentally. The Nusselt number in this study could be raised by a factor of up to 6.32 times as compared to the smooth duct Nusselt number. An artificially roughened wall with V-ribs was analysed experimentally by Maithani and Saini [132] in an attempt to improve the convection heat transfer rate of solar air channels by varying the values of artificial ribs parameters such as (whilst fixing the relative roughness height value at 0.043) angle of attack between 30° – 75° and relative roughness pitch between 6 – 12. The Reynolds number was in the range of 4,000 to 18,000. A maximum increase in the Nusselt number by a factor of 3.6 times that of the smooth duct value was determined.

Moreover, many other different artificial shapes have been introduced on the hot wall of the domain to test their effects on heat transfer coefficients [133-135]. An artificial W-shaped ribs roughness on the absorber plate of a solar heater rectangular channel was examined experimentally by Lanjewar*, et al.* [136] in an attempt to raise the heat transfer coefficient. Different roughness parameters have been investigated with a Reynolds number range of 2,300 to 14,000, and compared to the results achieved with a smooth absorber plate. The highest Nusselt number increase, Nu_R/Nu_S, was 2.36. An artificially roughened reverse L-shaped rib was used by Gawande*, et al.* [137] at Reynolds numbers $3{,}800 \leq Re \leq 18{,}000$, a relative roughness height, e/Dh, of 0.042, and a relative pitch range of $7.14 \leq P/e \leq 17.86$ to experimentally and numerically investigate the heat transfer enhancement rate. It was concluded that at a constant relative roughness height, Nusselt number increases as the relative roughness pitch decreases. At a P/e of 7.14, a Re of 15,000 and fixed e/Dh, the maximum heat transfer coefficient was achieved, which gave a Nu_R/Nu_S of 2.827. An experimental study was completed by Pandey and Bajpai [138] on convective heat transfer enhancement in a rectangular roughened duct to analyse the effect of roughness parameters such as height and pitch of roughness at different Reynolds numbers in the range 2,100 to 21,000. In comparison to a smooth channel, the maximum ratio of the roughened Nusselt number to the smooth Nusselt number was 5.85. An experimental investigation of heat transfer enhancement due to artificially roughened rib-groove within a rectangular solar heater duct was studied by Jaurker*, et al.* [123]. Several values of rib-groove roughness parameters were analysed over a range of Reynolds numbers between 3000 and 21,000. The maximum Nusselt number in the roughened case was 2.7 times greater than that of the smooth case.

It was noticed from the literature survey of artificially roughened cavities sub-section, and to the best of the author's knowledge, that the experimental and numerical investigations mostly concentrate on different rib shapes and their optimization. Even though artificial roughness has an incredible positive impact on convection heat transfer enhancement, it has not been sufficiently used in practice. Ultimately, no effort has been made to enhance the heat transfer performance of lid-driven cavities using different shaped artificial ribs and then comparing them with smooth/traditional bottom wall cases of turbulent mixed convection using the URANS method. Therefore, this will form one of the objectives of this research.

2.4 Conclusion

Based on the literature survey, and to the best of the authors' knowledge, it can be summarized that the research of the heat convection in lid-driven cavity problems has been continually developed, however: Most researchers used conventional fluids; very limited work on 3D lid-driven cavity; too little attention has been paid to the study of turbulent flow by using an advanced model such as

URANS and LES methods; no work has been done to study a 3D mixed convection lid-driven enclosure filled with nanofluids; no work has been done to study a 3D turbulent mixed convection flow of clockwise and anticlockwise rotating cylinder within lid-driven enclosure; no work has been done to study a mixed convection with roughness moving wall cavity. Thus, filling these gaps will form the main objectives of this thesis.

Chapter 3 Methodology

3.1 Introduction

Computational Fluid Dynamics (CFD) techniques are used to solve and study complex fluid flow and heat transfer problems. CFD is a computer-based tool for simulating the behaviour of systems involving fluid flow, heat transfer, and other related physical processes. It works by solving the equations of fluid flow over a region of interest, with specified conditions at the boundaries of that region. Additionally, CFD sees widespread use in various industrial and engineering fields as it can solve several system configurations at the same time and at a reduced cost compared with experimental studies. The region of interest in which the flow simulation is to be done is referred to as the computational domain of the problem(s). Basically, CFD is mainly used as a design tool, particularly for the purposes of design optimization, process optimization and parametric study. The principles behind the CFD simulations carried out in this project depend on the finite volume method (FVM) that the ANSYS©FLUENT (13-18) [139] solver uses. In this case, the domain of the model to be examined is discretized into a finite set of control volumes which are referred to as meshes or cells; therefore, the ICEM 16.2 [139] CFD has been used to create the domains and to generate the grids. The general conservation equations for mass, momentum and energy are then solved for this set of control volumes. Other transport equations, such as the equations for species, may also be applied.

In this thesis, CFD techniques are applied in the study of mixed convection heat transfer and flow characteristics in four lid-driven cavities which differ in terms of being filled either with conventional fluids or different nanofluids with different fluid properties, their geometries, boundary conditions and dimensionless numbers such as the Reynolds, Richardson and Grashof numbers. This chapter includes a brief characterization of the governing equations, thermophysical properties of the working fluids, dimensionless numbers, discretized equations, numerical models that include sub-sections describing the numerical solvers, pressure-velocity coupling and fluid flow computation using the SIMPLE and SIMPLEC algorithms, as well as the under-relaxation factor. Finally, the turbulence methods, which are the Reynolds-Averaged Navier-Stokes (RANS) and Large Eddy Simulation (LES) methods, and code validation are presented at the end of this chapter.

3.2 Governing equations

The governing equations are presented in this section for the CFD analysis of the present lid-driven enclosure studies. The continuity, momentum and the energy equations can be written for the three-dimensional flow of an incompressible fluid [140].

Continuity equation:

$$\frac{\partial u_i}{\partial x_i} = 0 \tag{3.1}$$

Momentum equation:

$$\frac{\partial u_i}{\partial t} + \frac{\partial (u_j u_i)}{\partial x_j} = -\frac{1}{\rho}\frac{\partial P}{\partial x_i} + \nu\left(\frac{\partial^2 u_i}{\partial x_i \partial x_i}\right) + F_i \tag{3.2}$$

where F_i is a body force

Energy equation:

$$\frac{\partial (T)}{\partial t} + \frac{\partial \left(u_j T\right)}{\partial x_i} = \frac{k}{\left(\rho C_p\right)}\left(\frac{\partial^2 T}{\partial x_i \partial x_i}\right) \tag{3.3}$$

3.3 Thermophysical properties of the working fluids

The thermophysical properties of the base fluid and nanoparticle types are presented in Table 3-1. The nanofluids being used correspond to a mixture of water (base fluid) with aluminium oxide, silicon dioxide, copper oxide, titanium dioxide or zinc oxide. The required properties of this work include density, heat capacity, effective thermal conductivity, effective dynamic viscosity and thermal expansion.

Table 3-1: Thermophysical properties of water and nanoparticles [141-144].

Materials	ρ (Kg/m³)	Cp (J/kg. K)	k (W/m. K)	μ (Ns/m²)	$\beta \times 10^{-5}$ (K-1)
pure water (H_2O)	996.5	4181	0.613	0.0001	21
aluminium oxide (Al_2O_3)	3970	765	40	-	0.58
silicon dioxide (SiO_2)	2200	705	36	-	0.63
copper (CuO)	6500	533	17.65	-	0.85
titanium dioxide (TiO_2)	4250	686.2	8.9538	-	0.17
zinc oxide (ZnO)	5600	495.2	13	-	0.72

The density and heat capacity, as stated by Ghasemi and Aminossadati [145], are calculated as shown below:

$$\rho_{nf} = (1-\phi)\rho_{bf} + \phi\rho_{np} \tag{3.4}$$

$$\left(\rho C_p\right)_{nf} = (1-\phi)\left(\rho C_p\right)_{bf} + \phi\left(\rho C_p\right)_{np} \tag{3.5}$$

where ϕ is a volume fraction of nanoparticle.

The effective thermal conductivity of a nanofluid, as stated by Vajjha*, et al.* [146], is given as per below:

$$k_{eff} = k_{Static} + k_{Brownian} \tag{3.6}$$

$$k_{Static} = k_{bf}\left[\frac{\left(k_{np} + 2k_{bf}\right) - 2\phi(k_{bf} - k_{np})}{\left(k_{np} + 2k_{bf}\right) + \phi(k_{bf} + k_{np})}\right] \tag{3.7}$$

$$k_{Brownian} = 5 \times 10^4 \beta\ \phi\rho_f \mathrm{C_{p,f}} \sqrt{\frac{\mathrm{k\,T}}{2\rho_{\mathrm{np}}\mathrm{d_{np}}}}.f(\mathrm{T},\phi) \tag{3.8}$$

where the Boltzmann constant is: $\mathrm{k} = 103807 \times 10^{-23}\,\mathrm{J\,K^{-1}}$ (3.9)

$$f(\mathrm{T},\phi) = (2.8217 \times 10^{-2}\phi + 3.917 \times 10^{-3})\left(\frac{\mathrm{T}}{\mathrm{T_0}}\right) + (-3.0699 \times 10^{-2}\phi - 3.91123 \times 10^{-3}) \tag{3.10}$$

Table 3-2: Fraction of the liquid volume that moves with nanoparticles [147, 148].

Nanoparticle types	$\boldsymbol{\beta}$	**Volume fraction**
copper oxide (CuO)	$\beta = 9.8810(100\phi)^{-0.9446}$	$1\% \leq \phi \leq 6\%$
zinc oxide (ZnO)	$\beta = 8.4407(100\phi)^{-1.07304}$	$1\% \leq \phi \leq 7\%$
aluminium oxide (Al_2O_3)	$\beta = 0.0017(100\phi)^{-0.841}$	$1\% \leq \phi \leq 10\%$
silicon dioxide (SiO_2)	$\beta = 1.9526(100\phi)^{-1.4594}$	$1\% \leq \phi \leq 10\%$

The dynamic viscosity of nanofluids, as stated by Corcione [149], can be calculated by using the equation below:

$$\frac{\mu_{nf}}{\mu_{bf}} = \frac{1}{1 - 34.87\left(\frac{d_{np}}{d_{bf}}\right)^{-0.3} \phi^{1.03}} \tag{3.11}$$

The equivalent diameter of the base fluid molecule can be calculated using the equation below:

$$d_{bf} = \left[\frac{6M}{N\pi\rho_{bf}}\right]^{\frac{1}{3}} \tag{3.12}$$

where:

M: Molecular weight of the base fluid.

N: Avogadro number $= 6.022 \times 10^{23}$ mol^{-1}

Finally, the thermal expansion of a nanofluid, as stated by Ghasemi and Aminossadati [145], is given as per below:

$$(\rho\beta)_{nf} = (1 - \phi)(\rho\beta)_{bf} + \phi(\rho\beta)_{np} \tag{3.13}$$

3.4 Dimensionless numbers of fluid mechanics and heat transfer

Some key dimensionless numbers used in the present analysis are listed below:

Reynolds number (Re): This is a dimensionless number that gives the ratio of inertial forces to viscous forces.

$$Re = \frac{inertial\ forces}{viscous\ forces} = \frac{\rho VL}{\mu}$$

When the fluid has a high viscosity or there is a low fluid motion, the flow is laminar; however, the flow will be turbulent in the instance of a high Reynolds number or a low viscosity.

Grashof number (Gr): This is a dimensionless number that gives the ratio of the buoyancy to the viscous forces of the fluid. It is usually involved in the study of natural convection.

$$Gr = \frac{g\beta(T_s - T_\infty)L^3}{\nu^2}$$

The ratio Gr/Re^2 is an expression of the mixed convection, and is called the Richardson number. When the Richardson number is much greater than unity, buoyancy is the dominant force; however, the opposite is true when the Richardson number is much less than unity.

Nusselt number (Nu): This is a dimensionless number that expresses the ratio of convective to conductive heat transfer.

$$Nu = \frac{convection\ heat\ transfer}{conduction\ heat\ transfer} = \frac{hL}{K}$$

3.5 The discretized equations

There are two general methods by which to solve the partial differential equations, namely those of analytical and numerical methods. Although the use of analytical methods always provides exact results, researchers can face various pitfalls when employing them, in particular with complex flow issues. Conversely, a numerical solution can reach closed results, but usually cannot give an exact solution; however, most complex flow problems can nevertheless be solved through numerical analysis. Nevertheless, choosing the optimal numerical schemes and appropriate physical models can provide highly accurate results.

Dividing the continuous domain into a finite number of cells is an important means by which to solve the transport equations with high accuracy. These cells are known as ‘control volumes’, and have a node point that is located in the centre of each cell. A numerical solution can be obtained via a number of methods such as the finite element method (FEM), the finite difference method (FDM) and the finite volume method (FVM). The latter method, which FLUENT utilises, has been chosen in the current research to overcome the transport equations governing the flow problems. As based on FLUENT [139], there are several numerical schemes that can be used. Some brief definitions of the numerical schemes so employed are given as follows:

- The first-order upwind scheme is the simplest available numerical scheme [150]. When it is involved and according to the donor-cell concept and as shown in Figure 3-1, at $u_w > 0$ and $u_e > 0$ respectively, the face values ϕ_w and ϕ_e are approximated to their upstream neighbouring values This scheme can be acceptable when using a quadrilateral or hexahedral mesh. Although this scheme is stable and satisfies flow direction, it is preferable that it not be used with triangular or tetrahedral meshes because of the possibility of discretization errors. However, it is frequently used as a starting point for other calculations.
- The second-order upwind scheme provides good results with complex flows compared to the first-order upwind method. Generally, it is used with triangular and tetrahedral meshes. However, some calculations need to be started with the first-order model and then change to the second-order model, such as flows with high Mach number.
- The QUICK (the quadratic upwind interpolation for convective kinetics) scheme is suitable for use with quadrilateral, hexahedral and hybrid mesh types. It is useful in the case of rotating flows. However, it might prove unstable in high gradient regions.
- The Boundary Centre Differencing scheme fits with the LES approach in view of its meritoriously low diffusion. Although it is highly accurate compared to the first-order upwind scheme, it might lead to oscillations in the solution when the Peclet number is greater than 2.

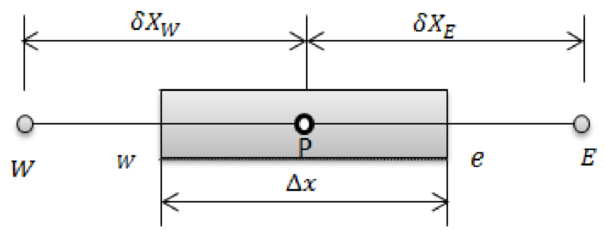

Figure 3-1: Schematic diagram of a control volume around a node by using FVM.

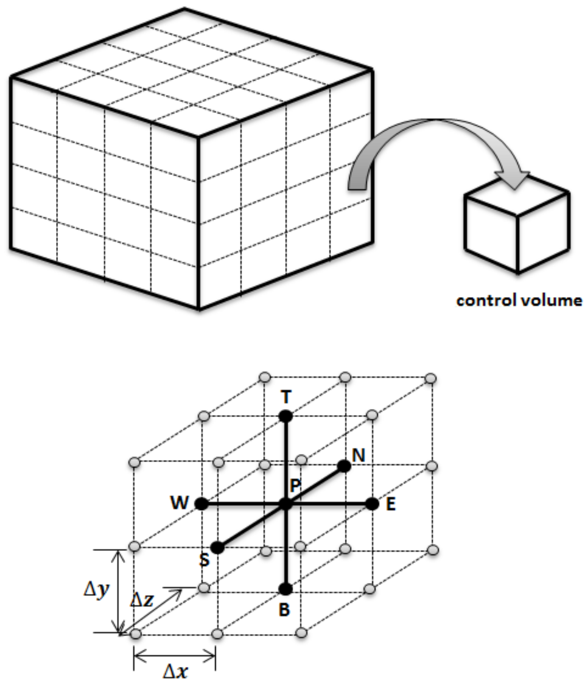

Figure 3-2: Schematic diagram of a discretized computational domain.

3.6 Numerical models

3.6.1 Numerical solvers

Pressure-based and density-based solvers are the two numerical methods available in FLUENT [139]. It is known that the pressure-based solution is usually utilized to solve the Navier-Stokes equations for low speed, incompressible or mildly compressible flows, while high speed or compressible flows can be solved using the density-based solver. However, both of these solvers can be used to solve a wide number of simple and complex flow cases due to a sequence of the extension and the development that has been completed on these solvers. The velocity field can be obtained from the momentum equations in both solvers. The density field can be calculated using the continuity equation in the density-based approach, whilst the use of a pressure, or pressure correction, equation can determine the pressure field in a pressure-based approach. In the CFD model of the mixed convection heat transfer problem, the pressure-based solver is chosen to treat the incompressible flow in the current studies. Differences in densities (buoyancy) can be caused by local temperature variations (natural convection) or differences in mass concentration or differences in the density of multiphase flow. Nevertheless, a variation in local pressure could generate buoyancy in the ideal gases, and real fluids can be ignored because of this tiny change. When the density change is quite small, the Boussinesq model can be used. Boussinesq approximation is a way to solve non-isothermal flow, such as free convection cases, without solving the full compressible formulation of the Navier-Stokes equations. Boussinesq approximation can decrease the nonlinearity of the problem by assuming that changes in density have no impact on the flow field, excluding buoyancy term, which helps to reach the convergence faster.

3.6.2 Pressure-velocity coupling

Pressure-velocity coupling points to the numerical algorithm using a combination of momentum and continuity equations to derive the equation of the pressure or pressure correction when a pressure-based solver is involved. Pressure-velocity coupling can be calculated by employing Equation (3.14) to been an extra term for pressure by the reconfiguration of the continuity equation. There are four types of algorithm in FLUENT [139]: SIMPLE, SIMPLEC, PISO and Coupled. The pressure-based segregated algorithm is utilized with all these schemes except for the Coupled algorithm, which uses the pressure-based coupled solver. Based on the literature and code validation, the SIMPLE and SIMPLEC algorithms have been chosen for use in the current research.

$$\begin{aligned} Jf = \rho_f \frac{a_{p,c_0} v_{n,c_0} + a_{p,c_1} v_{n,c_1}}{a_{p,c_0} a_{p,c_1}} \\ + d_f \left(\left(p_{c_0} + (\nabla p)_{c_0} . \overrightarrow{r_0} \right) - \left(p_{c_1} + (\nabla p)_{c_1} . \overrightarrow{r_0} \right) \right) \\ = \hat{J}_f + d_f \left(p_{c_0} - p_{c_1} \right) \end{aligned} \tag{3.14}$$

where v_{n,c_0}, v_{n,c_1} and p_{c_0}, p_{c_1} are respectively represent the velocities and pressures of two cells.

$\hat{J}_f$ refers to the influence of the velocity in cells.

d_f is a function of the average of momentum equation.

3.6.2.1 SIMPLE and SIMPLEC algorithms

SIMPLE is an acronym for Semi-Implicit Method for Pressure-Linked Equations. It is a numerical procedure that generally sees use in solving the Navier-Stokes equations. The SIMPLE algorithm has been widely used by many researchers to solve different types of fluid flow and heat transfer problem since its development in the 1970s by Prof. Brian Spalding and his student Suhas Patankar [151, 152] at Imperial College London. The concept of the procedure is essentially a guess and a correction procedure for the calculation of pressure. In other words, a trial pressure (p^*) is utilized to determine the velocity (u^*) in the momentum equation, which can predict the corrected pressure that expresses the corrected pressure and the pressure correction terms. On the other hand, the SIMPLEC algorithm is a modified version of the SIMPLE algorithm, as developed by van Doormal and Raithby in 1984 [153]. Basically, compared to the SIMPLE algorithm, the SIMPLEC algorithm works by neglecting the influence of dropping velocity neighbour terms. In other words, the SIMPLEC algorithm can provide a faster convergence than SIMPLE; however, both algorithms are suitable for use in the existing research. Equation (3.15) refers to the expressed of the corrected pressure and the pressure correction terms.

$$\mathrm{p}' = \mathrm{p} - \mathrm{p}^* \tag{3.15}$$

Based on the estimated pressure, the velocity correction can be expressed as:

$$\mathrm{u}' = \mathrm{u} - \mathrm{u}^*, \qquad \mathrm{w}' = \mathrm{w} - \mathrm{w}^* \quad and \qquad \mathrm{v}' = \mathrm{v} - \mathrm{v}^* \tag{3.16}$$

3.6.2.2 Under-relaxation factor

The under-relaxation factor, α, is used in the pressure-based solver to stabilize the iteration of the simulation for the pressure-based solver. Using the under-relaxation factor can reduce the numerical solution error in each iteration. Hence, convergence can be reached faster, and the stability of the calculations can also be improved. The new value of ϕ depends on ϕ_{old}, and $\Delta\phi$ can thus be written as Equation (3.17). In ANSYS©FLUENT, the default under-relaxation parameters for all variables are optimally set for the largest possible number of cases.

However, some turbulent flows or high Rayleigh number natural convection studies require a reduction in the under-relaxation factor.

$$\phi = \phi_{old} + \alpha \Delta \phi \tag{3.17}$$

where $0 < \alpha < 1$

3.7 Turbulence methods

Either turbulent gas or liquid flow occurs when the flow has a high Reynolds number or low viscosity. It is widely known that heat transfer can be rapidly enhanced by turbulent flow, unlike when the flow is laminar which leads to the development of an insulating blanket near solid walls Saha*, et al.* [154]. Any intermixing of the fluid that might otherwise be possible would not occur when flow motion is slow because the boundary layer velocity reduces smoothly due to viscous drag, which can lead the heat transfer being purely reliant on molecular convection and conduction. In contrast, the heat transfer rate can be enhanced significantly by raising the fluid velocity, which generates turbulent vortices where the boundary layers break away from the cavity walls and mix with the bulk fluid away from the obstructed enclosure walls Choi*, et al.* [35]. Consequently, the use of the turbulent flow model has increased dramatically for heat convection problems over the last few years. The fluid flow within moving wall cavities can be influenced by numerous physical variables such as the speed of lid-driven enclosures, using rotating objects inside the enclosure, involving artificial roughness beside heat sources distribution. Three types of turbulence model have been used in recent work which corresponds to the standard *k-ε* model of the URANS approach, the subgrid-scale model of Smagorinsky-Lilly LES method, and the Wall-Adapting Local Eddy-viscosity (WALE) of the LES approach. Additionally, the laminar viscous model is used in Chapter 4.

3.7.1 Reynolds-Averaged Navier-Stokes (RANS) method

The RANS approach has the most economic models for computing complex turbulent flow, such as the *k-ε* and *k-ω* models. RANS models are suitable for many engineering applications and typically provide the level of accuracy required. Incompressible time-averaged Navier-Stokes equations were computationally solved using both the steady RANS and unsteady RANS methods, the latter retaining transient terms compared to the steady model. Unsteady RANS computation is commonly used for large-scale turbulent flow. The standard *k-ε* turbulence model is one of the most popular turbulence models that is used regularly with turbulent flow cases and sees considerable use in mixed convection fluid flow in lid-driven enclosures. The benefit of this type of turbulent model, in terms of both the accuracy of its results and its ability to predict complex fluid flow problems, has convinced researchers of the utility of this model; hence, it has also been chosen for use in this research. This kind of model has two equations of transport to deal with the properties of turbulent flows. Equations (3.18) and (3.19) below represent the turbulence kinetic energy (*k*) and the dissipation rate (ε) [155]. The latter variable determines the scale of the turbulence, whereas the first variable, *k*, determines the energy in the turbulence.

$$\frac{\partial}{\partial t}(\rho k) + \frac{\partial}{\partial x_i}(\rho k u_i) = \frac{\partial}{\partial x_j}\left[\left(\mu + \frac{\mu_t}{\sigma_k}\right)\frac{\partial k}{\partial x_j}\right] + P_k + P_b - \rho\varepsilon + S_k \tag{3.18}$$

$$\frac{\partial}{\partial t}(\rho\varepsilon) + \frac{\partial}{\partial x_i}(\rho\varepsilon u_i) = \frac{\partial}{\partial x_j}\left[\left(\mu + \frac{\mu_t}{\sigma_\varepsilon}\right)\frac{\partial k}{\partial x_j}\right] + C_{1\varepsilon}\frac{\epsilon}{k}(P_k + C_{3\varepsilon}P_b) - C_{2\varepsilon}\rho\frac{\epsilon^2}{k} + S_\varepsilon \tag{3.19}$$

where $C_{1\varepsilon}$, $C_{2\varepsilon}$ and $C_{3\varepsilon}$ are model constants and S_k and S_ε refer to the user-defined source terms. The remaining terms are given in Equations (3.20), (3.21) and (3.22).

Turbulent viscosity: $$\mu_t = \rho C_\mu \frac{k^2}{\varepsilon} \tag{3.20}$$

Production of *k*: $$P_k = -\rho\overline{u_i' u_j'}\frac{\partial u_j}{\partial x_i} \tag{3.21}$$

Effect of buoyancy: $$P_b = \beta g_i \frac{\mu_t}{Pr_t}\frac{\partial T}{\partial x_i} \tag{3.22}$$

3.7.2 Large Eddy Simulation (LES) method

The LES method is an important and useful mathematical method that can be used to treat turbulent fluid flow problems. Usually, the URANS equations are used to simulate time-dependent turbulence cases, but in some situations this method is unable to give a reasonable result. Using LES instead of URANS can provide a result closer to the experimental one. The Navier-Stokes equations are filtered when using LES, which means that larger vortices than the size of the filter are resolved, and smaller vortices than the filter can be modelled. However, it has certain specific requirements compared to RANS such as fine grids, which are better with tetrahedral rather than hexahedral mesh elements, so therefore small-time steps are needed. The Courant-Friedrichs-Lewy number, CFL, calculates the time step as shown in Equation (3.23). In general, for numerical stability, CFL number should be kept under 0.5 at all times. Therefore, CFL number in present research was 0.3 at all time in presence of LES method. In addition, in the instance of studying boundary layer structures, the LES geometry should have y^+ not greater than 1 and the LES method needs a low aspect ratio for the mesh elements to avoid produce high values of cutoff-length. The LES approach is suitable for use with high Reynolds numbers. Moreover, LES sees frequent use with unstable and unsteady flows, whilst the geometrical case needs the full region of the geometry, even with an asymmetric geometry. Equation (3.24) shows a typical spatial filtering operation in LES method as it is written in [156, 157].

$$CFL = \Delta t \left(\frac{\bar{u}_i}{\Delta x_i} \right) \tag{3.23}$$

$$\overline{\psi(\boldsymbol{x}, t)} = \int_{-\infty}^{\infty} \int_{-\infty}^{\infty} \psi\,(\boldsymbol{r}, t')\; G(x - \boldsymbol{r}, t - t') d\boldsymbol{r} dt' \tag{3.24}$$

Total flow variable:	ψ
Filtered flow variable:	$\bar{\psi}$
Small scale spatial fluctuation about $\tilde{\psi}(\boldsymbol{x}, t)$:	ψ'
Filter kernel:	G

Smagorinsky (1963) provided the first subgrid-scale model for LES, based on Prandtl's mixing length theory. Deardorff (1970) used LES to investigate the turbulence in a channel flow, which might be regarded as the first engineering application of LES. A successful LES model should be able to mimic the energy transfer from the resolved scales to the subgrid-scale. The subgrid-scale model of the Smagorinsky-Lilly LES method is given by [158]:

$$\tau_{ij} - \frac{\delta_{ij}}{3}\tau_{kk} = -2\nu_{sgs}\bar{S}_{ij} = -2C\bar{\Delta}^2|\bar{S}|\bar{S}_{ij} = -2C\beta_{ij} \tag{3.25}$$

where

$$\beta_{ij} = -\bar{\Delta}^2|\bar{S}|\bar{S}_{ij} \tag{3.26}$$

$$\bar{S}_{ij} = \frac{1}{2}(\frac{\partial\bar{u}_i}{\partial x_j} + \frac{\partial\bar{u}_j}{\partial x_i}) \tag{3.27}$$

$$\bar{\Delta}= (\bar{\Delta}_x\bar{\Delta}_y\bar{\Delta}_z)^{\frac{1}{3}} \tag{3.28}$$

$$|\bar{S}| = (2\bar{S}_{ij}\bar{S}_{ij})^{\frac{1}{2}} \tag{3.29}$$

The subgrid-scale (SGS) model used for WALE (Wall-Adapting Local Eddy-viscosity) in the LES approach is employed, as developed by Nicoud and Ducros [159] and Ben-Cheikh*, et al.* [160]:

$$\mu_t = \rho L_s^2 \frac{\left(S_{ij}^d S_{ij}^d\right)^{\frac{3}{2}}}{\left(\bar{S}_{ij}\bar{S}_{ij}\right)^{\frac{5}{2}} + \left(S_{ij}^d S_{ij}^d\right)^{\frac{5}{2}}} \tag{3.30}$$

where L_s and S_{ij}^d can be defined as follows:

$$L_s = \min\left(kd, C_W V^{\frac{1}{3}}\right) \tag{3.31}$$

where $C_W = 0.325$

$V^{\frac{1}{3}}$ is the volume of the cells ($V = \Delta x\Delta y\Delta z$)

$$S_{ij}^d = \frac{1}{2}\left(\bar{g}_{ij}^2 + \bar{g}_{ji}^2\right) - \frac{1}{3}\delta_{ij}\bar{g}_{kk}^2 \tag{3.32}$$

where $\bar{g}_{ij} = \frac{\partial\bar{u}_i}{\partial x_j}$ (3.33)

$$\bar{S}_{ij} = \frac{1}{2}(\frac{\partial\bar{u}_i}{\partial x_j} + \frac{\partial\bar{u}_j}{\partial x_i}) \tag{3.34}$$

3.8 Code validations

Before starting any new numerical study, the numerical solver must be validated thoroughly against previous investigations with regards to achieving the necessities of running new simulations. In this section, the numerical results from the current CFD model are compared with available results from the seven journal papers discussed in the literature review.

Firstly, the present results have been validated against the results of Mamun, *et al.* [24], who analysed mixed convection air flow in a trapezoidal lid-driven cavity heated from the bottom wall. Figure 3-3 shows a comparison of the code validation in terms of isotherms and streamlines. The isotherms and streamlines were obtained for Richardson numbers in the range between 0.1 – 10.

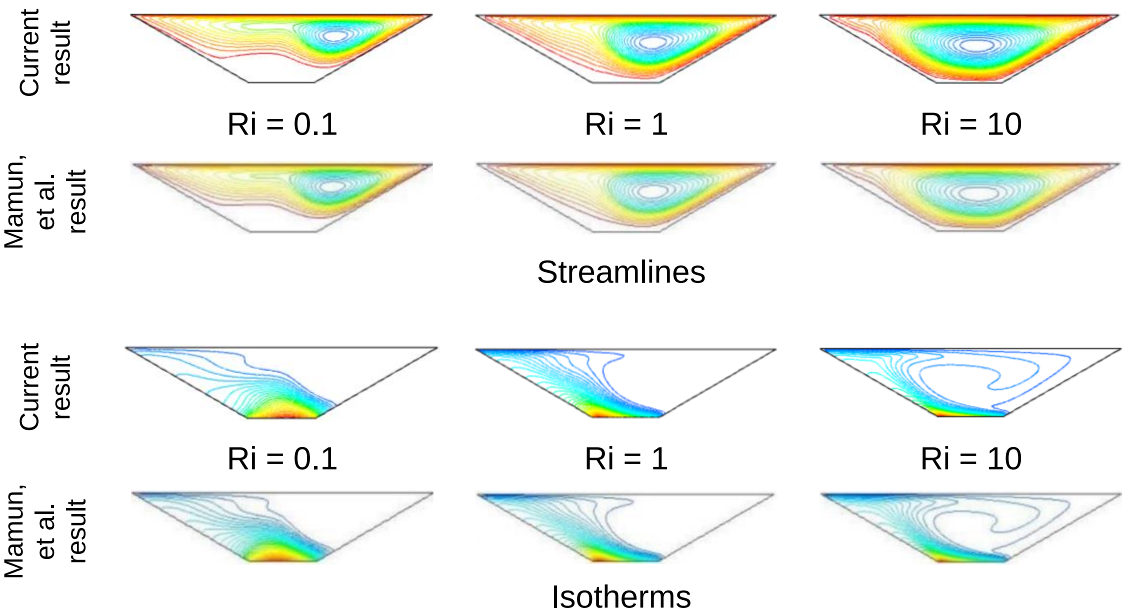

Figure 3-3: Comparison of the present results with the results of Mamun, *et al.* [24], and Guo and Sharif [78] for isotherms and streamlines at Re = 400, A = 1 and γ = 30°.

Secondly, the study by Guo and Sharif [78] was selected for validation, because of its similarity to the current study boundary condition. These authors studied mixed convection heat transfer in a rectangular cavity with constant heat flux, as heated from the bottom wall, while the isothermal sidewalls moved downward with uniform velocity and were maintained at a constant temperature. A comparison of the Nusselt number variation has been achieved at different aspect ratios (A). As shown in Figure 3-4, it is clear that the present results are in good agreement with aspect ratios in the range 0.5 – 2.

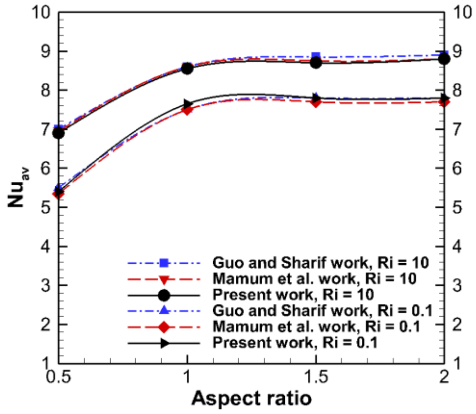

Figure 3-4: Comparison of the Nusselt numbers for the present results with the results of Mamun*, et al.* [24], and Guo and Sharif [78] at Ri = 0.1 and 10, Re = 100 and E = 0.6.

The *third validation* was completed for the results of Sharif [161], as displayed in Figure 3-5 and Table 3-3, for a laminar mixed convection flow in a top-heated moving wall cavity filled with water at given Reynolds number and a range of Richardson numbers and geometry rotational angles. In addition, as shown in Figure 3-6 for the isotherm and streamline contours comparison, further good agreement has been achieved as well with regards to completing code validation over a wide range of comparisons. The comparison was completed at geometry inclination angles ranging between 0° - 30°, Richardson number of 1, Rayleigh number of 10^6 and an aspect ratio of 10. The *fourth validation*, as shown in Figure 3-9 and Table 3-4, was completed for the work of Chen and Cheng [162] who performed experimental and numerical laminar simulations for mixed convection heat transfer and flow patterns of air within an arc-shaped cavity with a cold moving top wall and heated stationary arc wall in terms of local Nusselt number. Various Grashof and Reynolds numbers were examined. As well as, the experimental and numerical results have been validated with present outcomes in terms of streamline and isotherm counters. The investigation considered the laminar mixed convection heat transfer of a moving top wall arc-shaped enclosure filled with air. Figure 3-7 and Figure 3-8 illustrate the comparison of streamline and isotherm counters for the present results and previous achievements in the literature. Overall, it can be seen that the similarity is sufficiently good to have confidence in the present CFD solver.

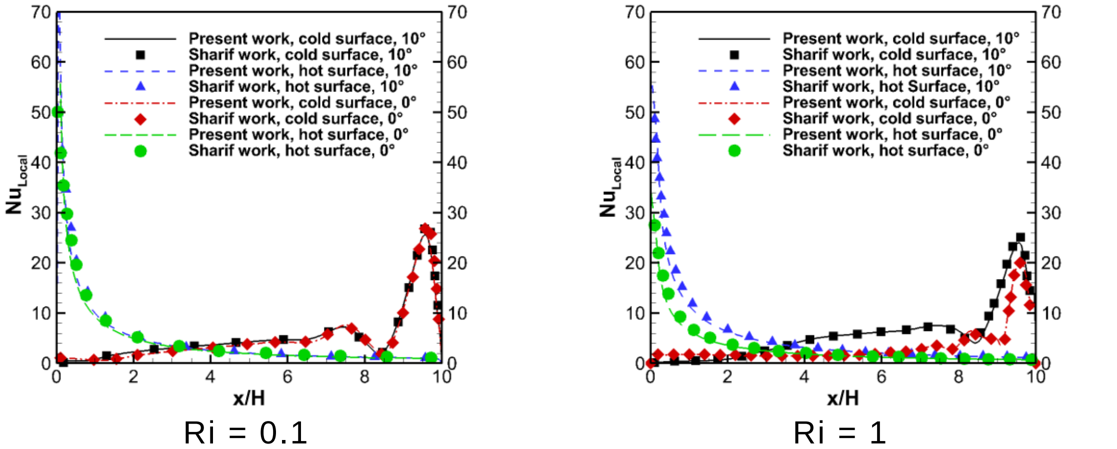

Figure 3-5: Comparison of the local Nusselt numbers for the present URANS modelling with the results of Sharif [161] at different inclination angles, γ = 0° - 10°.

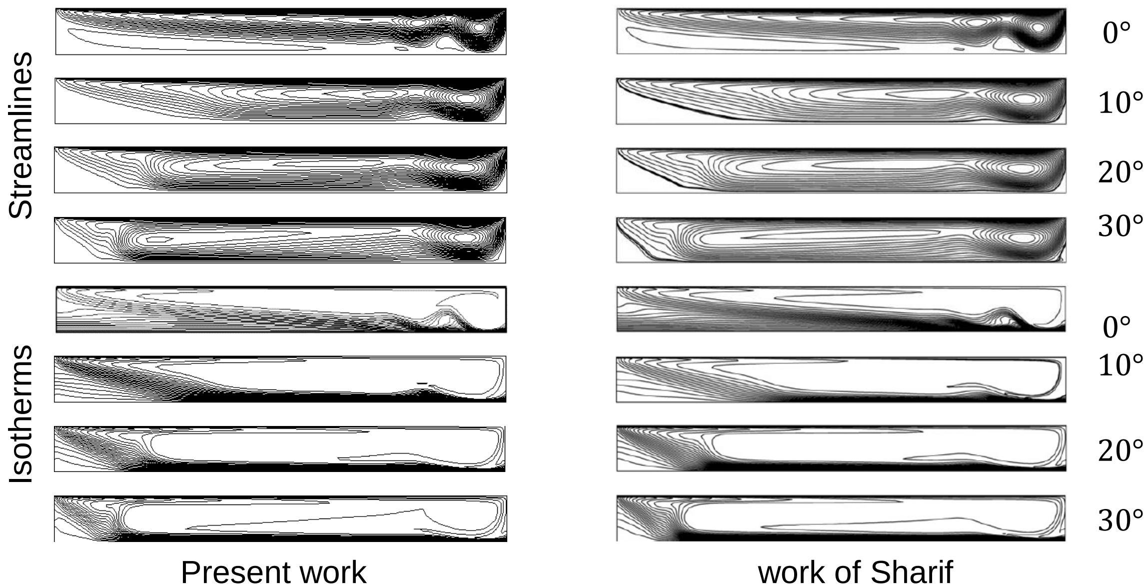

Figure 3-6: Comparison of the present work in terms of streamline and isotherm variations with the work of Sharif [161].

Fifthly, the validation of a two-phase mixture model of nanofluids has been achieved, as displayed in Figure 3-10, which clearly shows that the current predictions for the average Nusselt number are in good agreement with those obtained by Alinia*, et al.* [91]. Their research was intended for use with a two-phase mixture model of nanofluids within a two-sidewall, lid-driven enclosure. *Sixthly*, choosing the right model of RANS method has been completed by comparing standard k-ε outcomes to the experimental and numerical results of Prasad and Koseff [163] and Peng*, et al.* [164], respectively, to be certain that the current CFD solver can provide highly accurate results. Two different subgrid-scale models of LES method, which are Smagorinsky-Lilly and WALE have been compared against the experimental result of Prasad and Koseff [163] and the Smagorinsky-Lilly result of Padilla*, et al.* [165] to make sure that the current subgrade-scale model is reliable to provide accurate results.

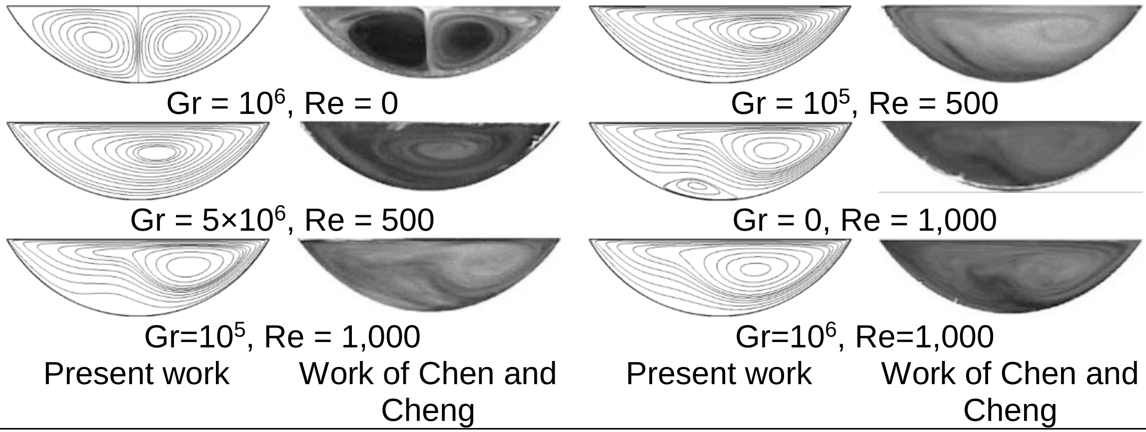

Figure 3-7: Comparison of the streamlines variations determined in the present work with the previous experimental work of Chen and Cheng [162].

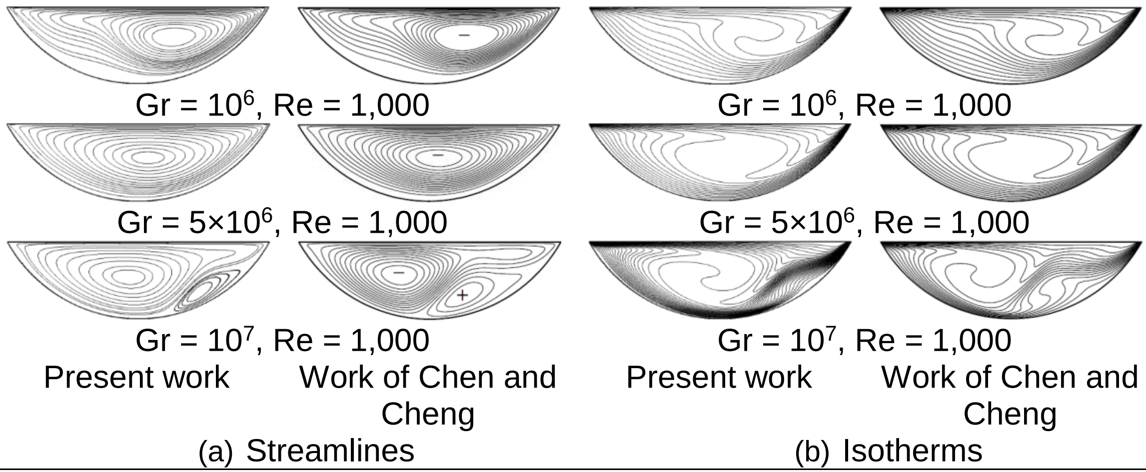

Figure 3-8: Comparison of the present work with the simulations of Chen and Cheng [162] for (a) streamlines and (b) isotherms.

As presented in Figure 3-11, the LES and URANS predictions from the present study were validated in terms of the mean velocity profiles at similar conditions of previous works and Reynolds number of 10,000. Essentially, it can be noted that both current subgrid-scale models of LES approach have provided high quality outcomes and they are ready to be used in new simulation of turbulence cases. As well as, the standard k-ε model has proved its ability to run the new simulation of unsteady turbulent flow.

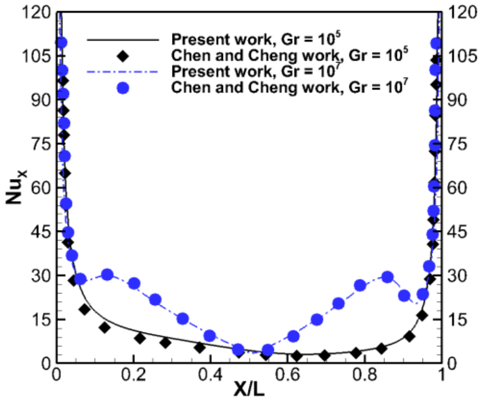

Figure 3-9: Comparison of the local Nusselt numbers for the present URANS model with that of Chen and Cheng [162].

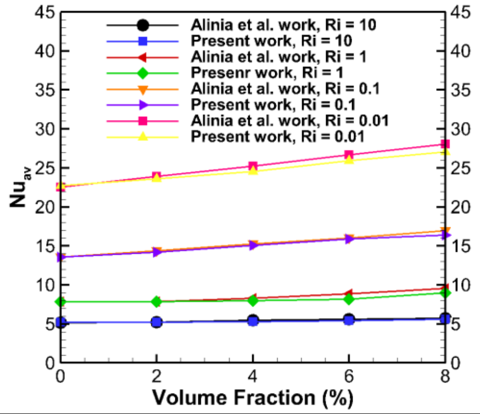

Figure 3-10: Comparison of the average Nusselt number determined for the present work with that of Alinia, *et al.* [91].

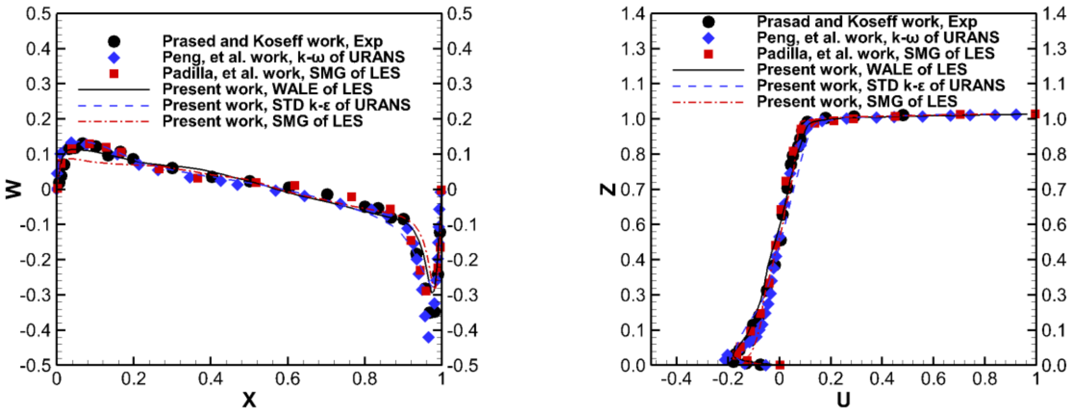

Left velocity Right velocity

Figure 3-11: Comparison of the mean velocity profiles for the current LES and URANS work with the results of Prasad and Koseff [163], Padilla, *et al.* [165], and Peng, *et al.* [164] at Re = 10,000.

Lastly, the validation of the 2D rotating solid cylinder within a moving wall cavity is achieved in this study. The comparison is made by using the following dimensionless parameters: Gr = 10^4, Pr = 6.95, 1 ≤ Ri ≤ 10 and 1 ≤ Ω ≤ 10. The present findings have been compared with the results of Chatterjee, *et al.* [62] in terms of dimensionless velocity profiles along the vertical line at x = 0.25. Good agreement has been found, as presented in Figure 3-12 and Table 3-5. Isotherms and streamlines are displayed respectively in Figure 3-13 and Figure 3-14 at a fixed Grashof number of 10^4 and a Prandtl number of 6.95. A range of Richardson numbers and the rotational speed of the cylinder have been considered in this validation.

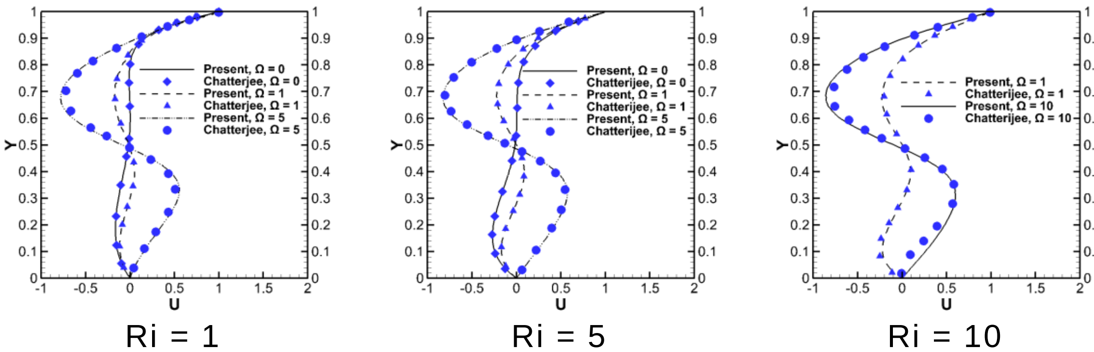

Figure 3-12: Comparison of the dimensionless velocity profiles determined in the present work along the vertical line at x = 0.25 with the results of Chatterjee*, et al.* [62].

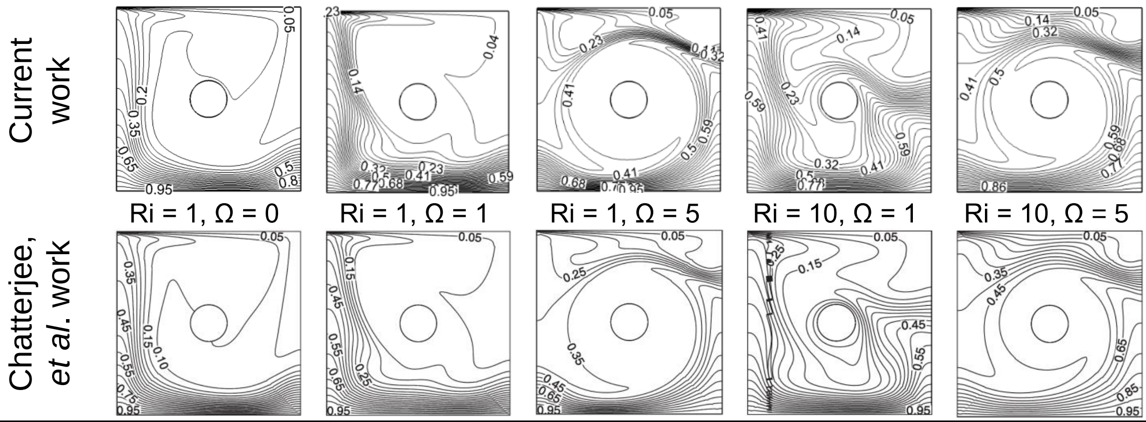

Figure 3-13: Comparison of the isotherms determined in the present work of those determined by Chatterjee*, et al.* [62].

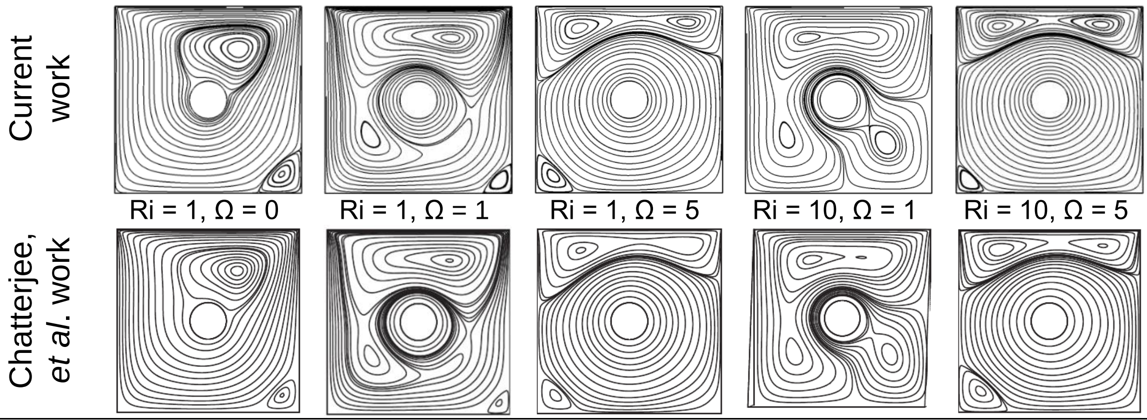

Figure 3-14: Comparison of the streamlines determined in the present work with those determined by Chatterjee*, et al.* [62].

Obviously, the present simulation results for all the validation cases have all shown good agreement with those from the previous related investigations, demonstrating that the current simulation methods are highly reliable and accurate.

Table 3-3: The percentage variations of the present result against the result of Sharif [161].

Inclination angle	$\gamma = 0$	$\gamma = 10$
Ri = 0.1		
Percentage variation (cold surface)	0.843%	1.147%
Percentage variation (hot surface)	1.355%	1.854%
Ri = 1		
Percentage variation (cold surface)	1.056%	0.945%
Percentage variation (hot surface)	2.603%	3.478%

Table 3-4: The percentage variations of the present result against the result of Chen and Cheng [162].

Grashof number	$Gr = 10^5$	$Gr = 10^7$
Percentage variation	4.184%	2.794%

Table 3-5: The percentage variations of the present result against the result of Chatterjee*, et al.* [62].

Rotational speed	$\Omega = 0$	$\Omega = 1$	$\Omega = 5$
Ri = 1			
Percentage variation	1.394%	1.455%	2.017%
Ri = 5			
Percentage variation	1.334%	1.849%	2.361%
Ri = 10			
Percentage variation	-	2.482%	4.143%

Chapter 4 Mixed convection heat transfer of a 2D lid-driven top wall trapezoidal enclosure

4.1 Motivation and introduction

There is a notable lack of information concerning nanofluids rather than conventional fluids within a trapezoidal lid-driven cavity. It is obvious from the literature review that the case of mixed convective heat transfer in trapezoidal enclosures utilizing nanofluids seems not to have been investigated in the past and this has motivated the present study. In other words, most of the previous research on trapezoidal enclosures involved conventional fluids. As well as, no work has been accomplished in the open literature that involved to investigate the effects of different nanofluid parameters, such as, nanofluid types, volume fraction and nanoparticles size in trapezoidal domains on the heat convection besides the effects of the inclination angels of the sidewall, rotation angles of the geometry, flow direction of the top wall lid-driven enclosure and aspect ratio of the cavity.

Therefore, this chapter discusses the simulated results of the CFD model with regards to a laminar mixed convection heat transfer in a two-dimensional trapezoidal lid-driven enclosure filled with nanofluids. The bottom wall of the enclosure is heated, while the upper wall is cooled at a lower temperature and the other two sidewalls are adiabatic. The governing equations for both fluid flow and heat transfer are solved by using the finite volume method (FVM). Four types of nanofluids (Al_2O_3, CuO, SiO_2, and TiO_2 in pure water) at a nanoparticle volume fraction (ϕ) in the range of 1 – 4% and nanoparticles diameter in the range of 25 – 70 nm have been applied. This chapter considers a Richardson number in the range of 0.1 – 10 and a fixed Reynolds number of 100. The trapezoidal lid-driven enclosure was studied for rotational angles (Φ) in the range of 30˚ – 60˚, inclination sidewalls angles (γ) in the range of 30˚ – 60˚, and various aspect ratios (A) ranging from 0.5 to 2. This chapter also covers the effects of opposing and aiding flow on the heat transfer enhancement. The results and the discussion are based on the Nusselt number plots which are located on the bottom wall, and isotherm and streamline contours. This chapter includes three parts, namely the numerical model, which includes the physical model, the boundary conditions, the numerical procedure, and the grid independent test, the numerical results derived from this model, and a discussion section. The material reported herein has been published in the literature [166].

4.2 Numerical model

4.2.1 Physical model

The schematic diagram of a trapezoidal lid-driven enclosure, for two cases, is shown in Figure 4-1. The first case consists of the cold wall moving in the positive x-direction (opposing flow conditions). The second case involves the cold wall moving in the negative x-direction (aiding flow conditions). Both the height and length of the trapezoidal lid-driven enclosure vary in accordance with the change of the aspect ratio (A = H/W), inclination angle, γ, or with the rotation angle, Φ.

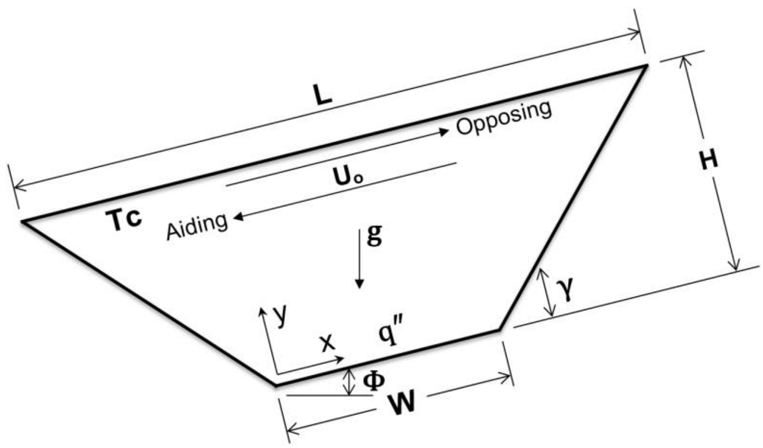

Figure 4-1: Schematic diagram of the trapezoidal lid-driven cavity.

4.2.2 Boundary conditions

The boundary conditions for the present problem are specified for the computational domain as shown in Figure 4-1. This figure demonstrates the general trapezoidal lid-driven cavity model, whose bottom wall and top wall are subjected to heat flux (q") and low temperature (Tc), respectively, while the sidewalls are kept adiabatic. Two cases of thermal boundary conditions for the top moving wall were considered: the first is where the cold wall is moving in the positive x-direction (opposing flow conditions), where the shear flow, which is caused by the moving top wall, opposes the buoyancy-driven flow, which is in turn influenced by the thermal non-homogeneity of the cavity boundaries; the second is where the cold wall is moving in the negative x-direction (aiding flow conditions), where the shear flow assists the buoyancy flow. The cavity height is 'H', the width of the bottom hot wall is 'W', and the cavity is inclined at an angle Φ to the horizontal reference axis. The inclination angle of the sidewalls of the cavity is γ. Flow and heat transfer phenomena in the cavity are investigated for a series of Richardson numbers (Ri), aspect ratios (A = H/W) and rotational angles, Φ, of the cavity.

4.2.3 Numerical procedure

The numerical computations were carried out by solving the governing conservations along with the boundary conditions by using the finite volume method (FVM) [167]. The second-order upwind differencing scheme was considered for the convective terms. The diffusion term, in the momentum and energy equations, is approximated by a second-order central difference which gives a stable solution. The dimensionless physical parameters were therefore calculated from the computed velocity and temperature distributions. The flow field was solved by using the SIMPLE algorithm [167]. The iterations were carried out until the sum of residuals for all computational cells became negligible (10^{-5}).

4.2.4 Grid independence test

In this section, a grid independence test was carried out to obtain the most suitable mesh face number and size for this particular geometry. In this study, ten node numbers are considered, 758, 1,030, 2,262, 2,794, 3,406, 3,970, 5,470, 7,170, 8,942 and 11,064 at Ri = 1, Re = 400 and A = 1. Given that the discretization grid is triangular, unstructured and non-uniform as shown in Figure 4-2. All the last four node numbers gave almost identical results for the Nusselt number so determined as illustrated in Figure 4-3. Ultimately, a mesh number of 5,470 was used in this chapter as this represented the best compromise in terms of both accuracy and computational time.

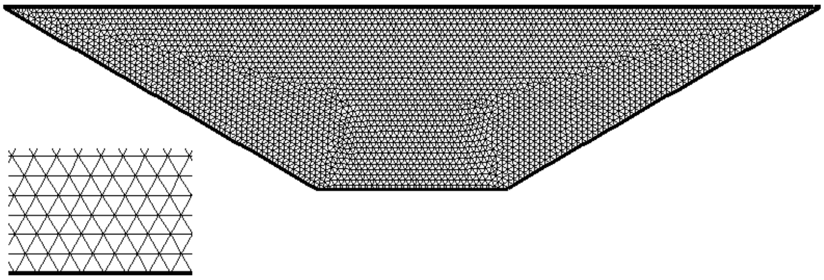

Figure 4-2: Computational mesh of the trapezoidal lid-driven cavity.

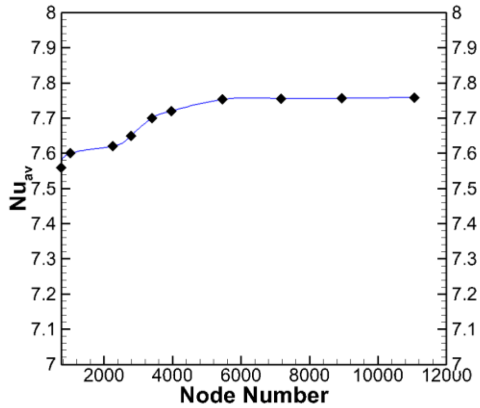

Figure 4-3: Convergence of the average Nusselt number with grid refinement.

4.3 Results and discussion

This section includes the relevant numerical results for mixed convection heat transfer in a trapezoidal lid-driven cavity when varying parameters such as the type of nanofluid, volume fraction of nanoparticles, nanoparticle diameters, Richardson number, rotational angle, inclination angle, aspect ratio and the direction of motion of the cold wall. The results are presented in terms of the Nusselt number on the bottom wall, and the isotherms and streamlines determined. Before starting a new numerical simulation, it needs to be validated a giants previous related studies to be certain that new simulated results are in right condition. Thus, this chapter has been validated against the similar published works that have accomplished by Mamun*, et al.* [24], Guo and Sharif [78] Guo and Sharif [78] and Alinia*, et al.* [91], more details about the validation are discussed in section 3.8.

4.3.1 The effect of nanoparticle type

Four different types of nanoparticles, Al_2O_3, CuO, SiO_2, and TiO_2, were examined. The Nusselt numbers at an aspect ratio = 1, Re = 100 and different values of Richardson number, 0.1 – 10, are shown for different nanofluids in Figure 4-4a – d. It has been demonstrated that nanofluids possess higher Nusselt numbers than pure water. In other words, these results indicate that the four types of nanofluids have comparatively higher heat transfer rates than pure water. From the results, it is additionally clear that the SiO_2-H_2O nanofluid has the best heat transfer rate, followed by Al_2O_3-H_2O, TiO_2-H_2O and CuO-H_2O. Consequently, SiO_2-H_2O possesses a higher thermal conductivity than the other nanofluids tested. It also has the highest average velocity due to having the lowest density in comparison to the other nanofluids.

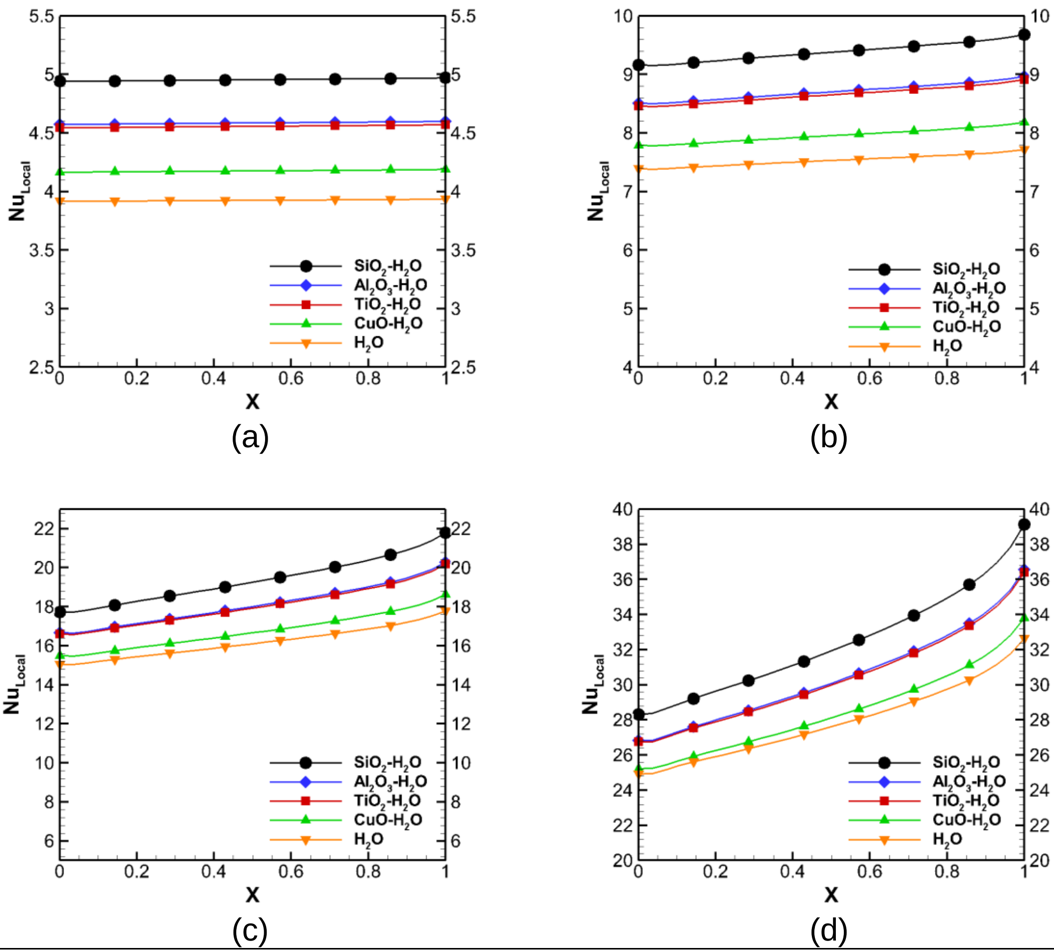

Figure 4-4: Variation of the Nusselt numbers with x-position for different nanofluid types at Re = 100, (a) Ri = 0.1, (b) Ri = 1, (c) Ri = 5 and (d) Ri = 10.

The fluid velocity plays an important role in heat transfer regarding mixed convection and this explains the emergence of the SiO_2-H_2O solution's relatively high heat transfer coefficient. It can also be seen that the Nu number increased with increasing Ri number. Since SiO_2-H_2O has the highest heat transfer rate, it will be used in all the followed result sections of this chapter.

4.3.2 The effect of nanoparticle volume fraction

The effect of nanoparticle volume fraction, in the range of 1 – 4% and using different values of Richardson number at a fixed of Re = 100 and using the opposing flow case, on the Nusselt number is shown in Figure 4-5a – c.

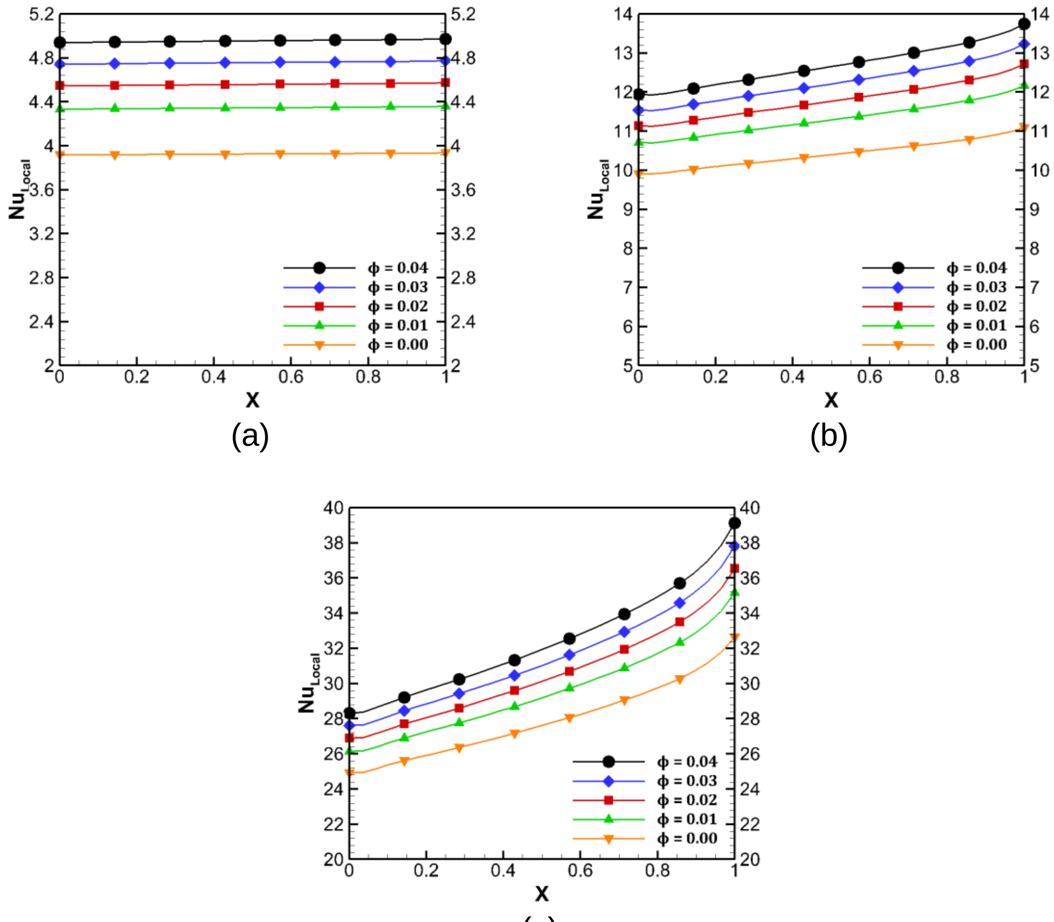

Figure 4-5: The Nusselt numbers with x-position for different volume fractions at Re = 100, (a) Ri = 0.1, (b) Ri = 3, (c) Ri = 10.

The results demonstrate that increasing nanoparticle volume fraction enhances the Nusselt number, due to the fact that as the volume fraction increases, the thermal conductivity of the working fluid increases, besides irregular and random movements of particles boost the energy exchange rates in the fluid, generating a penalty on the wall shear stress which consequently enhances the thermal dispersion of the flow. In addition, at any given volume fraction, the Nu number increases as Ri number raises.

4.3.3 The effect of nanoparticle diameter

This study used SiO_2-H_2O as a working fluid with other fixed parameters such as the inclination angle of sidewalls, 30°, a Re value of 100 and a volume fraction of 4%; the Richardson number was in the range of 0.1 – 10. The nanoparticle diameters considered were in the range of 25 – 70 nm. As illustrated in Figure 4-6a – c, the results demonstrate that the nanofluid including smaller particle diameters has a higher Nusselt number. The effects of particle size may be attributed to two causes: firstly, due to the high specific surface area of the nanoparticles, and secondly due to Brownian motion. As the particle size reduces, the surface area per unit volume increases; as the heat transfer is dependent on the surface area, the effectiveness of nanoparticles in transferring heat to the base liquid raises. However, reducing the particle size means increasing the velocity of their associated Brownian motion, which again adds up to the contribution of the nanoparticles to the total heat transfer by continuously creating additional paths to the heat flow in the fluid. As depicted in this figure, the nanofluid containing 25 nm nanoparticle diameters has the highest Nusselt number, whereas the nanofluid with a nanoparticle diameter of 70 nm has the lowest Nusselt number. In all cases, it can be observed that the Nu number increases with increasing Ri number for all nanoparticles diameters.

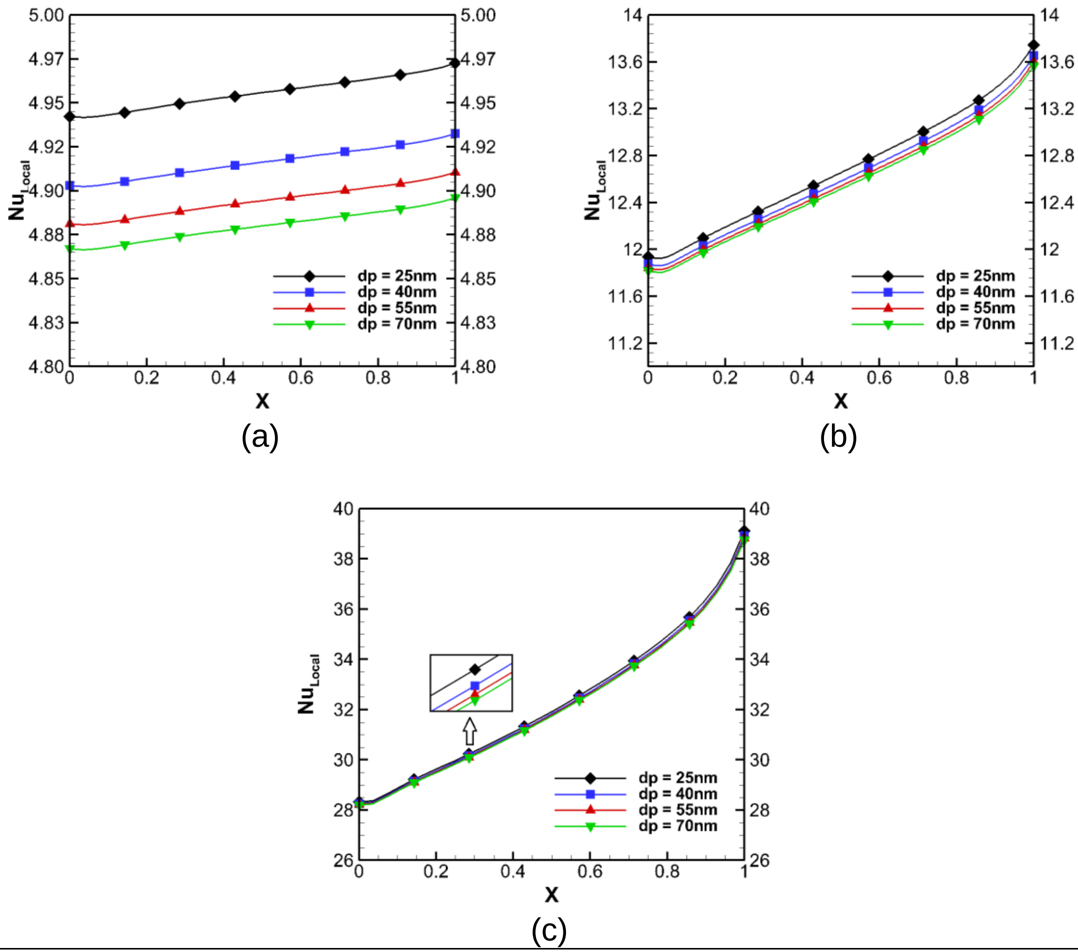

Figure 4-6: Variation of the Nusselt numbers with x-position for different nanoparticle diameters at Re = 100, (a) Ri = 0.1, (b) Ri = 3, (c) Ri = 10.

4.3.4 The effect of rotational angle

The effect of rotational angle (Φ) was studied for different Ri numbers with a fixed value of Re = 100 and an under opposing flow condition with inclination sidewalls angle of 30˚. As shown in Figure 4-7a, the results demonstrate that the Nu_{av} is responsive to rotational angle. In particular, the Nu number increases as the rotational angle (Φ) decreases from 60˚ – 30˚. This phenomenon can be ascribed to the fact that the lid-driven movement becomes prone to enhance the heat transfer, because it enhances fluid circulation within the cavity.

The effect of rotational angle on both the streamlines and the isotherms is also presented in Figure 4-7b for different Ri numbers. As these figures show, an increase of the Ri number (Ri > 1) generates natural convection which in turn induces circulation at the bottom wall of the cavity. This circulation casting

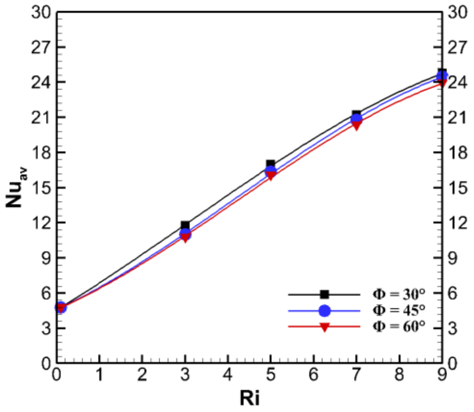

(a)

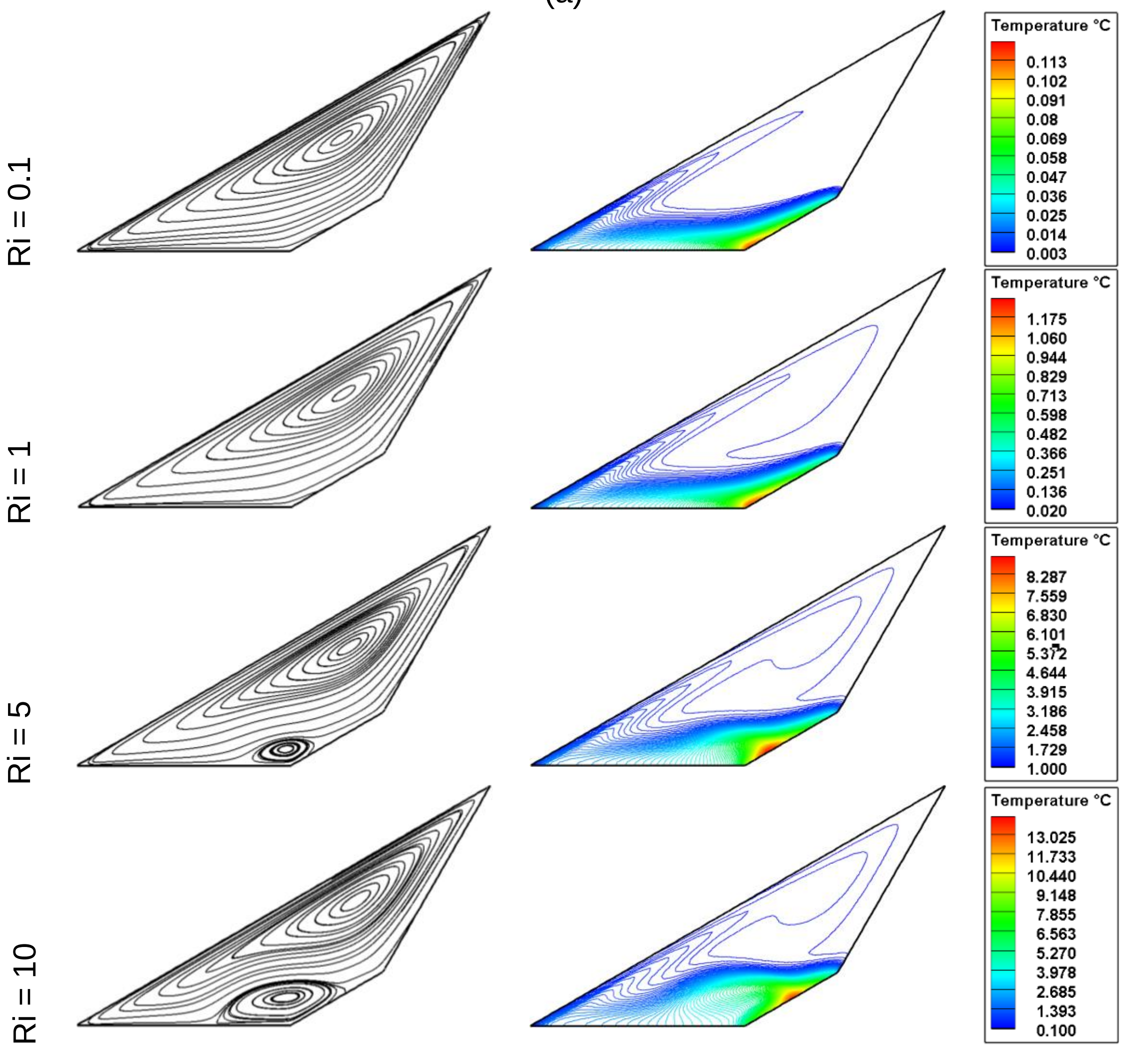

(b)

Figure 4-7: (a) The average Nusselt number with Ri numbers at different rotational angles and Re = 100, (b) streamlines (left) and isotherms (right) for different Richardson numbers and $\Phi = 30^{\circ}$.

process, encouraged by natural convection, is enhanced as the Ri number increases. The isotherm maps change accordingly with streamlines, and as the

Ri number progresses, the isotherm and streamline contours change noticeably. This indicated that natural convection is dominating the heat transfer in this particular case. By contrast, the shear-driven circulation, located at the upper right side, becomes smaller due to the increase in Ri number which dominates the natural convection.

4.3.5 The effect of sidewall inclination angle

The effect of the inclination angle of the adiabatic sidewalls on the Nusselt number was investigated, a summary of which is shown in Figure 4-8a. The inclination angle of the sidewalls was varied from 30˚ to 60˚ for several Ri numbers in the range of 0.1 – 10. The results were obtained at Re = 100 and in the opposing flow case. The results show that the Nusselt number is highest at γ = 30˚. This can be ascribed to the fact that the lid-driven movement enhances heat transfer. In other words, by decreasing the inclination angle the length of the lid-driven wall is increased and this would lead to enhancing the heat transfer.

The impact of varying the inclination angle of the sidewalls of the trapezoidal enclosure for different Ri numbers on the streamline and isotherm contours is shown in Figure 4-8b for γ = 30˚. For the small values of the Ri number, the shear effect that is influenced by the movement of the top wall is dominant. The fluid flow is characterised by a primary recirculating eddy of approximately the size of the cavity, which is generated by the movement of the top lid. The isothermal contour maps are clustered near the bottom and top walls, resulting in steep temperature gradients in these regions.

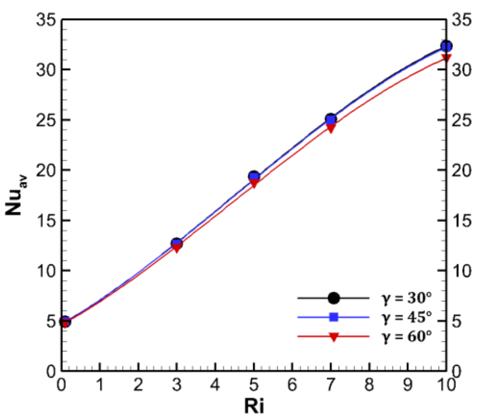

(a)

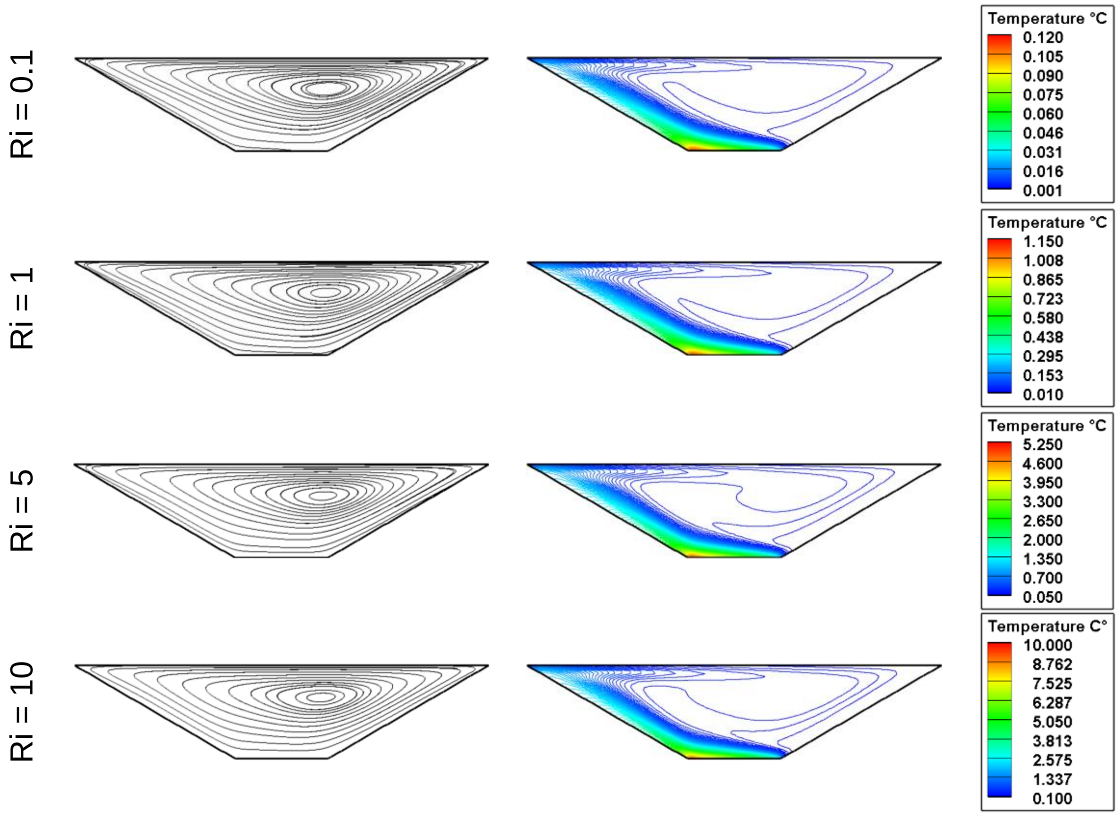

(b)

Figure 4-8: (a) The average Nusselt number with the Richardson number for different inclination angles at Re = 100, (b) streamlines (left) and isotherms (right) for different Richardson numbers at $\gamma = 30^{\circ}$.

4.3.6 The effects of aspect ratio and flow direction

The effect of different aspect ratios, A, in the range of 0.5 – 2 of the cavities on the Nusselt number for an inclination angle of sidewalls of 30˚ and for the opposing flow case is shown in Figure 4-9a. The Richardson number range was taken as between 0.1 – 10, whilst the Reynolds number was fixed at 100. The results demonstrate that the Nusselt number increases with increasing aspect ratio. This is due to the fact that the cavity volume increases in accordance with both the aspect ratio and the presence of a larger volume of cooling fluid. This process is consequently involved in moderating the heat source, leading to an increased cooling effect.

The effect of thermal boundary conditions (opposing and aiding flow), in the top moving wall at Φ = 30˚ and Re = 100, is shown in Figure 4-9b. The results show that the Nusselt number of aiding flow is higher than that of opposing flow. When aiding flow involved, the body force has the same direction as the shear driven flow direction, which accelerates the fluid and results in an increase of Nusselt number. However, for opposing flow the body force moves opposite to the shear driven flow direction, thus retarding the flow which may cause flow reversal within the upper region of the cross-section. The Nusselt number results were, therefore, lower for opposing flow than those for aiding flow. As the Ri number increases, the convection flow fields become stronger, thus resulting in better heat transfer.

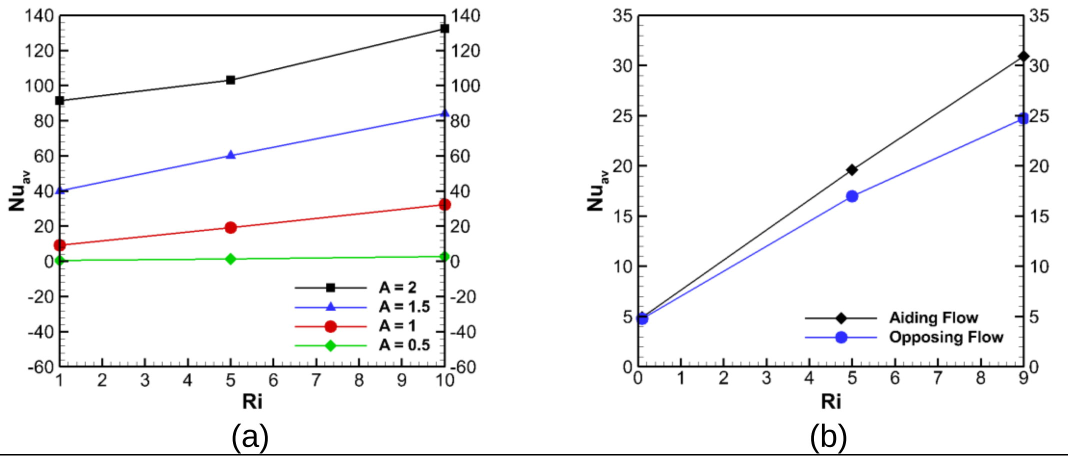

Figure 4-9: (a) The average Nusselt number with the Richardson number for different aspect ratios at Re = 100, (b) the average Nusselt number with the Richardson number for different flow directions at Re = 100 and Φ = 30°.

4.4 Conclusion

The problem of steady laminar mixed convective flow and heat transfer for different types of nanofluids composed of mixtures of water and Al_2O_3-H_2O, CuO-H_2O, SiO_2-H_2O, and TiO_2-H_2O, in a lid-driven trapezoidal enclosure, was formulated and solved numerically using a second-order finite volume solver. This solver was validated by direct comparisons with previously published research on special cases of the problem, the results of which proved to be in good concordance. Graphical results for various parametric conditions were presented and discussed. The main achievements of the numerical study were that:

- Heat transfer mechanisms and flow characteristics inside the enclosure are strongly dependent on the Richardson number.

- SiO_2-H_2O provides the highest Nusselt number, followed by Al_2O_3-H_2O, TiO_2-H_2O and CuO-H_2O, while pure water generates the lowest Nusselt number.
- The Nusselt number raises when increasing the nanoparticle volume fraction and the aspect ratio, as well as when decreasing the nanoparticle diameter.
- The Nusselt number is responsive to the rotational angle (Φ), and increases when either Φ or the inclination angle (γ) changes from 30° to 60° at all values of the Richardson number.
- The direction of the lid-driven movement affects the heat transfer phenomena.
- The aiding flow condition always induces a better heat transfer rate than the opposing flow condition.

Chapter 5 Mixed convection heat transfer of a 3D lid-driven sidewalls square enclosure

5.1 Motivation and introduction

The development in the computational power has allowed a large number of methodologies to be involved in investigations of heat convection of lid-driven enclosure that contains the turbulent fluid flow. For instance, the Unsteady Reynolds-Averaged Naiver-Stokes (URANS) with various models and Large Eddy Simulation (LES) with different subgrid-scale models. The presented literature survey discussed various aspects of heat convection in different cavities. Thus, it is not difficult to conclude that the majority of numerical investigations so far is restricted to 2D geometry and only very limited investigations have been achieved on 3D lid-driven cavity problems. Furthermore, too little attention has been paid to studying the turbulent flow by using an advanced turbulence method such as LES or URANS, and to analysing the heat convection and flow patterns in details. Two-phase model, nanofluid types, volume fraction and nanoparticles size have not been studied at turbulent flow condition by applying URANS and LES methods.

Accordingly, this chapter explores the Computational Fluid Dynamics (CFD) study of unsteady mixed convection heat transfer in a 3D closed cavity with constant heat flux located in the central part of the bottom wall. The sidewalls are isothermal and move vertically in the same direction. The other remaining walls that form the geometry are maintained stationary and adiabatic. This chapter is accomplished with various Reynolds numbers, Re = 5,000, 10,000, 15,000 and 30,000. The numerical methodology based on the finite volume method is utilised. The simulations and analysis have been carried out by evaluating the performance of two different turbulence methods, which are the URANS LES, in terms of the flow vectors, the isotherm contours, the turbulence kinetic energy distributions, and the average Nusselt number (Nu_{av}) and the local Nusselt (Nu_{Local}) number along the hot part of the bottom wall. This chapter is divided into three sections: the numerical model, the results and discussion, and the summary at the end. The numerical model section contains five subsections exploring the physical model, the boundary conditions, the numerical procedure and the grid independence test. Section two includes the results and discussion of the conventional fluid part and the two-phase mixture nanofluids part of the three different nanoparticle types, CuO, ZnO and SiO_2, which are mixed with pure water in the nanoparticle diameter range of 25 – 85 nm and the nanoparticle concentration in the range of 0.00 to 0.08. The comparison results of LES and URANS approaches are completed to further acknowledge the velocity vectors, the instantaneous temperature field and the average Nusselt number. The influence of nanofluids types, the nanoparticles diameters and the volume fractions are discussed through the local and average Nusselt numbers, the turbulence kinetic energy and the root-mean-square velocity as well as the isotherm contours and velocity vectors. Two different journal papers and one conference paper have been published from the contents of this chapter [168-170].

5.2 Numerical model

5.2.1 Physical model

The main cubic geometry parameters are sketched in Figure 5-1. The sidewalls of the enclosure are moving vertically downward with a uniform velocity and are fixed at the cold temperature. While the central part of the bottom wall (l) is heated at a constant heat flux, whereas the side parts of the bottom wall and the remaining walls of the cavity are kept adiabatic and motionless. This kind of study can represent the practical applications, such as air cooling of the electronic devices. In this case, the moving sidewalls refer to the cold airflow along the cavity sides that are blown downwards by the effects of the fan or the jet from the cavity top. The flow in the enclosure is a result of the movement of the sidewalls and the heat source at the bottom wall.

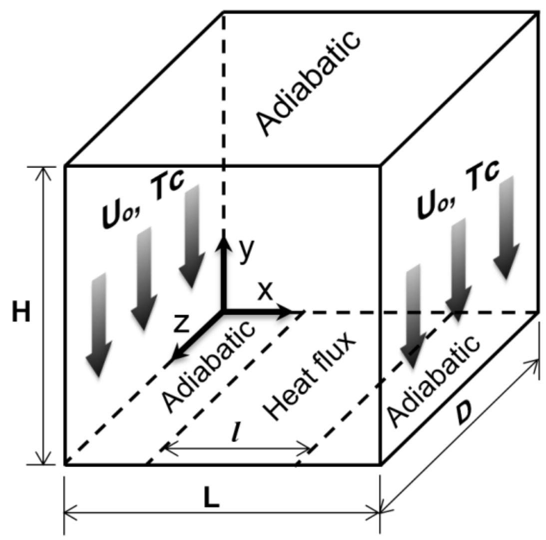

Figure 5-1: Schematic diagram of the cubic lid-driven cavity.

5.2.2 Boundary conditions

The boundary conditions for the present problem are specified as follows; the top wall, back and front walls of the domain are kept adiabatic and stationary (U = V = W = 0). The bottom wall is divided into three parts, first part ($0 < X < (1-E)/2$) and second part ($(1+E)/2 < X < 1$) are fixed adiabatic and motionless ($U = 0$, $V = 0$, $W = 0$), while the middle part ($(1 - E)/2 \leq X \leq (1 + E)/2$) is kept isothermal and stationary ($U = 0$, $V = 0$, $W = 0$). The condition for $(1 - E)/2 \leq X \leq (1 + E)/2$ at the bottom wall arises as a consequence of constant heat flux, q''. The sidewalls of the enclosure are moving vertically downward with a uniform velocity and are cooled at low temperature ($T = T_C$, $U = 0$, $V = U_0$, $W = 0$).

5.2.3 Numerical procedure

The current investigations employ the commercial CFD code ANSYS©FLUENT (version R15.0) [139] to solve the governing equations of heat and fluid flow, based on the finite volume method (FVM). Both the URANS and the LES methods are applied to the two-phase mixture nanofluids inside the cavity. The thermo-physical properties formula for the nanofluids mixture are introduced into the software via User Defined Functions (UDFs) as shown in the Appendix A of this thesis. The popular SIMPLE procedure is utilised for dealing with the pressure-velocity coupling equations, and the QUICK scheme is applied to the convection terms of the momentum and energy equations, whilst the implicit second order scheme is used for the time evaluation terms. The simulation results are concluded once the iteration residuals for all the required parameters are below 10^{-6}.

5.2.4 Grid independence test

One of the main matters in CFD studies is grid independence test, which is necessary in order to obtain the most suitable mesh number and quality for the cubic lid-driven enclosure. Discretising the domain is realised by hexahedral, mesh and the mesh close to the cubic walls are refined as displayed in Figure 5-2. The grid independence test is carried out by using the URANS approach with the standard *k-ε* model at constant values of Re = 5,000, and Ri = 1. The convergence criteria were set as 10^{-6} for the discretised continuity, momentum and energy equations. Five different node numbers are tested in this model, including 120,000, 410,625, 980,000, 1,699,200 and 1,921,875, with the non-dimensional time step being 0.0001, the dimensionless wall distance, $y^+ \approx 1$ and the Courant-Friedrichs-Lewy number, CFL = 0.3. As illustrated in Figure 5-3, there is a little difference between the results as by employing the node number either equal to or higher than 980000. Therefore, the number of grid points used in this chapter is chosen (which corresponds to1,699,200) with the aim to obtain accurate results and to reach a grid independence.

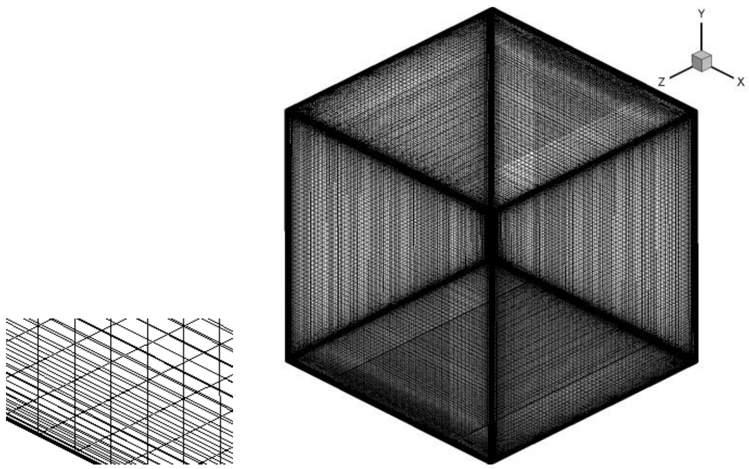

Figure 5-2: Computational mesh of the cubic lid-driven cavity.

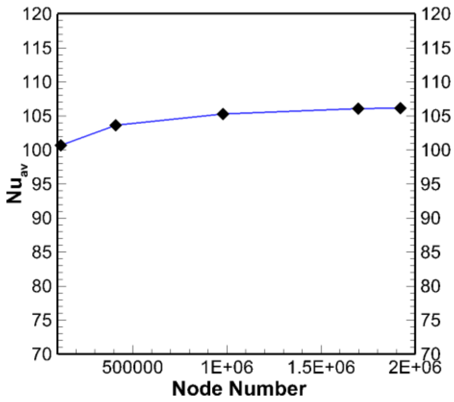

Figure 5-3: Convergence of the average Nusselt number with grid refinement.

5.3 Results and discussion

Since this chapter has numerous attainments, the data of this chapter has been divided into two sections, which are conventional fluid and nanofluid section, with a view to have clear vision. Several similar works of different studies of Sharif [161], Chen and Cheng [162], Alinia*, et al.* [91], Prasad and Koseff [163], Padilla*, et al.* [165], and Peng*, et al.* [164] have been compered against the current simulation code in terms of code validation to ensure that the new modelling has been building correctly. More details have been revealed about the validation part in section 3.8.

5.3.1 Conventional fluid

The computed mixed convection flow and heat transfer of pure water in the three-dimensional CFD cases are examined in this section. Two different turbulent methods are utilized, which are the unsteady RANS and the LES methods. The outcomes are presented in terms of the Nusselt number, the isotherms contours, the turbulence kinetic energy distributions and the velocity vectors.

5.3.1.1 URANS method

Figure 5-4 outlines the local Nusselt number curves regarding the given four values of the Reynolds number (Re = 5,000, 10,000, 15,000 and 30,000) along the midline of the heated part of the bottom wall to investigate the influences of the Reynolds numbers. The standard *k-ε* turbulence model with time dependence is used. In particular, the curves illustrate that increasing the Re values leads to a significant enhancement in the local Nusselt number, which is the consequences of increment in the velocity with the higher Re number. Since the higher movement of the fluid near the sidewalls is caused by the moving walls besides the temperature differences, it can be seen that the local Nusselt number near the sides of the geometry is higher than that in the middle. The distributions of the local Nusselt number are symmetric about the midline because of the symmetric boundaries of the current test case.

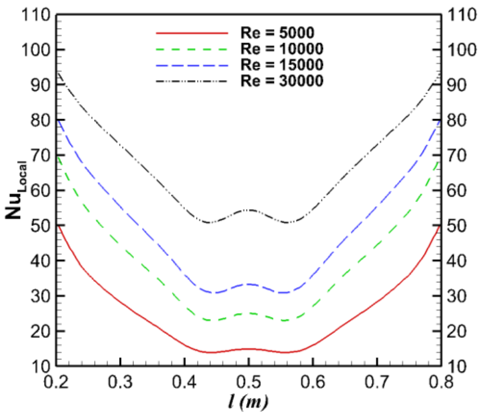

Figure 5-4: Local Nusselt number along the midline of the bottom wall for different Reynolds numbers.

The turbulence kinetic energy is plotted in Figure 5-5 for different Reynolds numbers at the horizontal midline of the bottom wall, z = 0.5. The calculated values indicate that the augmented Re value leads to the enhancement of the fluctuation kinetic energy, which is the reason of increasing the value of fluid velocity within the enclosure. In addition, the turbulence kinetic energy raises gradually by increasing the Re, especially in the lid-driven areas. This phenomenon is due to the presence of a higher turbulence velocity in these regions.

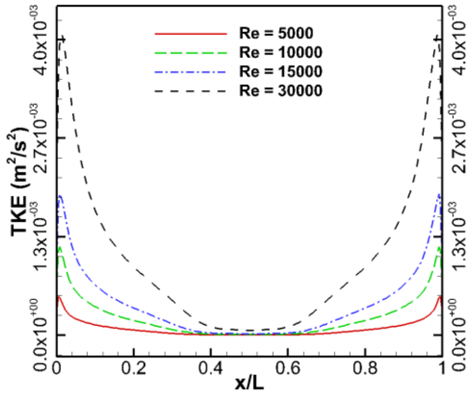

Figure 5-5: Turbulence kinetic energy along the midline of the bottom wall for different Reynolds numbers.

5.3.1.2 Comparison between URANS and LES methods

In this section, a comprehensive comparison and an explanation of the results involving both the Smagorinsky LES model and the standard *k-ε* URANS model are presented for two Reynolds numbers, Re = 5,000 and 10,000. Two different plane locations have been selected to get better vision and understanding about the velocity and temperature field distributions. The power spectral density of the turbulence kinetic energy, which is shown in Figure 5-6, demonstrates that the LES simulations are well resolved. The slope of -5/3 is observed visibly in the inertial subrange which is known to represent the generic feature of turbulent flows. The current simulation can therefore be regarded as possessing the characteristics of a fully turbulent flow.

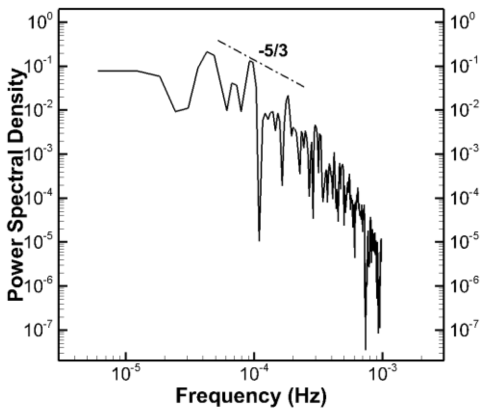

Figure 5-6: Power spectral density of the turbulence kinetic energy.

The numerical results between the URANS and LES in terms of flow vectors have been compared in details. Figure 5-7a illustrates the flow behaviour for the x-y plane located at the middle of the z-axis, while Figure 5-7b deals with the y-z plane located at the midway of the x-axis. Since the current case represents a symmetric domain, it can be noticed clearly that the flow structure is divided into two symmetric flow parts. Notably, the effects of forced convection, which is caused by the moving sidewalls, are dominating, especially in the layers close to the moving walls. The flow thereabout the moving-walls is dragged due to shear and impinges onto the stationary-walls. With more details, the flow deflects in the horizontal direction at the corners of the domain. The two primary vortices (rotating clockwise and anticlockwise) nearby the domain centre are distinctly seen in Figure 5-7a, and these vortices are controlling the flow patterns by using either the URANS or the LES method. Furthermore, the shown vectors in Figure 5-7 plainly detect the existence of secondary eddies nearby the top corners and bottom centre, which are known as downstream and upstream secondary eddies, especially from the LES results. Lower secondary eddies are also revealed on the sides of the bottom wall. However, it can be seen obviously that the secondary eddies are shown more clearly by using the LES approach for both selected planes and Reynolds numbers. Furthermore, increasing the Reynolds number to 10,000 it shows the ability differences between the two methods in dealing with turbulent flow. The effect of changing the Reynolds number on the flow pattern is rather limited by using the URANS, unlike the LES approach, which is able to show clearly the secondary eddies.

The URANS and LES predictions are compared now according to the instantaneous temperature distributions at the selected Reynolds number, Re = 5,000, for two different plane locations. Figure 5-8 demonstrates the snapshots of instantaneous temperature patterns of the x-y plane located at the midway of the z-axis. Figure 5-8a presents the temperature contours at t = 10 sec. Hither, it can be recognized that the URANS method predicted a semi-laminar plume rising from the heat source.

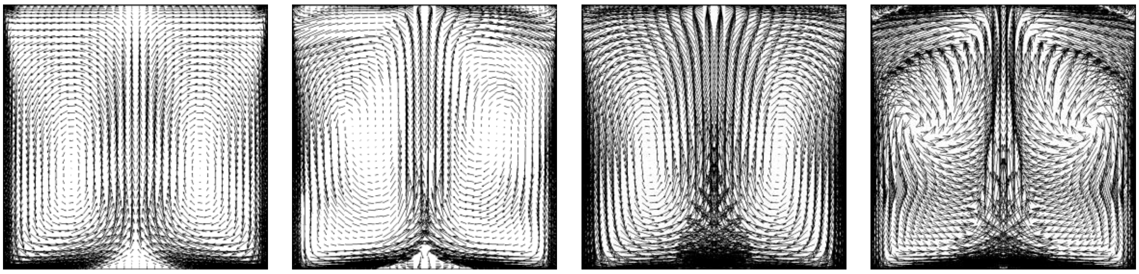

Re=5,000 Re=10,000

(a)The x-y plane located at the middle of the z-axis

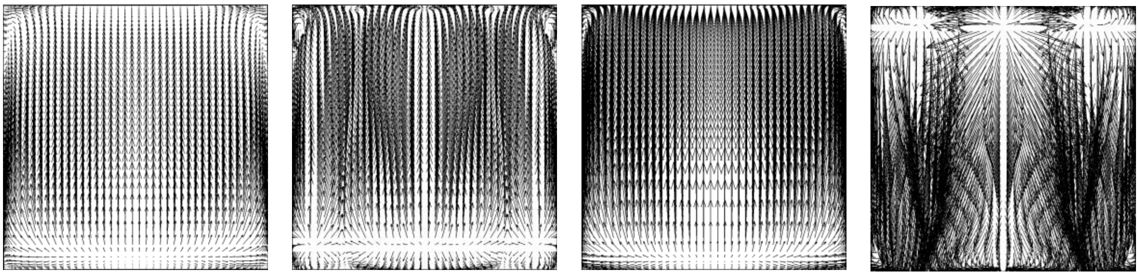

Re=5,000 Re=10,000

URANS LES URANS LES

(b)The y-z plane located at the middle of the x-axis

Figure 5-7: Flow vectors comparison between the URANS and LES method.

By contrast, the LES method predicted the two primary vortices (clockwise and anticlockwise) rising from the heat source area. At t = 16 sec, it can be observed that the URANS approach started showing the vortex in the middle of the cavity and the upper part of the domain in a thermally stratified state, whereas the two primary vortices predicted by the LES method keep expanding. At t = 28 sec, the first two symmetric vortices (clockwise and anticlockwise) appear by harnessing the URANS thereabout the sides of the bottom wall; however, by using the LES approach, apart from the two primary vortexes, two secondary eddies are shown nearby the sides of the bottom wall, where two small secondary eddies appear on the heated part of the bottom wall and at the corners of the top wall.

Moreover, Figure 5-9 exhibits the snapshots of instantaneous temperature distributions of the y-z plane which is located at the centre line of the x-axis. This analysis demonstrates that from the beginning the URANS method provides thermally stratified isotherms that are almost parallel in the horizontal direction, except for the areas close to the moving walls. These parallel lines maintain their shapes until they cover the entire cavity. Whilst, the LES predictions indicate clear differences in comparison to the URANS method. This aspect explains that, at t

= 28 sec, multi-vortices have formed and keep flourishing until they cover the whole domain.

Furthermore, it can be observed from the temperature snapshots that the heat transfer thereabout the heat source is dominated by the natural convection. However, this domination is dwindling gradually by moving forward towards the centre and the sides of the domain as the forced convection is controlling the mechanism of heat transfer in the cavity due to the moving sidewalls.

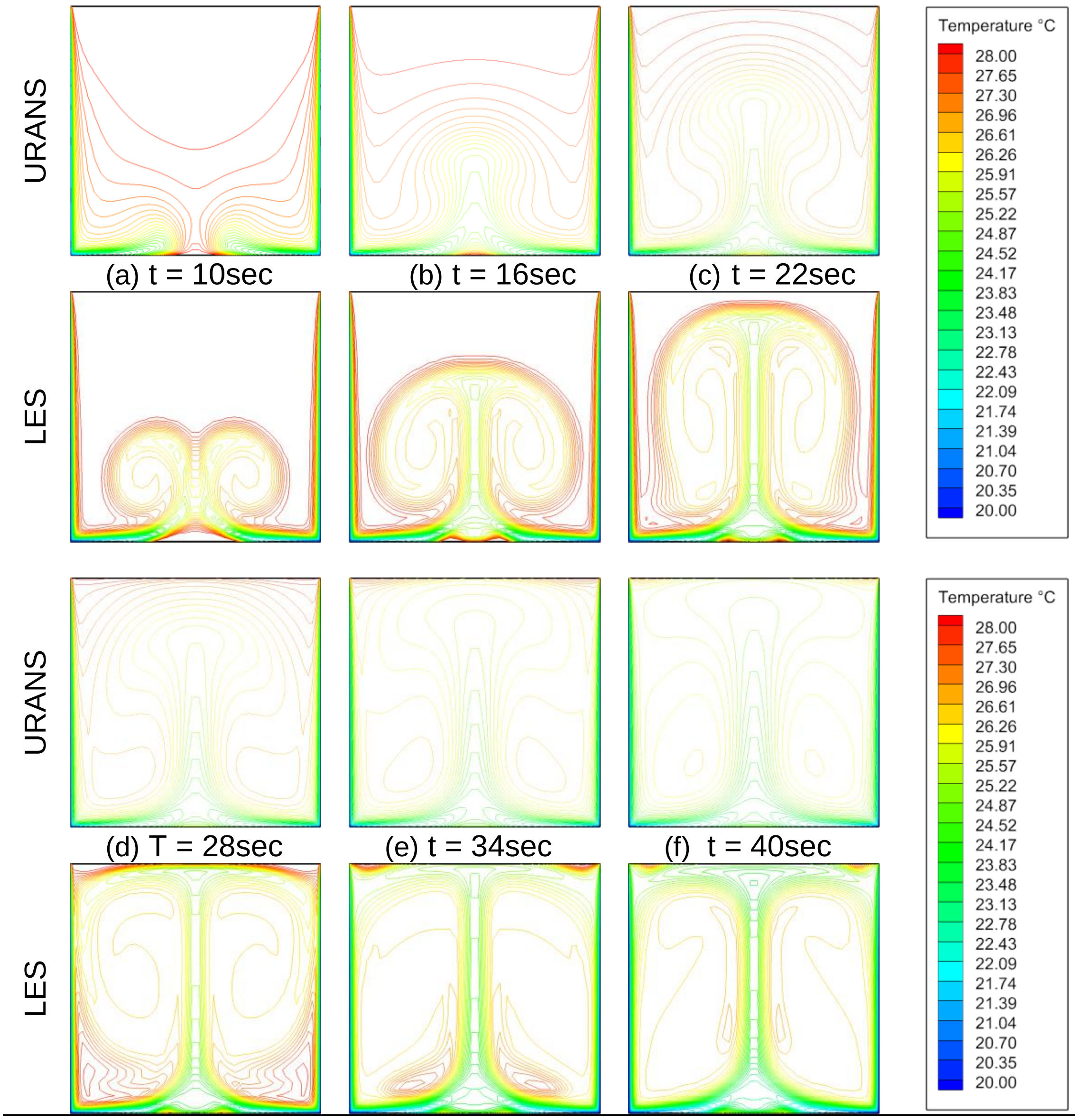

Figure 5-8: Instantaneous isotherm comparison between URANS and LES for the x-y plane located at the middle of the z-axis, at Re = 5,000.

By taking other factors into account, the URANS simulation needed less computation time (22 sec) to reach the fully developed state, whereas, the LES run needed 28 sec. In comparison, it can be seen obviously from the temperature snapshots that the LES results can predict more flow details within the cavity and both the temperature and the velocity vector distributions are more realistic. Figure 5-10 indicates comparative results of the two turbulent methods in terms of the average Nusselt number in relation to three high values of the Reynolds number.

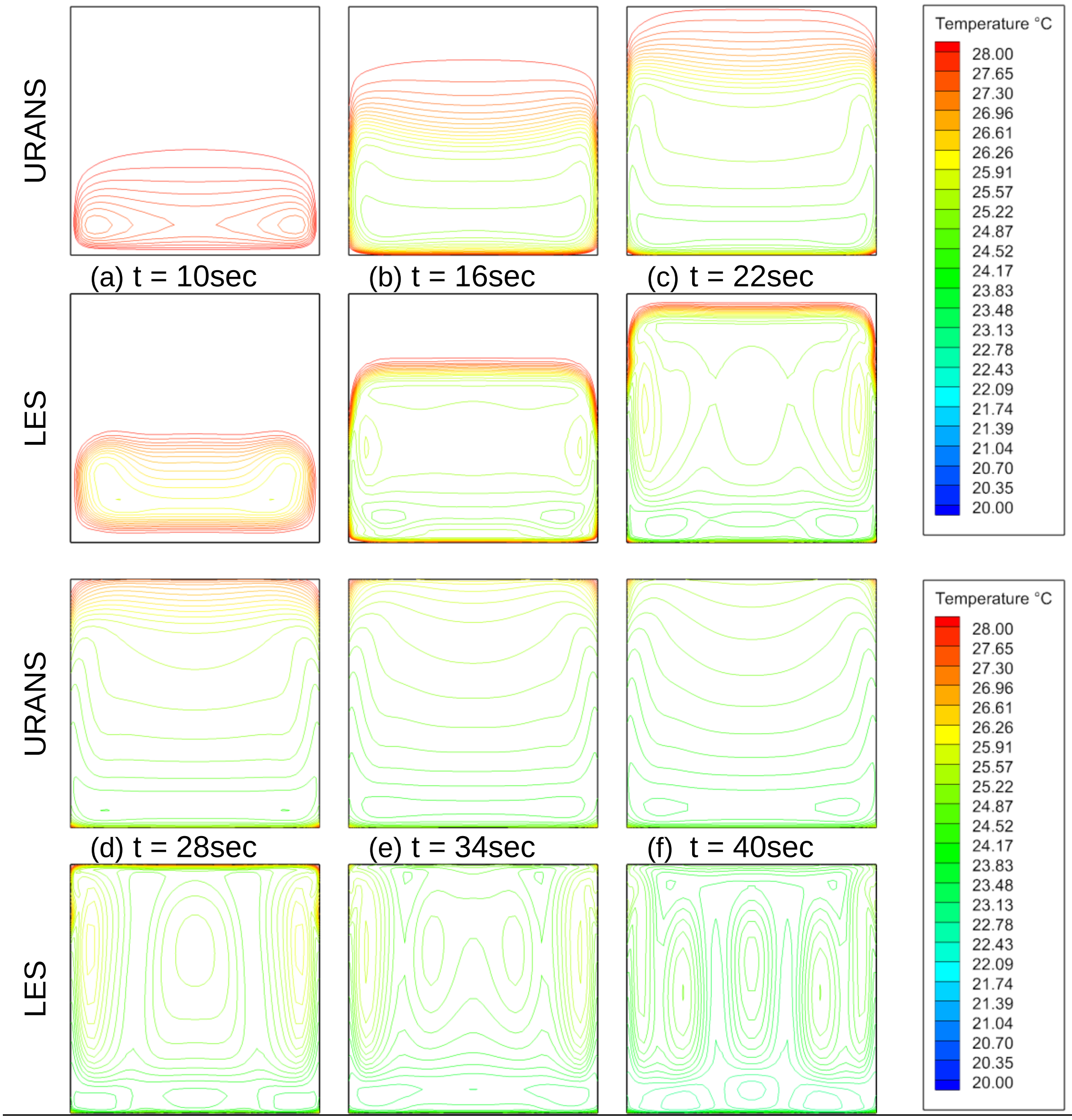

Figure 5-9: Instantaneous isotherm comparison between URANS and LES for the y-z plane located at the middle of the x-axis, at Re = 5,000.

In general, it indicated that enhancement in the average Nusselt number can be achieved by increasing the Reynolds number with constant Grashof number. Furthermore, it can be observed that the LES method predicts slightly higher average Nusselt numbers, compared to those calculated by utilizing the URANS method, because of their different ways of dealing with turbulence.

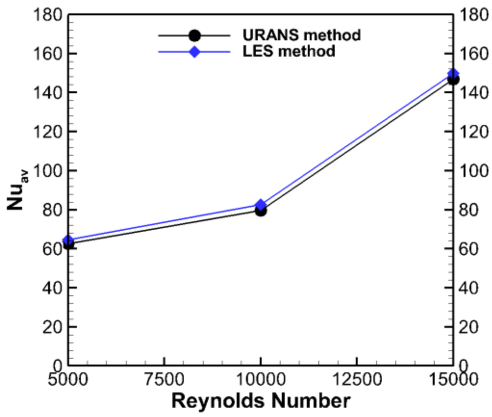

Figure 5-10: Comparison of the average Nusselt numbers for different Reynolds numbers.

5.3.2 Nanofluids

The computational results obtained for mixed convection heat transfer of several types of nanofluids, inside the cubic enclosure with moving sidewalls, are explored in this section. The outcomes are presented in terms of the Nusselt number, the isotherm contour, the turbulence kinetic energy, the root-mean-square velocity and the flow vector by using both URANS and LES methods.

5.3.2.1 The influence of nanofluid type

Herein are three different types of nanofluids, SiO_2-H_2O, ZnO-H_2O and CuO-H_2O, in comparison to just pure water, H_2O, have been investigated in this section at volume fraction in the range between 0.00 – 0.06, Re = 15,000 and nanoparticles size, dp = 25nm. This study aims to reveal their performance differences in terms of the Nusselt number and turbulence kinetic energy. The local Nusselt numbers, positioned on the midline of the x-y plane for different nanofluids and various volume fraction of nanoparticles, are displayed in Figure 5-11. The local Nusselt number distributions are symmetric due to the symmetrical boundary conditions. In addition, it is obvious that the Nusselt numbers at the edges of the curves are higher than those in the middle, where the maximum temperature and minimum heat transfer rate yield the lowest local Nusselt number. This process from the presence of a higher velocity at the moving walls than at the centre of the enclosure. For considering all values of nanoparticles concentrations, SiO_2-H_2O has produced the highest Nusselt number and is followed by ZnO-H_2O, CuO-H_2O and pure water due to the effects of different thermo-physical properties contained in those fluids. In other words, the velocity of the fluid plays a significant role in the heat transfer coefficient, especially in the case of forced or mixed convection which is followed by the conductivity of the fluid and other properties. Since SiO_2 has the lowest density compared to other nanoparticles and possesses a higher conductivity than pure water, SiO_2-H_2O can produce the highest Nusselt number.

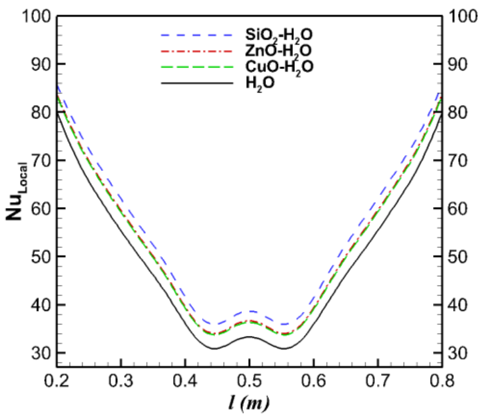

(a) ϕ = 0.02

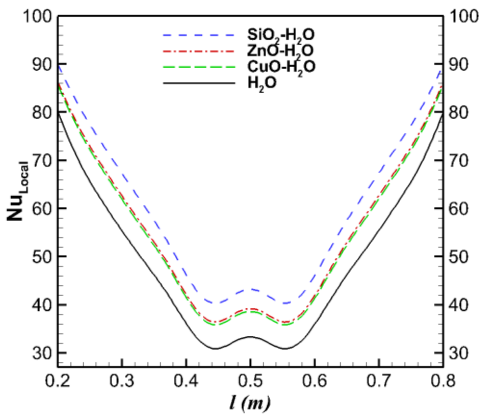

(b) ϕ = 0.04

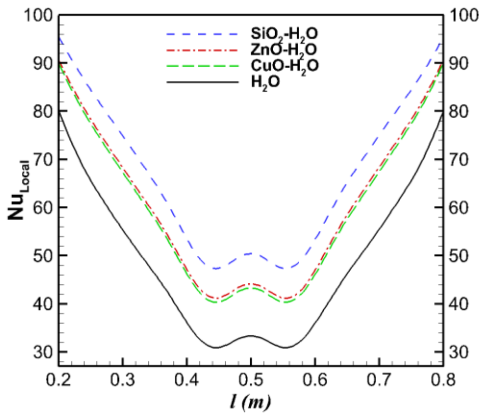

(c) ϕ = 0.06

Figure 5-11: Local Nusselt number for different nanofluids and volume fractions.

In order to provide a better understanding of the Nusselt number's effects, Table 5-1 presents the average Nusselt numbers according to four different working fluids. Generally, it can be seen that the Nu_{av} increases gradually by increasing the volume fraction of nanoparticles for all types of fluids, and the influence of SiO_2-H_2O on the Nu_{av} is more defined according to all four values of volume fraction.

Table 5-1: The effects of nanofluid types on the Nusselt number at different values of volume fraction.

	H_2O	CuO-H_2O	ZnO-H_2O	SiO_2-H_2O
$\phi = 0.00$	49.6786	49.6786	49.6786	49.6786
Nu_{av} Increase %	-	*% 0.00*	*% 0.00*	*% 0.00*
$\phi = 0.02$	49.6786	53.11935	53.46512	55.62882
Nu_{av} Increase %	-	*% 3.44*	*% 3.78*	*% 5.95*
$\phi = 0.04$	49.6786	55.52771	56.16312	60.39918
Nu_{av} Increase %	-	*% 5.84*	*% 6.48*	*% 10.72*
$\phi = 0.06$	49.6786	60.42795	61.3118	67.49895
Nu_{av} Increase %	-	*% 10.74*	*% 11.63*	*% 17.82*

The fluctuating kinetic energy profiles on the midline of the x-y plane are exhibited in Figure 5-12 at constant Reynolds and Grashof numbers for different nanofluids with three concentration values of nanoparticles mixing with the base fluid. Mostly, the turbulence kinetic energies at the centre of the midline roughly have the same values for all different fluids. In contrast, at the sides of the midline, all fluids show discernible nonlinear increases of the turbulence kinetic energy whether with changing the types of fluids or changing the volume fraction. All these functions are due to the nature of the thermo-physical properties of the fluids and their effects on the fluid velocities. As a result, SiO_2-H_2O displays the highest turbulence kinetic energy, as explained in the Nusselt number distributions.

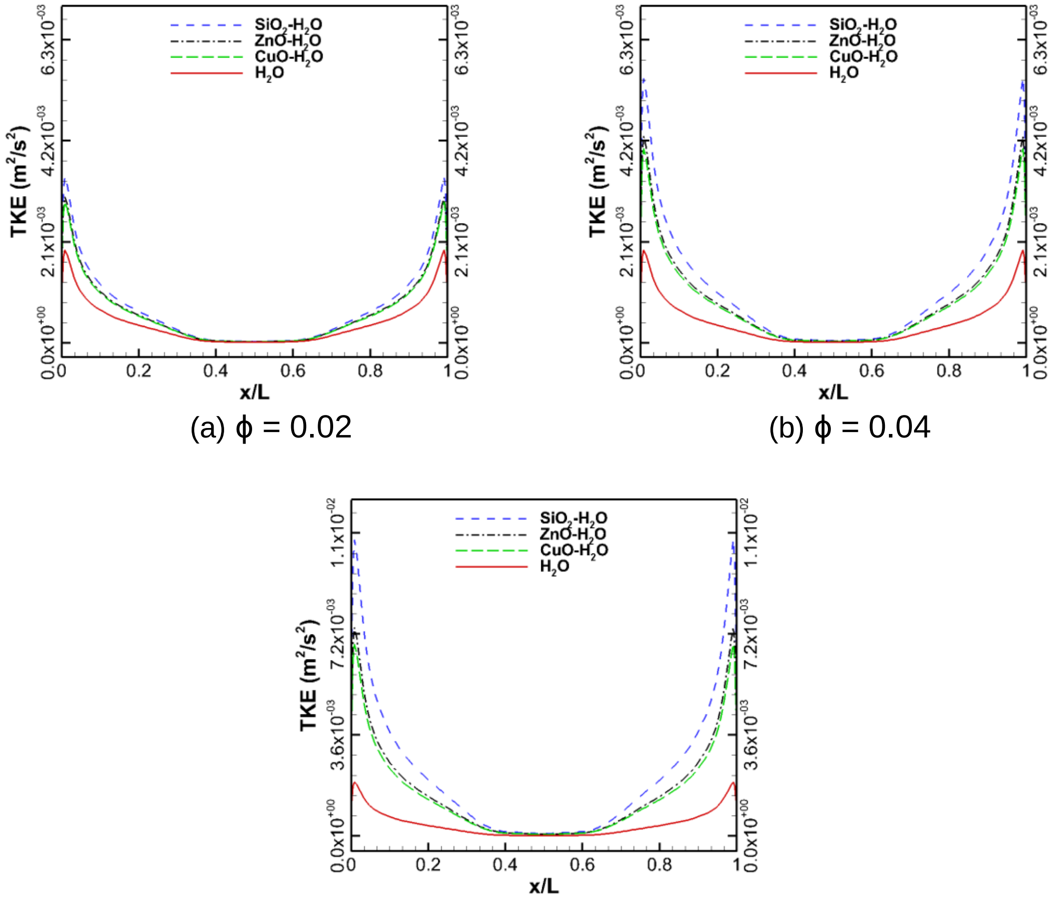

Figure 5-12: Turbulence kinetic energy for different nanofluids and volume fractions.

5.3.2.2 The influence of nanoparticle diameter

The working fluid SiO_2-H_2O with nanoparticles volume fraction 8% is selected to determine the effects of the nanoparticles size on the heat transfer in terms of Nusselt number. Figure 5-13 proves that a reduction in the nanoparticles diameter from 85 nm to 25 nm has a noticeable influence on the local Nusselt number, because decrementing in nanoparticles size at the same concentration leads to increasing both the surface area of nanoparticles and the Brownian motion velocity of the nanoparticles, which will increase the heat transfer in return. Moreover, it can be seen that a nonlinear relation between the diameter of the nanoparticles and the Nusselt number is predicted.

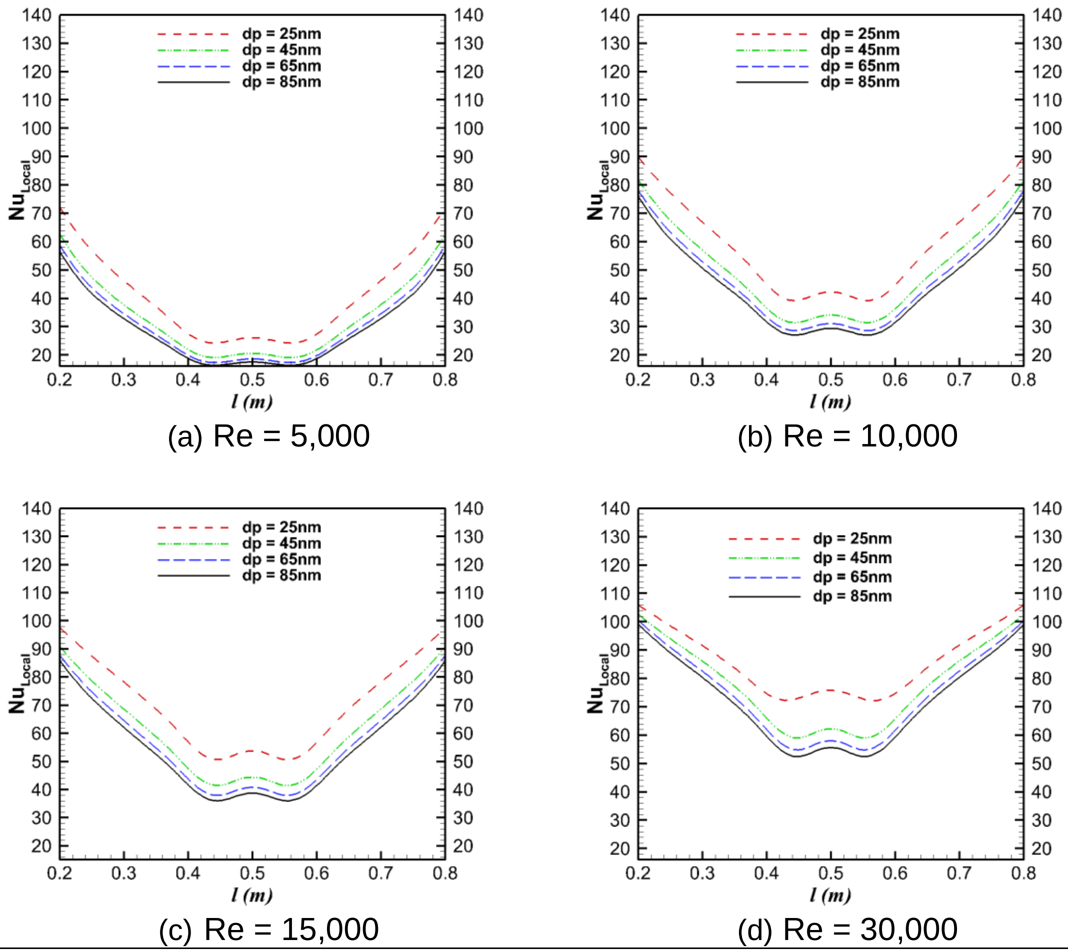

Figure 5-13: Local Nusselt number distributions for different nanoparticles diameters.

Table 5-2 displays the effects on the average Nusselt number due to the change in the size of nanoparticles for four Reynolds numbers. It is evident that increasing diameter size leads to the decrease in the Nu_{av} numbers, because of the reduction both in the surface area of the nanoparticles and in the fluid velocity.

Table 5-2: The effects of nanoparticles diameter on the Nusselt number at various values of Reynolds number.

	dp = 85nm	dp = 65nm	dp = 45nm	dp = 25nm
Re = 5,000	29.80632	31.32692	34.07325	41.40925
Nu_{av} Increase %	-	*% 1.52*	*% 4.27*	*% 11.60*
Re = 10,000	45.34784	47.36077	50.89725	59.77192
Nu_{av} Increase %	-	*% 2.01*	*% 5.54*	*% 14.42*
Re = 15,000	55.70584	57.88258	61.64008	70.70755
Nu_{av} Increase %	-	*% 2.17*	*% 5.93*	*% 15.00*
Re = 30,000	72.70905	74.85098	78.45065	86.21242
Nu_{av} Increase %	-	*% 2.14*	*% 5.74*	*% 13.50*

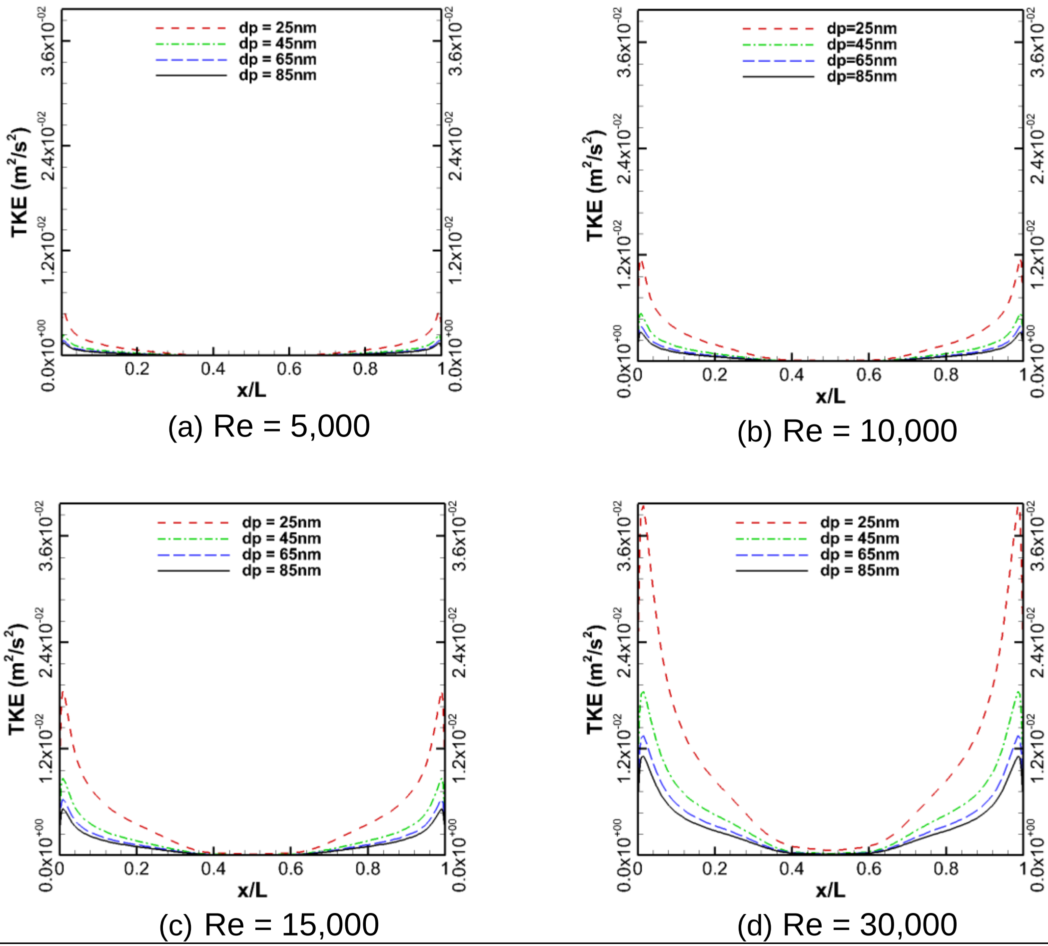

Figure 5-14: Turbulence kinetic energy distributions for different nanoparticles size.

Decreases the nanoparticles diameter increasing the turbulence kinetic energy, as observed from Figure 5-14, as well as, at all values of the Reynolds number the diameter of 25nm shows the highest fluctuation turbulent energy. This is due to the increment in both the velocity and the conductivity of the working fluid caused by the diameter reduction.

5.3.2.3 The influence of volume fraction

As shown earlier in this study the nanofluid SiO_2-H_2O provides the best heat transfer coefficient among the selected fluids, so investigations of various solid volume fractions, ϕ = 0.00, 0.02, 0.04, 0.06 and 0.08, of SiO_2-H_2O for different high values of Reynolds number, Re = 5,000, 10,000, 15,000 and 30,000, have been conducted. The distribution of the local Nusselt number on the midline of the bottom wall at z = 0.5 is plotted in Figure 5-15. The curves show that growing in volume fraction with the same Reynolds number enhances the Nusselt number due to the higher thermal conductivity of the nanofluids than that of the pure water. The sensitivity of the Nusselt number to the volume fraction increases with increasing the Reynolds number. Moreover, at constant value of volume fraction of SiO_2, the increment in the Reynolds number leads to a discernible enhancement in the Nusselt number, which comes from the increase in the fluid velocity.

Table 5-3 shows the average Nusselt number comparison among five different values of volume fraction in the range of 0 – 0.08 and for four different values of Reynolds number. Generally, the Nu_{av} increases gradually with increasing volume fraction for all Reynolds number values, and obviously the influences of the highest volume fraction and Reynolds number on the Nu_{av} are more discernible.

The turbulence kinetic energy distributions for various volume fractions and different values of Reynolds number have been studied here. Figure 5-16 displays the turbulence kinetic energy curves on the midline of the bottom wall of the cavity at several Reynolds numbers and nanoparticles concentrations, respectively. It can be seen clearly that the responses of the turbulence kinetic energy to the changes of volume fraction are much less than to the changes of the Reynolds number, because of the significant increase in the flow velocity through increasing the Reynolds number.

Table 5-3: The effects of volume fraction on the Nusselt number at various values of Reynolds number.

	ϕ = 0.00	ϕ = 0.02	ϕ = 0.04	ϕ = 0.06	ϕ = 0.08
Re = 5,000	25.80345	26.8966	29.02242	32.98182	41.40925
Nu_{av} Increase %	-	*% 1.09*	*% 3.21*	*% 7.17*	*% 15.60*
Re = 10,000	39.9006	41.42454	44.32331	49.52177	59.77192
Nu_{av} Increase %	-	*% 1.52*	*% 4.42*	*% 9.62*	*% 19.87*
Re = 15,000	49.6786	51.38977	54.5933	60.19113	70.70755
Nu_{av} Increase %	-	*% 1.71*	*% 4.91*	*% 10.51*	*% 21.02*
Re = 30,000	67.46731	68.89562	72.63527	77.91314	86.21242
Nu_{av} Increase %	-	*% 1.42*	*% 5.16*	*% 10.44*	*% 18.74*

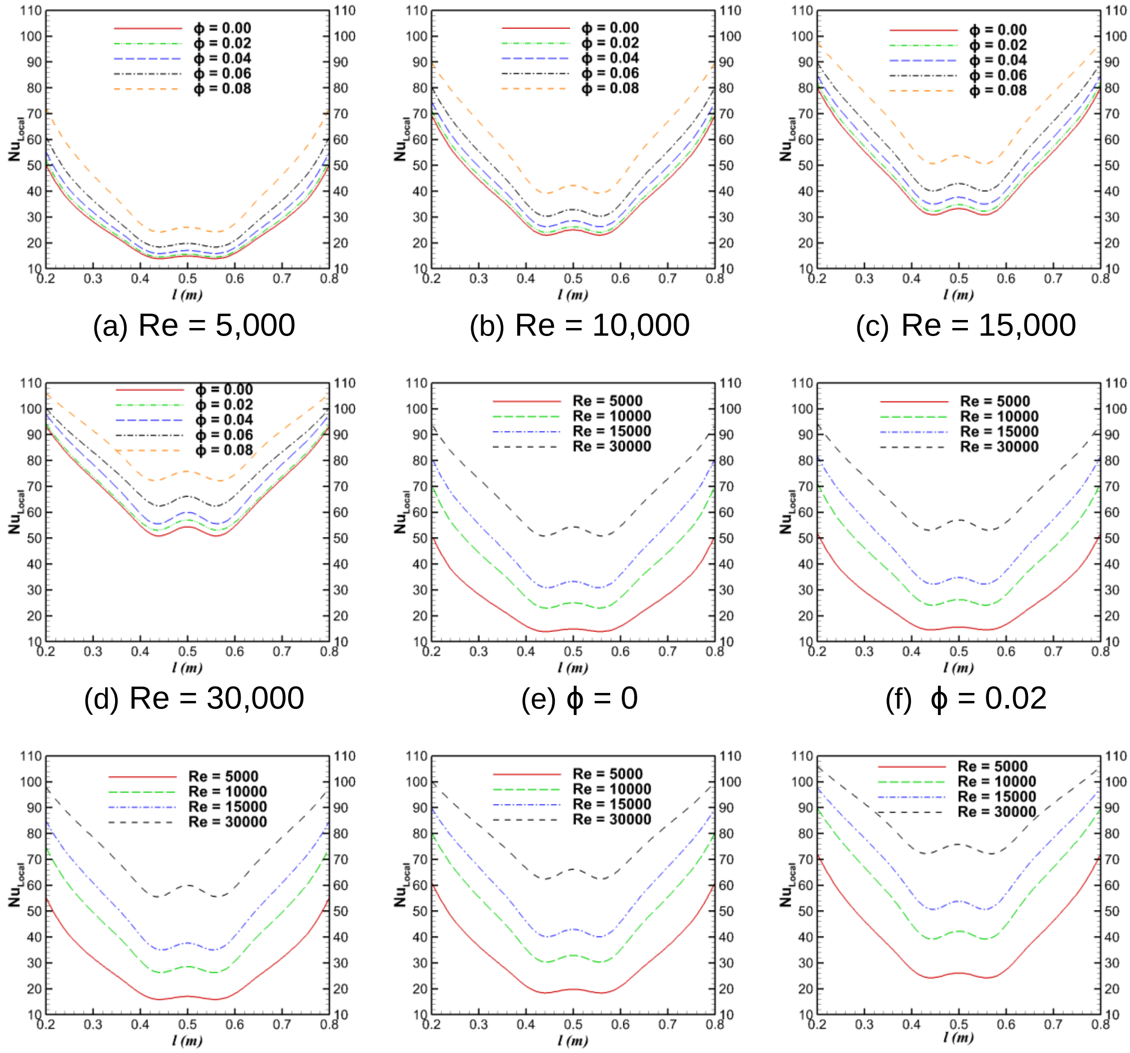

(a) Re = 5,000 (b) Re = 10,000 (c) Re = 15,000

(d) Re = 30,000 (e) ϕ = 0 (f) ϕ = 0.02

(g) ϕ = 0.04 (h) ϕ = 0.06 (i) ϕ = 0.08

Figure 5-15: Local Nusselt number distributions for different volume fractions.

Figure 5-17a – c presents the dimensionless root-mean-square velocity U_{rms} on the x-axis of the centrelines of the symmetric plane. As it can be seen, for any Reynolds number, U_{rms} in all different values of volume fraction is higher at the moving walls than that at the centre of the enclosure and much closer to the pure water.

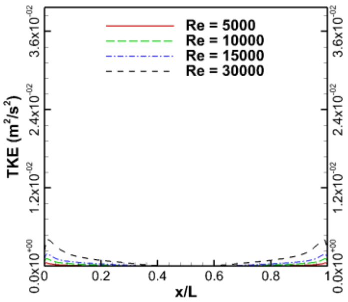

(a) $\phi = 0.00$

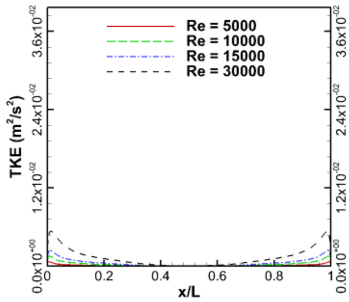

(b) $\phi = 0.02$

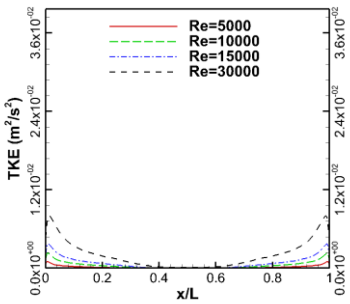

(c) $\phi = 0.04$

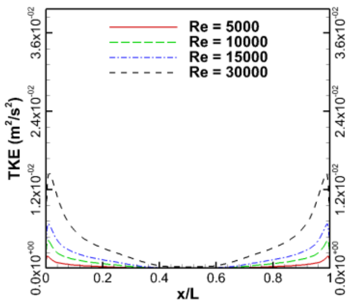

(d) $\phi = 0.06$

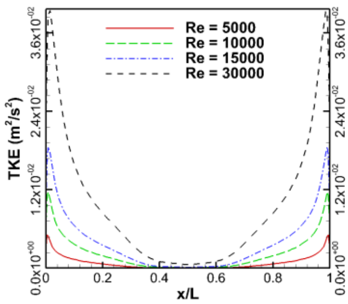

(e) $\phi = 0.08$

Figure 5-16: Turbulence kinetic energy distributions for different Reynolds numbers.

U_{rms} increases slightly by adding more nanoparticles and the increment ratio increases gradually by increasing the nanoparticles volume fraction. By looking from another angle of the effects of nanofluids on the fluctuation velocity (Figure 5-17d – h), it can be observed that the differences in U_{rms} values of using three different Reynolds numbers are roughly the same. As well as, the increase ratio of different concentrations of nanoparticles is roughly constant. The main reason for this increase in fluctuation velocity comes from the reduction of the dynamic viscosity of the working fluid by adding more nanoparticles, which causes the increase in the velocity accordingly.

The isotherm contours comparisons between the pure water and the nanofluid of SiO_2 with various volume fractions, $\phi = 0.00 – 0.08$, and at constant Grashof number and three values of Reynolds number, Re = 5,000, 10,000 and 15,000, have been made as shown in Figure 5-18.

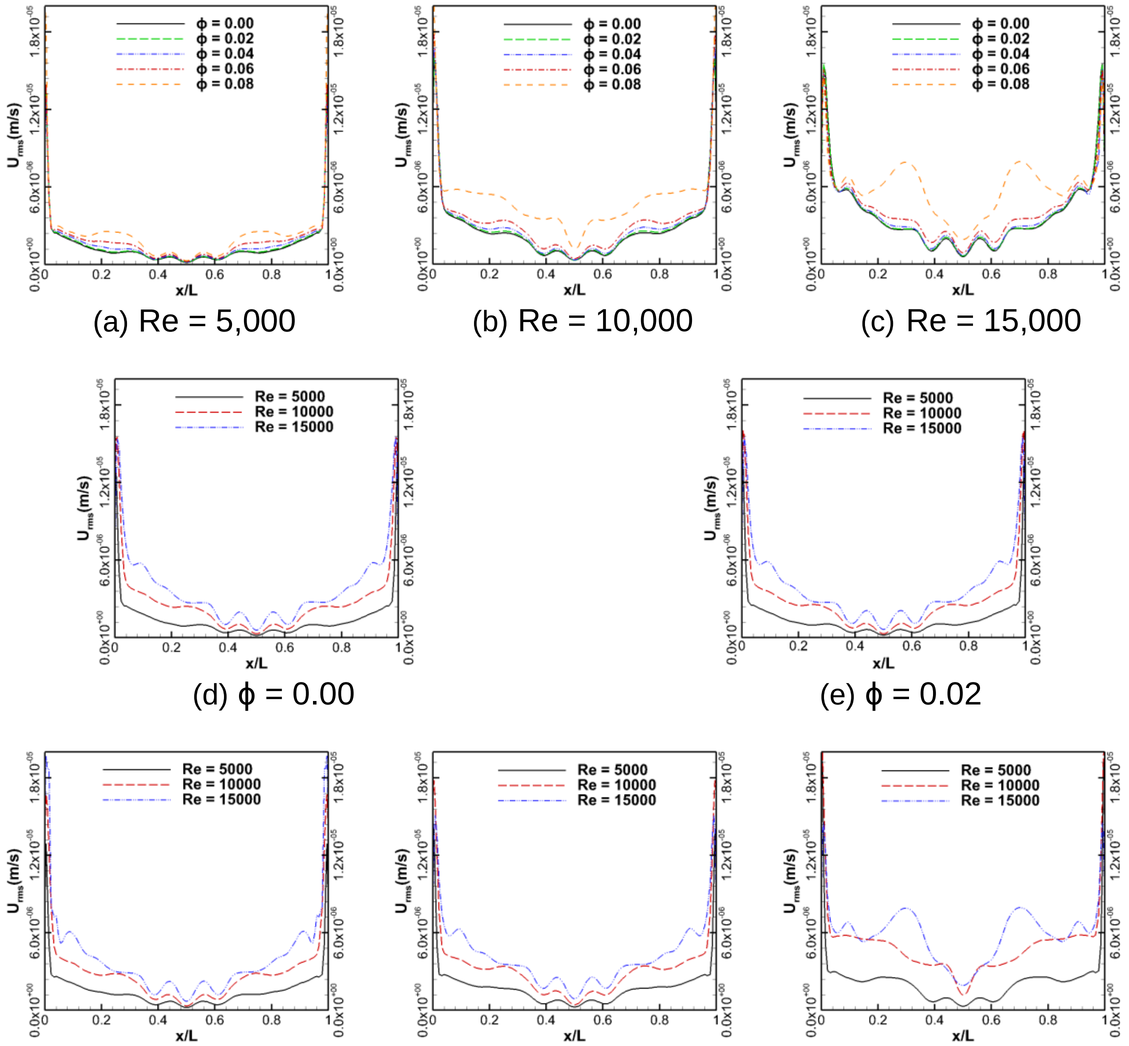

(a) Re = 5,000 (b) Re = 10,000 (c) Re = 15,000

(d) ϕ = 0.00 (e) ϕ = 0.02

(f) ϕ = 0.04 (g) ϕ = 0.06 (h) ϕ = 0.08

Figure 5-17: Root mean square velocity on the x-axis at different Reynolds numbers and volume fractions.

In general, for all Reynolds number values, it can be observed that the conduction effect increases with increasing the nanoparticles concentration. This indicates that the role of conduction increases in the cavity with increasing the conductivity of the working fluid due to increasing in volume fraction. In addition, it is obvious that the flow and temperature patterns are affected by the participation of nanoparticles in the working fluid, which means mixing nanoparticles with pure water causes a change in the behaviours of the flow field. The reduction is more pronounced at the highest volume fraction, ϕ = 0.08, and the lowest Reynolds number, Re = 5,000, where conduction dominates. However, the reduction is only slightly for the highest Reynolds number, Re = 30,000, where the forced convection is dominant.

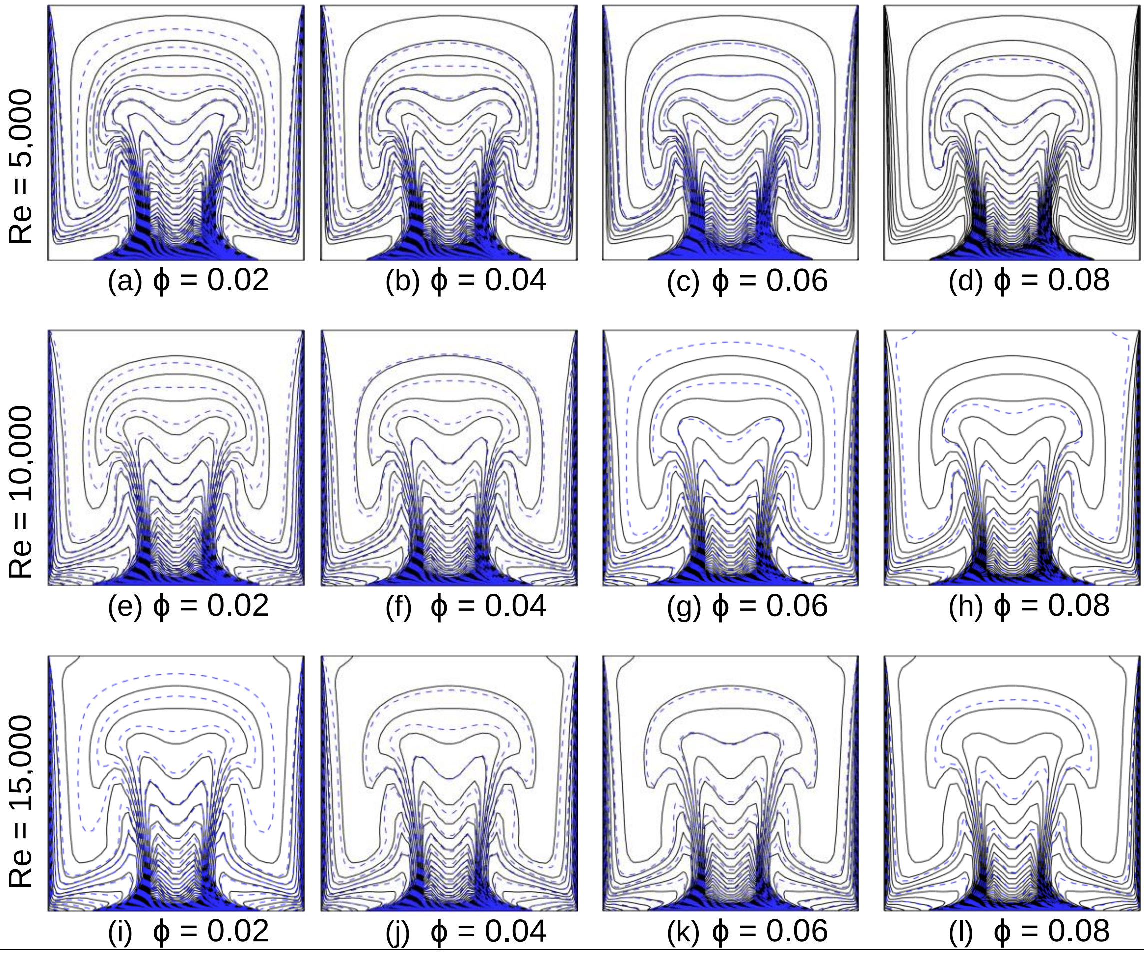

Figure 5-18: Isotherms comparison for SiO_2-H_2O (---) with pure water (–) at various values of Reynolds number and volume fraction.

5.3.2.4 Isotherm contours and velocity vectors by LES

Isotherms and vectors of the x-y plane located at the midway of the z-axis are shown in Figure 5-19 by using the LES method at Re = 10,000 to display the effects of nanoparticles concentration on the heat and flow patterns. Basically, it can be observed that the plane is divided into two sympatric halves and in symmetrical shape. It can be seen that the increment in volume fraction causes changes in the details of flow characteristics. As well as, it can be figured out that the turbulence effect is increasing with adding more nanoparticles, because of the changes in fluid thermal properties of the working fluid apart from the fluid velocity change.

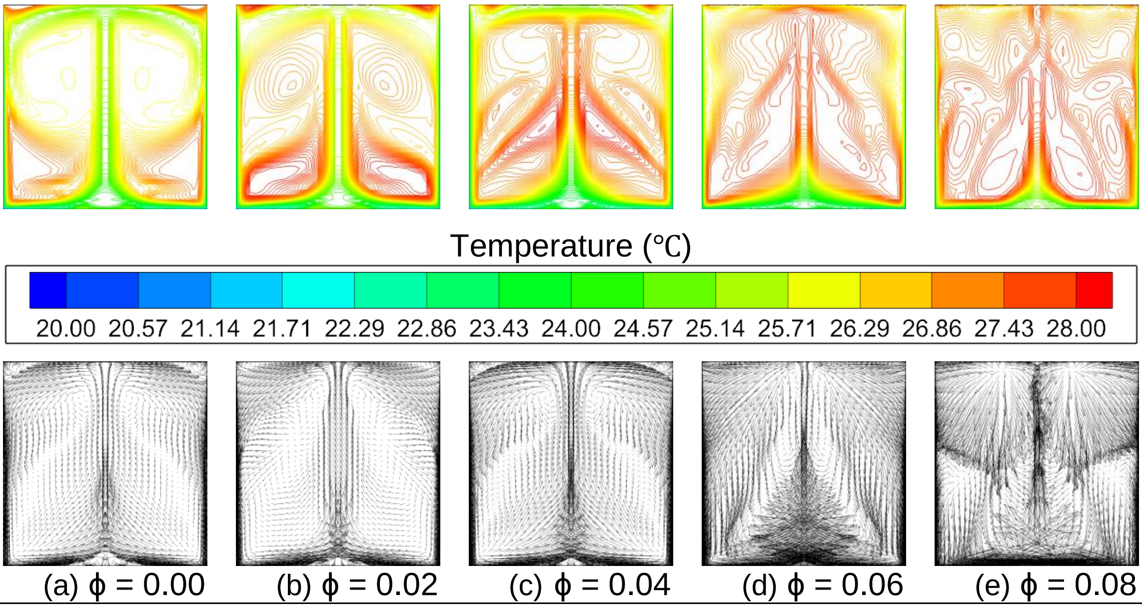

Figure 5-19: Isotherms and vectors for different volume fractions of the x-y plane at the middle of the z-axis, at Re = 10,000, by using LES.

5.3.2.5 Nusselt number comparison between URANS and LES

The comparison results of the two turbulent methods in terms of average Nusselt number, including five different values of volume fraction, are visualised in Figure 5-20. In general, it shows that increasing in the nanoparticles volume fraction will enhance the average Nusselt number inside the cavity by using both URANS and LES methods for the selected Reynolds numbers, Re = 5,000 and10,000, with constant Grashof number. Furthermore, it can be seen that the URANS modelling predicts slightly lower average Nusselt numbers for all volume fraction values compared to the ones derived by involving the LES approach, which reflects the nature of the two turbulence methods.

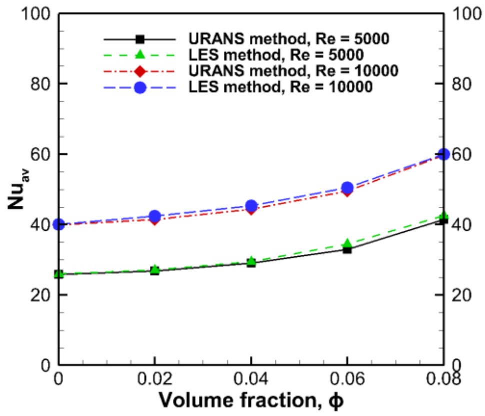

Figure 5-20: Comparison of the average Nusselt numbers for different Reynolds numbers and volume fractions.

5.4 Conclusion

This chapter has addressed a three-dimensional mixed convection heat transfer of water and nanofluids in the closed lid-driven cavity that is heated partially at the bottom wall and has driven sidewalls. Interesting behaviours of URANS and LES methods with varying Reynolds numbers have been investigated as the two-phase mixture model has been used to simulate the nanofluids mixtures. Some selected nanofluid types, nanoparticles concentration and nanoparticles diameter size have been studied at four high values of the Reynolds number. These parameters have been evaluated in terms of Nusselt number, turbulence kinetic energy, root-mean-square velocity, vector maps and isotherm contours. The discernible observations in this research have attempted to conclude the following points:

- For the given fluid types and Grashof number values, significant enhancement on the local and average Nusselt numbers can be achieved due to increasing in the Reynolds number.
- Adding nanoparticles to the base fluid provides higher heat transfer coefficient and turbulence kinetic energy compared to the conventional fluid, and SiO_2 nanoparticles show the best heat transfer rate, followed by ZnO and CuO.
- At any values of Reynolds number, discernible augmentation in the Nusselt number and turbulence kinetic energy has been observed by either adding more nanoparticles to the base fluid (higher volume fraction) or increasing the surface area of the nanoparticles (lower nanoparticles diameter).
- It has been shown that flow and temperature patterns can be affected by the presence of nanoparticles, and the influence on patterns increase is more significant by either decreasing the Reynolds number or increasing the nanoparticles volume fraction.
- The highest local Nusselt number occurs at the edges of the heat source surface, while the lowest local Nusselt number occurs at the centre of the heat source.
- The Reynolds number has a considerable effect on the flow structure and the turbulence kinetic energy, especially with the high speed regimes near the moving sidewalls of the enclosure.

- The flow structures in most areas of the cavity have been driven by the forced convection, except that the area near the heat source is mostly controlled by the natural convection.
- At fully developed state, two main symmetric vortexes, clockwise and anticlockwise, are covering most of the cavity, while the secondary eddies have been predicted at the corners of the cavity, especially by the LES method.

Chapter 6 Mixed convection heat transfer of a 3D lid-driven top wall square enclosure containing a rotating cylinder

6.1 Motivation and introduction

Expansion of the development of the flow behaviour of mixed convection lid-driven cavity that contains a rotating cylinder through a numerical investigation at different conditions can help to establish more designing options in the field. By considering the literature review and to the authors' best knowledge, it can be concluded that only the 2D mixed convection heat transfer in a plane moving wall square cavity with rotating cylinder was studied using either classic fluids or nanofluids. However, no researcher has given attention to the LES modelling of the 3D mixed convection within a cubic enclosure with a rotational cylinder and comparing it to the URANS modelling. A study considering the effects of three-dimensional rotating cylinders in terms of their speeds and directions (clockwise and anticlockwise) within a top lid-driven closed cavity on turbulent nanofluid flow, and involving the Unsteady RANS method, is unprecedented.

Hence, in this chapter, a turbulent 3D mixed convective flow of pure water, H_2O, and nanofluid, SiO_2-H_2O, inside a differentially heated moving top wall enclosure containing an insulated rotating cylinder is numerically investigated. A cooled lid-driven top wall and a heated bottom wall are the only thermally uninsulated walls in this domain. Clockwise and anticlockwise directions of the rotating cylinder over a range of rotational speeds, $-5 \leq \Omega \leq 10$, are studied in detail with the Reynolds numbers of 5,000, 10,000, 15,000 and 30,000, and a constant Grashof number in order to enhance the convection heat transfer efficiency within the lid-driven enclosure. The performance of two turbulence methods, the Large Eddy Simulation (LES) approach with the WALE subgrid-scale model and the Unsteady Reynolds-Averaged Navier-Stokes (URANS) approach with the standard k-ε model, has been evaluated in this chapter, and the relevant results and discussion are presented in two sections. The first section includes the results of an anticlockwise rotating cylinder within the moving wall cavity filled with conventional fluid. The second section refers to the results of a clockwise and an anticlockwise rotating cylinder within the cavity filled with either nanofluids or water. Both steady and unsteady RANS outcomes are presented separately. The comparison between URANS and LES approach is studied through 3D isotherms and isosurface temperatures, velocity vectors and Nusselt numbers. The local and average Nusselt numbers, mean velocity profiles and velocity components, streamlines, isotherms and isosurface temperatures are derived and presented in the second section of the results and discussion to gain a good understanding of the effects of clockwise and anticlockwise rotational cylinder directions and nanofluids on the heat transfer and flow patterns. Two journal papers have been published from this chapter's materials [171, 172] beside one conference paper [173].

6.2 Numerical model

6.2.1 Physical model

The schematic diagram and main geometry parameters of the cubic moving top wall cavity with rotating cylinder are shown in Figure 6-1. The top wall of the cubic enclosure is treated as a cold moving wall, while the bottom wall is maintained at hot constant temperature. The rest walls of the geometry are assumed thermally adiabatic and stationary except the central cylinder which is assumed as a rotating part (clockwise and anticlockwise).

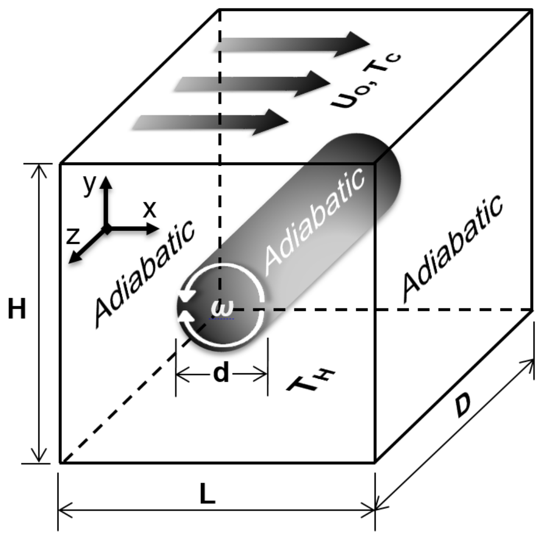

Figure 6-1: Schematic diagram of the cubic lid-driven cavity with rotating cylinder.

6.2.2 Boundary conditions

The boundary conditions for the current study are defined as; the top wall is assumed as a cold moving wall at uniform velocity ($T = T_C, U = U_0, V = 0, W = 0$). Whilst, the bottom wall is kept motionless and hot ($T = T_H, U = V = W = 0$). The other remaining walls (sides, rear and front walls) that forming the enclosure are thermally adiabatic and stationary ($U = V = W = 0$). Finally, the central horizontal cylinder is adiabatic and rotating object at uniform rotational speeds and different rotational directions ($\omega = (\Omega \times 2U_0) / d, d = 0.2L$).

6.2.3 Numerical procedure

The numerical simulations of fluid flow and heat transfer were conducted by utilizing the Computational Fluid Dynamic (CFD) techniques. The finite volume method (FVM) and SIMPLEC algorithm were used to discretize the governing equations and to deal with the pressure-velocity coupling equations. The commercial code ANSYS©FLUENT (version R16.2) [139] was adapted to complete the simulations. Both steady and unsteady Reynolds-Averaged Navier-Stokes equations were solved besides the LES method. The QUICK and implicit second order scheme were used to respectively deal with the convection and the time evaluation terms. The CFD results were collected when the convergence criteria of 10^{-5} were satisfied at each time step.

6.2.4 Grid independence test

It is known that the grid independence test plays a considerable role in a CFD simulation regarding the results prediction time and accuracy. The mesh features such as density and quality were carefully considered in this study to avoid the numerical errors and to reach better computational efficiency. As shown in Figure 6-2, hexahedral cells were created in this work by ANSYS©ICEM 16.2 [139]. In addition, the meshes nearby the walls are refined, particularly in the area close to the circular cylinder, heated bottom wall and cooled top wall. However, the generated grids of the whole domain were fine enough to capture the details of the fluid structures and thermal distribution within the cavity. As illustrated in Figure 6-3, several grid numbers (125,868, 292,440, 496,800, 929,160 and 1,260,762) were tested in order to figure out the suitable mesh number. The final chosen number of grid points in the current study was 929160, which was proved satisfactory by different indicators that are important in order to obtain high quality results: the non-dimensional time step is 0.004, the dimensionless wall distance $y^+ \approx 1$ and the Courant-Friedrichs-Lewy number CFL = 0.3. Moreover, the minimum orthogonal quality is 0.7267 and the aspect ratio changes from less than 8 in the key interesting areas to 27.326 far away from the domain walls and the circular cylinder.

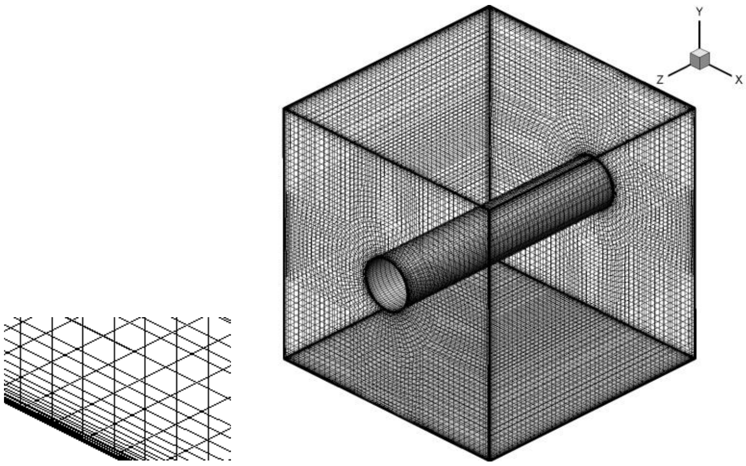

Figure 6-2: Computational mesh of the cubic lid-driven cavity with rotating cylinder.

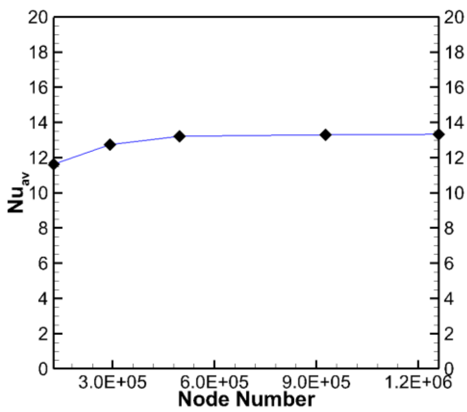

Figure 6-3: Convergence of the average Nusselt number on the bottom wall at Reynolds number of 5,000 and rotational speed of 0 with grid refinement.

6.3 Results and discussion

Anticlockwise rotating cylinder within lid-driven enclosure filled with conventional fluid and clockwise and anticlockwise rotating cylinder within lid-driven enclosure filled with nanofluid are the main two data sections dividing this chapter. However, the numerical solver has been compared alongside many related investigations that have performed previously by Chatterjee*, et al.* [62], Prasad and Koseff [163], Peng*, et al.* [164], Alinia*, et al.* [91] and Padilla*, et al.* [165], to be certain that current solver is ready for new simulation. Additional information about the validation part can be seen in section 3.8.

6.3.1 Anticlockwise rotating cylinder (conventional fluid)

This phase aims to understand and explore the combined impacts of the moving wall and rotating cylinder on the heat convection and flow patterns under turbulent flow conditions. The completed simulations include four Reynolds numbers, Re = 5,000, 10,000, 15,000 and 30,000, and four rotational cylinder speed values, Ω = 0, 1, 5 and 10.

6.3.1.1 RANS method

The Reynolds-Averaged Navier-Stokes equations are known as the time-averaged equations of movement for the fluid flow. This section is completed by using the RANS method to study the flow and thermal fields and velocity distributions in a 2D lid-driven enclosure that contains a rotating circular cylinder.

The isotherms and streamlines contours are plotted in Figure 6-4 at various controlling parameters, Reynolds numbers, Re = 5,000, 10,000, 15,000 and 30,000, and rotational speeds, Ω = 0, 1, 5 and 10. These contours arise by the coupled impacts of forced shear flow (rotating cylinder and moving top wall forces) besides the buoyancy flow due to the heat differences between the top and bottom walls. It can be observed that the influences of both forced actions dominate on most of the heat distribution and flow patterns within the enclosure, aside from the minor effect of the driven buoyancy. Substantially, the shear layers are generated nearby the moving objects and their magnitudes totally depend on the values of the speed of the rotating cylinder and the moving top wall. At all values of the Reynolds number and when the inner cylinder is stationary (Ω = 0), the flow field patterns are the consequence of the moving-lid movement and the temperature differences. A clockwise rotating primary eddy, which is formed as a result of the movement of the lid, is encased in most of the cavity besides four small secondary eddies which are placed at the bottom wall corners (anticlockwise), the top of the left wall (anticlockwise) and the right top of the cylinder (clockwise). It can be observed that increasing the Reynolds number leads to decreasing the secondary eddies sizes. Whilst the inner cylinder is rotating at low velocity value, $\Omega = 1$, the flow field's evolution results from the combined action of the lid-driven movement, the rotating cylinder motion and the buoyancy driven effect. Although some shear layers appear thereabout the inner cylinder at all Reynolds number values, the domination of the main eddy, which is formed by the linear movement of the top wall, covers most of the enclosure regions. However, the influence due to the movement of the rotating cylinder is increased by using high rotational speeds, $\Omega = 5$ and $\Omega = 10$. Consequently, it can be seen that the effect of the linear movement of the top wall appears as two clockwise vortices and adjacent to the top surface of the cavity. In addition, the two anticlockwise eddies nearby the bottom walls became clockwise when the rotating speed controls most of the enclosure zones. In general, an increment in linear speed of the lid-driven or in rotation speed of the inner cylinder provides better temperature distribution in the domain, and more particularly when both speeds are high (Re = 30,000 and $\Omega = 10$).

The curves of the dimensionless horizontal velocity distribution along the vertical line, that is located at (0.25, 0, 0) and (0.25, 1, 0), for various values of the Reynolds number, Re = 5,000 – 30,000, and rotational velocity, $\Omega = 0 – 10$, are presented in Figure 6-5. Slight differences can be figured out when the rotational speed is equal to zero or one, unlike when the rotating cylinder dominates the flow patterns at high Ω values. Moreover, it can be concluded that Reynolds number can change the values of the velocity distribution, while the rotating cylinder is holding the direction of the flow in the cavity.

6.3.1.2 URANS method

The Unsteady Reynolds-Averaged Navier-Stokes equations depend on the time-averaged equations of movement for the fluid flow. This section is completed by using the URANS method to investigate the heat transfer characteristics and Nusselt number in a 3D lid-driven enclosure containing a rotating circular cylinder.

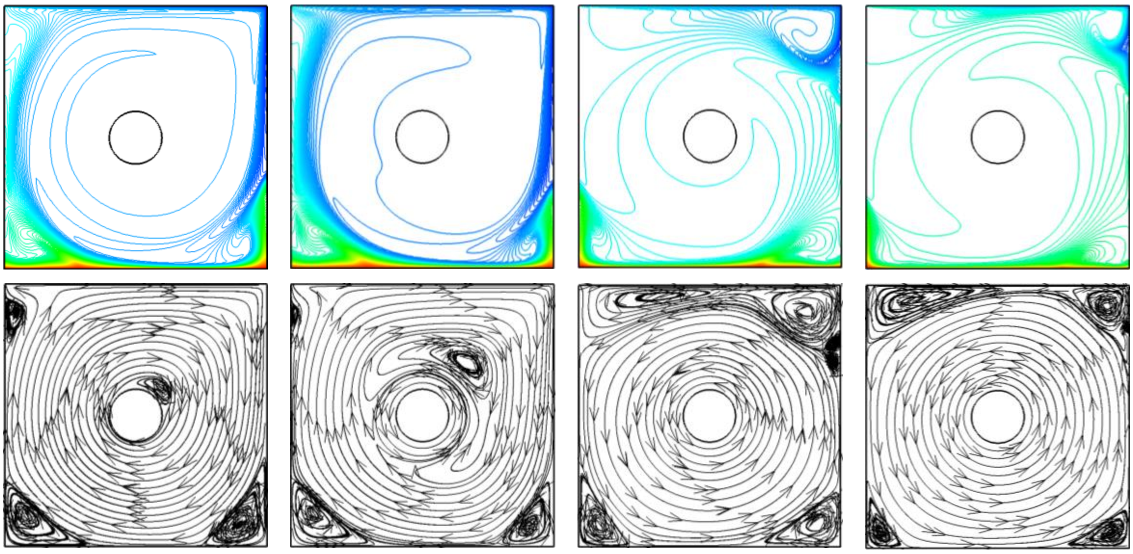

Ω = 0 Ω = 1 Ω = 5 Ω = 10

Re = 5,000

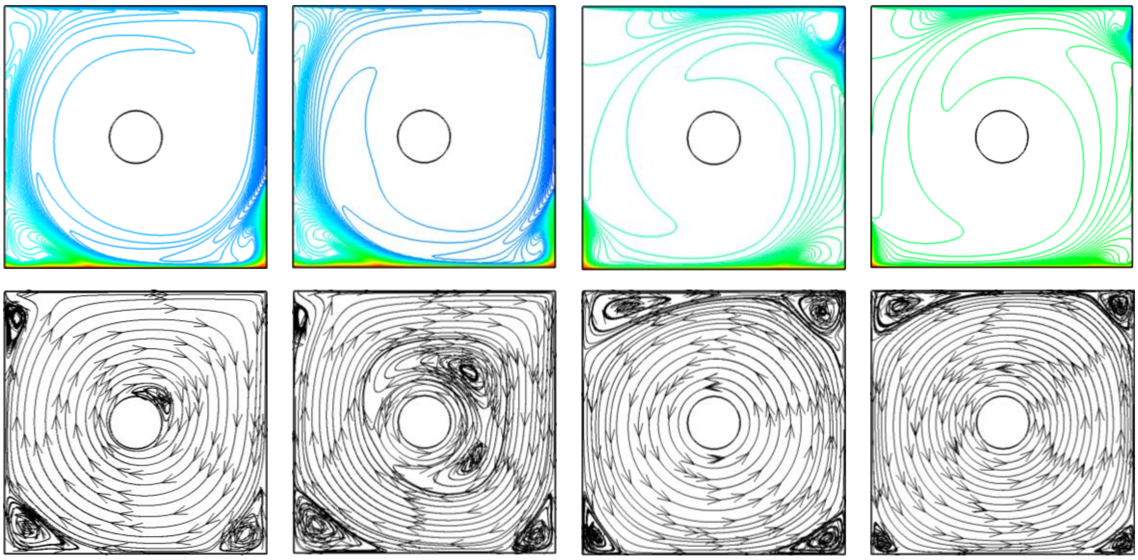

Ω = 0 Ω = 1 Ω = 5 Ω = 10

Re = 10,000

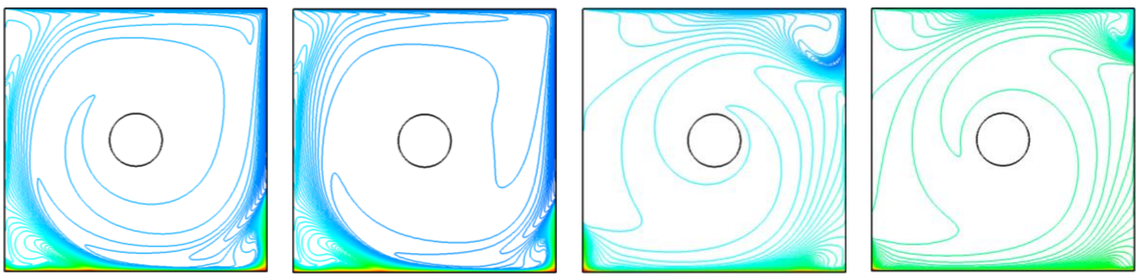

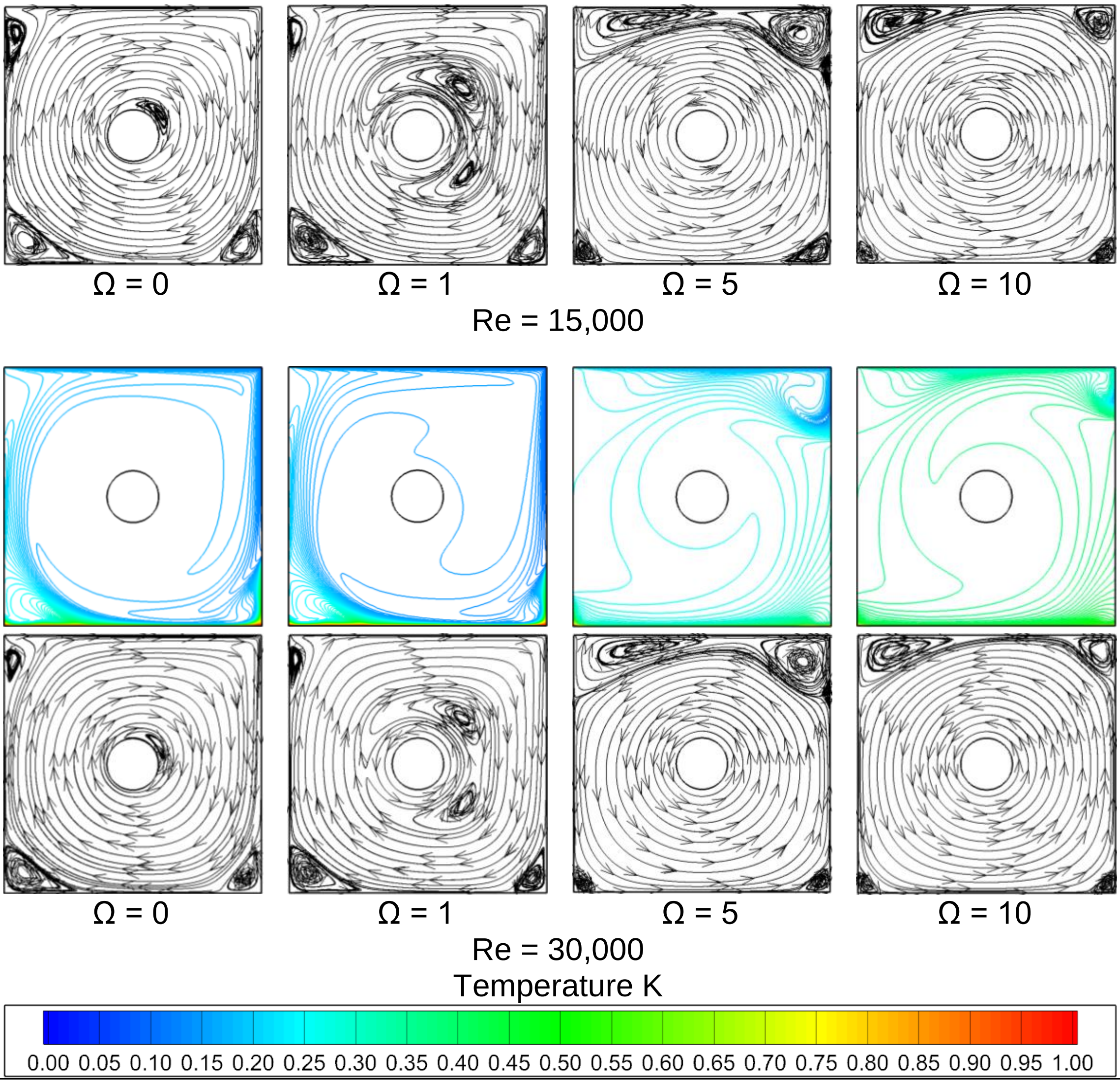

Figure 6-4: Isotherms and streamlines contours for different Reynolds numbers and rotating speeds.

Figure 6-6 illustrates the influences of varying rotational speeds of the cylinder, Ω = 0, 1, 5 and Reynolds numbers, Re = 5,000, 10,000 and 15,000, on three-dimensional profiles of the isotherms and its isosurface temperatures for the nine cases studies of the cavity in order to understand the flow patterns and the related heat distribution. It can be observed that when the dimensionless rotational velocity is stationary, Ω = 0, the top moving wall is controlling all the fluid behaviours and the heat transfer distribution besides the limited buoyancy effect due to the different temperatures of the top and bottom walls. It can be noticed that the flow direction is clockwise. However, when the cylinder is moving in the rotational direction at rotating speed equal to one, it can be argued that the rotating force controls the region around the cylinder whereas most of the area of the enclosure is driven by the moving top wall. By comparison to the rotating speed equal to five, this measure shows that most of the cavity's area is covered by the affected flow due to the rotating cylinder's force. Nonetheless, in both cases (Ω = 1 and 5) it can be seen that the homogeneity of the temperature division inside the domain is higher than that in the stationary cylinder case.

Figure 6-7 shows the average Nusselt number for the chosen values of rotational speed, Ω = 0, 1 and 10, and Reynolds number, Re = 5,000, 10,000 and 15,000, at the midline of the bottom wall. The standard *k-ε* viscous model with time dependence is exercised in this investigation.

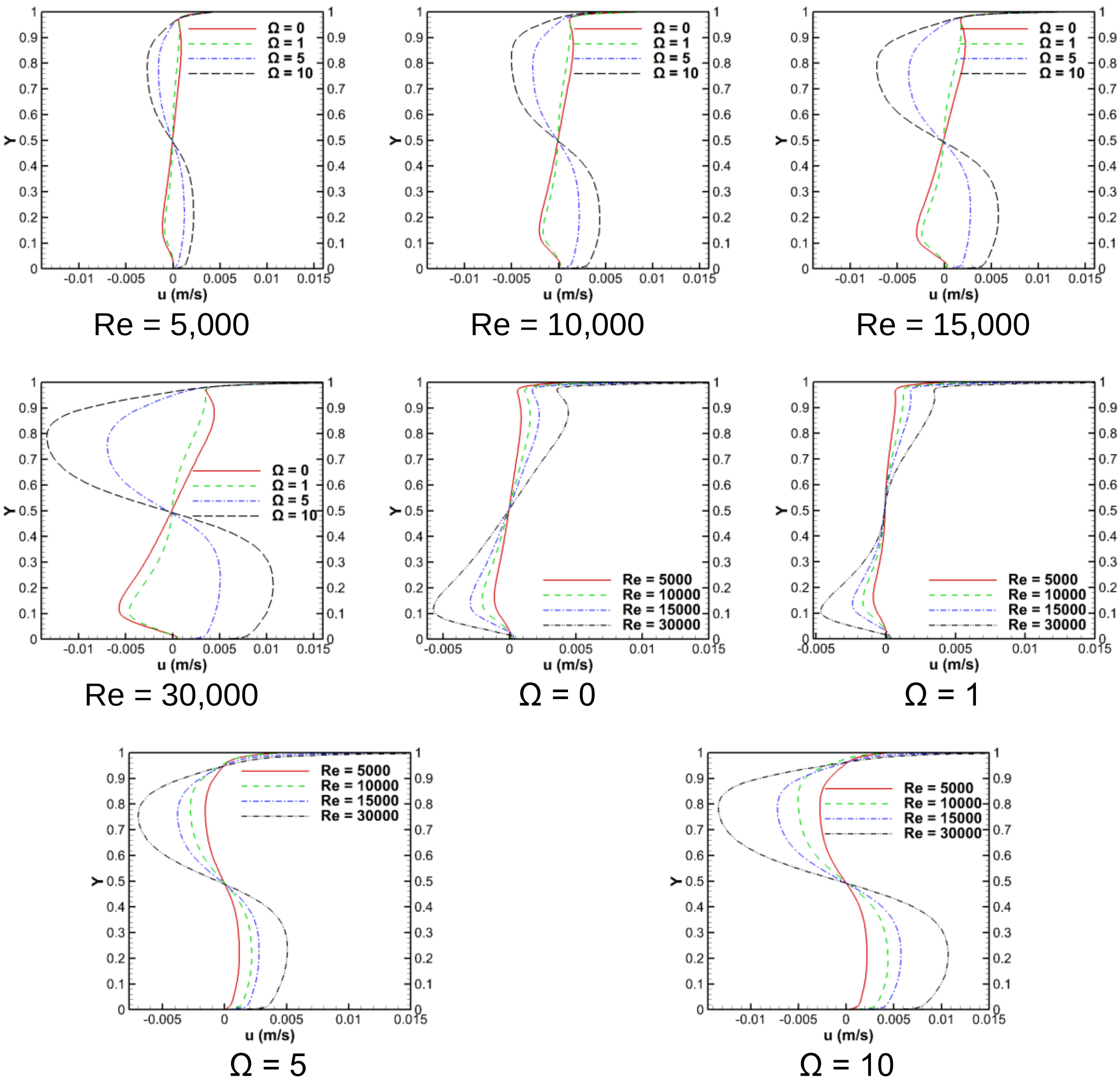

Figure 6-5: Velocity distribution along the vertical line for different Reynolds numbers and rotational speeds.

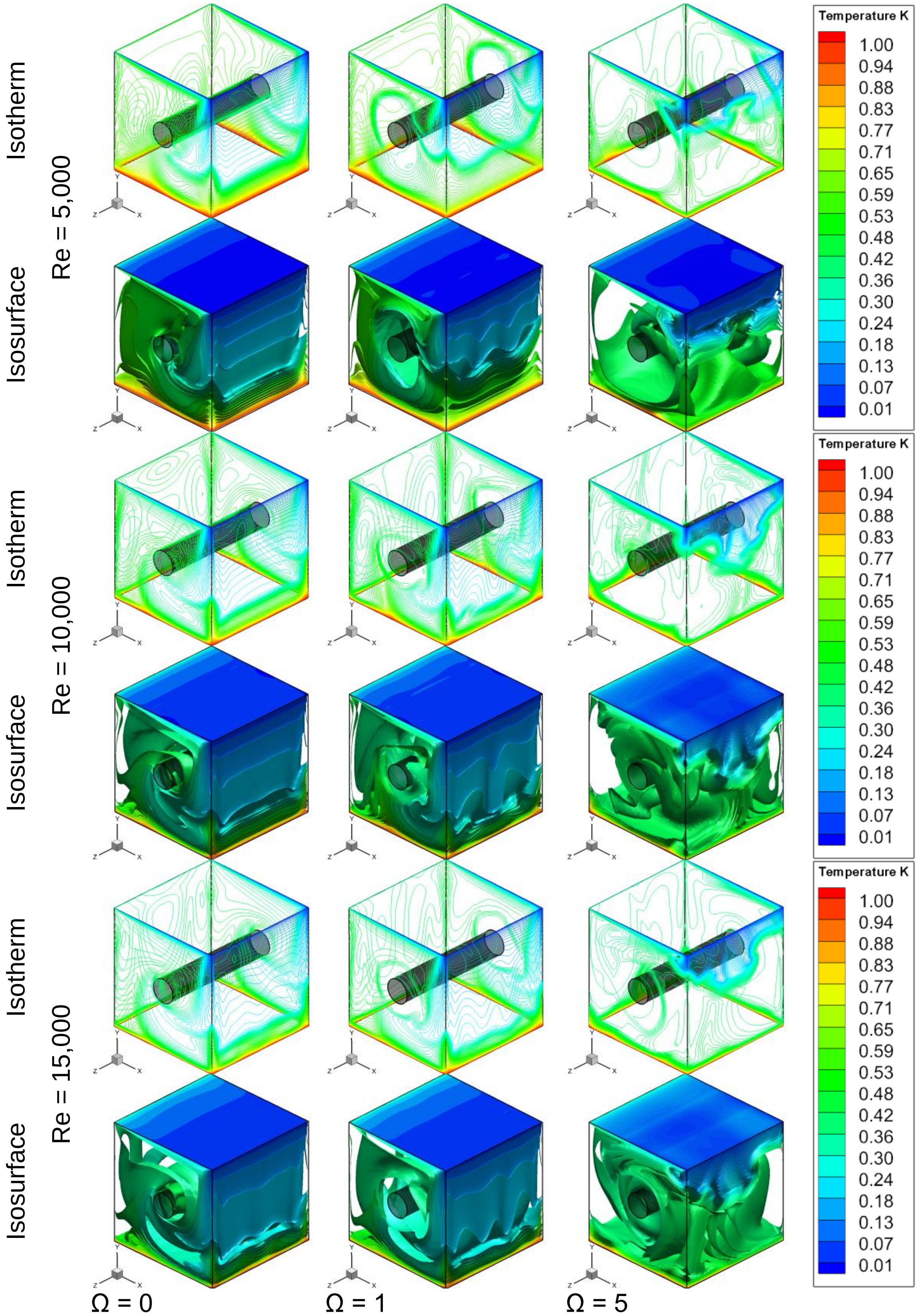

Figure 6-6: Three-dimensional isotherms and isosurfaces temperature at different Reynolds numbers and rotational speeds.

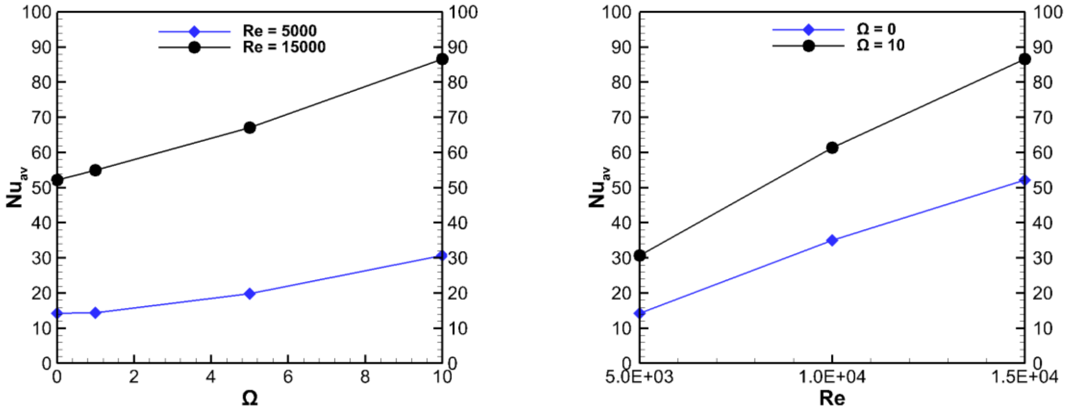

Rotational speeds Reynolds numbers

Figure 6-7: Average Nusselt number distributions at the bottom wall for different Reynolds numbers and rotational cylinder speeds.

Essentially, the figure illustrates that increasing either Re or Ω values leads to a remarkable enhancement in the average Nusselt number which is mainly the consequences of the increased flow velocity. Since the higher motion of the fluid occurs at higher Reynolds number and rotation speed, it can be concluded that the highest Nusselt number occurs when Reynolds number = 15,000 and the rotational speed = 10.

The local Nusselt number distributions along the midline of the heated top wall (0, 1, 0.5 and 1, 1, 0.5) are shown in Figure 6-8 for various values of the rotational speed and Reynolds number. Essentially, it demonstrates that Reynolds number has a meaningful effect on the top wall local Nusselt number for all the cylinder rotational speeds. On the other hand, at the rotational speed, $0 \leq \Omega \leq 5$, and at all Reynolds number values, Re = 5,000 – 15,000, it can be noticed that by changing the rotational speed no distinct change has been detected on the top moving wall local Nusselt number. This can be clarified as the consequences of the strong domination of the lid-driven motion on the heat transfer of the top wall. However, when the rotational speed is equal to 10, it can be observed the clear influences of the rotating cylinder on the top wall heat transfer. These influences increase gradually as increasing Reynolds number.

6.3.1.3 Comparison between URANS and LES

Hereinafter, inclusive comparison and discussion will be focused on the findings generated from simulating the unsteady turbulent flow of combined convection heat transfer in the lid-driven cavity containing rotating circular cylinder by involving the WALE subgrid-scale model of the LES method and the standard *k-ε* model of the URANS method. The simulations are completed for two Reynolds numbers, Re = 5,000 and 10,000, and three rotational speeds, Ω = 0, 1 and 5.

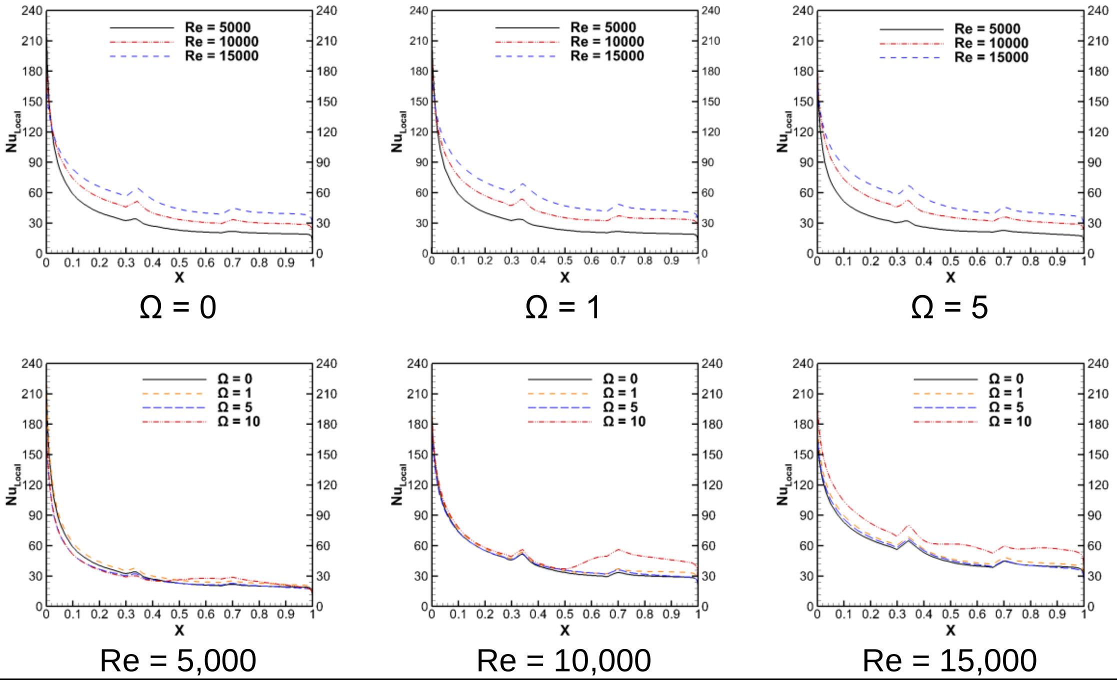

Figure 6-8: Local Nusselt number of the top moving wall for different Reynolds numbers and rotational cylinder speeds.

The outcomes and comparisons are presented in terms of velocity vectors, isotherms, isosurface temperatures and local Nusselt numbers. The power spectral density profiles of the velocity magnitude at five selected points within the domain in order to confirm the LES simulations are correctly performed are shown in Figure 6-9 for Re = 10,000 and Ω = 1. It can be noticed that the slope of -5/3 in the inertial subrange is observed, showing that the present simulations can be regarded as having the features of a fully turbulent flow. In addition, the results of the LES method are accepted only after reaching the fully developed flow state. Figure 6-10 illustrates the U_{rms} profile evolution along a line located in the cavity at (0.25, 1, 0.5) and (0.25, 0, 0.5) for different simulation times. It can be seen that after 45 seconds, the flow reaches the steady state. However, the statistical simulations results are collected after 50 seconds to ensure their high quality.

The computational results from the LES and URANS methods are compared at chosen rotational speeds of the circular cylinder, Ω = 0, 1 and 5, and Reynolds numbers, Re = 5,000. The three-dimensional isotherms and isosurface temperatures are offered in Figure 6-11 to analyse the differences between the LES and URANS behaviours. Generally, for stationary cylinder it can be argued that the moving top wall is controlling the flow patterns and the heat transfer.

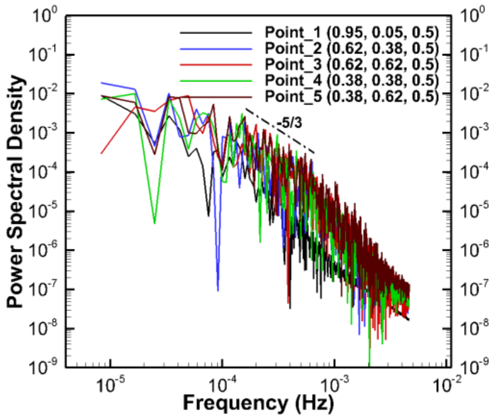

Figure 6-9: Spectral analysis of velocity magnitude at selected locations for Re = 10,000, Ω = 1.

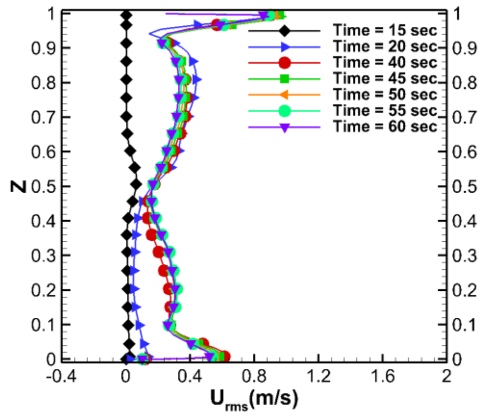

Figure 6-10: Root mean square velocity profiles at different simulation times.

However, for Ω = 1, it can be noticed that the force that comes from the rotational cylinder starts influencing the central part of the enclosure. This influence is growing strongly when the rotational speed reaches five. Hence, increasing the rotational speed enhances significantly the heat transfer distribution.

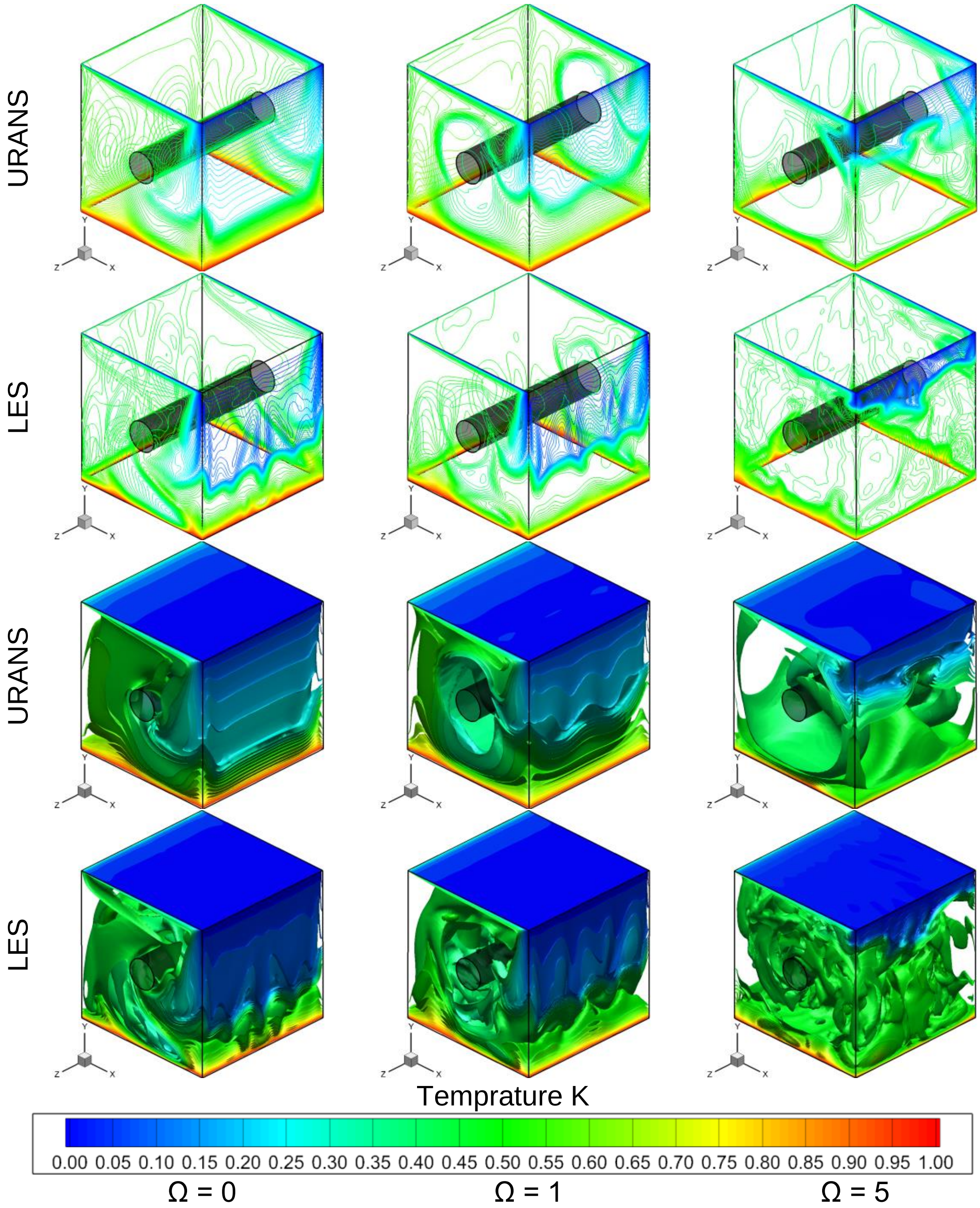

Figure 6-11: Three-dimensional isotherms and isosurface temperatures distribution comparison of URANS and LES at Re = 5,000.

In comparison of the turbulent prediction approaches, it can be pointed out from the shown figure that both methods have demonstrated a good ability in catching the primary vortices of the flow for all cases shown in Figure 6-11. However, the secondary vortices appear clearly by using the LES prediction and these vortices increase at either a higher Reynolds number or a higher rotational speed.

The flow vectors of both URANS and LES methods have been investigated for Reynolds number, Re = 5,000, and rotating speed, Ω = 0, 1 and 5. Figure 6-12a illustrates the flow behaviours for the y-z plane located in the middle of the z-axis, and Figure 6-12b states the x-y plane located in the midway of the x-axis. It is known that LES method requires special mesh features, such as high grid number and finer then what RANS method needs. Therefore, slight difference can be noted in the mesh number of the images of those two turbulent methods. In other words, based on the grid independence test, the last three node numbers provide mostly the same results, thus, the node number of 496,800 has been used with URANS in this section. Generally, for both approaches and when the circular cylinder is stationary, it can be noticed that the controlling influence of forced convection is due to the moving top wall, especially for the layers nearby the lid-driven wall. The flow nearby the lid-driven wall is drawn due to the shear force and it impinges onto the motionless-walls.

The primary vortex (rotating clockwise) covering the domain centre is distinctly seen in Figure 6-12b and this vortex controls most of the flow patterns, as predicted by either URANS or LES method. Further, the displayed vectors in Figure 6-12 reveal the presence of the secondary vortices thereabout the domain corners and the top right of the cylinder. However, it can be observed distinctly that the secondary vortices become more visible from the LES prediction for both selected planes, especially when increasing the rotational speed of the cylinder.

The superiority of the LES method over the RANS modelling for this flow type is clearly demonstrated in Figure 6-12a – b in capturing more detailed secondary eddies, which reflects the fundamental difference between the two approaches. Essentially the RANS approach uses the time averaging procedure to obtain the Reynolds averaged transport equations for the mean flow quantities and all scales (both large and small) of turbulence are represented by a model such as the standard k-ε model adapted in this paper. In contrast, the LES approach employs the space filtering procedure to derive the transport equations for both the mean flow quantities and the large scales of turbulence, and only the smaller scale eddies that cannot be resolved by the computational grid are modelled by an SGS model such as the WALE model used in the comparison.

Figure 6-13 illustrates the comparison between the LES and URANS methods in terms of local Nusselt number on the line that is located at the left of the top lid-driven wall (0, 1, 0.5 and 0.005, 1, 0.5) for different rotational speeds of the circular cylinder, $0 \le \Omega \le 5$, and at Re = 10,000.

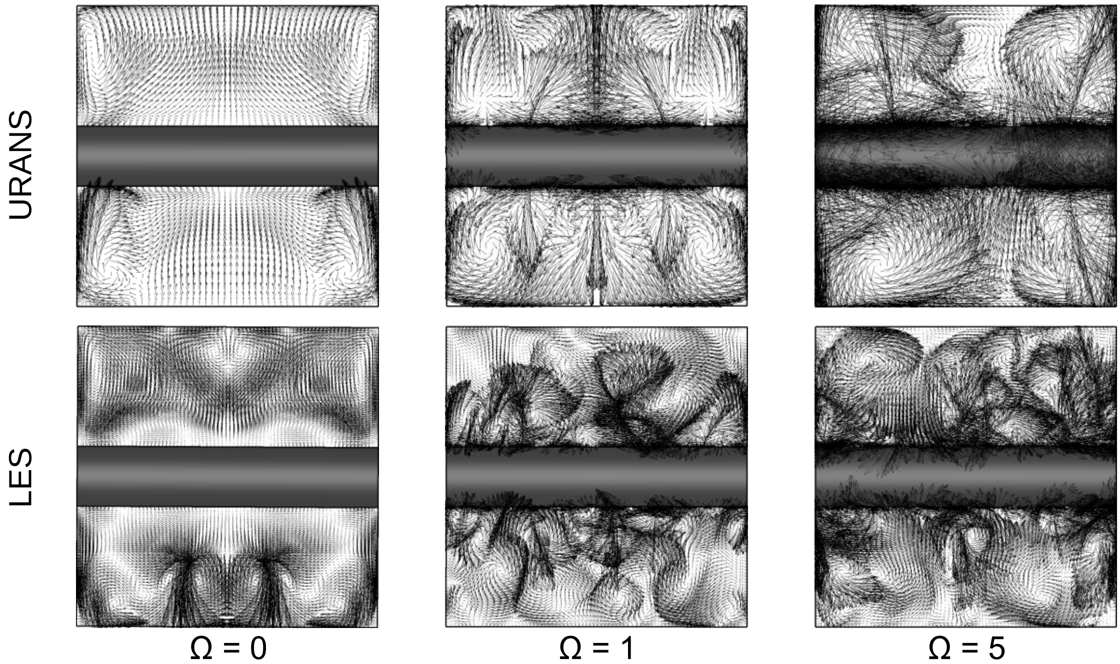

(a) y-z plane located in the middle of the z-axis

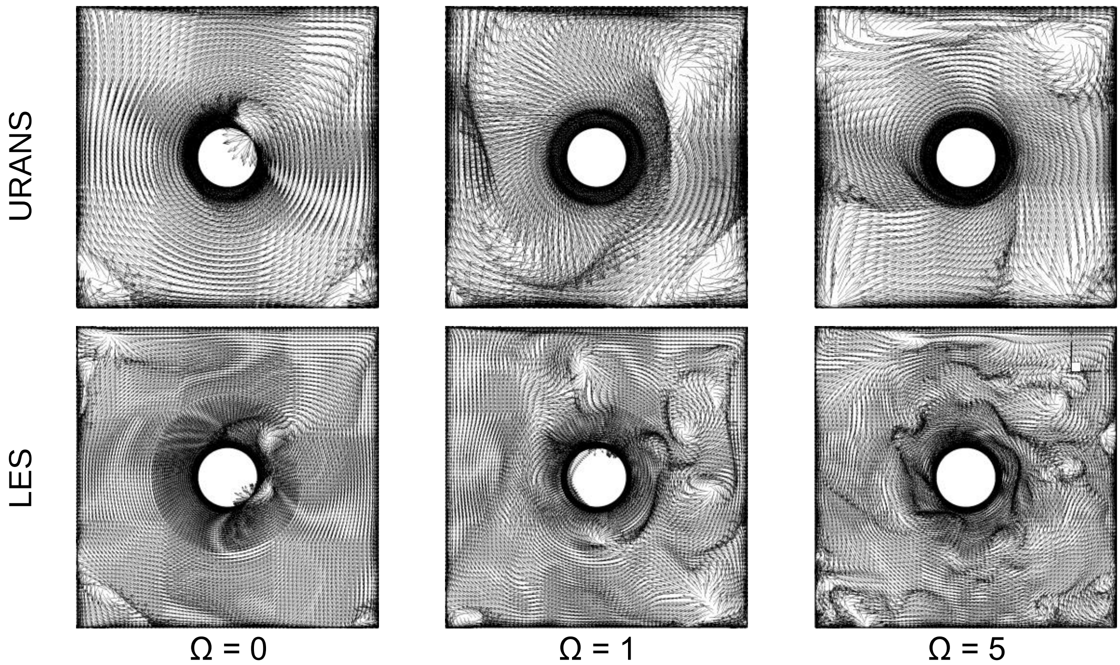

(b) x-y plane located in the middle of the z-axis

Figure 6-12: Flow vectors comparison between URANS and LES at Re = 5,000.

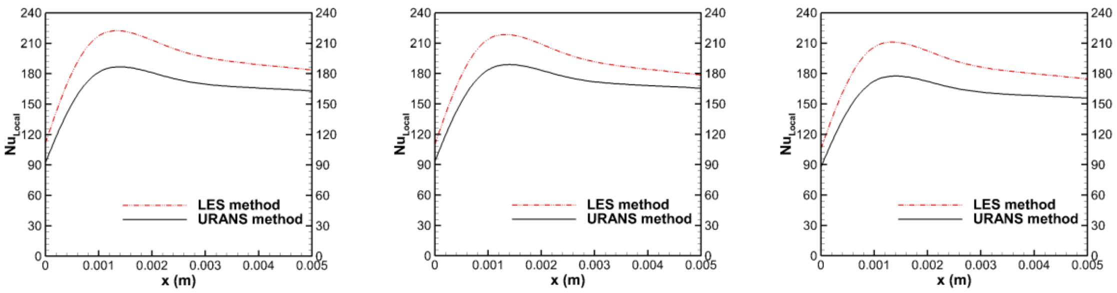

Ω = 0 Ω = 1 Ω = 5

Figure 6-13: Comparison of local Nusselt number for different rotational speeds and at Re = 10,000.

For all rotational speeds, it can be clearly noticed that the LES approach shows distinct advantages over the URANS approach in predicting higher heat transfer coefficients in the region that is closer to the moving wall of the cavity, owing to its ability in capturing the contribution from the secondary vortices.

6.3.2 Clockwise and anticlockwise rotating cylinder (nanofluid)

Three cases of rotational cylinder conditions have been addressed in this work. The first case (Case1) is when the cylinder is stationary ($\Omega = 0$). The second case (Case2) is when the rotational direction of the cylinder is clockwise ($\Omega < 0$), whereas the third case (Case3) is when the cylinder rotates in the anticlockwise direction ($\Omega > 0$). For more information, when the cylinder rotates in the clockwise direction, it favours the lid-driven motion, unlike when the cylinder rotates in the anticlockwise direction, which opposes the lid-driven wall movement.

6.3.2.1 Flow and thermal field

Figure 6-14 and Figure 6-15 respectively, display the isotherms and streamlines contours, and isosurface temperatures of pure water for Reynolds numbers Re = 5,000 and 10,000, and rotational speeds, $-5 \leq \Omega \leq 5$ to show the influences of rotational speed and direction on the turbulent flow in the cavity. Essentially, it was demonstrated that the effect of increasing the Reynolds number is more significant when the cylinder is rotating in the anticlockwise direction. By focusing on the rotational speed condition, it can be seen that for both Reynolds numbers, and when the rotational movement and lid-driven movement were in the same direction, the forces of both movements supported each other, which led to rotating the whole fluid field in the same direction and producing a reduced number of secondary vortices, unlike when the lid-driven motion and rotational motion were in opposed directions, 1≤ Ω ≤ 5, which produces more secondary eddies within the domain, especially at higher values of Reynolds number and rotational speed. At Ω = 0, it was demonstrated that the force of the top wall movement was driving the flow structure beyond the minor influence of the buoyancy effect. In the comparison between pure fluid and nanofluid, it can be clearly observed from Figure 6-16 that involving a nanofluid has its positive influences on the flow patterns and heat distributions across all the study cases.

6.3.2.2 Mean velocity profile

The variation of the mean velocity profiles of the horizontal lines at 0.25, 0, 0 and 0.25, 1, 0, for the pure water and nanofluid at Reynolds numbers of Re = 5,000 – 10,000 and rotational speeds -5 ≤ Ω ≤ 5 are shown in Figure 6-17. Generally, it can be observed that at all values of Reynolds number and rotational speed, the velocity near the moving wall is controlled by the lid movement. In addition, it might be noted that the effect of changing the rotating directions on the mean velocity profiles, especially at the bottom half of the geometry (y-axis height is 0.5 m), is less influenced by the moving top wall. Moreover, at Ω = 5 and Re = 5,000, it can be concluded that the rotating cylinder is controlling the velocity profile over the whole domain, unlike when the Reynolds number is increased to 10,000, which limited the control of the rotating cylinder to just the bottom part of the cavity.

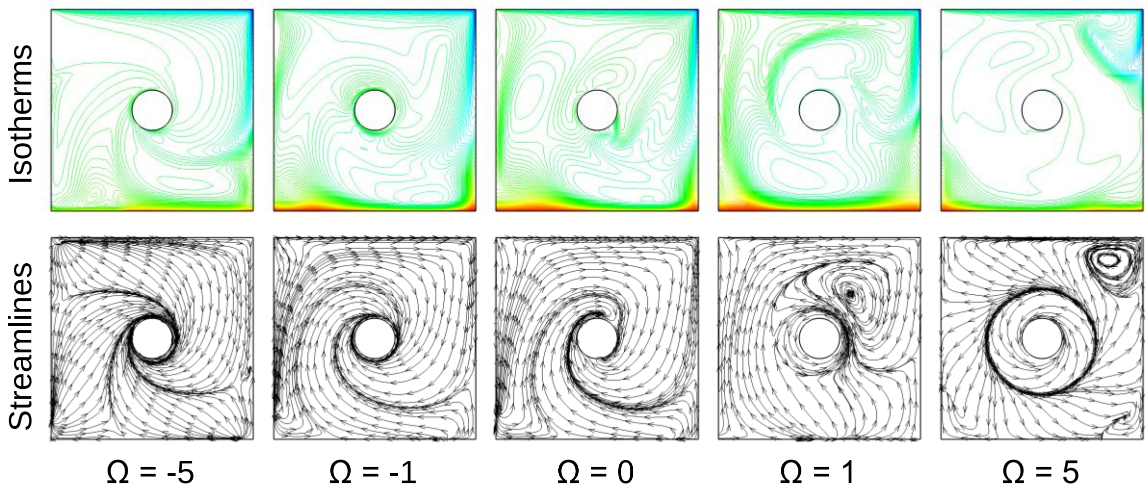

(a) Re = 5,000

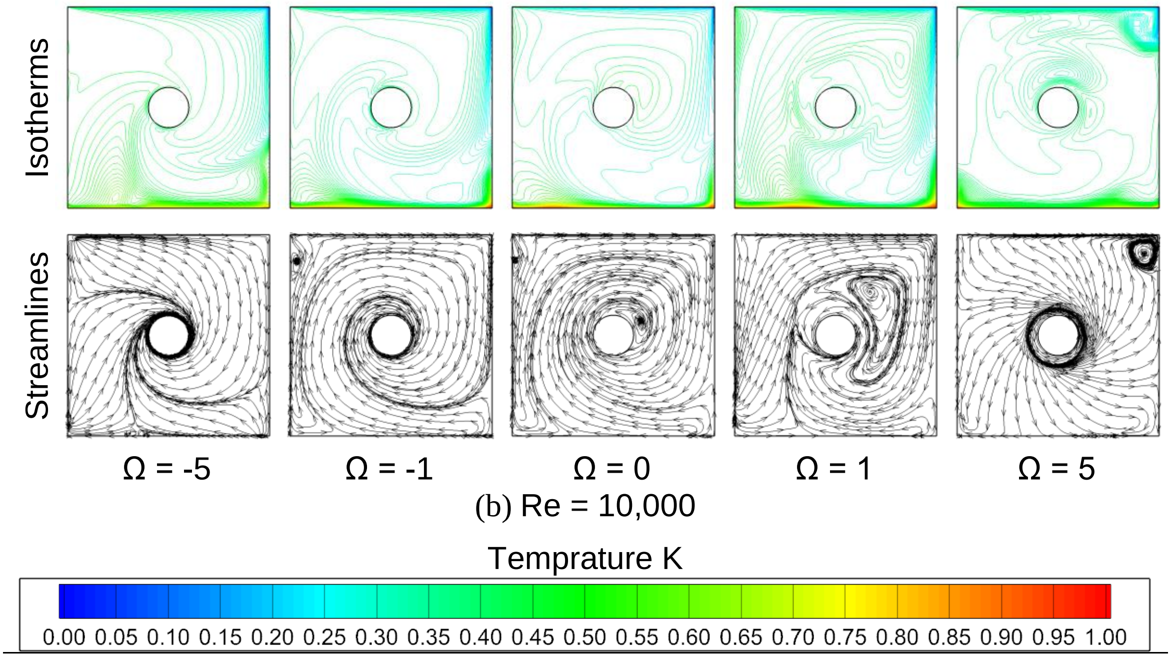

Figure 6-14: Isotherms and streamlines contours for ϕ = 0 at different Reynolds numbers and rotational speeds.

By effectively introducing nanoparticles into the pure water, it can be seen that for both Reynolds number values, the rotational speed of 5 had a significant influence on the whole flow domain.

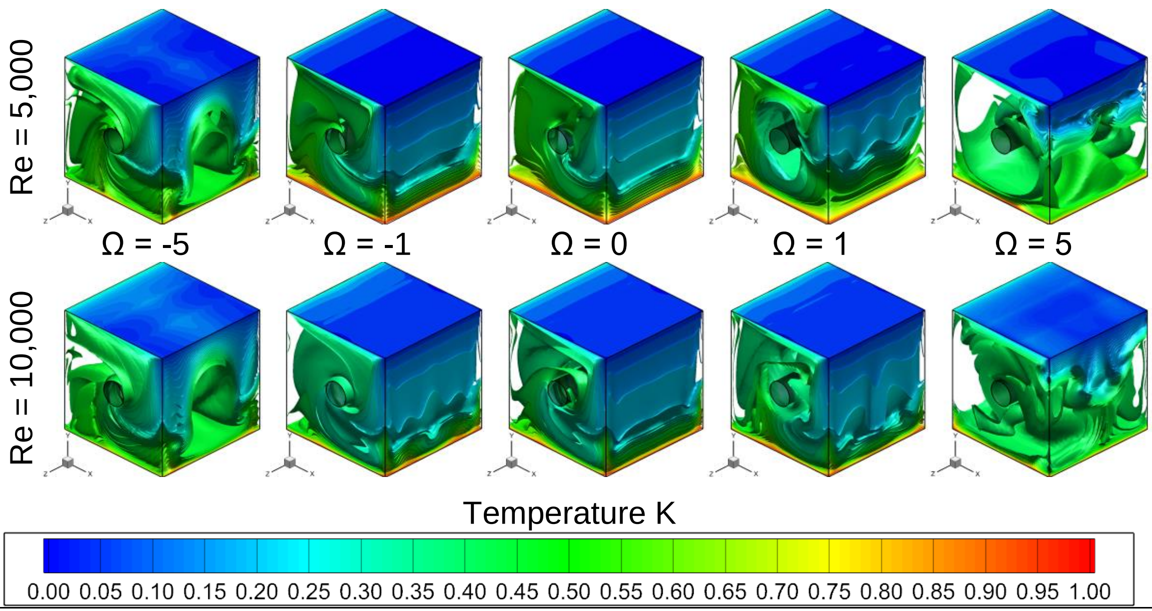

Figure 6-15: Three-dimensional isosurface profiles comparing the clockwise and anticlockwise rotation of the cylinder for ϕ = 0.

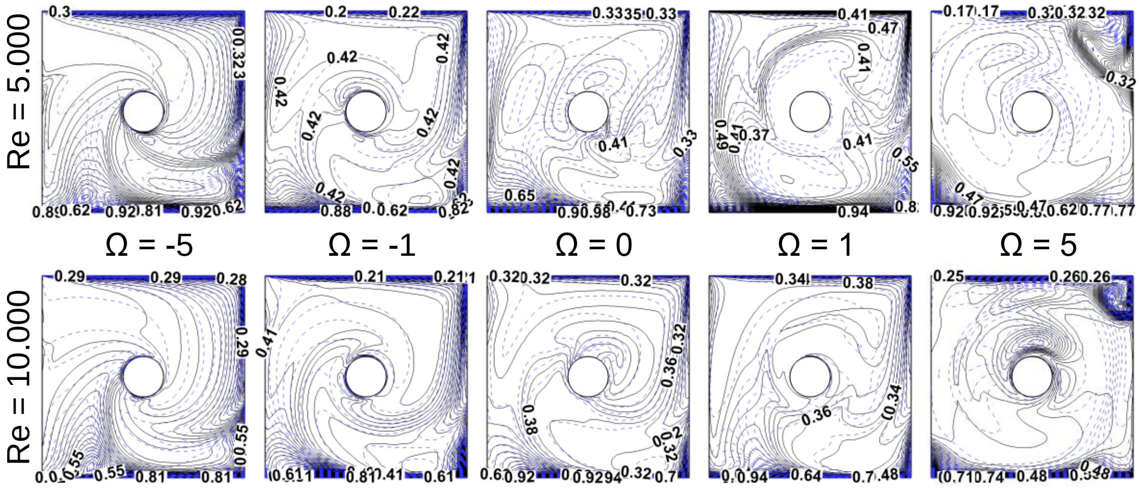

Figure 6-16: Isotherm contour comparisons between pure fluid (ϕ = 0, solid lines) and nanofluid (ϕ = 0.025, broken lines) for different Reynolds numbers and rotational speeds.

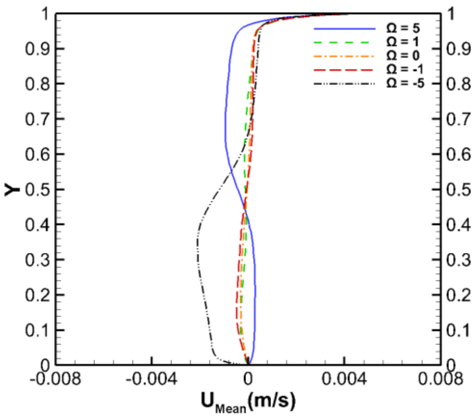

(a) Re = 5,000 and ϕ = 0

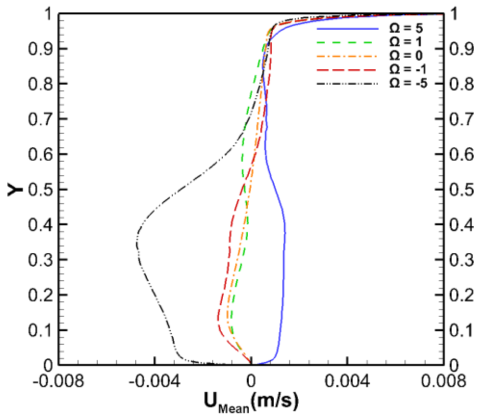

(b) Re = 10,000 and ϕ = 0

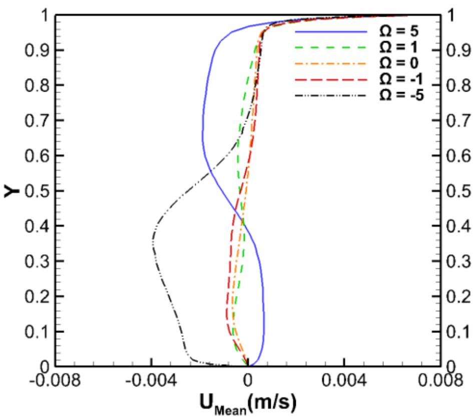

(c) Re = 5,000 and ϕ = 0.025

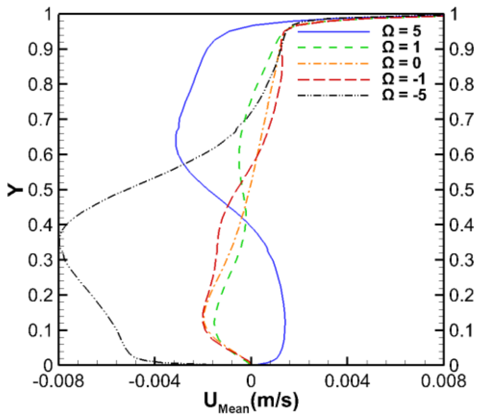

(d) Re = 10,000 and ϕ = 0.025

Figure 6-17: Mean velocity profiles at vertical lines.

6.3.2.3 Wall shear stress

The wall shear stress can be calculated from the dynamic viscosity of the fluid multiplied by the fluid velocity gradient at the wall. The variations in the wall shear stress at the moving top wall and the heated bottom wall for the selected rotational cylinder speeds and directions for the two Reynolds number values are shown in Figure 6-18. Clearly, at the top wall for both Reynolds numbers and a rotational speed within the range -1 ≤ Ω ≤ 5, the wall shear stress values are essentially unchanged. This is due to the fact that, either a speed or direction change of the rotational cylinder could not affect the velocity profiles in the boundary layers near the top wall significantly. A noticeable effect was observed when the rotational speed became -5, suggesting that the boundary layer profile due to the top lid movement is now somewhat affected by the fluid motion due to the cylinder rotation.

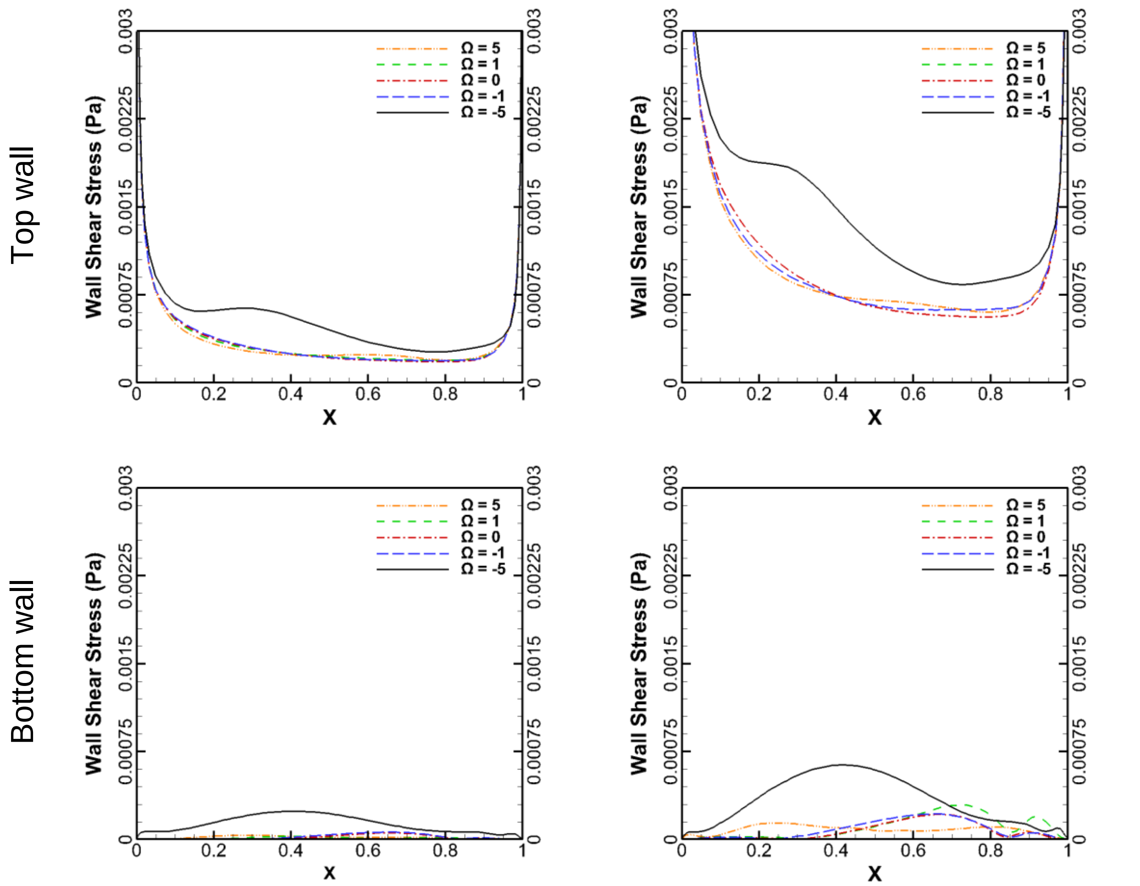

(a) Re = 5,000 (b) Re = 10,000

Figure 6-18: Wall shear stress profiles for different rotational speeds and Reynolds numbers at the top and bottom walls.

On the other hand, at the bottom wall, the wall shear stress is less affected by the moving top wall, and the rotational cylinder plays a leading role in bottom wall shear stress. As a result, the wall shear distributions show certain variations for different rotation speeds and directions, reaching their maximum effect when the rotational speed reached -5. Clearly, the overall shear stress levels at the bottom wall are much lower in comparison to the top wall. Furthermore, the wall shear stresses are linked closely to the heat transfer coefficients, which will be discussed in more detail in section 6.3.2.5.

6.3.2.4 Turbulence kinetic energy

It is well known that the root mean square (RMS) calculation of the fluid velocity fluctuations is defined as the turbulence kinetic energy (TKE), which represents the kinetic energy of the fluid motion per unit mass associated with the turbulent eddies. The TKE profiles at the two selected positions, one at the mid-height between the centre of the cylinder and the bottom wall (y = 0.25) and the other at the mid-height between the cylinder centre and the top wall (y = 0.75) are shown in Figure 6-19, which illustrates the effects of changing the cylinder at rotational speeds and directions for the two Reynolds number values of Re = 5,000, and 10,000. The simulated results indicate that for both Reynolds numbers, the TKE trend behaviours are more or less the same as for the corresponding rotational speed, though their magnitudes increase significantly as the Reynolds number increases from 5,000 to 10,000. At either Reynolds number, it can be determined that the rotating cylinder has a substantial effect on the TKE profiles, especially with the rotational speed being -5 at y = 0.25 and with rotational speeds being of 5 and -5 at y, x = 0.75.

6.3.2.5 Nusselt number

It is widely recognised that heat transfer can be rapidly enhanced by involving turbulent flow, unlike when the flow is laminar, which can develop an insulating blanket near the solid walls Saha*, et al.* [154]. Any intermixing of the fluid would not happen when the flow motion is slow because the boundary layer velocity reduces smoothly due to the viscous drag, which can lead the heat transfer relying only on molecular convection and conduction.

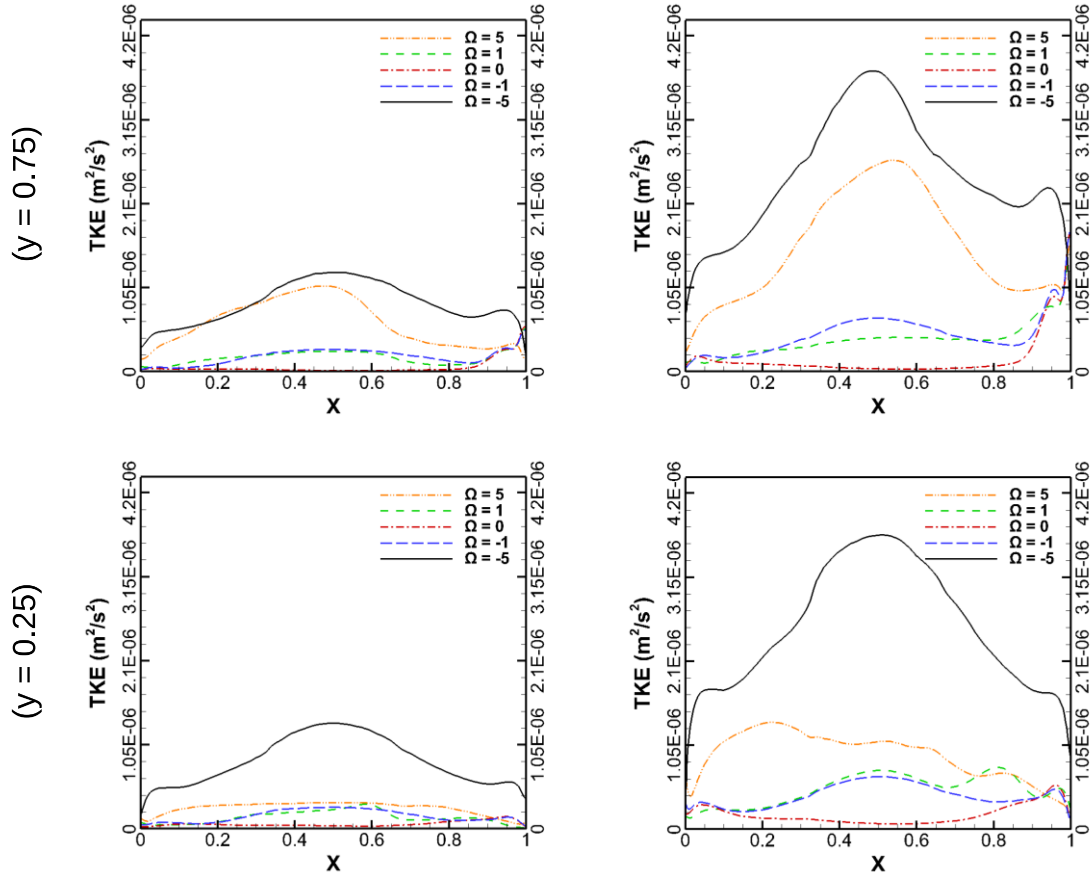

(a) Re = 5,000 (b) Re = 10,000

Figure 6-19: Turbulence kinetic energy profiles for different rotational speeds and Reynolds numbers.

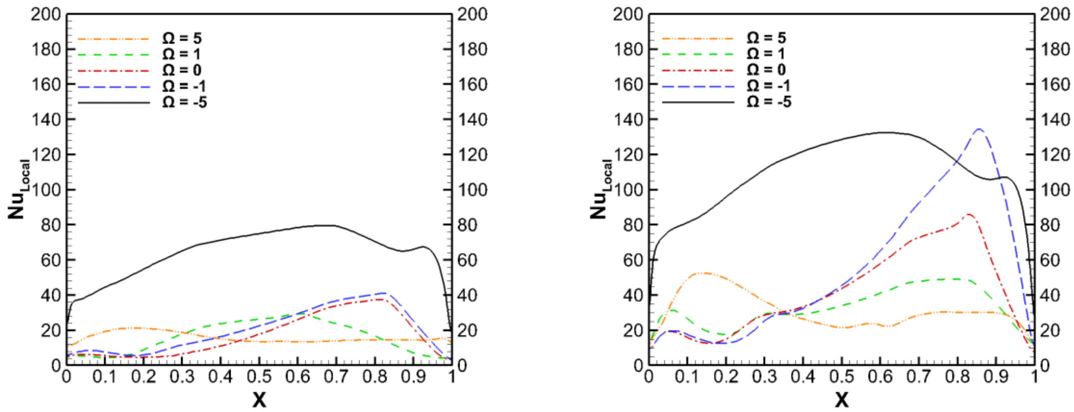

(a) Re = 5,000 and $\phi = 0$ (b) Re = 10,000 and $\phi = 0$

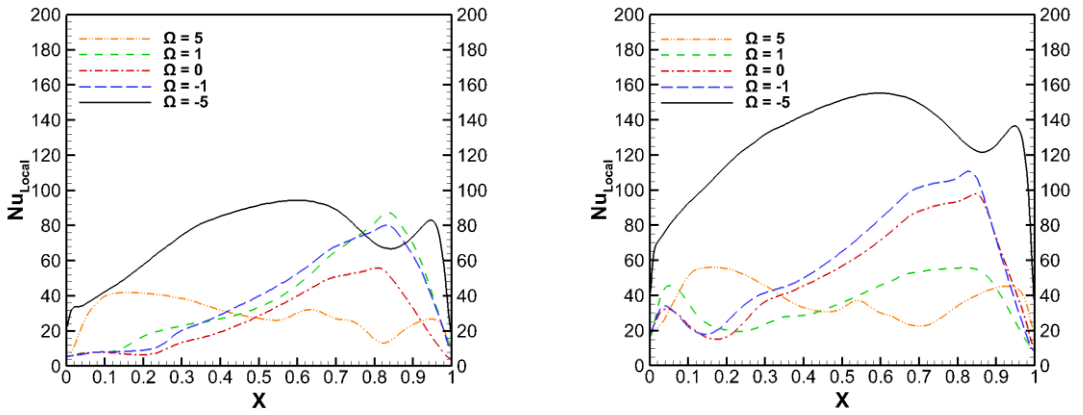

(c) Re = 5,000 and ϕ = 0.025 (d) Re = 10,000 and ϕ = 0.025

Figure 6-20: Local Nusselt numbers at the bottom wall for pure fluid and nanofluid.

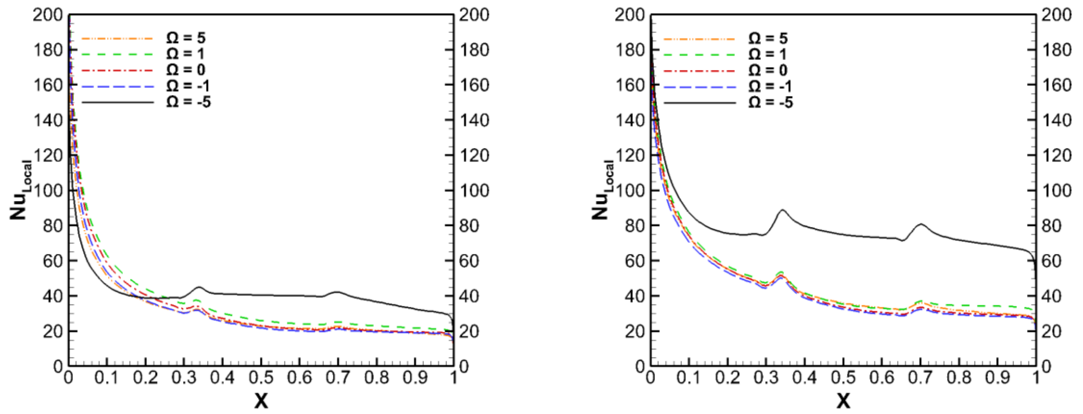

(a) Re = 5,000 and ϕ = 0 (b) Re = 10,000 and ϕ = 0

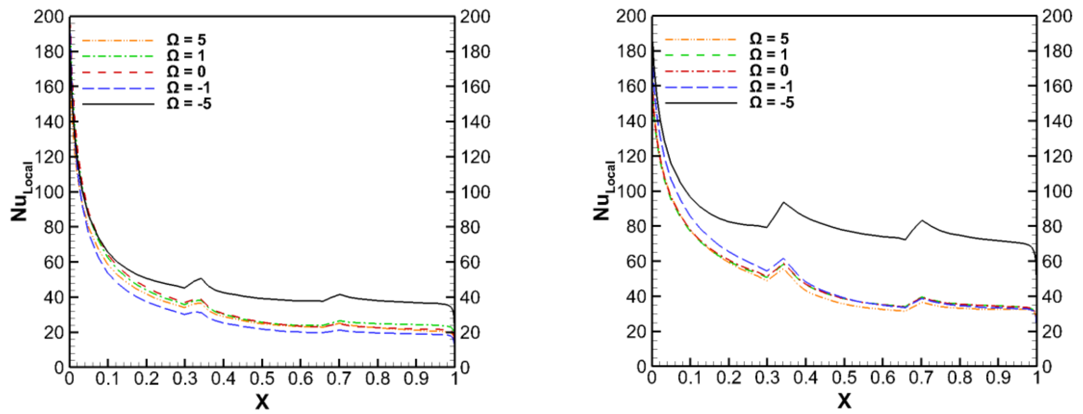

(c) Re = 5,000 and ϕ = 0.025 (d) Re = 10,000 and ϕ = 0.025

Figure 6-21: Local Nusselt numbers at the top moving wall for pure fluid and nanofluid.

By contrast, the heat transfer rate can be enhanced significantly by incrementing the fluid velocity, which generates turbulent vortices where the boundary layers break away from the cavity walls and mix with the bulk of the fluid further from the obstructed enclosure walls Choi*, et al.* [35]. Figure 6-20 and Figure 6-21 illustrate the local Nusselt number distributions for pure water and the nanofluid for the selected Reynolds numbers, Re = 5,000 and 10,000, and rotational speeds, $-5 \leq \Omega \leq 5$, for turbulent flow condition at the midlines of the bottom and top walls, respectively. For both Reynolds numbers, the bottom wall Nusselt numbers are affected by changing either the rotational speed or the rotational direction. The combined motion of the moving top wall and rotating cylinder provide for higher local Nusselt numbers at the bottom wall, particularly when the rotational speed is -5. On the other hand, the influences of the rotational speed on the moving top wall for both Reynolds numbers are less remarkable unless the rotational speed is -5, as the heat transfer characteristics in this region are mainly controlled by the fluid motion due to the wall movement. It is worth noting that the heat transfer distributions at the top and bottom walls bear a close resemblance to the wall shear profiles, as discussed in section 6.3.2.3, which can be explained by the well-known Reynolds analogy between heat and momentum transfer. Both the top and bottom wall Nusselt numbers for pure water and the nanofluid at different Reynolds numbers and rotational speeds are compared in Table 6-1 to quantify the nanofluid's effect on the heat transfer coefficient. It can be observed that for all different Reynolds numbers and rotational speed cases, the effects of the nanofluid on the heat transfer coefficients were always positive, and were more visible at the bottom wall than at the top wall.

Table 6-1: Average Nusselt numbers comparison between pure fluid and nanofluid at the top and bottom walls.

Rotational speed		Ω = -5	Ω = -1	Ω = 0	Ω = 1	Ω = 5
Top	Nu_{nf}/Nu_{H2O} (Re = 5,000)	59.97/55.41 = 1.08	50.24/41.76 = 1.20	47.11/44.77 = 1.05	46.99/47.85 = 0.98	42.78/39.74 = 1.07
	Nu_{nf}/Nu_{H2O} (Re = 10,000)	87.85/84.20 = 1.04	58.63/50.39 = 1.16	55.65/53.17 = 1.04	55.29/55.89 = 0.98	54.00/53.24 = 1.01
Bottom	Nu_{nf}/Nu_{H2O} (Re = 5,000)	63.92/56.83 = 1.12	31.83/17.14 = 1.85	21.74/14.26 = 1.52	31.92/14.40 = 2.21	25.14/14.85 = 1.69
	Nu_{nf}/Nu_{H2O} (Re = 10,000)	113.48/96.00 = 1.18	32.23/28.96 = 1.11	50.31/34.98 = 1.43	45.76/44.82 = 2.02	33.44/26.80 = 1.24

6.4 Conclusion

The three-dimensional problem of turbulent flow within the lid-driven cubical enclosure, which is differentially heated and contains a rotating cylinder, is addressed by involving both pure water and nanofluid and simulated by using the finite volume method. The influences of various values of both the rotational speed and direction of the circular cylinder and the Reynolds number are examined, and the striking performances of the URANS and LES approaches are scrutinized. The simulations cover a range of cylinder rotation speeds, $-5 \leq \Omega \leq 10$, and Reynolds numbers, Re = 5,000, 10,000, 15,000 and 30,000. The currently acquired outcomes have revealed interesting behaviours of the turbulent flow and thermal fields in the obstructed enclosure, and the following are the itemized observations from the present research:

- The temperature distributions and flow patterns are found to be influenced by both the speeds and the directions of the cylinder rotation, and nanofluid is always positively effective on the heat transfer enhancement.
- The highest value of Nusselt number occurs at the highest Reynolds number and rotational speed because of the high increment in the fluid motion.
- The bottom wall shear stress can be influenced by both the rotational speeds and Reynolds numbers, whereas the top wall shear stress values remain roughly the same for different rotational speeds and directions, except for $\Omega = -5$.
- For the stationary cylinder, $\Omega = 0$, the flow is mainly driven by the moving top wall, and is assisted by the buoyancy effect due to the temperature differences between the top and bottom walls. The central main eddy (clockwise) controls most of the domain, whilst the secondary vortices are shown clearly at the corners of the enclosure, particularly by the LES approach.
- For $\Omega = 1$, it is observed that the rotating cylinder has gained control over the regions surrounding the cylinder by creating an eddy that is circumscribed about the proximity of the cylinder. Many secondary vortices appear in this case because of the opposite direction actions by the moving top wall and the rotating cylinder.
- However, when the rotational speed is increased to five, it is noticed that the rotating cylinder dominates more regions than the moving top wall and the buoyancy induced flow. Herein, the primary vortex (anticlockwise) is led by

the forced rotational movement and the number of the secondary vortices is increased as a result of the increment in the flow movement.

- For all the Reynolds number values reported here, it is shown that the effects of the rotational speeds, $1 \leq \Omega \leq 10$, are remarkable on the Nusselt number on the cool bottom wall, but their effects on the top moving wall can be neglected unless the rotational speed reaches 10.
- When Ω = -5, the lowest number of secondary eddies was found and the highest Nusselt number observed, especially in the case of the latter when the nanofluid was involved, unlike when Ω = 5 where the highest number of secondary vortices was produced.
- The cylinder rotation speed has a weaker influence on the top wall than on the bottom wall, where the largest difference in bottom wall Nusselt number between the conventional fluid and the nanofluid was found at a rotational speed of Ω = 1.
- In all cases of different Reynolds numbers and rotational speeds, it is demonstrated convincingly that the LES method can capture more detailed secondary eddies than the URANS model.

Chapter 7 Mixed convection of a 3D lid-driven cavity containing a rotating cylinder and a heated wall with artificial roughness

7.1 Motivation and introduction

Applying a new force on a mixed convection of a 3D top wall lid-driven cavity containing a clockwise and anticlockwise rotating cylinder could help to increase the convection heat transfer performance. It is noticed from the literature survey, and to the best of the authors' knowledge, that the experimental and numerical investigations mostly concentrate on different rib shapes and their optimization. Even though the artificial roughness has an incredibly positive impact on the convection heat transfer enhancement, it has not been sufficiently used in practice. Ultimately, no effort has been made to enhance the heat transfer performance of lid-driven cavities using different shaped artificial ribs and then comparing them with the smooth/traditional bottom wall cases of turbulent mixed convection using the URANS method. In addition, combining three different forces like lid-driven, rotating cylinder and artificial roughness besides the buoyancy force of heat difference, is totally new. As well as, involving two different rib shapes and heights with the presence of clockwise and anticlockwise rotating cylinder at two high Reynolds numbers has not been completed in the literature.

Therefore, the main aim of this chapter is to comprehensively analyse and understand the heat transfer process using a roughened, heated bottom wall with two artificial rib types (R-s and R-c) due to unsteady mixed convection in a 3D moving top wall enclosure that has a central rotating cylinder, and to compare these cases with the smooth bottom wall case. These different cases (roughened and smooth bottom walls) are considered at various clockwise and anticlockwise rotational speeds, $-5 \leq \Omega \leq 5$, and Reynolds numbers of 5,000 and 10,000. The top and bottom walls of the cavity are differentially heated, whilst the remaining cavity walls are assumed to be stationary and adiabatic. A standard *k-ε* model for the Unsteady Reynolds-Averaged Navier-Stokes (URANS) equations is used to deal with the turbulent flow. The heat transfer improvement is carefully considered and analysed through the detailed examinations of the flow and thermal fields, the mean velocity profiles, the wall shear stresses, the turbulence kinetic energy and the local and average Nusselt numbers. Overall, heat transfer enhancement has been achieved with the numerical model developed in this chapter. A journal paper has been published from the achievement of this study [174] besides a conference paper [175].

7.2 Numerical model

7.2.1 Physical model

Figure 7-1 shows three 3D sketches of different bottom wall conditions for the same top wall lid-driven obstructed enclosure, which includes a thermally insulated rotating cylinder with diameter, d = 0.2L. The roughness parameters are represented by the rib heights (e) of 10 or 5 mm, rib pitch (p) of 90 mm, relative roughness height (e/D_h) of 0.01 or 0.02, and relative roughness pitch (p/e) of 9. Three different cases are involved in this research, namely those of case 1, (S), which indicates a smooth bottom wall, case 2, (R-s), which indicates the square roughened ribs on the bottom wall with a rib height of 10 mm, and case 3, (R-c), which indicates the half-circle roughened ribs on the bottom wall with a rib height of 5 mm.

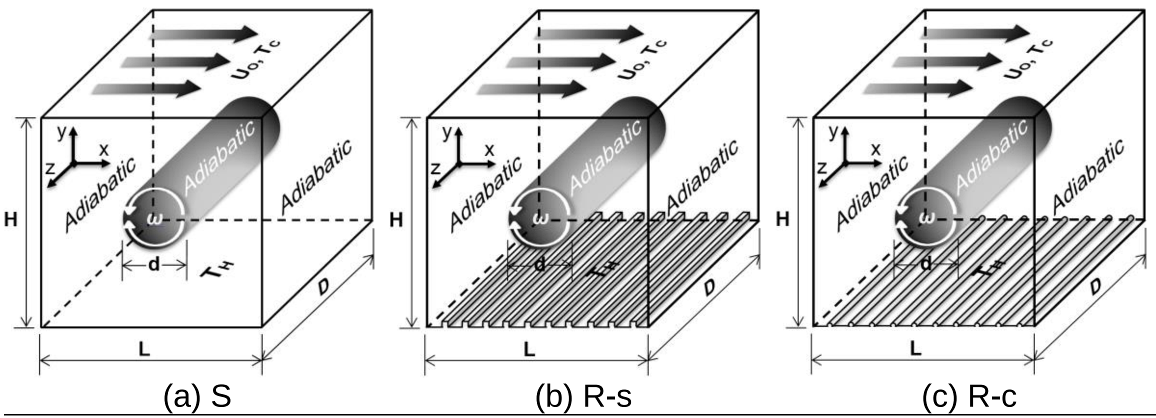

Figure 7-1: The schematic diagrams of the lid-driven cavity containing a rotating cylinder in the cases of (a) S, (b) R-s and (c) R-c.

7.2.2 Boundary conditions

The boundary conditions for the present models are shown as follows; the top wall is a cold moving wall at uniform velocity ($T = T_C,\ U = U_0,\ V = 0,\ W = 0$). Whereas, the sidewalls, rear wall and front wall of the geometry are defined as adiabatic and motionless plates ($U = V = W = 0$). The central horizontal cylinder is adiabatic and rotating object at uniform rotational speeds and different rotational directions ($\omega = (\Omega \times 2U_0) / d,\ d = 0.2L$). Finally, the bottom walls of all different cases (S, R-s and R-c) are stationary and hot walls ($T = T_H,\ U = V = W = 0$).

7.2.3 Numerical procedure

The lid-driven cavity was filled with H_2O as the convective fluid with regards to studying the mixed convection heat transfer enhancement due to applying two artificial roughness shapes on the heated bottom wall of the domain, and comparing these to the smooth heated bottom wall. The equations governing the heat and momentum transfer and the pressure-velocity coupling equations were solved by employing the finite volume method (FVM) and SIMPLEC algorithm of the commercial CFD code ANSYS©FLUENT (version R16.2) [139]. The convection and time evolution terms were completed by engaging the QUICK scheme and the implicit second-order scheme, respectively. The standard k-ε turbulence model was employed in the URANS solver. The convergence criteria of the simulations were chosen to be 10^{-5} to obtain the high-accuracy results.

7.2.4 Grid independence test

Obtaining the most suitable meshes for the present domains has been carefully considered in order to gain high accuracy results. Hexahedral grids are used to discretise the domains as demonstrated in Figure 7-2. Refined meshes have been used to cover the closest layers to the cubic walls, particularly the artificially roughened areas. Since different domains are used in this research, three grid independence tests are completed that use the standard k-ε model of the URANS method at a Reynolds number of 5,000 and a rotational cylinder speed of zero. A non-dimensional time step of 0.004 and the dimensionless wall distance of about 1 were used in this research. The first grid independence test was carried out for the smooth bottom wall domain case, (S) as presented in Figure 7-3a. Five mesh numbers were examined for this domain in order to obtain the best mesh quality, which were 125,868, 292,440, 496,800, 928,160 and 1,260,762. The most suitable mesh number of 928,160 was chosen in terms of the obtained data quality and a reasonable overall simulation time. The second grid independence test was accomplished for the roughened bottom wall case, R-s as shown in Figure 7-3b. Capturing most of the heat transfer in the region of the artificial ribs required the use of a large mesh number. Several mesh numbers were tested and the most appropriate mesh number of 2,204,532 was selected. Finally, for the third case, R-c, a mesh number of 2,505,294 was chosen, which gave the most appropriate results as exposed in Figure 7-3c.

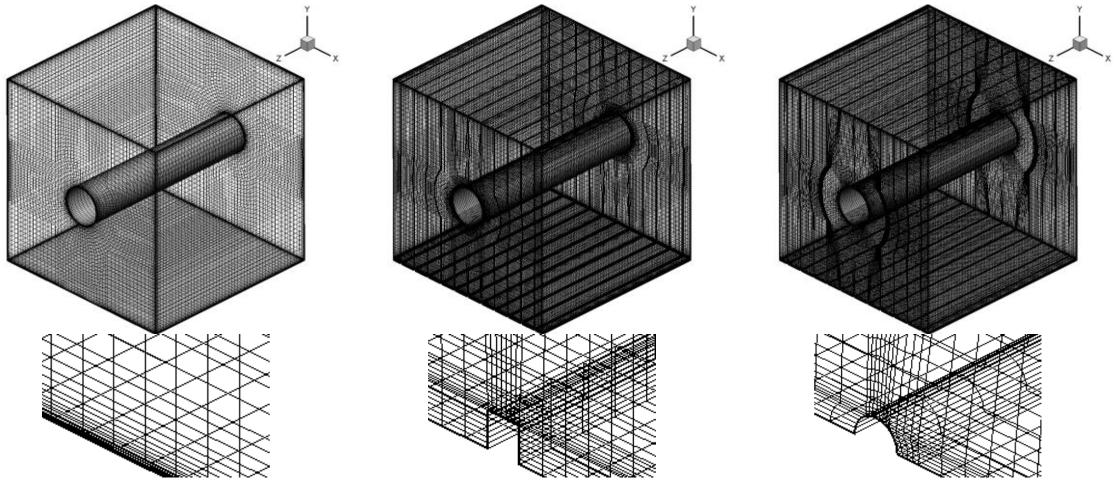

(a) S (b) R-s (c) R-c

Figure 7-2: Computational mesh of the lid-driven cavity containing a rotating cylinder in the cases of (a) S, (b) R-s and (c) R-c.

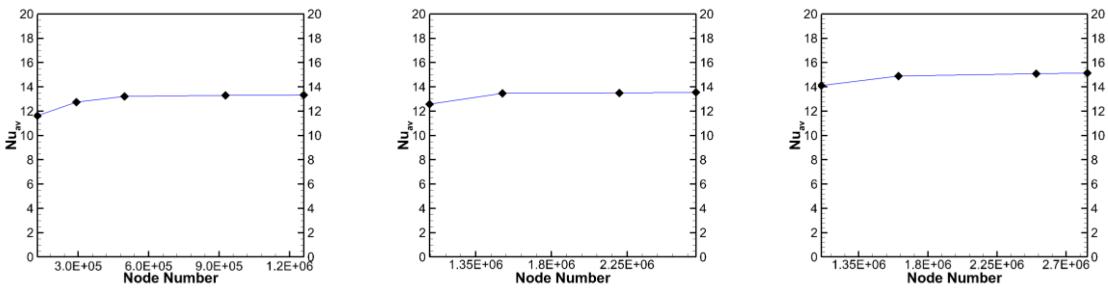

(a) S (b) R-s (c) R-c

Figure 7-3: Convergence of the average Nusselt number on the bottom wall at Reynolds number of 5,000 and rotational speed of 0 with grid refinement in the cases of (a) S, (b) R-s and (c) R-c.

In addition, it is known that the RANS (Reynolds-Averaged Navier-Stokes) method models all of the turbulent fluctuations in the flow. However, using the appropriate mesh number and structure can help enhance the quality of the result. In the current research, the meshes close to the solid walls have been refined carefully besides using the near wall function, which ensures to provide the accurate resolution of the flow variables across the near wall layers, as shown in Table 7-1.

Table 7-1: Grid sensitivity study against the average Nusselt number on the bottom wall at Reynolds number of 5,000 and rotational speed of 0.

Case, S	Grid1	Grid2	Grid3	Grid4	Grid5
Mesh number	125,868	292,440	496,800	928,160	1,260,762
Nu_{av} (bottom wall)	11.6386	12.7467	13.2308	13.2997	13.3245
Case, R-s					
Mesh number	1,074,950	1,509,485	2,204,532	2,659,392	-
Nu_{av} (bottom wall)	12.5899	13.4704	13.5096	13.5493	-
Case, R-c					
Mesh number	1,105,984	1,608,543	2,505,294	2,838,579	-
Nu_{av} (bottom wall)	14.1085	14.9045	15.0813	15.1594	-

7.3 Results and discussion

The simulation results for the unsteady turbulent mixed convective fluid flow and heat transfer within a 3D enclosed geometry with a top lid-driven wall and rotating central cylinder located horizontally within the cavity with an artificially roughened heated bottom wall were analysed in this section for two Reynolds numbers, 5,000 and 10,000, and for rotational speeds of the cylinder in the range of $-5 \leq \Omega \leq 5$. Two different artificial rib shapes, square (R-s) and half-circle (R-c), were studied and compared to the smooth bottom wall case. The flow and thermal fields, the mean velocity profiles, the wall shear stresses, the turbulence kinetic energy and the Nusselt numbers were presented as the results of this research. The numerical solver of the current research has been validated in contradiction of various similar published results of Chatterjee*, et al.* [62], Sharif [161], Chen and Cheng [162], Alinia*, et al.* [91], Prasad and Koseff [163], Padilla*, et al.* [165], and Peng, *et al.* [164] respecting to reach the necessities of running new simulations. However, further details have been released about the validation part in section 3.8.

7.3.1 Flow and thermal field

Two different comparisons are presented here, the first of which was to compare the effect of two rib shapes (R-s and R-c) of diverse roughness on the heated bottom wall with that of a heated smooth bottom wall (S) at a Reynolds number of 5,000. The second comparison was completed for the square ribs (R-s) on the heated bottom wall against a smooth heated bottom wall at two Reynolds numbers, 5,000 and 10,000. Figure 7-4 and Figure 7-5 illustrated the isotherm, streamline and velocity magnitude slides within the domain at a z-axis value of 0.05, as well as Figure 7-6, which shows the isosurface temperatures in order to understand the flow and heat transfer distribution for different bottom wall roughnesses and rotational speeds and directions, in the range of $-5 \leq \Omega \leq 5$, of the cylinder. Broadly, it was demonstrated that the use of any artificially roughened wall type can significantly affect the turbulent fluid flow and heat transfer distribution when the cylinder was rotating in either direction and at any speed. When the rotational speed, Ω, was set equal to zero, it can be seen from both figures showing the isotherms and streamlines that the fluid flow and heat distribution due to each of the different bottom wall conditions have roughly the same behaviour; in other words, the presence of the roughness was not clearly effective on the fluid flow patterns, therefore only one clockwise main vortex can be seen which covers the whole domain. This phenomenon was thought to occur due to low fluid flow circulation in the region of the bottom wall; when the cylinder rotates, however, this can help increase the influence of the artificial ribs on the turbulent flow. Moreover, even though the artificial ribs have different heights (5 and 10 mm), it can be observed that both the square (R-s, 10 mm) and the half-circle (R-c, 5 mm) ribs have nearly the same effect on the fluid flow and heat transfer when the cylinder direction favours the moving top wall motion, $\Omega = -1$ or -5. This could explain the domination effects of the rotational cylinder over that of the artificial roughness. However, the shapes of the roughened ribs dominate the fluid flow and heat distribution effects when the rotational cylinder direction opposes the direction of motion of the moving top wall, Ω = 1 or 5.

Concentrating on the zoomed section (Figure 7-5) of the bottom wall cases with regard to the streamlines can help understand the main reason behind the dramatic heat transfer enhancement due to the use of the two rib configurations. Increasing the heated surface area by artificially roughening it can help enhance the heat transfer rate in addition to the main reason for the increased heat transfer augmentation, which is the physical effect of the artificial ribs on the turbulent fluid flow behaviour. The secondary vortex often causes a positive vorticity, when it is quickly engulfed by the main vortex. Finally, it can be seen that the rib shapes for the R-s case could create more isolated vortices in the region on the sides of the ribs, unlike the rib shapes of the R-c case.

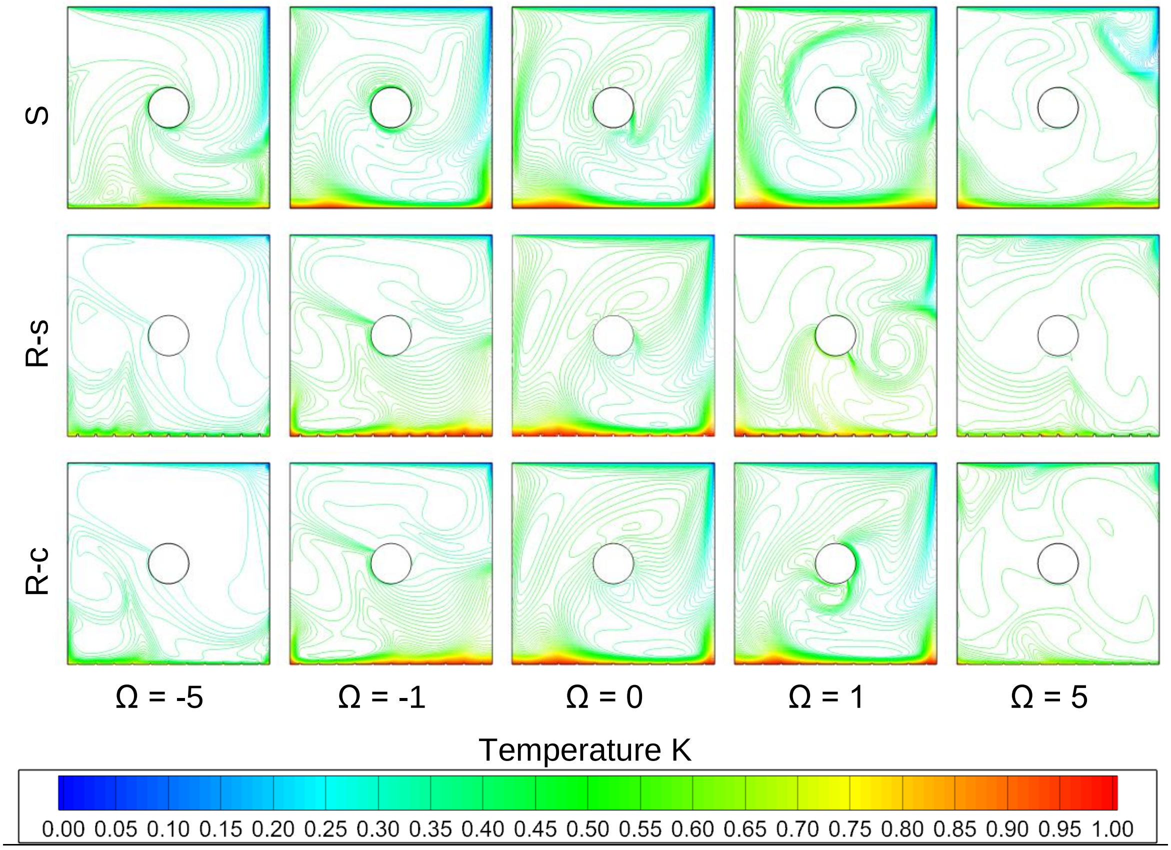

Figure 7-4: The isotherm contour comparison for different bottom wall conditions, (a) S, (b) R-s and (c) R-c, at Re = 5,000 and -5 ≤ Ω ≤ 5.

The results for the two different Reynolds numbers, 5,000 and 10,000, in order to compare the roughened bottom wall (R-s) with the smooth bottom wall (S) concerning the impacts of high velocity of the flow movement within the domain under various conditions, are shown in Figure 7-7, Figure 7-8 and Figure 7-9 in terms of isotherm, streamline and velocity magnitude slides, and isosurface temperatures, respectively. Briefly, increasing the Reynolds number for either the smooth bottom wall (S) cavity or the roughened bottom wall (R-s) cavity has a particularly significant impact on the secondary eddy sizes and circulation fluid flow speeds.

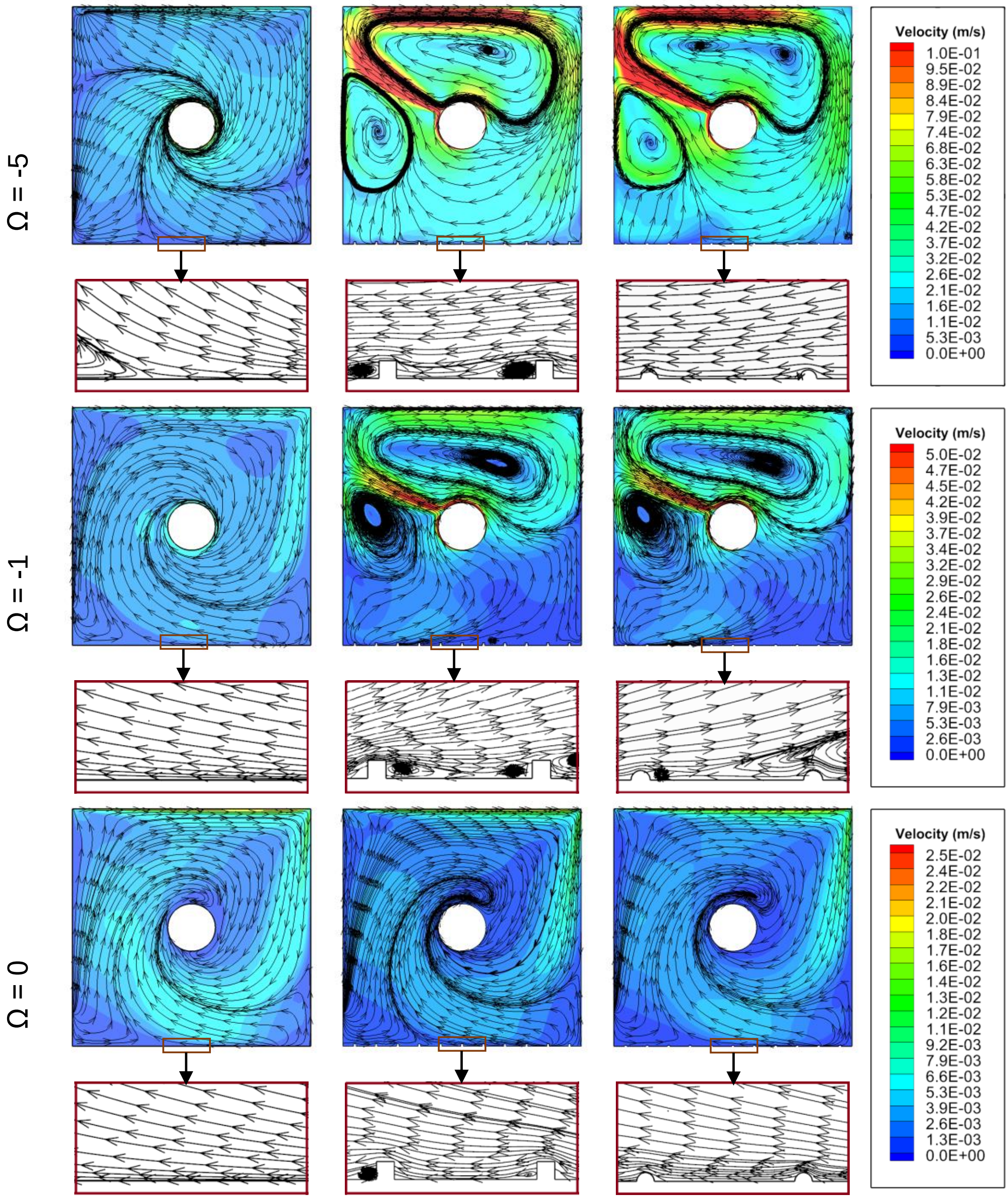

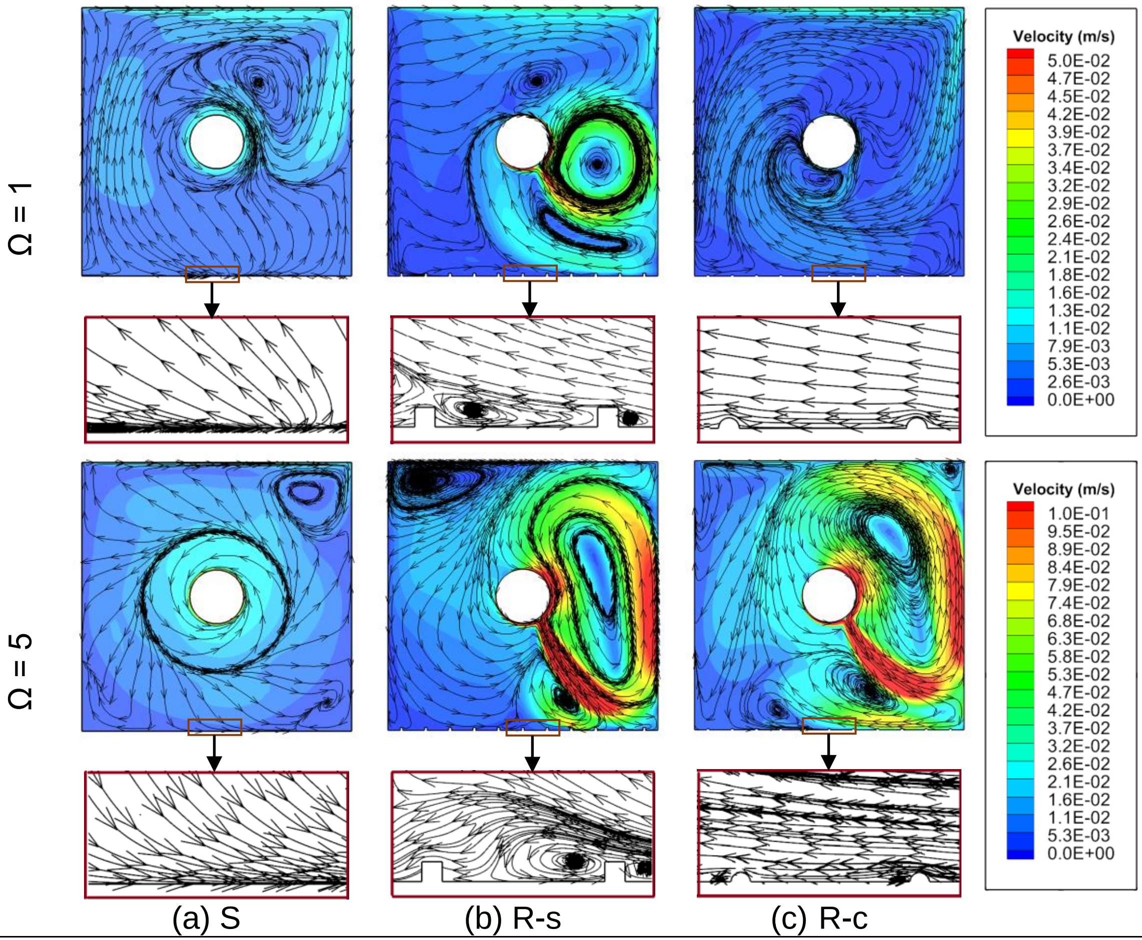

Figure 7-5: Comparison of the streamline and velocity magnatude contours and their zoomed bottom wall sections for different bottom wall conditions, (a) S, (b) R-s and (c) R-c, at Re = 5,000 and -5 ≤ Ω ≤ 5.

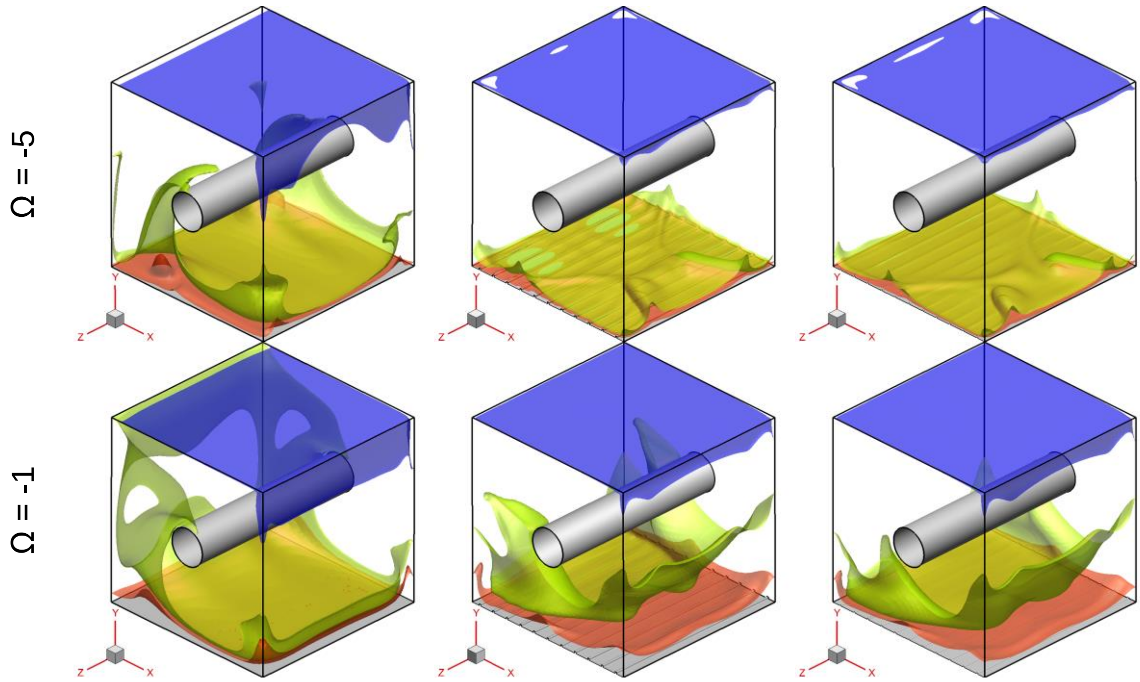

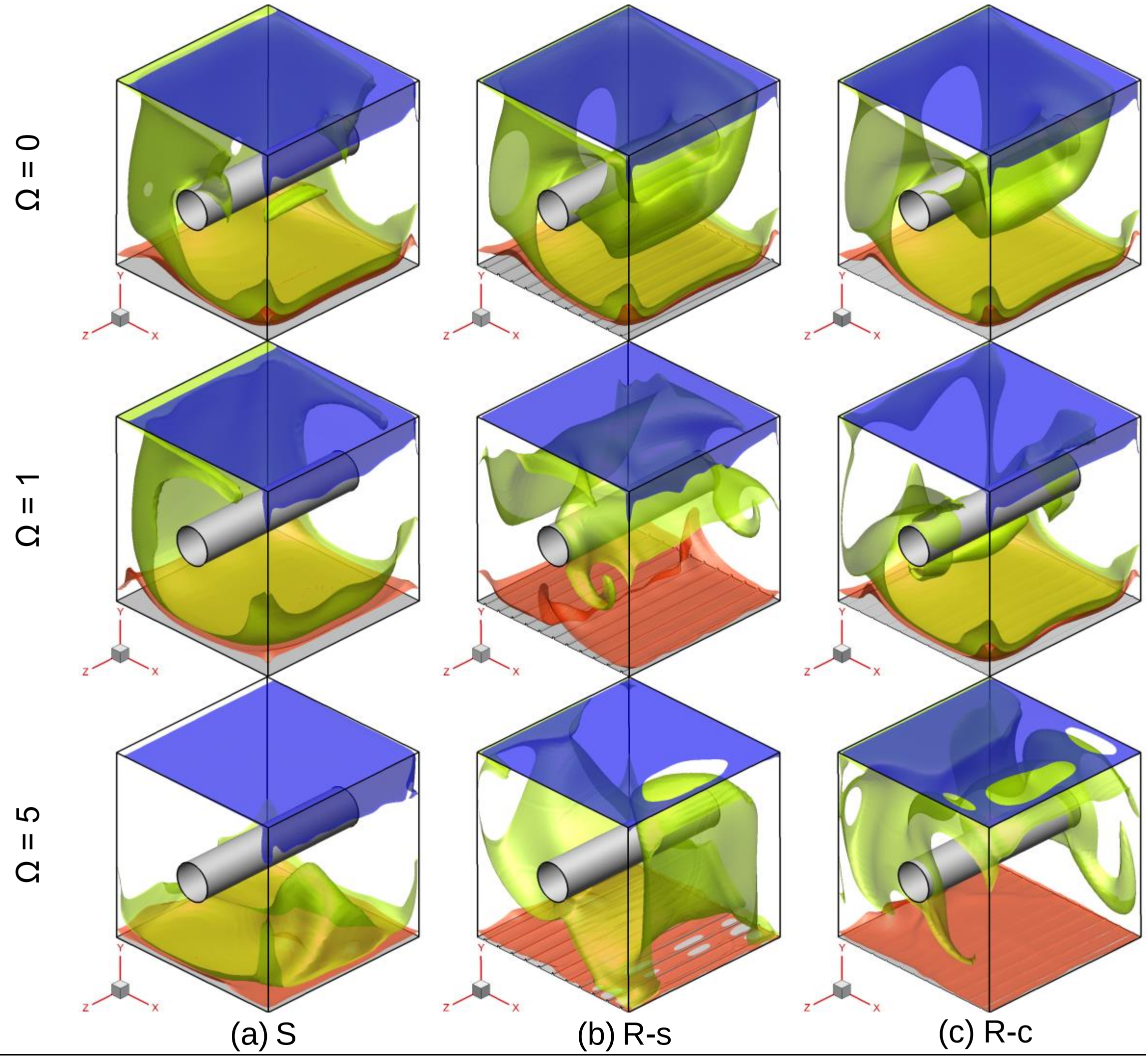

Figure 7-6: Comparison of the three-dimensional isosurface profiles for different bottom wall conditions, (a) S, (b) R-s and (c) R-c, at Re = 5,000 and -5 ≤ Ω ≤ 5

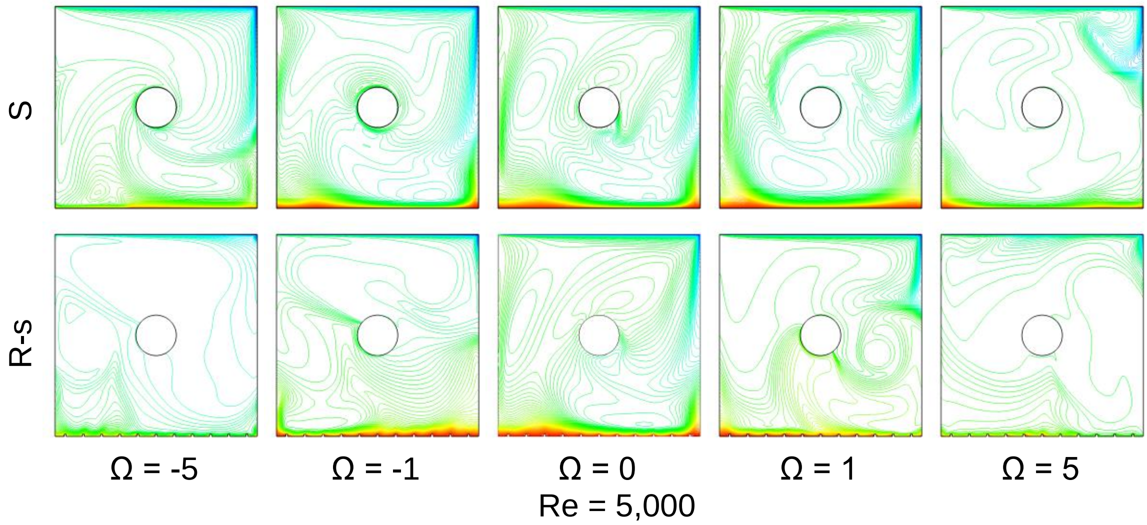

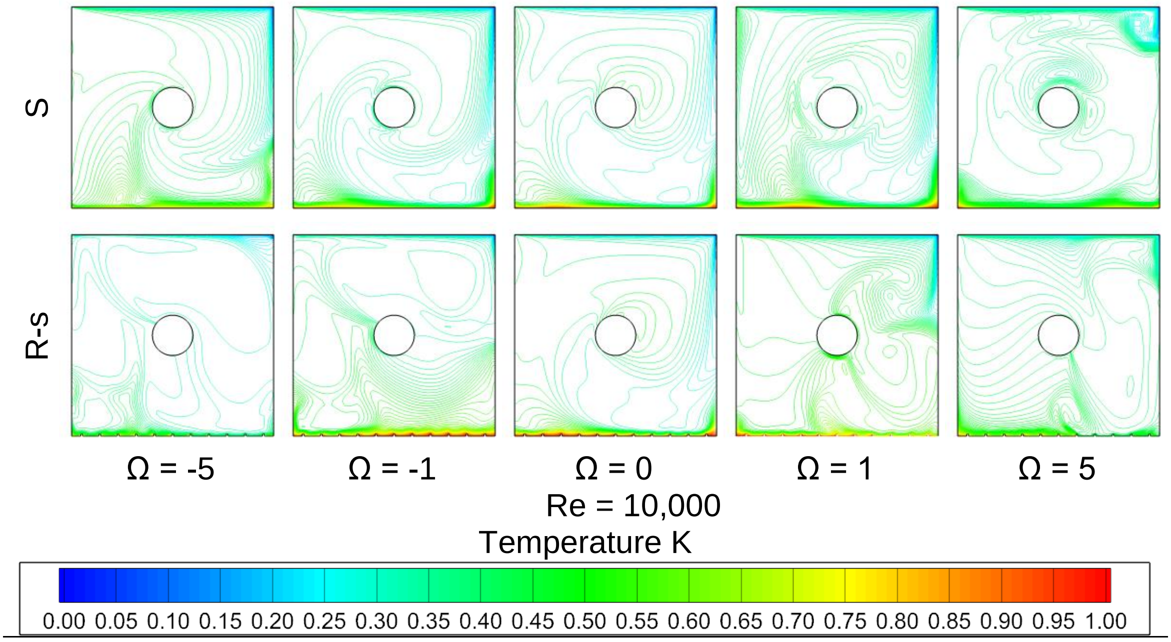

Figure 7-7: The isotherm and streamline contours for different Reynolds numbers, 5,000 and 10,000, and bottom wall conditions (S, R-s and R-c), at -5 ≤ Ω ≤ 5.

7.3.2 Mean velocity profile

The mean velocity profiles along the line between the two points, 0.25, 0.0, 0.5 and 0.25, 1.0, 0.5, is analysed in this section for different heated bottom wall cases (R-s, R-c and S) as shown in Figure 7-10. The main aim here is to compare the impacts of two different rib shapes on the bottom wall of the enclosure with the smooth bottom wall case on the mean velocity profiles at a Reynolds number of 5,000 and various rotational speeds and directions of the cylinder. It can be noted that both rib shapes are relatively ineffective when the cylinder is motionless, while major effects can be observed when the cylinder moves in any direction or at any speed. In addition, at Ω = -1 or -5, both rib shapes have similar effects on the mean velocity profiles, whereas at Ω = 1 or 5, there are clearly observed differences in the mean velocity profile behavours as a result of directly involving the roughness in the fluid flow, as mentioned in section 7.3.1 in connection with the roughness of the wall and the rotational state of the cylinder. Similar mean velocity distributions with higher values have been found, as shown in Figure 7-11, when the Reynolds number is increased from 5,000 to 10,000.

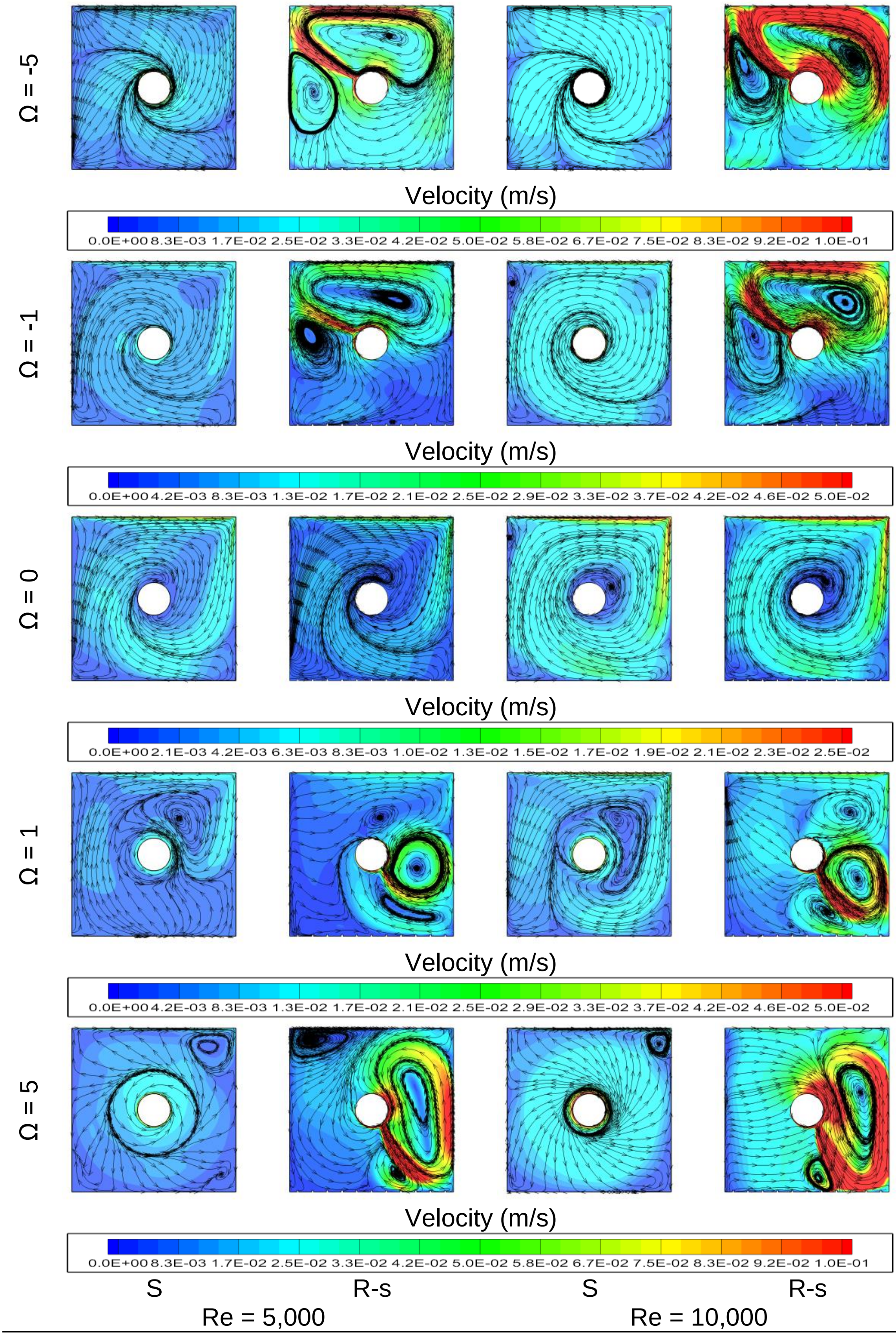

Figure 7-8: The streamline and velocity magnitude contours for different Reynolds numbers, 5,000 and 10,000, and bottom wall conditions (S, R-s and R-c), at $-5 \le \Omega \le 5$.

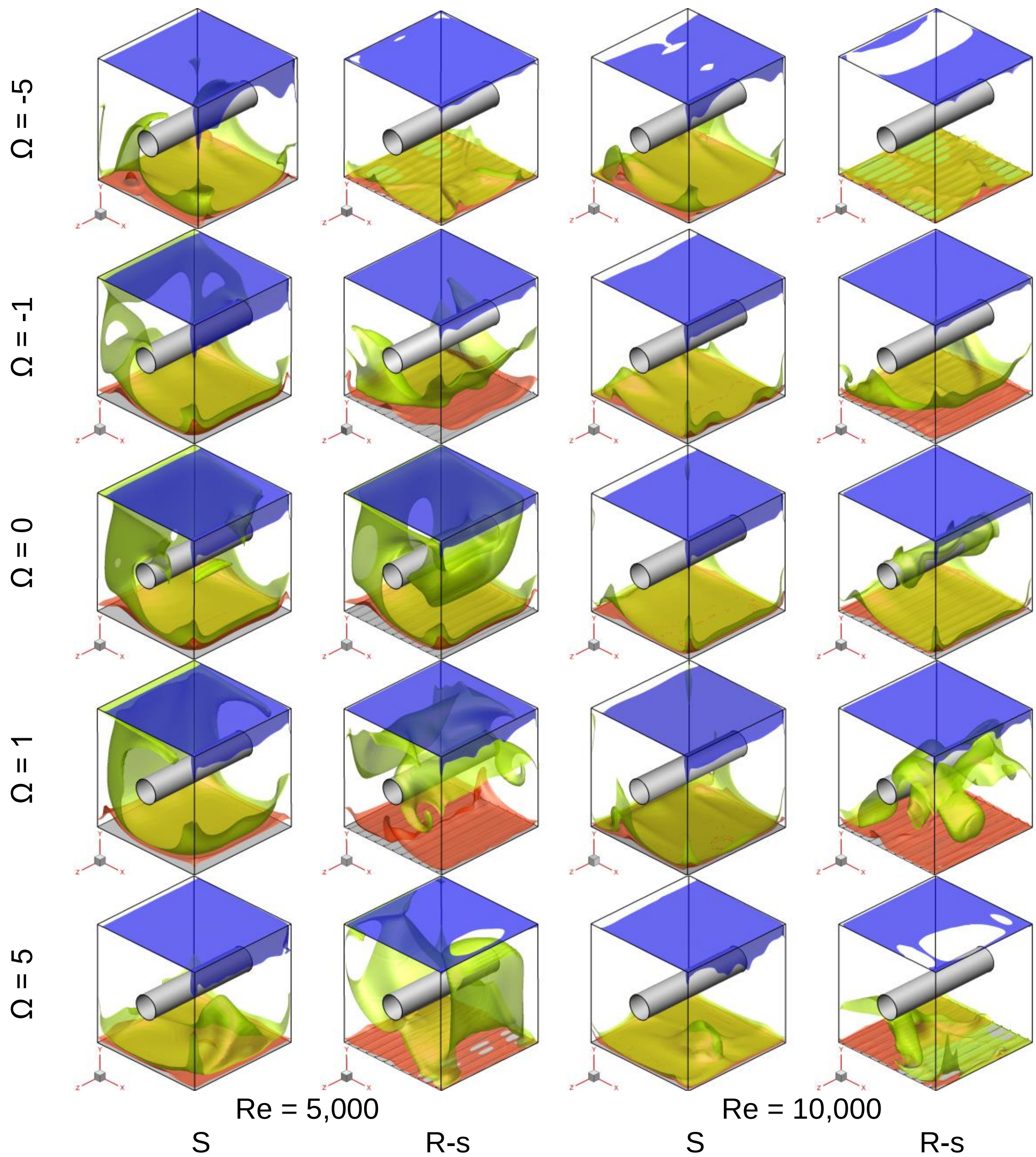

Figure 7-9: Comparison of the three-dimensional isosurface profiles for different Reynolds numbers, 5,000 and 10,000, and bottom wall conditions (S and R-s), at -5 ≤ Ω ≤ 5.

7.3.3 Wall shear stress

Diverse cases studying the wall shear stresses on the moving top wall were completed for various clockwise and anticlockwise rotational speeds of the horizontal cylinder inside the domain. Since there is a connection between the momentum of the cylinder and the heat transfer, analysing the differences using two different artificial roughness shapes on the bottom wall and comparing to the smooth bottom wall case were carried out at different rotational speeds, -5 ≤ Ω ≤

5, and Reynolds numbers, 5,000 and 10,000. The impacts of using different heated bottom wall conditions (R-s, R-c and S) on the wall shear stresses at a Reynolds number of 5,000, and rotational speeds of -5 ≤ Ω ≤ 5 are presented in Figure 7-12. Firstly, when the rotational speed is equal to 0 or 1, it can be clearly seen that roughly the same conducts and values for the wall shear stress curves were found.

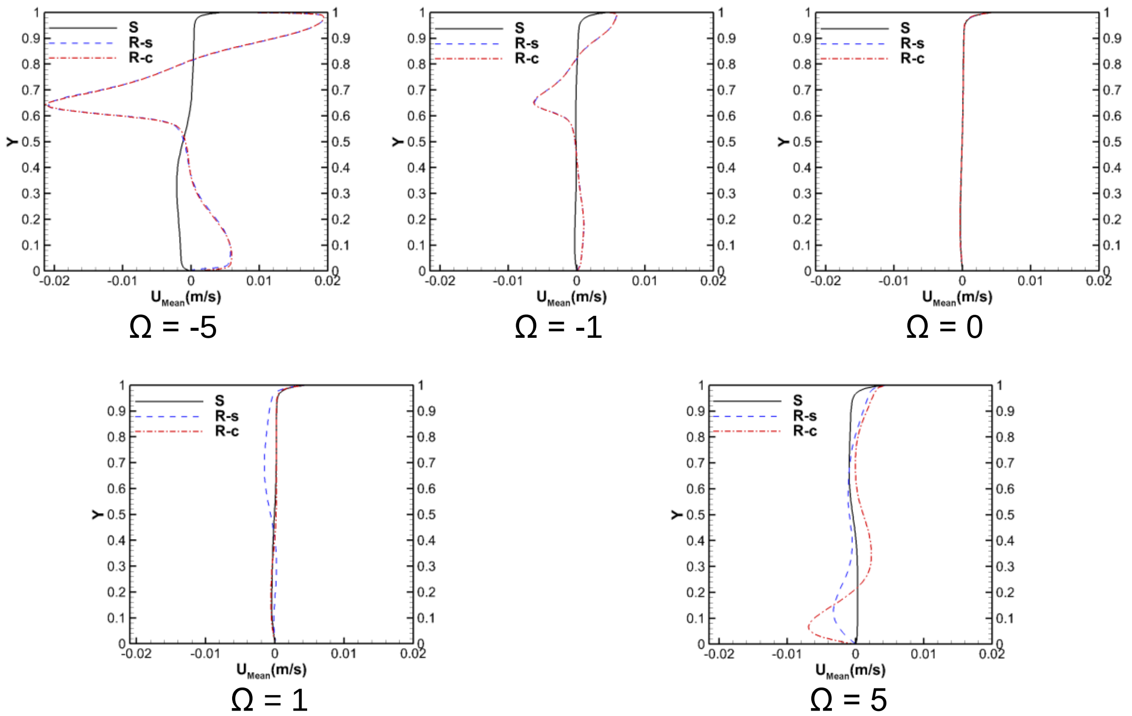

Figure 7-10: The mean velocity profiles for different bottom wall conditions (S, R-s and R-c) at Re = 5,000 and -5 ≤ Ω ≤ 5.

The presence of slight dissimilarities between the roughened bottom wall cases and the smooth wall case were established when the rotational speed was -1. This is a consequence of the effects of the bottom wall ribs matching the rotational effects of the wall shear stress behaviour.

Interesting results were achieved with regards to the average wall shear stress on the heated bottom wall, as illustrated in Figure 7-13. It should be noted that for all rotational speeds values, the R-c case induces a greater shear stress on the bottom wall than the R-s case, unlike the findings for the top wall shear stress.

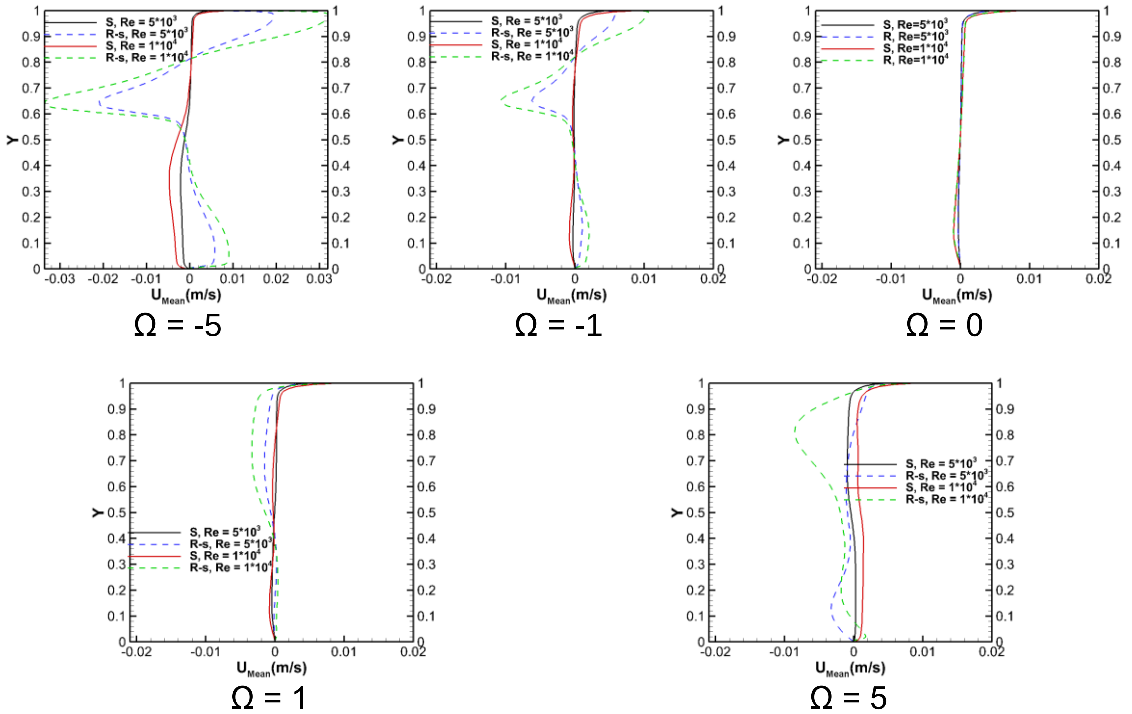

Figure 7-11: Comparison of the mean velocity profiles for different Reynolds numbers, 5,000 and 10,000, and bottom wall conditions (S and R-s) at $-5 \leq \Omega \leq 5$.

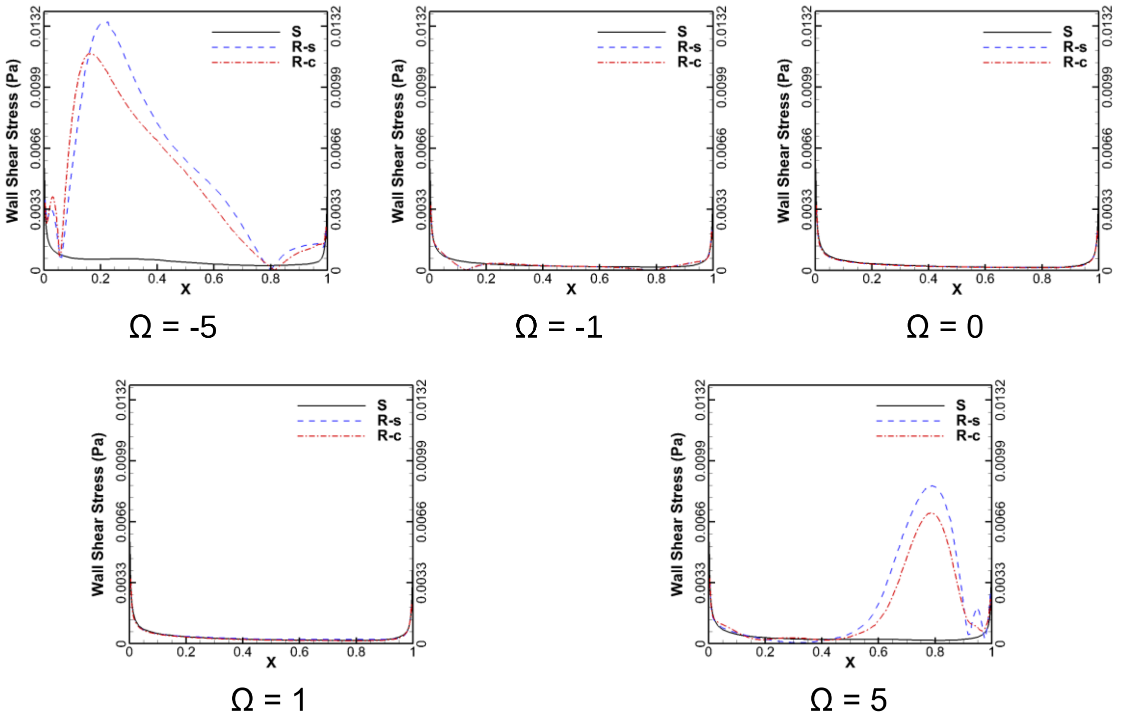

Figure 7-12: The top wall shear stresses for different bottom wall conditions (S, R-s and R-c) at Re = 5,000 and $-5 \leq \Omega \leq 5$.

This might be a result of the actions of the different rib shapes used on the bottom wall. The first rib shape is square, which could have created negative secondary vortices on the rib sides, whereas, the half circle rib shape could help reduce the formation of negative eddies on the rib sides.

Figure 7-14 displays a comparison of the roughened bottom wall (R-s) and the smooth bottom wall (S) for two Reynolds number values of 5,000 and 10,000 to understand the effect of the increasing turbulence with increasing the Reynolds number and by using artificial roughness. For any rotational motion of the cylinder, the influences of artificial roughness on the top wall shear stress can be clearly observed, particularly at high rotational speed values of Ω = 5 and -5. Additionally, increasing the Reynolds number to 10,000 shows a greater impact on the wall shear stresses.

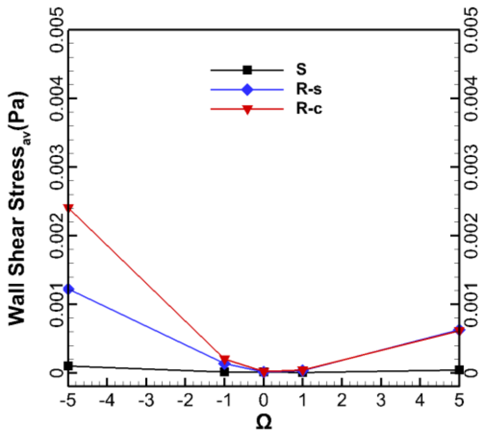

Figure 7-13: The bottom wall shear stresses for different bottom wall conditions (S, R-s and R-c) at Re = 5,000 and -5 ≤ Ω ≤ 5.

A comparison of the average wall shear stresses of the smooth bottom wall case in contrast with the R-s roughened bottom wall case is shown in Figure 7-15 at the cylinder rotational speeds in the range of -5 to 5 and the Reynolds numbers of 5,000 and 10,000. It was shown earlier in this section that artificial roughness increases the wall shear stress, which can be clearly observed by increasing the Reynolds number, which happens as a result of increasing the fluid flow circulation velocity within the domain.

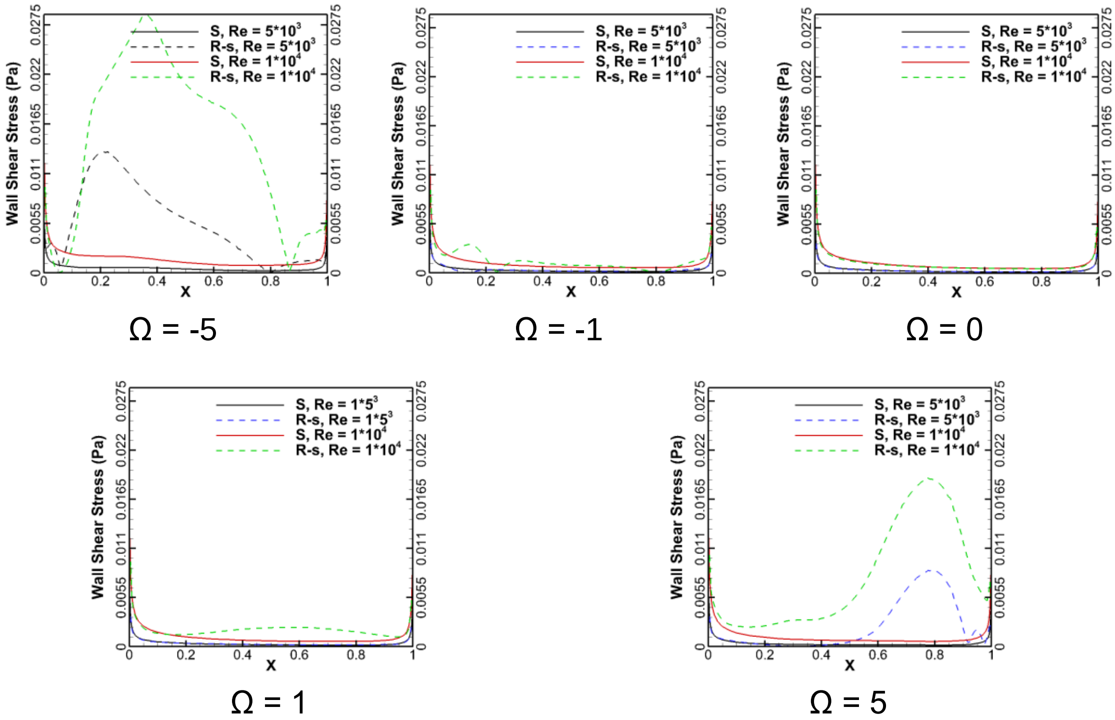

Figure 7-14: Comparison of the top wall shear stresses for different Reynolds numbers, 5,000 and 10,000, and bottom wall conditions (S and R-s) at -5 ≤ Ω ≤ 5.

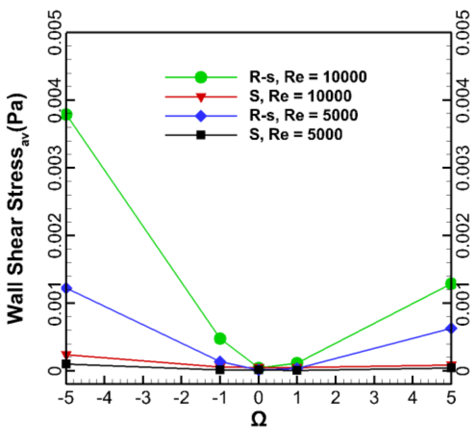

Figure 7-15: Comparison of the bottom wall shear stresses for different Reynolds numbers, 5,000 and 10,000, and bottom wall conditions (S and R-s) at -5 ≤ Ω ≤ 5.

7.3.4 Turbulence kinetic energy

The artificial ribs arrangement disturbs the development of boundary layer, which causes an increment in turbulence kinetic energy. Turbulence kinetic energy is known as the mean kinetic energy per unit mass associated with swirls in turbulent flow [137]. Therefor turbulence kinetic energy directly refers to the strength of the turbulence in the fluid flow. Studying the effect of the artificial roughness on the turbulence kinetic energy besides the impact of the Reynolds number, Re = 5,000 and 10,000, have been accomplished in detail at different rotational speeds, -5 ≤ Ω ≤ 5, of the central cylinder in this section. Two main comparisons have been completed and analysed in terms of turbulence kinetic energy to have clear vision about the influences of the artificial roughness.

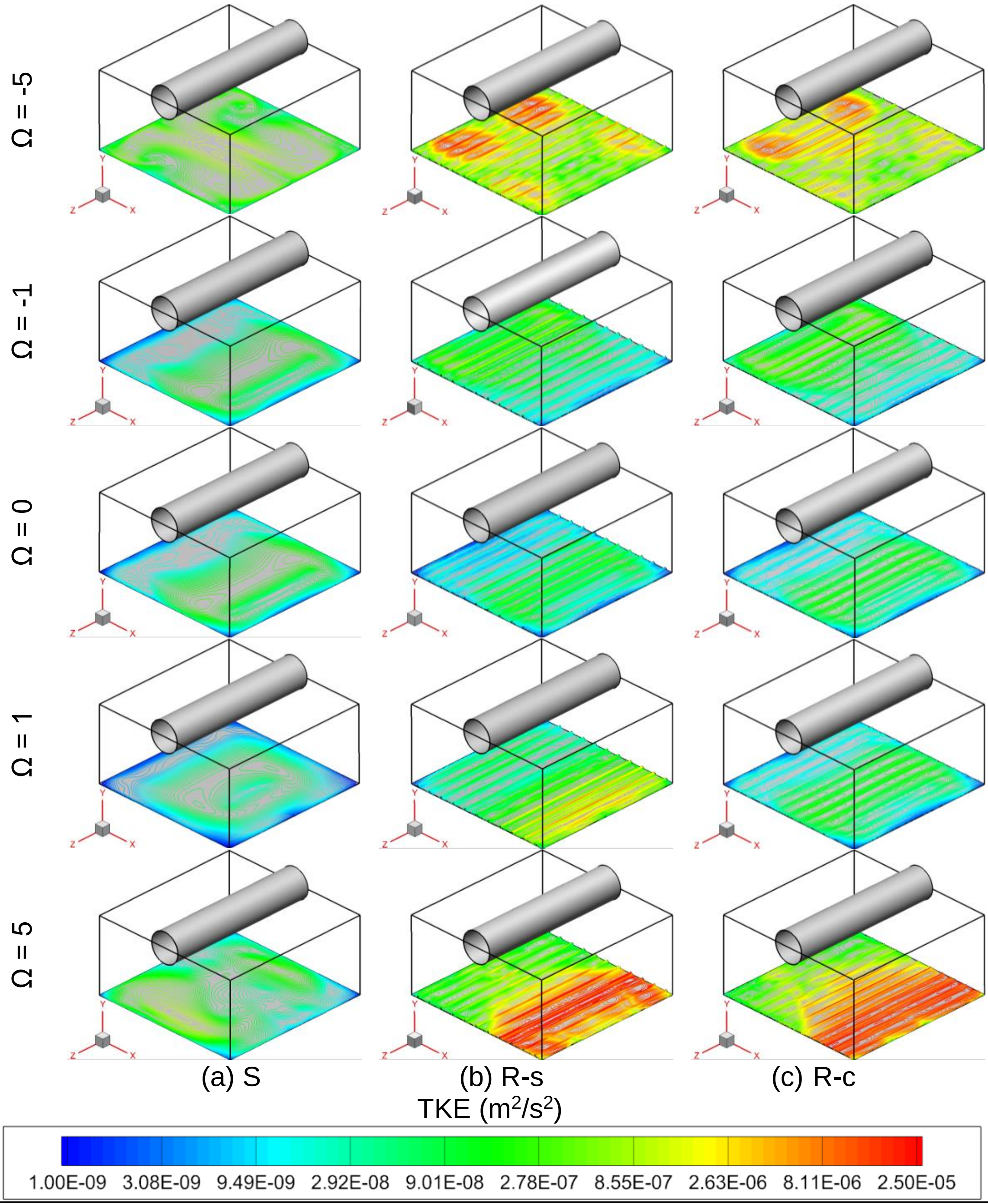

Figure 7-16: The turbelunt kinetic energy contour comparision for different bottom wall conditions, (a) S, (b) R-s and (c) R-c, at Re = 5,000 and -5 ≤ Ω ≤ 5.

The first comparison represents the results of the classic smooth bottom wall case that has been compared against those cases containing artificial ribs at Reynolds number of 5,000 and rotational speed in range of $-5 \leq \Omega \leq 5$, while the second comparison concentrates on the impacts of the artificial roughness (R-s) on the turbulence kinetic energy at different Reynolds numbers, 5,000 and 10,000, and rotational speeds. Figure 7-16 shows the turbulence kinetic energy maps on the bottom walls of the three different cases, S, R-s and R-c. Firstly, the effects of the both artificial ribs can be easily noticed. Secondly, it is known that adding a rotating object within an enclosure can influence the fluid flow [62, 100, 176], currently, at any case of the three cases (S, R-s and R-c), an obvious impact of the rotating cylinder has been found. Thirdly, a strong relationship between the ribs and the rotational speed and direction were achieved in this section. It can be seen clearly by increasing the rotational speed which can rapidly increases the effect of the artificial roughness on the turbulence kinetic energy. A comparison of average turbulence kinetic energy on the bottom wall has been shown in Figure 7-17 for the three cases of the research at Re of 5,000 and rotational speed of $-5 \leq \Omega \leq 5$ to have enough image about the effect of the ribs on the turbulent flow. Overall, the artificial roughness shows an interesting impact on the turbulence, especially at high rotational speed. As well as, roughness case of R-c provides higher turbulence kinetic energy compares to another one, which shows the impact of the rib shapes on the turbulent flow.

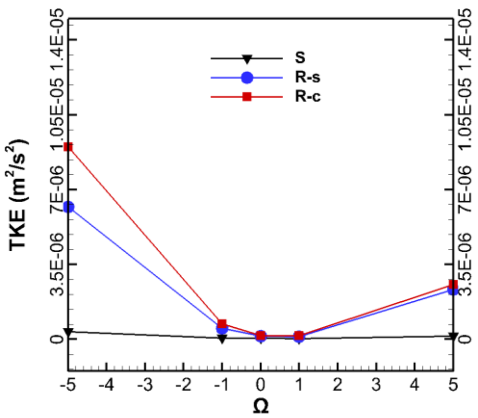

Figure 7-17: Comparison of the bottom wall average kinetic energy for different bottom wall conditions (S, R-s and R-c) at Re = 5,000 and $-5 \leq \Omega \leq 5$.

On the other hand, the second comparison is shown in Figure 7-18 and Figure 7-19, which respectively refer to the turbulence kinetic energy contours and the average turbulence kinetic energy of S and R-s cases at Reynolds number of 5,000 and 10,000 and rotational speed in range of -5 ≤ Ω ≤ 5.

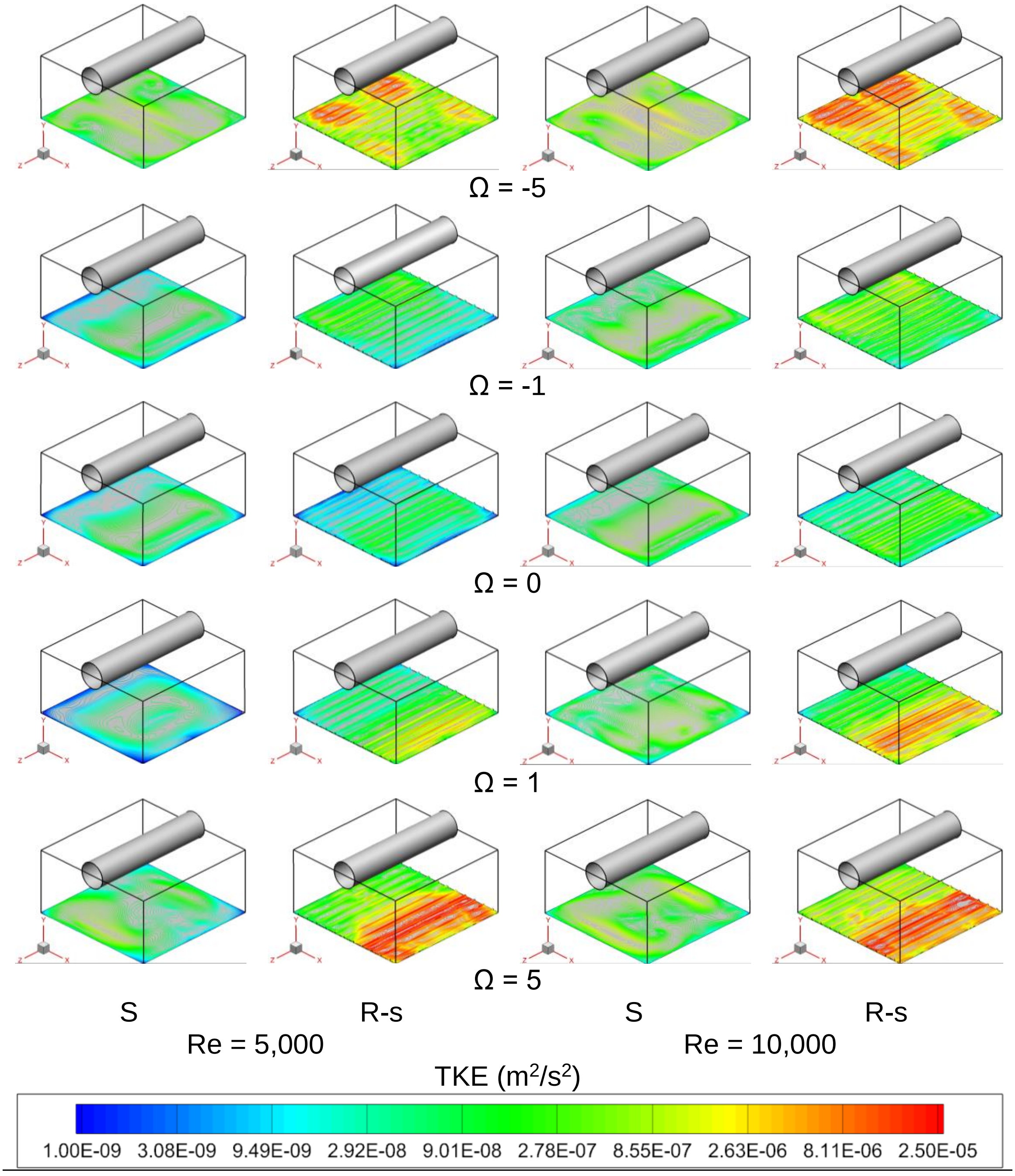

Figure 7-18: The turbulence kinetic energy comparison for different Reynolds numbers, 5,000 and 10,000, and bottom wall conditions(S and R-s), at -5 ≤ Ω ≤ 5.

Essentially, at both cases, S and R-s, it can be seen from the two figures that the turbulence kinetic energy can be raised due to increase in velocity with the increase in Reynolds number, especially at the high rotational speed and in the presence of the artificial ribs, which help to increase the turbulence rate.

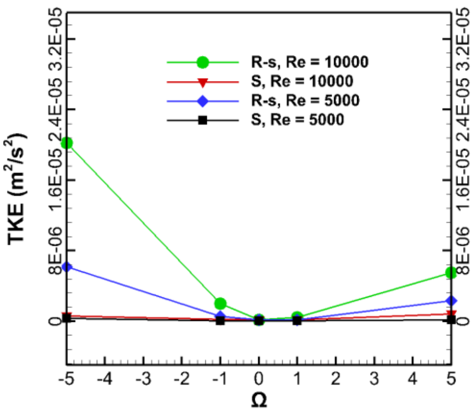

Figure 7-19: Comparison of the average bottom wall turblent kinetic energy for different Reynolds numbers, 5,000 and 10,000, and bottom wall conditions (S and R-s) at -5 ≤ Ω ≤ 5.

7.3.5 Nusselt number

Increasing the turbulence of fluid flow inside the enclosure in terms of either changing the rotational speed and direction or involving the artificial roughness is a good way to break the insulating blanket near the solid walls and to enhance the convective heat transfer rate. In the case of the smooth bottom wall (S), the fluid movement relies entirely on the top lid motion (Ω = 0), and it can be recognized that there is a slight increase in the local Nusselt numbers on the top moving wall, as shown in Figure 7-20, compared to the local Nusselt numbers of the two roughened bottom wall cases (R-s and R-c). This phenomenon is the results of the action of the artificial ribs, which cause a decrease in the fluid circulation inside the cavity. However, the matching top wall and rotational cylinder movements in the same or different directions can obviously show the effects of the artificial roughness on the heat transfer enhancement.

Studying the heat transfer augmentation of the three dissimilar cases of the heated bottom wall has been completed with reference to the average Nusselt number, as shown in Figure 7-21 and Table 7-2. Overall, it has been demonstrated that any artificial roughness has a positive effect on the heat transfer. Moreover, the impact of the artificial ribs increases as the rotational speed of the cylinder raises.

In comparison, the roughness of the ribs in the case of R-c has a stronger influence on the bottom wall Nusselt number than the roughness of the ribs in the case of R-s, due to the ribs' shape and their consequent effects on the fluid flow patterns. It may also be noted that the rib shape has a stronger impact on the heat and flow convection than the rib height. Considering Figure 7-21, more positive vortices are created near the bottom wall in the case of R-c than those of the R-s case. Consequently, the bottom wall average Nusselt numbers are higher in the R-c case than the R-s case, unlike the Nusselt numbers on the top moving wall of the enclosure. Nonetheless, the positive effects of the ribs' shape for R-s case have greater effects on the top, cold wall in terms of the heat transfer improvement, as mentioned earlier.

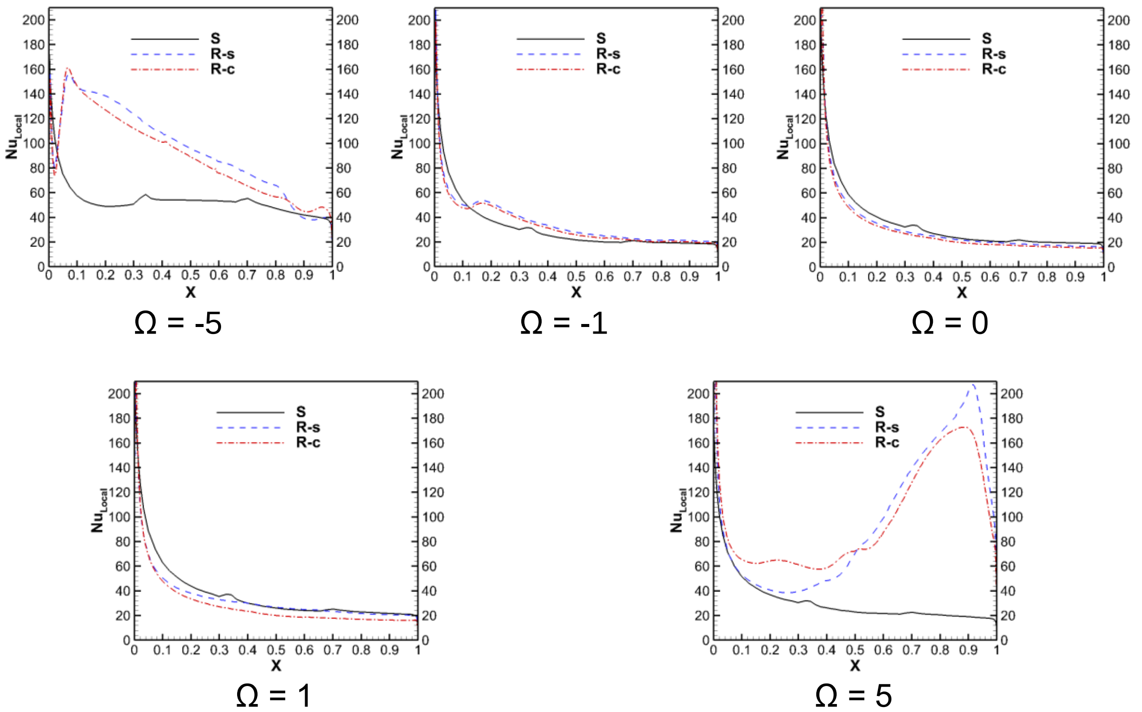

Figure 7-20: Comparison of the top wall local Nusselt number for different bottom wall conditions (S and R-s) at Re = 5,000 and -5 ≤ Ω ≤ 5.

In addition, Figure 7-22 and Figure 7-23 (and Table 7-3) illustrate a comparison of two different Reynolds numbers for the smooth (S) and roughened (R-s) bottom wall cases. Essentially, the various cases show a positive enhancement in heat transfer due to the Reynolds number increase, as it was mentioned in the literature review [177]. Changing the rotational speed or direction has a significant influence on the Nusselt number, especially when a rough bottom wall is used in the simulation. No material changes in the Nusselt number profiles have been observed by increasing the Reynolds number, which can improve the effects of roughness on the bottom wall and rotating cylinder on the heat transfer enhancement and distribution, particularly when the cylinder is rotated in the clockwise direction.

Table 7-2: The influences of different bottom wall conditions (S, R-s and R-c) on the bottom wall average Nusselt numbers at the Reynolds number of 5,000 and for various cylinder rotational speeds and directions.

Nu_{av} (bottom wall)	Ω = -5	Ω = -1	Ω = 0	Ω = 1	Ω = 5
S	39.50823	15.27429	13.29972	11.27348	20.99149
R-s	108.7822	32.09538	13.50961	19.71569	104.2078
R-c	130.8228	35.81228	15.0814	21.2345	115.8902
R-s/S	2.753405	2.101269	1.015781	1.748856	4.964288
R-c/S	3.31128	2.344612	1.133964	1.88358	5.520819

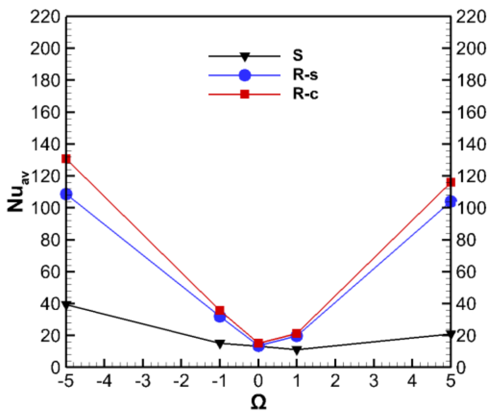

Figure 7-21: Comparison of the bottom wall average Nusselt numbers for different bottom wall conditions (S and R-s) at Re = 5,000 and -5 ≤ Ω ≤ 5.

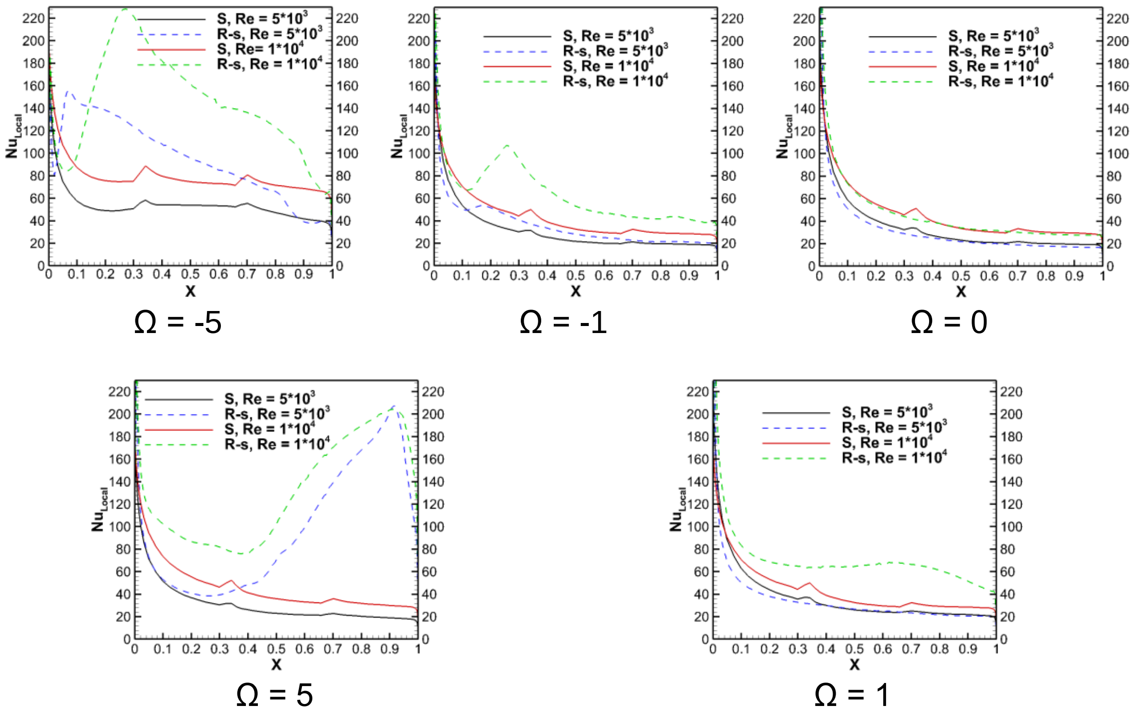

Figure 7-22: Comparison of the top wall local Nusselt numbers for different Reynolds numbers, 5,000 and 10,000, and bottom wall conditions (S and R-s) at -5 ≤ Ω ≤ 5.

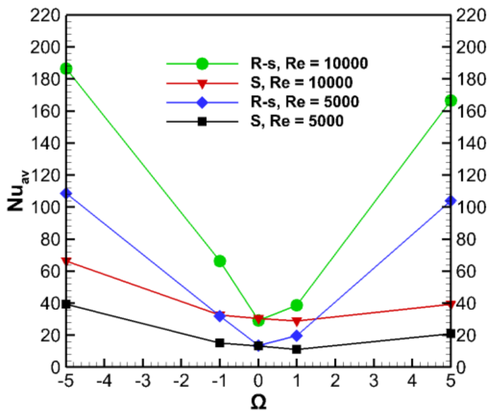

Figure 7-23: Comparison of the average bottom wall Nusselt number for different Reynolds numbers, 5,000 and 10,000, and bottom wall conditions (S and R-s) at -5 ≤ Ω ≤ 5.

Table 7-3: The effects of different Reynolds numbers, 5,000 and 10,000 and bottom wall conditions (S and R-s) on the average bottom wall Nusselt number at various cylinder rotational speeds and directions, besides the ratio of R-s/S at different Reynolds numbers and the ratio of Reynolds number, 10,000/5,000 at different cases (R-s and S).

Nu_{av} (bottom wall)	Ω = -5	Ω = -1	Ω = 0	Ω = 1	Ω = 5
S, Re = 5,000	39.50823	15.27429	13.29972	11.27348	20.99149
R-s, Re = 5,000	108.7822	32.09538	13.50961	19.71569	104.2078
S, Re = 10,000	66.38224	32.67043	30.55762	28.84999	39.36365
R-s, Re = 10,000	186.4106	66.48337	29.31835	38.73923	166.4869
R-s/S, Re = 5,000	2.753405	2.101269	1.015781	1.748856	4.964288
R-s/S, Re = 10,000	2.80814	2.034971	0.959445	1.342782	4.229457
S, Re = 10,000/5,000	1.680213	2.138917	2.297614	2.559103	1.875219
R-s, Re = 10,000/5,000	1.713614	2.071431	2.170185	1.964893	1.597643

7.4 Conclusion

The 3D CFD analysis of an artificially roughened and smooth bottom walls of a cubic lid-driven enclosure that contains a central, rotating cylinder has been carried out in this chapter in order to study the enhancement in convective heat transfer. The effects of adding two different roughness shapes (R-s and R-c) on the hot bottom wall have been compared to the smooth bottom wall case (S), as well as the impacts of the Reynolds number and the clockwise and anticlockwise rotational motions of the cylinder on the heat transfer enhancement have been investigated. The main outcomes of the numerical simulations were that:

- Significant effects have been discovered on the fluid flow patterns, the mean velocity profiles, the wall shear stresses and turbulence kinetic energies due to the use of any roughened hot bottom walls.
- A degree of influence due to the artificial ribs on the fluid flow and heat transfer has been noticed when the rotational speed of the cylinder is set to zero.
- A direct correlation has been noted between the cylinder rotational speed and the effects of the artificial roughness on the heat transfer when the rotational speed increases the artificial ribs enhance the heat transfer.
- Even though the shape of the ribs has a different impact on the top and bottom wall Nusselt numbers, both artificial rib shapes can enhance the heat transfer rate compared to the smooth bottom wall case.

- The artificial roughness shape has a more powerful effect on the fluid flow and heat transfer than the roughness height.
- Both the local and the average Nusselt numbers increase with the use of any artificial roughness types, or by increasing the cylinder rotational speed or the Reynolds number.

Chapter 8 Conclusion and recommended future work

8.1 Conclusion

In this thesis, several CFD models for mixed convection heat transfer in moving wall cavities have been studied under laminar and turbulent fluid flow conditions. The ICEM CFD has been used to create the geometries and to generate the meshes, whilst the ANSYS©FLUENT has been used to deal with the transport equations and to anatomize the simulated results. The finite volume method is utilised to discretise the conservation equations for mass, momentum and energy. Three different geometry shapes are employed, which are: first, a moving top wall trapezoidal shape cavity; second, a sidewalls lid-driven cubic enclosure; and third, a moving top wall cubic cavity. Some modifications have been applied to the third cavity, namely those of adding a central rotating cylinder and two different artificial roughness shapes on the enclosure bottom wall. Both conventional fluid and five diverse nanofluids types, have been studied and analysed in this project. From the current studies, the following conclusions can be drawn:

8.1.1 Mixed convection heat transfer of a 2D lid-driven top wall trapezoidal enclosure

The steady-state laminar combined convection of a trapezoidal top lid-driven wall has been characterised at a fixed Reynolds number of 100 and at Richardson numbers in the range of 0.1 – 10 through streamlines and isotherms contours, and Nusselt numbers for different system aspects (nanofluid type, nanofluid volume fraction, nanofluid diameter, geometry rotational and inclination angles, geometry aspect ratio and flow direction) with regards to enhancing convective heat transfer. Firstly, four types of nanofluids made from water mixed with nanoparticles (Al_2O_3, CuO, SiO_2 or TiO_2) have been investigated and compared with the conventional fluid (H_2O) to find the best nanoparticle types in terms of heat transfer enhancement.

The realizations of Chapter 4 can be briefly presented as following: *firstly*, it has been determined that SiO_2-H_2O provides the highest ratio of heat transfer because of its lower density and high conductivity; *secondly*, it has been found that the heat transfer convection increases with either adding more nanoparticles of SiO_2 within H_2O or decreasing the nanoparticle size; *thirdly*, the Nusselt number responds to both the rotational and the inclination angles; *lastly*, increasing the aspect ratio leads to enhancing the heat convection, and aiding the flow provides higher Nusselt number than opposing the flow at the rotational angle of 30°.

8.1.2 Mixed convection heat transfer of a 3D lid-driven sidewalls square enclosure

The investigations of turbulent flow of mixed convective fluids inside the cubic moving sidewalls enclosure have been undertaken at Reynolds numbers in the range of 5,000 – 30,000 to move forward in research considering enhancement of convective heat transfer of lid-driven cavities. The performance of both the standard *k-ε* turbulence model of the URANS approach and the Smagorinsky-Lilly subgrid-scale model of the LES approach have been studied and compared. Studying the effect of increasing the 3D turbulence on the heat transfer is completed for four fluid types, SiO_2-H_2O, ZnO-H_2O, CuO-H_2O and pure H_2O. Firstly, this study has concentrated on water flow to study the influence of high Reynolds number values on heat transfer and the flow patterns of the URANS and LES approaches through the turbulence kinetic energy, velocity vectors, instantaneous temperature fields and Nusselt numbers.

The outcomes of Chapter 5 can be succinctly written as following: *firstly*, it is concluded that the Reynolds number has a remarkable influence on the turbulence kinetic energy, the flow structure and both the average and local Nusselt numbers; *secondly*, a two-mixture model has been used to both deal with the turbulence effect in three different nanofluids and compare them to pure water by utilizing either LES or URANS; *thirdly*, it is found that using a mixture of nanofluids offers a higher turbulence kinetic energy and heat transfer ratio, particularly when raising the nanoparticle concentration and decreasing the nanoparticle sizes; *finally*, the LES method has shown a greater ability than the URANS method in terms of modelling secondary eddies.

8.1.3 Mixed convection heat transfer of a 3D lid-driven top wall square enclosure containing a rotating cylinder

Turbulent flow of both the nanofluid of SiO_2-H_2O and pure water within a top wall lid-driven cubic cavity containing a cylinder that can be rotated either clockwise or anticlockwise at a speed ranging from 0 – 10 and a Reynolds number in range of 5,000 – 3,0000 has been used to analyse and enhance the heat convection coefficient by using the standard *k-ε* turbulence model of the URANS method and the subgrid-scale (SGS) model of WALE (Wall-Adapting Local Eddy-viscosity) of the LES method. Focusing on the effects of a rotating circular object on heat transfer and flow behaviour is the principal goal for this 3D turbulent flow, in addition to using a nanofluid. Clockwise and anticlockwise rotational directions have been studied in detail.

Based on the results of Chapter 6, it has been generally concluded that: *firstly*, utilizing the rotating cylinder or raising the Reynolds number has a remarkable impact on the heat transfer and fluid flow patterns, especially at high rotational speeds; *secondly*, at the rotational speed of 1, the circular object controls its surrounded areas. However, at the rotational speed equal to 5, the rotating cylinder dominates the fluid circulation. Therefore, the fluid circulation is in the anticlockwise direction except for the region near the top wall that is strongly driven by the lid movement; *thirdly*, at Ω = 10 the cylinder can affect the whole domain including the area in the region of the moving top wall; *fourthly*, matching the two movements of the cavity resulted in an increase in the Nusselt number, especially at the top wall; *fifthly*, the nanofluid has always produced a noteworthy enhancement on heat transfer; *lastly*, the LES method has shown certain advantages over the URANS method in capturing more detailed eddies, and subsequently, slightly higher Nusselt numbers have been observed using the LES approach.

8.1.4 Mixed convection of a 3D lid-driven enclosure containing a rotating cylinder and a heated wall with artificial roughness

Two different artificial roughness shapes (half circle and square ribs) have been added to the heated bottom wall of a 3D top lid-driven square cavity containing a rotating cylinder to enhance the convective heat transfer. A comparison of these two roughened cases with the smooth bottom wall enclosure has been carried out. The standard *k-ε* turbulence model of the URANS approach is used to deal with the turbulent flow.

Briefly, the achievements of Chapter 7 have been concluded as following: *firstly*, considerable leverages have been found in the flow behaviours, mean velocity profiles, wall shear stresses, turbulence kinetic energy and Nusselt numbers; *secondly*, slight differences in fluid flow and heat transfer are observed by using a roughened bottom wall and a stationary cylinder; *thirdly*, an interesting relationship between the artificially roughened walls and the rotating cylinder has been noticed, and a strong impact is found on the fluid flow patterns and heat transfer enhancement when the cylinder is rotating in the clockwise or anticlockwise direction, especially at a high rotational speed; *finally*, it has been observed that the rib shape has a greater influence on the heat transfer than the rib height.

8.2 Recommended future work

Convective heat transfer in a cavity is one of the most highly studied subjects because of its wide applications, as mentioned earlier in the literature review. Therefore, it may be noted from the literature review that numerous researchers have been continually working on this topic. Surely, considerable work on convective heat transfer will be published over time. Based on this project, the following recommendations could be made for a future work:

- In order to gain a greater knowledge of heat transfer enhancement, an experimental setup can be constructed to validate the numerical results of this study. Additionally, other physical models can be used.

- The study of nanofluids in such geometries could be extended with the use of other nanoparticles (Ag, Au, SiC or SiN) and other base fluids (ethylene glycol or engine oil).
- The study of the same geometries with different boundary conditions could be conducted e.g. the bottom wall can be lid-driven, or the sidewalls can be heated.
- The study could be extended to other types of geometry parameters such as different inclination angles, rotational angles and aspect ratios. Different dimensionless numbers, such as the Reynolds number, Richardson number and Grashof number, can be applied.
- A numerical study of three-dimensional turbulent mixed convection in a trapezoidal lid-driven enclosure filled with nanofluids could also be undertaken.

References

[1] R. Manglik, Heat transfer enhancement, in, Wiley, New York, 2003, pp. 1029-1130.

[2] J.C. Maxwell, A treatise on electricity and magnetism, Clarendon Press, (1981).

[3] A.S. Ahuja, Augmentation of heat transport in laminar flow of polystyrene suspensions. I. Experiments and results, Journal of Applied Physics, 46(8) (1975) 3408-3416.

[4] A.S. Ahuja, Augmentation of heat transport in laminar flow of polystyrene suspensions. II. Analysis of the data, Journal of Applied Physics, 46(8) (1975) 3417-3425.

[5] S. Chol, Enhancing thermal conductivity of fluids with nanoparticles, ASME-Publications-Fed, 231 (1995) 99-106.

[6] H. Masuda, A. Ebata, K. Teramae, Alteration of thermal conductivity and viscosity of liquid by dispersing ultra-fine particles. Dispersion of Al2O3, SiO2 and TiO2 ultra-fine particles, (1993).

[7] D.H. Kumar, H.E. Patel, V.R. Kumar, T. Sundararajan, T. Pradeep, S.K. Das, Model for heat conduction in nanofluids, Physical Review Letters, 93(14) (2004) 144301.

[8] S. Wu, D. Zhu, X. Li, H. Li, J. Lei, Thermal energy storage behavior of Al 2 O 3–H 2 O nanofluids, Thermochimica Acta, 483(1) (2009) 73-77.

[9] R. Rusconi, E. Rodari, R. Piazza, Optical measurements of the thermal properties of nanofluids, Applied Physics Letters, 89(26) (2006) 261916.

[10] D.C. Venerus, M.S. Kabadi, S. Lee, V. Perez-Luna, Study of thermal transport in nanoparticle suspensions using forced Rayleigh scattering, Journal of Applied Physics, 100(9) (2006) 094310.

[11] S.A. Putnam, D.G. Cahill, P.V. Braun, Z. Ge, R.G. Shimmin, Thermal conductivity of nanoparticle suspensions, Journal of Applied Physics, 99(8) (2006) 084308.

[12] K. Hong, T.-K. Hong, H.-S. Yang, Thermal conductivity of Fe nanofluids depending on the cluster size of nanoparticles, Applied Physics Letters, 88(3) (2006) 031901.

[13] D. Wen, Y. Ding, Effective thermal conductivity of aqueous suspensions of carbon nanotubes (carbon nanotube nanofluids), Journal of Thermophysics and Heat Transfer, 18(4) (2004) 481-485.

[14] S. You, J. Kim, K. Kim, Effect of nanoparticles on critical heat flux of water in pool boiling heat transfer, Applied Physics Letters, 83(16) (2003) 3374-3376.

[15] S. Li, J. Eastman, Measuring thermal conductivity of fluids containing oxide nanoparticles, J. Heat Transf, 121(2) (1999) 280-289.

[16] S. Göktepe, K. Atalık, H. Ertürk, Comparison of single and two-phase models for nanofluid convection at the entrance of a uniformly heated tube, International Journal of Thermal Sciences, 80 (2014) 83-92.

[17] A.K. Kareem, S. Gao, A.Q. Ahmed, Unsteady simulations of mixed convection heat transfer in a 3D closed lid-driven cavity, International Journal of Heat and Mass Transfer, 100 (2016) 121-130.

[18] D. Chatterjee, B. Mondal, P. Halder, Hydromagnetic mixed convective transport in a vertical lid-driven cavity including a heat conducting rotating circular cylinder, Numerical Heat Transfer, Part A: Applications, 65(1) (2014) 48-65.

[19] S. Hussain, S. Ahmad, K. Mehmood, M. Sagheer, Effects of inclination angle on mixed convective nanofluid flow in a double lid-driven cavity with discrete heat sources, International Journal of Heat and Mass Transfer, 106 (2017) 847-860.

[20] C.-C. Liao, C.-A. Lin, Mixed convection of a heated rotating cylinder in a square enclosure, International Journal of Heat and Mass Transfer, 72 (2014) 9-22.

[21] R. Roslan, H. Saleh, I. Hashim, A. Bataineh, Natural convection in an enclosure containing a sinusoidally heated cylindrical source, International Journal of Heat and Mass Transfer, 70 (2014) 119-127.

[22] A. Ben-Nakhi, A.J. Chamkha, Conjugate natural convection around a finned pipe in a square enclosure with internal heat generation, International Journal of Heat and Mass Transfer, 50(11) (2007) 2260-2271.

[23] A.K. Kareem, S. Gao, Mixed convection heat transfer of turbulent flow in a three-dimensional lid-driven cavity with a rotating cylinder, International Journal of Heat and Mass Transfer, 112 (2017) 185-200.

[24] M. Mamun, T. Tanim, M. Rahman, R. Saidur, S. Nagata, Mixed convection analysis in trapezoidal cavity with a moving lid, International Journal of Mechanical and Materials Engineering, 5(1) (2010) 18-28.

[25] G. Wang, X. Meng, M. Zeng, H. Ozoe, Q. Wang, Natural convection heat transfer of copper–water nanofluid in a square cavity with time-periodic boundary temperature, Heat Transfer Engineering, 35(6-8) (2014) 630-640.

[26] Y.-P. Hu, Y.-R. Li, C.-M. Wu, Comparison investigation on natural convection of cold water near its density maximum in annular enclosures with complex configurations, International Journal of Heat and Mass Transfer, 72 (2014) 572-584.

[27] M. Alipanah, A. Ranjbar, A. Zahmatkesh, Numerical study of natural convection in vertical enclosures utilizing nanofluid, Advances in Mechanical Engineering, 6 (2014) 392610.

[28] S. Singh, R. Bhargava, Numerical study of natural convection within a wavy enclosure using Meshfree approach: effect of corner heating, The Scientific World Journal, 2014 (2014).

[29] F. Karimi, H.T. Xu, Z. Wang, M. Yang, Y. Zhang, Numerical Simulation of Unsteady Natural Convection from Heated Horizontal Circular Cylinders in a Square Enclosure, Numerical Heat Transfer, Part A: Applications, 65(8) (2014) 715-731.

[30] H.S. Yoon, Y.G. Park, J.H. Jung, Natural Convection in a Square Enclosure with Differentially Heated Two Horizontal Cylinders, Numerical Heat Transfer, Part A: Applications, 65(4) (2014) 302-326.

[31] E. Sourtiji, D. Ganji, M. Gorji-Bandpy, S. Seyyedi, Numerical study of periodic natural convection in a nanofluid-filled enclosure due to transitional temperature of heat source, Powder Technology, 259 (2014) 65-73.

[32] J. Cajas, C. Treviño, Transient heating and entropy generation of a fluid inside a large aspect ratio cavity, International Journal of Thermal Sciences, 64 (2013) 220-231.

[33] S.C. Saha, M.M.K. Khan, Y. Gu, Unsteady buoyancy driven flows and heat transfer through coupled thermal boundary layers in a partitioned triangular enclosure, International Journal of Heat and Mass Transfer, 68 (2014) 375-382.

[34] A.K. Sharma, K. Velusamy, C. Balaji, Turbulent natural convection in an enclosure with localized heating from below, International Journal of Thermal Sciences, 46(12) (2007) 1232-1241.

[35] C. Choi, S. Jeong, M.Y. Ha, H.S. Yoon, Effect of a circular cylinder's location on natural convection in a rhombus enclosure, International Journal of Heat and Mass Transfer, 77 (2014) 60-73.

[36] Y. Hu, Y. He, C. Qi, B. Jiang, H.I. Schlaberg, Experimental and numerical study of natural convection in a square enclosure filled with nanofluid, International Journal of Heat and Mass Transfer, 78 (2014) 380-392.

[37] A. Mahmoudi, I. Mejri, M.A. Abbassi, A. Omri, Analysis of MHD natural convection in a nanofluid-filled open cavity with non uniform boundary condition in the presence of uniform heat generation/absorption, Powder Technology, 269 (2015) 275-289.

[38] Y.G. Park, H.S. Yoon, M.Y. Ha, Natural convection in square enclosure with hot and cold cylinders at different vertical locations, International Journal of Heat and Mass Transfer, 55(25) (2012) 7911-7925.

[39] A. Sojoudi, S.C. Saha, Y. Gu, M.A. Hossain, Steady natural convection of non-Newtonian power-law fluid in a trapezoidal enclosure, Advances in Mechanical Engineering, 5 (2013) 653108.

[40] D. Henderson, H. Junaidi, T. Muneer, T. Grassie, J. Currie, Experimental and CFD investigation of an ICSSWH at various inclinations, Renewable and Sustainable Energy Reviews, 11(6) (2007) 1087-1116.

[41] C. Cianfrini, M. Corcione, P.P. Dell'Omo, Natural convection in tilted square cavities with differentially heated opposite walls, International Journal of Thermal Sciences, 44(5) (2005) 441-451.

[42] Y. Varol, H.F. Oztop, Free convection in a shallow wavy enclosure, International communications in heat and mass transfer, 33(6) (2006) 764-771.

[43] H.F. Oztop, E. Abu-Nada, Y. Varol, A. Chamkha, Natural convection in wavy enclosures with volumetric heat sources, International Journal of Thermal Sciences, 50(4) (2011) 502-514.

[44] M.M. Ganzarolli, L.F. Milanez, Natural convection in rectangular enclosures heated from below and symmetrically cooled from the sides, International Journal of Heat and Mass Transfer, 38(6) (1995) 1063-1073.

[45] T. Basak, S. Roy, A. Balakrishnan, Effects of thermal boundary conditions on natural convection flows within a square cavity, International Journal of Heat and Mass Transfer, 49(23) (2006) 4525-4535.

[46] A. Sojoudi, S.C. Saha, Y. Gu, M. Hossain, Steady Natural Convection of Non-Newtonian Power-Law Fluid in a Trapezoidal Enclosure, Advances in Mechanical Engineering, 2013 (2013).

[47] E.H. Ridouane, A. Campo, M. Hasnaoui, Turbulent natural convection in an air-filled isosceles triangular enclosure, International Journal of Heat and Fluid Flow, 27(3) (2006) 476-489.

[48] P.H. Carvalho, M.J. de Lemos, Turbulent free convection in a porous cavity using the two-temperature model and the high Reynolds closure, International Journal of Heat and Mass Transfer, 79 (2014) 105-115.

[49] J. Serrano-Arellano, M. Gijón-Rivera, J. Riesco-Ávila, F. Elizalde-Blancas, Numerical study of the double diffusive convection phenomena in a closed cavity with internal CO< sub> 2</sub> point sources, International Journal of Heat and Mass Transfer, 71 (2014) 664-674.

[50] Z. Zhang, W. Chen, Z. Zhu, Y. Li, Numerical exploration of turbulent air natural-convection in a differentially heated square cavity at Ra= 5.33× 109, Heat and Mass Transfer, 50(12) (2014) 1737-1749.

[51] C.-J. Ho, M. Chen, Z. Li, Numerical simulation of natural convection of nanofluid in a square enclosure: effects due to uncertainties of viscosity and

thermal conductivity, International Journal of Heat and Mass Transfer, 51(17) (2008) 4506-4516.

[52] C. Cianfrini, M. Corcione, E. Habib, A. Quintino, Buoyancy-induced convection in Al2O3/water nanofluids from an enclosed heater, European Journal of Mechanics - B/Fluids, 48 (2014) 123-134.

[53] M. Alipanah, A. Ranjbar, A. Zahmatkesh, Numerical Study of Natural Convection in Vertical Enclosures Utilizing Nanofluid, Advances in Mechanical Engineering, 2014 (2014).

[54] P. Ternik, Conduction and convection heat transfer characteristics of water–Au nanofluid in a cubic enclosure with differentially heated side walls, International Journal of Heat and Mass Transfer, 80 (2015) 368-375.

[55] M. Saidi, G. Karimi, Free convection cooling in modified L-shape enclosures using copper–water nanofluid, Energy, (2014).

[56] H.M. Elshehabey, F. Hady, S.E. Ahmed, R. Mohamed, Numerical investigation for natural convection of a nanofluid in an inclined L-shaped cavity in the presence of an inclined magnetic field, International Communications in Heat and Mass Transfer, 57 (2014) 228-238.

[57] M. Bouhalleb, H. Abbassi, Natural convection of nanofluids in enclosures with low aspect ratios, International Journal of Hydrogen Energy, (2014).

[58] M. Rahman, S. Saha, S. Mojumder, S. Mekhilef, R. Saidur, Numerical simulation of unsteady heat transfer in a half-moon shape enclosure with variable thermal boundary condition for different nanofluids, Numerical Heat Transfer, Part B: Fundamentals, 65(3) (2014) 282-301.

[59] F. Selimefendigil, H.F. Öztop, Numerical study of MHD mixed convection in a nanofluid filled lid driven square enclosure with a rotating cylinder, International Journal of Heat and Mass Transfer, 78 (2014) 741-754.

[60] M. Kalteh, K. Javaherdeh, T. Azarbarzin, Numerical solution of nanofluid mixed convection heat transfer in a lid-driven square cavity with a triangular heat source, Powder Technology, 253 (2014) 780-788.

[61] B. Pekmen, M. Tezer-Sezgin, MHD flow and heat transfer in a lid-driven porous enclosure, Computers & Fluids, 89 (2014) 191-199.

[62] D. Chatterjee, S.K. Gupta, B. Mondal, Mixed convective transport in a lid-driven cavity containing a nanofluid and a rotating circular cylinder at the center, International Communications in Heat and Mass Transfer, 56 (2014) 71-78.

[63] M.A. Ismael, I. Pop, A.J. Chamkha, Mixed convection in a lid-driven square cavity with partial slip, International Journal of Thermal Sciences, 82 (2014) 47-61.

[64] Power & Data, http://poweranddata.info/2014/05/19/data-center-cooling/, in: POWERandDATAinfo, Access Date; 12/06/2018.

[65] T. Cheng, Characteristics of mixed convection heat transfer in a lid-driven square cavity with various Richardson and Prandtl numbers, International Journal of Thermal Sciences, 50(2) (2011) 197-205.

[66] T. Basak, S. Roy, S.K. Singh, I. Pop, Analysis of mixed convection in a lid-driven porous square cavity with linearly heated side wall (s), International Journal of Heat and Mass Transfer, 53(9) (2010) 1819-1840.

[67] T. Basak, S. Roy, P.K. Sharma, I. Pop, Analysis of mixed convection flows within a square cavity with linearly heated side wall (s), International Journal of Heat and Mass Transfer, 52(9) (2009) 2224-2242.

[68] T. Basak, S. Roy, P.K. Sharma, I. Pop, Analysis of mixed convection flows within a square cavity with uniform and non-uniform heating of bottom wall, International Journal of Thermal Sciences, 48(5) (2009) 891-912.

[69] A.M. Al-Amiri, K.M. Khanafer, I. Pop, Numerical simulation of combined thermal and mass transport in a square lid-driven cavity, International journal of thermal sciences, 46(7) (2007) 662-671.

[70] M. Moallemi, K. Jang, Prandtl number effects on laminar mixed convection heat transfer in a lid-driven cavity, International Journal of Heat and Mass Transfer, 35(8) (1992) 1881-1892.

[71] I. Reima, J.M. Hyun, K. Kunio, Convection in a differentially-heated square cavity with a torsionally-oscillating lid, International journal of heat and mass transfer, 35(5) (1992) 1069-1076.

[72] B. Ghasemi, S. Aminossadati, Comparison of mixed convection in a square cavity with an oscillating versus a constant velocity wall, Numerical Heat Transfer, Part A: Applications, 54(7) (2008) 726-743.

[73] H.F. Oztop, I. Dagtekin, Mixed convection in two-sided lid-driven differentially heated square cavity, International journal of heat and mass transfer, 47(8) (2004) 1761-1769.

[74] D.Z. Noor, P.R. Kanna, M.-J. Chern, Flow and heat transfer in a driven square cavity with double-sided oscillating lids in anti-phase, International Journal of Heat and Mass Transfer, 52(13) (2009) 3009-3023.

[75] E. Vishnuvardhanarao, M.K. Das, Laminar mixed convection in a parallel two-sided lid-driven differentially heated square cavity filled with a fluid-saturated porous medium, Numerical Heat Transfer, Part A: Applications, 53(1) (2007) 88-110.

[76] O. Aydm, Aiding and opposing mechanisms of mixed convection in a shear- and buoyancy-driven cavity, International communications in heat and mass transfer, 26(7) (1999) 1019-1028.

[77] V. Sivakumar, S. Sivasankaran, P. Prakash, J. Lee, Effect of heating location and size on mixed convection in lid-driven cavities, Computers & Mathematics with Applications, 59(9) (2010) 3053-3065.

[78] G. Guo, M.A. Sharif, Mixed convection in rectangular cavities at various aspect ratios with moving isothermal sidewalls and constant flux heat source on the bottom wall, International journal of thermal sciences, 43(5) (2004) 465-475.

[79] C.-L. Chen, C.-H. Cheng, Numerical study of the effects of lid oscillation on the periodic flow pattern and convection heat transfer in a triangular cavity, International Communications in Heat and Mass Transfer, 36(6) (2009) 590-596.

[80] A. Mohamad, R. Viskanta, Flow and heat transfer in a lid-driven cavity filled with a stably stratified fluid, Applied mathematical modelling, 19(8) (1995) 465-472.

[81] N. Ouertatani, N.B. Cheikh, B.B. Beya, T. Lili, A. Campo, Mixed convection in a double lid-driven cubic cavity, International Journal of Thermal Sciences, 48(7) (2009) 1265-1272.

[82] K. Khanafer, Comparison of flow and heat transfer characteristics in a lid-driven cavity between flexible and modified geometry of a heated bottom wall, International Journal of Heat and Mass Transfer, 78 (2014) 1032-1041.

[83] M. Bhattacharya, T. Basak, H.F. Oztop, Y. Varol, Mixed convection and role of multiple solutions in lid-driven trapezoidal enclosures, International Journal of Heat and Mass Transfer, 63 (2013) 366-388.

[84] E. Abu-Nada, A.J. Chamkha, Mixed convection flow in a lid-driven inclined square enclosure filled with a nanofluid, European Journal of Mechanics-B/Fluids, 29(6) (2010) 472-482.

[85] B. Ghasemi, S. Aminossadati, Mixed convection in a lid-driven triangular enclosure filled with nanofluids, International Communications in Heat and Mass Transfer, 37(8) (2010) 1142-1148.

[86] E. Abu-Nada, A.J. Chamkha, Mixed convection flow of a nanofluid in a lid-driven cavity with a wavy wall, International Communications in Heat and Mass Transfer, 57 (2014) 36-47.

[87] J. Serna, F. Velasco, A. Soto Meca, Application of network simulation method to viscous flows: The nanofluid heated lid cavity under pulsating flow, Computers & Fluids, 91 (2014) 10-20.

[88] A. Karimipour, M. Hemmat Esfe, M.R. Safaei, D. Toghraie Semiromi, S. Jafari, S. Kazi, Mixed convection of copper–water nanofluid in a shallow inclined lid driven cavity using the lattice Boltzmann method, Physica A: Statistical Mechanics and its Applications, 402 (2014) 150-168.

[89] M. Billah, M. Rahman, M. Razzak, R. Saidur, S. Mekhilef, Unsteady buoyancy-driven heat transfer enhancement of nanofluids in an inclined

triangular enclosure, International Communications in Heat and Mass Transfer, 49 (2013) 115-127.

[90] M. Goodarzi, M. Safaei, K. Vafai, G. Ahmadi, M. Dahari, S. Kazi, N. Jomhari, Investigation of nanofluid mixed convection in a shallow cavity using a two-phase mixture model, International Journal of Thermal Sciences, 75 (2014) 204-220.

[91] M. Alinia, D. Ganji, M. Gorji-Bandpy, Numerical study of mixed convection in an inclined two sided lid driven cavity filled with nanofluid using two-phase mixture model, International Communications in Heat and Mass Transfer, 38(10) (2011) 1428-1435.

[92] L. Pingan, G. Ye, M. Hairong, H. Liu, Numerical simulations on natural convection in a square cavity containing a circular pipe, in: Computer Design and Applications (ICCDA), 2010 International Conference on, IEEE, 2010, pp. V3-485-V483-489.

[93] R. Shyam, M. Sairamu, N. Nirmalkar, R. Chhabra, Free convection from a heated circular cylinder in confined power-law fluids, International Journal of Thermal Sciences, 74 (2013) 156-173.

[94] B. Souayeh, N. Ben-Cheikh, B. Ben-Beya, Numerical simulation of three-dimensional natural convection in a cubic enclosure induced by an isothermally-heated circular cylinder at different inclinations, International Journal of Thermal Sciences, 110 (2016) 325-339.

[95] S.A. Nabavizadeh, S. Talebi, M. Sefid, M. Nourmohammadzadeh, Natural convection in a square cavity containing a sinusoidal cylinder, International journal of thermal sciences, 51 (2012) 112-120.

[96] H.F. Oztop, Z. Zhao, B. Yu, Fluid flow due to combined convection in lid-driven enclosure having a circular body, International Journal of Heat and Fluid Flow, 30(5) (2009) 886-901.

[97] K.M. Gangawane, Computational analysis of mixed convection heat transfer characteristics in lid-driven cavity containing triangular block with constant heat flux: Effect of Prandtl and Grashof numbers, International Journal of Heat and Mass Transfer, 105 (2017) 34-57.

[98] K. Mehmood, S. Hussain, M. Sagheer, Mixed convection in alumina-water nanofluid filled lid-driven square cavity with an isothermally heated square blockage inside with magnetic field effect: Introduction, International Journal of Heat and Mass Transfer, 109 (2017) 397-409.

[99] S. Ray, D. Chatterjee, MHD mixed convection in a lid-driven cavity including heat conducting circular solid object and corner heaters with Joule heating, International Communications in Heat and Mass Transfer, 57 (2014) 200-207.

[100] S.H. Hussain, A.K. Hussein, Mixed convection heat transfer in a differentially heated square enclosure with a conductive rotating circular cylinder

at different vertical locations, International Communications in Heat and Mass Transfer, 38(2) (2011) 263-274.

[101] M. Billah, M. Rahman, U.M. Sharif, N. Rahim, R. Saidur, M. Hasanuzzaman, Numerical analysis of fluid flow due to mixed convection in a lid-driven cavity having a heated circular hollow cylinder, International Communications in Heat and Mass Transfer, 38(8) (2011) 1093-1103.

[102] K. Khanafer, S. Aithal, Laminar mixed convection flow and heat transfer characteristics in a lid driven cavity with a circular cylinder, International Journal of Heat and Mass Transfer, 66 (2013) 200-209.

[103] A.W. Islam, M.A. Sharif, E.S. Carlson, Mixed convection in a lid driven square cavity with an isothermally heated square blockage inside, International Journal of Heat and Mass Transfer, 55(19) (2012) 5244-5255.

[104] R. Roslan, H. Saleh, I. Hashim, Effect of rotating cylinder on heat transfer in a square enclosure filled with nanofluids, International Journal of Heat and Mass Transfer, 55(23) (2012) 7247-7256.

[105] V. Costa, A. Raimundo, Steady mixed convection in a differentially heated square enclosure with an active rotating circular cylinder, International Journal of Heat and Mass Transfer, 53(5) (2010) 1208-1219.

[106] S. Mirzakhanlari, K.M. Shirvan, M. Mamourian, A.J. Chamkha, Increment of mixed convection heat transfer and decrement of drag coefficient in a lid-driven nanofluid-filled cavity with a conductive rotating circular cylinder at different horizontal locations: A sensitivity analysis, Powder Technology, 305 (2017) 495-508.

[107] F. Garoosi, F. Hoseininejad, Numerical study of natural and mixed convection heat transfer between differentially heated cylinders in an adiabatic enclosure filled with nanofluid, Journal of Molecular Liquids, 215 (2016) 1-17.

[108] C. Sun, B. Yu, H.F. Oztop, Y. Wang, J. Wei, Control of mixed convection in lid-driven enclosures using conductive triangular fins, International Journal of Heat and Mass Transfer, 54(4) (2011) 894-909.

[109] S. Bansal, D. Chatterjee, Magneto-convective transport of nanofluid in a vertical lid-driven cavity including a heat-conducting rotating circular cylinder, Numerical Heat Transfer, Part A: Applications, 68(4) (2015) 411-431.

[110] D. Chatterjee, P. Halder, MHD mixed convective transport in square enclosure with two rotating circular cylinders, Numerical Heat Transfer, Part A: Applications, 65(8) (2014) 802-824.

[111] D. Chatterjee, P. Halder, Magnetoconvective transport in a lid-driven square enclosure with two rotating circular cylinders, Heat Transfer Engineering, 37(2) (2016) 198-209.

[112] H.S. Yoon, M.Y. Ha, B.S. Kim, D.H. Yu, Effect of the position of a circular cylinder in a square enclosure on natural convection at Rayleigh number of 10 7, Physics of Fluids, 21(4) (2009) 047101.

[113] A. Sekimoto, G. Kawahara, K. Sekiyama, M. Uhlmann, A. Pinelli, Turbulence-and buoyancy-driven secondary flow in a horizontal square duct heated from below, Physics of fluids, 23(7) (2011) 075103.

[114] M.Y. Ha, I.-K. Kim, H.S. Yoon, S. Lee, Unsteady fluid flow and temperature fields in a horizontal enclosure with an adiabatic body, Physics of Fluids, 14(9) (2002) 3189-3202.

[115] L. Shui-lian, M. Xiang-rui, W. Xin-li, Heat transfer and friction factor correlations for solar air collectors with hemispherical protrusion artificial roughness on the absorber plate, Solar Energy, 118 (2015) 460-468.

[116] K. Khanafer, S. Aithal, Mixed convection heat transfer in a lid-driven cavity with a rotating circular cylinder, International Communications in Heat and Mass Transfer, 86 (2017) 131-142.

[117] P. Biswal, M. Roy, S. Roy, T. Basak, Analysis of heatline based visualization for thermal management during mixed convection of hot/cold fluids within entrapped triangular cavities, Journal of the Taiwan Institute of Chemical Engineers, (2017).

[118] G.E. Ovando-Chacon, S.L. Ovando-Chacon, J.C. Prince-Avelino, M.A. Romo-Medina, Numerical study of the heater length effect on the heating of a solid circular obstruction centered in an open cavity, European Journal of Mechanics - B/Fluids, 42 (2013) 176-185.

[119] A.M. Rashad, S. Abbasbandy, A.J. Chamkha, Mixed convection flow of a micropolar fluid over a continuously moving vertical surface immersed in a thermally and solutally stratified medium with chemical reaction, Journal of the Taiwan Institute of Chemical Engineers, 45(5) (2014) 2163-2169.

[120] G. Swapna, L. Kumar, P. Rana, B. Singh, Finite element modeling of a double-diffusive mixed convection flow of a chemically-reacting magneto-micropolar fluid with convective boundary condition, Journal of the Taiwan Institute of Chemical Engineers, 47 (2015) 18-27.

[121] A.K. Kareem, H.A. Mohammed, A.K. Hussein, S. Gao, Numerical investigation of mixed convection heat transfer of nanofluids in a lid-driven trapezoidal cavity, International Communications in Heat and Mass Transfer, 77 (2016) 195-205.

[122] A. Khaleel, S. Gao, CFD Investigation of Turbulent Mixed Convection Heat Transfer in a Closed Lid-Driven Cavity, World Academy of Science, Engineering and Technology, International Journal of Civil, Environmental, Structural, Construction and Architectural Engineering, 9(12) (2015) 1564-1569.

[123] A. Jaurker, J. Saini, B. Gandhi, Heat transfer and friction characteristics of rectangular solar air heater duct using rib-grooved artificial roughness, Solar Energy, 80(8) (2006) 895-907.

[124] A. Kumar, R. Saini, J. Saini, Experimental investigation on heat transfer and fluid flow characteristics of air flow in a rectangular duct with Multi v-shaped rib with gap roughness on the heated plate, Solar Energy, 86(6) (2012) 1733-1749.

[125] T. Alam, R.P. Saini, J.S. Saini, Experimental investigation on heat transfer enhancement due to V-shaped perforated blocks in a rectangular duct of solar air heater, Energy Conversion and Management, 81 (2014) 374-383.

[126] R. Karwa, G. Chitoshiya, Performance study of solar air heater having v-down discrete ribs on absorber plate, Energy, 55 (2013) 939-955.

[127] S. Singh, S. Chander, J.S. Saini, Thermo-hydraulic performance due to relative roughness pitch in V-down rib with gap in solar air heater duct—Comparison with similar rib roughness geometries, Renewable and Sustainable Energy Reviews, 43 (2015) 1159-1166.

[128] D. Jin, M. Zhang, P. Wang, S. Xu, Numerical investigation of heat transfer and fluid flow in a solar air heater duct with multi V-shaped ribs on the absorber plate, Energy, 89 (2015) 178-190.

[129] T. Rajaseenivasan, S. Srinivasan, K. Srithar, Comprehensive study on solar air heater with circular and V-type turbulators attached on absorber plate, Energy, 88 (2015) 863-873.

[130] N.S. Deo, S. Chander, J. Saini, Performance analysis of solar air heater duct roughened with multigap V-down ribs combined with staggered ribs, Renewable Energy, 91 (2016) 484-500.

[131] V. Hans, R. Saini, J. Saini, Heat transfer and friction factor correlations for a solar air heater duct roughened artificially with multiple v-ribs, Solar Energy, 84(6) (2010) 898-911.

[132] R. Maithani, J. Saini, Heat transfer and friction factor correlations for a solar air heater duct roughened artificially with V-ribs with symmetrical gaps, Experimental Thermal and Fluid Science, 70 (2016) 220-227.

[133] A.P. Singh, Varun, Siddhartha, Effect of artificial roughness on heat transfer and friction characteristics having multiple arc shaped roughness element on the absorber plate, Solar Energy, 105 (2014) 479-493.

[134] A.P. Singh, Varun, Siddhartha, Heat transfer and friction factor correlations for multiple arc shape roughness elements on the absorber plate used in solar air heaters, Experimental Thermal and Fluid Science, 54 (2014) 117-126.

[135] N.K. Pandey, V.K. Bajpai, Varun, Experimental investigation of heat transfer augmentation using multiple arcs with gap on absorber plate of solar air heater, Solar Energy, 134 (2016) 314-326.

[136] A. Lanjewar, J. Bhagoria, R. Sarviya, Heat transfer and friction in solar air heater duct with W-shaped rib roughness on absorber plate, Energy, 36(7) (2011) 4531-4541.

[137] V.B. Gawande, A. Dhoble, D. Zodpe, S. Chamoli, Experimental and CFD investigation of convection heat transfer in solar air heater with reverse L-shaped ribs, Solar Energy, 131 (2016) 275-295.

[138] N. Pandey, V. Bajpai, Experimental investigation of heat transfer augmentation using multiple arcs with gap on absorber plate of solar air heater, Solar Energy, 134 (2016) 314-326.

[139] A. FLUENT, 15.0 Theory Guide, Ansys Inc, 5 (2013).

[140] H.K. Versteeg, W. Malalasekera, An introduction to computational fluid dynamics: the finite volume method, Pearson Education, 2007.

[141] E. Abu-Nada, A.J. Chamkha, Effect of nanofluid variable properties on natural convection in enclosures filled with a CuO–EG–water nanofluid, International Journal of Thermal Sciences, 49(12) (2010) 2339-2352.

[142] H. Mohammed, A. Al-Shamani, J. Sheriff, Thermal and hydraulic characteristics of turbulent nanofluids flow in a rib–groove channel, International Communications in Heat and Mass Transfer, 39(10) (2012) 1584-1594.

[143] M. Jahanshahi, S. Hosseinizadeh, M. Alipanah, A. Dehghani, G. Vakilinejad, Numerical simulation of free convection based on experimental measured conductivity in a square cavity using water/SiO 2 nanofluid, International communications in heat and mass transfer, 37(6) (2010) 687-694.

[144] R.S. Vajjha, D.K. Das, Experimental determination of thermal conductivity of three nanofluids and development of new correlations, International Journal of Heat and Mass Transfer, 52(21) (2009) 4675-4682.

[145] B. Ghasemi, S. Aminossadati, Brownian motion of nanoparticles in a triangular enclosure with natural convection, International Journal of Thermal Sciences, 49(6) (2010) 931-940.

[146] R.S. Vajjha, D.K. Das, D.P. Kulkarni, Development of new correlations for convective heat transfer and friction factor in turbulent regime for nanofluids, International Journal of Heat and Mass Transfer, 53(21) (2010) 4607-4618.

[147] R.S. Vajjha, D.K. Das, Specific heat measurement of three nanofluids and development of new correlations, Journal of heat transfer, 131(7) (2009) 071601.

[148] B.C. Sahoo, Measurement of rheological and thermal properties and the freeze-thaw characteristics of nanofluids, 2008.

[149] M. Corcione, Heat transfer features of buoyancy-driven nanofluids inside rectangular enclosures differentially heated at the sidewalls, International Journal of Thermal Sciences, 49(9) (2010) 1536-1546.

[150] J. Tu, G.H. Yeoh, C. Liu, Computational fluid dynamics: a practical approach, Butterworth-Heinemann, 2007.

[151] S.V. Patankar, D.B. Spalding, A calculation procedure for heat, mass and momentum transfer in three-dimensional parabolic flows, International journal of heat and mass transfer, 15(10) (1972) 1787-1806.

[152] L. Mangani, C. Bianchini, Heat transfer applications in turbomachinery, in: Proceedings of the OpenFOAM International Conference, 2007.

[153] J.P. Van Doormaal, G.D. Raithby, ENHANCEMENTS OF THE SIMPLE METHOD FOR PREDICTING INCOMPRESSIBLE FLUID FLOWS, Numerical Heat Transfer, 7(2) (1984) 147-163.

[154] S.C. Saha, M.M.K. Khan, Y.T. Gu, Unsteady buoyancy driven flows and heat transfer through coupled thermal boundary layers in a partitioned triangular enclosure, International Journal of Heat and Mass Transfer, 68 (2014) 375-382.

[155] P. Huang, J. Bardina, T. Coakley, Turbulence Modeling Validation, Testing, and Development, NASA Technical Memorandum, 110446 (1997).

[156] P. Sagaut, Large eddy simulation for incompressible flows: an introduction, Springer Science & Business Media, 2006.

[157] S.B. Pope, Turbulent flows, in, IOP Publishing, 2001.

[158] J. Smagorinsky, General circulation experiments with the primitive equations: I. the basic experiment*, Monthly weather review, 91(3) (1963) 99-164.

[159] F. Nicoud, F. Ducros, Subgrid-scale stress modelling based on the square of the velocity gradient tensor, Flow, turbulence and Combustion, 62(3) (1999) 183-200.

[160] N. Ben-Cheikh, F. Hammami, A. Campo, B. Ben-Beya, A dynamic sub-grid scale model for large eddy simulation of turbulent flows in a lid-driven cubical cavity, Comptes Rendus Mécanique, 340(10) (2012) 721-730.

[161] M. Sharif, Laminar mixed convection in shallow inclined driven cavities with hot moving lid on top and cooled from bottom, Applied thermal engineering, 27(5) (2007) 1036-1042.

[162] C.-L. Chen, C.-H. Cheng, Experimental and numerical study of mixed convection and flow pattern in a lid-driven arc-shape cavity, Heat and mass transfer, 41(1) (2004) 58-66.

[163] A.K. Prasad, J.R. Koseff, Reynolds number and end-wall effects on a lid-driven cavity flow, Physics of Fluids A: Fluid Dynamics (1989-1993), 1(2) (1989) 208-218.

[164] S.-H. Peng, P. Doerffer, W. Haase, Progress in Hybrid RANS-LES Modelling, (2009).

[165] E.L.M. Padilla, A.L. Martins, A. Silveira-Neto, A. Large-Eddy Simulation of the Three-Dimensional Unstable Flow in a Lid-Driven Cavity, in: 18th International Congress of Mechanical Engineering, Ouro Preto, COBEM, 2005, pp. 1-8.

[166] A.K. Kareem, H. Mohammed, A.K. Hussein, S. Gao, Numerical investigation of mixed convection heat transfer of nanofluids in a lid-driven trapezoidal cavity, International Communications in Heat and Mass Transfer, 77 (2016) 195-205.

[167] S. Patankar, Numerical heat transfer and fluid flow, CRC press, 1980.

[168] A.K. Kareem, S. Gao, A.Q. Ahmed, Unsteady simulations of mixed convection heat transfer in a 3D closed lid-driven cavity, International Journal of Heat and Mass Transfer, 100(Supplement C) (2016) 121-130.

[169] A.K. Kareem, S. Gao, Computational study of unsteady mixed convection heat transfer of nanofluids in a 3D closed lid-driven cavity, International Communications in Heat and Mass Transfer, 82(Supplement C) (2017) 125-138.

[170] A. Khaleel, S. Gao, CFD Investigation of Turbulent Mixed Convection Heat Transfer in a Closed Lid-Driven Cavity.

[171] A.K. Kareem, S. Gao, A comparison study of mixed convection heat transfer of turbulent nanofluid flow in a three-dimensional lid-driven enclosure with a clockwise versus an anticlockwise rotating cylinder, International Communications in Heat and Mass Transfer, 90 (2018) 44-55.

[172] A.K. Kareem, S. Gao, Mixed convection heat transfer of turbulent flow in a three-dimensional lid-driven cavity with a rotating cylinder, International Journal of Heat and Mass Transfer, 112(Supplement C) (2017) 185-200.

[173] A.K. Kareem, S. Gao, Mixed turbulent convection heat transfer in a 3D lid-driven cavity containing a rotating cylinder, in: 257th International Conference on Heat Transfer and Fluid Flow (ICHTFF), ISER, Toronto, Canada, 2018.

[174] A.K. Kareem, S. Gao, Mixed convection heat transfer enhancement in a cubic lid-driven cavity containing a rotating cylinder through the introduction of artificial roughness on the heated wall, Physics of Fluids, 30(2) (2018) 025103.

[175] A.K. Kareem, S. Gao, A.Q. Ahmed, Mixed Convection Enhancement in a 3D Lid-Driven Cavity Containing a Rotating Cylinder by Applying an Artificial Roughness, International Journal of Mechanical, Aerospace, Industrial, Mechatronic and Manufacturing Engineering, 12 (2018) 441-446.

[176] F. Selimefendigil, H.F. Öztop, Mixed convection of nanofluids in a three dimensional cavity with two adiabatic inner rotating cylinders, International Journal of Heat and Mass Transfer, 117(Supplement C) (2018) 331-343.

[177] B. Karbasifar, M. Akbari, D. Toghraie, Mixed convection of Water-Aluminum oxide nanofluid in an inclined lid-driven cavity containing a hot elliptical centric cylinder, International Journal of Heat and Mass Transfer, 116 (2018) 1237-1249.

Appendices

Appendix A: UDF codes for CFD model parameters

The UDFs for calculating the density of nanofluids (3.4)

```
#include "udf.h"

#define DEN_np      3970            /* Density of Nanoparticles……....kg/m^3 */
#define DEN_w       997.1           /* Density of Pure Water………....kg/m^3 */
#define VF          0.00 to 0.08    /* Volume Fraction of Nanoparticles…… */

DEFINE_PROPERTY(Cell_Density, cell, thread)

{

    double DEN_nf                       ;   /* Mixture Density…….kg/m^3 */
    DEN_nf = VF * DEN_np + ( 1 - VF ) * DEN_w      ;
    return DEN_nf                       ;

}
```

The UDFs for calculating the heat capacity of nanofluids (3.5)

```
#include "udf.h"
```

```
#define DEN_np      3970     /* Density of Nanoparticles………...kg/m^3 */
#define DEN_w       997.1    /* Density of Pure Water................kg/m^3 */
#define CP_np       765      /* Heat Capacity of Nanoparticles...J/kg*K */
#define CP_w        4179     /* Heat Capacity of Pure Water…....J/kg*K */
#define VF          0.08     /* Volume Fraction of Nanoparticles..........*/

DEFINE_SPECIFIC_HEAT(Specificheat, T, Tref, h, yi)

{

    double CP_nf                ;   /* Heat Capacity of Nanofluid ....J/kg*K */
    double DEN_nf               ;   /* Mixture Density of Nanofluid..kg/m^3 */
    DEN_nf = VF * DEN_np + ( 1 - VF ) * DEN_w                  ;
    *h =CP_nf*(T-Tref)                                         ;
    CP_nf =( (( 1 - VF ) *  DEN_w * CP_w ) + (VF *  DEN_np *   ;
    CP_np) ) / DEN_nf

    return CP_nf                                               ;

}
```

The UDFs for calculating the thermal conductivity of nanofluids (3.6)

```
#include "udf.h"
```

```
#define DEN_np   3970       /* Density of Nanoparticles....................kg/m^3 */

#define CP_np    765        /* Heat Capacity of Nanoparticles............/kg*K */

#define CON_np   36         /* Thermal Conductivity of
                               Nanoparticles…………………………...W/m-k */

#define DEN_w    997.1      /* Density of Pure Water........................kg/m^3 */

#define CP_w     4179       /* Heat Capacity of Pure Water..............J/kg*K */

#define CON_w    0.613      /* Thermal Conductivity of Pure Water...W/m-k */

#define VF       0.00-      /* Volume Fraction of Nanoparticles..................*/
                 0.08

#define DIA_np   1.00E-07   /* Diameter of Nanoparticles.............................*/


DEFINE_PROPERTY(Cell_Thermal_Conductivity, cell, thread)


{


    double temp            ;   /* Temperature.........................................K */

    double CON_static      ;   /* Static Thermal Conductivity..........W/m-K */

    double CON_browni      ;   /* Brownian Thermal Conductivity….W/m-K */

    double B               ;   /* The modeling Function of SiO2................*/

    double To              ;

    double K_boltzman      ;   /* Boltzman Constant..................................*/

    double F               ;   /* The modeling function (T,VF)...................*/

    double CON_eff         ;   /* Effective Thermal Conductivity......W/m-k */

    To= 290                ;

    CON_static = CON_w * ( ( CON_np + 2 * CON_w - 2 * ( CON_w -
    CON_np ) * VF) / ( CON_np + 2 * CON_w + ( CON_w - CON_np ) * VF
    ) )                                                              ;

    K_boltzman = 1.3807 * pow ( 10, -23 )                            ;
```

```
    B = 1.9526 * pow ( (100 * VF ), -1.4594 )                          ;

    temp = C_T ( cell,thread )                                          ;

    F = ( 2.8217 * pow ( 10, -2 ) * VF + 3.917 * pow ( 10,-3 ) ) * ( temp / To )
    + ( -3.0699 * pow ( 10, -2 ) - 3.91123 * pow ( 10, -3 ) )
                                                                        ;

    CON_browni = 5 * pow ( 10,4 ) * B * VF * DEN_w * CP_w * pow ( (
    K_boltzman * temp / 2 * DEN_np * DIA_np ), 0.5 ) * F
                                                                        ;

    CON_eff = CON_static + CON_browni                                    ;


    return CON_eff                                                      ;


}
```

The UDFs for calculating the dynamic viscosity of nanofluids (3.13)

```
#include "udf.h"


#define DEN_np    3970        /* Density of Nanoparticles................kg/m^3 */

#define DEN_w     997.1       /* Density of Pure Water....................kg/m^3 */

#define CON_w     0.613       /* Thermal Conductivity of Pure
                                 Water……………………………………W/m-k */

#define VF        0.00-       /* Volume Fraction of Nanoparticles..............*/
                  0.08

#define DIA_np    1.00E-07    /* Diameter of Nanoparticles..........................*/

#define VIS_w     8.90E-04    /* Dynamic Viscosity of Pure Water......Pa*S */


DEFINE_PROPERTY(Cell_Dynamic_Viscosity, cell, thread)
```

```
{

    double DIA_w      ;  /* Fluid Molecule Diameter...............................m */
    double Pi         ;  /* Constant Value................................................*/
    double M_w        ;  /* Molecular Weight of Pure Water.......................*/
    double N1         ;  /* Avogadro Number..................................1/mol */
    double VIS_nf     ;  /* Effective Dynamic Viscosity of Nanofluid.Pa*S */
    Pi= 3.14                                                                   ;
    M_w= 0.01801528                                                            ;
    N1= 6.022 * pow ( 10, 23 )                                                 ;
    DIA_w = pow ( ( 6* M_w / ( N1 *Pi *DEN_w ) ) , 0.33333 )                   ;
    VIS_nf = VIS_w / ( 1 - 34.87 * pow ( ( DIA_np / DIA_w ), ( -0.3 ) ) *      ;
    pow ( VF,1.03 ) )

    return VIS_nf                                                              ;

}
```